INAUGURAL - DISSERTATION

ZUR
ERLANGUNG DER DOKTORWÜRDE
DER
NATURWISSENSCHAFTLICH-MATHEMATISCHEN-GESAMTFAKULTÄT
DER
RUPRECHT-KARLS-UNIVERSITÄT
HEIDELBERG

vorgelegt von
Dipl.-Inf. Steffen Remmele
aus Sinsheim

Tag der mündlichen Prüfung: 20.06.2012

A Deconvolution Framework with Applications in Medical and Biological Imaging

Gutachter: Prof. Dr. Jürgen Hesser
Prof. Dr. Fred Hamprecht

Abstract

A deconvolution framework is presented in this thesis and applied to several problems in medical and biological imaging. The framework is designed to contain state of the art deconvolution methods, to be easily expandable and to combine different components arbitrarily. Deconvolution is an inverse problem and in order to cope with its ill-posed nature, suitable regularization techniques and additional restrictions are required.

A main objective of deconvolution methods is to restore degraded images acquired by fluorescence microscopy which has become an important tool in biological and medical sciences. Fluorescence microscopy images are degraded by out-of-focus blurring and noise and the deconvolution algorithms to restore these images are usually called deblurring methods. Many deblurring methods were proposed to restore these images in the last decade which are part of the deconvolution framework. In addition, existing deblurring techniques are improved and new components for the deconvolution framework are developed. A considerable improvement could be obtained by combining a state of the art regularization technique with an additional non-negativity constraint. A real biological screen analysing a specific protein in human cells is presented and shows the need to analyse structural information of fluorescence images. Such an analysis requires a good image quality which is the aim of the deblurring methods if the required image quality is not given.

For a reliable understanding of cells and cellular processes, high resolution 3D images of the investigated cells are necessary. However, the ability of fluorescence microscopes to image a cell in 3D is limited since the resolution along the optical axis is by a factor of three worse than the transversal resolution. Standard microscopy image deblurring techniques are able to improve the resolution but the problem of a lower resolution in direction along the optical axis remains. It is however possible to overcome this problem using Axial Tomography providing tilted views of the object by rotating it under the microscope. The rotated images contain additional information about the objects which can be used to improve the resolution along the optical axis. In this thesis, a sophisticated method to reconstruct a high resolution Axial Tomography image on basis of the developed deblurring methods is presented.

The deconvolution methods are also used to reconstruct the dose distribution in proton therapy on basis of measured PET images. Positron emitters are activated by proton beams but a PET image is not directly proportional to the delivered radiation dose distribution. A PET signal can be predicted by a convolution of the planned dose with specific filter functions. In this thesis, a dose reconstruction method based on PET images which reverses the convolution approach is presented and the potential to reconstruct the actually delivered dose distribution from measured PET images is investigated.

Last but not least, a new denoising method using higher-order statistic information of a given Gaussian noise signal is presented and compared to state of the art denoising methods.

Zusammenfassung

In dieser Arbeit wird ein Framework an Entfaltungsverfahren vorgestellt und auf verschiedene Probleme in der medizinischen und biologischen Bildgebung angewendet. Das Framework, welches Methoden des aktuellen Standes der Technik enthält, wurde entworfen, um leicht erweiterbar zu sein. Des Weiteren bietet es die Möglichkeit, verschiedene Komponenten beliebig zu kombinieren. Entfaltung ist ein inverses Problem und um mit der schlecht gestellten Natur dieses Problems zurecht zu kommen, sind geeignete Regularisierungsverfahren sowie zusätzliche Beschränkungen erforderlich.

Ein Hauptziel der Entfaltungsmethoden ist die Wiederherstellung von verschmierten und verrauschten Bildern, die mittels Fluoreszenzmikroskopie aufgenommen wurden. Durch Entfaltung sollen die Bilder wiederhergestellt werden. Viele solcher Verfahren wurden in den letzten Jahren entwickelt. Zusätzlich wurden bereits bestehende Techniken verbessert und neue Komponenten für das Framework entwickelt. Es ließ sich eine beachtliche Verbesserung erzielen, indem ein Regularisierungsverfahren mit einer zusätzlichen Einschränkung auf nicht negative Werte kombiniert wurde. Eine biologische Untersuchungsreihe, die ein spezielles Protein in menschlichen Zellen untersucht, wird vorgestellt und zeigt die Notwendigkeit, strukturelle Informationen in Fluoreszenzbildern zu analysieren. Für eine solche Analyse ist eine gute Bildqualität erforderlich. Sollte die geforderte Bildqualität nicht gegeben sein, kann diese durch die Entfaltungsmethoden ermöglicht werden.

Für ein zuverlässiges Verständnis von Prozessen in Zellen werden hoch aufgelöste 3D Bilder der untersuchten Zellen benötigt. Die Fähigkeiten von Fluoreszenzmikroskopen Bilder in 3D aufzunehmen sind jedoch eingeschränkt, da die Auflösung entlang der optischen Achse um einen Faktor drei schlechter ist als in die anderen beiden Dimensionen des Bildes. Entfaltungsverfahren sind zwar in der Lage, die Auflösung der Bilder zu verbessern, aber das Problem der schlechteren Auflösung in Richtung der optischen Achse wird dadurch nicht gelöst. Es ist möglich, dieses Problem mittels axialer Tomographie zu überwinden, in dem das Objekt unter dem Mikroskop rotiert und aus verschiedenen Blickwinkeln aufgenommen wird. Die so entstandenen Bilder enthalten zusätzlichen Informationen, die in einem neuen hochentwickelten Verfahren dazu verwendet werden, die Auflösung entlang der optischen Achse zu verbessern. Dieses neue Verfahren basiert auf den Entfaltungsmethoden.

Die Entfaltungsmethoden werden auch dazu verwendet, die Dosisverteilung in der Protonentherapie auf Basis von PET Bildern zu rekonstruieren. Ein bei der Protonenbestrahlung entstandenes PET Signal kann durch eine Faltung der geplanten Dosis mit einer speziellen Filterfunktion vorhergesagt werden. Eine Entfaltung des PET Signals erlaubt wiederum die Rekonstruktion der Dosis und bietet somit die Möglichkeiten, die tatsächlich abgegebene Dosis anhand von gemessenen PET Daten zu rekonstruieren.

Abschließend wird ein neues Entrauschungsverfahren vorgestellt, das statistische Informationen höherer Ordnung für ein gegebenes Gausssches Rauschsignal verwendet.

Erklärung

Hiermit erkläre ich, Steffen Remmele, dass ich die vorgelegte Dissertation selbst verfasst und mich dabei keiner anderen als der von mir ausdrücklich bezeichneten Quellen und Hilfen bedient habe.

Heidelberg, den 21.10.2011

Preface

This PHD thesis contains several different research projects with different project partners. Parts of this work have already been published at different national/international conferences and in journals.

A cell analysis tool was developed in cooperation with AG Nickel (Biochemical Center, University of Heidelberg). The analysis tool was presented at the MIAAB workshop in New York in 2008 [135] and an extension at the SPIE conference in Orlando, Florida in 2011 [136]. The tool was successfully used in the analysis of all screening data in the PHD thesis "Identification of Components of the Intracellular Transport Machinery of Acylated Proteins by a Genome-wide RNAi Screen" of Julia Ritzerfeld [139] and this work was published in the Genome Research journal in 2011 [140].

The improvements of the deconvolution framework were published and presented at various conferences. The new deblurring algorithm containing the Bregman distance was presented at the BVM conference in 2008 [137] while the accelerated version of the iterative Richardson-Lucy algorithm with Total Variation regularization was published at the BVM conference in 2009 [131]. The new deblurring method using a constraint conjugate gradient method to enforce non-negativity in combination with a background signal was presented at the World Congress on Medical Physics and Biomedical Engineering in 2009 [130].

The reconstruction of a high resolution image on basis of Axial Tomography images was a project in collaboration with the AG Cremer/Hausmann (Kirchhoff Institute for Physics, University of Heidelberg). Parts of the axial reconstruction approach were presented at the SPIE conference in Orlando, Florida in 2011 [134].

The dose deconvolution approach was developed in collaboration with Thomas Bortfeld and Harald Paganetti (Massachusetts General Hospital and Harvard Medical School) during my six month research visit at the MGH. Parts of the dose deconvolution method were presented at the joint AAPM/COMP conference in 2011 [133]. Furthermore, a paper containing a detailed description of the approach is accepted in the Physics in Medicine and Biology journal [132].

After proofing the feasibility of the Higher Order Statistics denoising approach, a joint project with the AG Steidl (Mathematical Image Processing and Data Analysis Group, University of Kaiserslautern) was started and an extension of the original approach with a substantial theoretical introduction is submitted to the Journal on Signal Processing [158].

Acknowledgement

First and foremost, I would like to thank my doctoral adviser Jürgen Hesser for giving me the opportunity to work in research and, most of all, that I could visit the Massachusetts General Hospital for six month.

I am really thankful to Julia Ritzerfeld and Walter Nickel for a great collaboration. I totally enjoyed our project and it is always great if the developed software tools are used and helpful.

I am grateful to all colleagues in the Department of Radiation Oncology at the Massachusetts General Hospital who made my research visit a very enjoyable period in my life. In particular, I would like to thank Thomas Bortfeld and Harald Paganetti for their valuable support and that they allowed me to work on this project.

I would like to thank the AG Cremer/Hausmann at the Kirchhoff Institute for Physics for their fruitful collaboration, especially Heinz Eipel for his support and many discussions.

I am also grateful to Tanja Teuber and Gabriele Steidl. Our collaboration was very illuminating and I enjoyed our discussions.

Special thanks goes to Christiane Glasbrenner and my colleagues Tobias Stutzmann and Jens Muders. In countless moments during the last years I was deeply grateful to have them close by. Their support, comments and encouragements helped me a lot.

I am also grateful to Tim and Ciamak. We started our studies together a long time ago and all became PHD students afterwards. We walked this road together and I am really happy to have met you.

My more private thanks go to my friends and family. I am really grateful to Andreas, Anna, Bryan, Chris, Connie, Denise, Dirk, Djiby, Dominik, Flo, Golli, Jenny, Joe, Johanna, Julia, Laura, Manu, Markus, Nico, Sabine, Sabine, Senta and Tobias for all your encouragements and diversions. Finally, I would like to thank my parents and my sister Nicole for all the love and support and for being present during this time. I wouldn't have made it without your help!

.

'So eine Arbeit wird eigentlich nie fertig,
man muß sie für fertig erklären,
wenn man nach Zeit und Umständen
das Mögliche getan hat.'

Johann Wolfgang von Goethe
Italienische Reise, 1787

Contents

Part I.

Introduction and Motivation

1. Preamble

Deconvolution is challenging research area and there are many applications in digital image processing. In this thesis, a deconvolution framework containing state of the art deconvolution methods is presented and the focus is on several applications in medical and biological imaging. In addition, the basic deconvolution framework is extended by improved deconvolution methods. Deconvolution means by definition to reverse a convolution which sounds quite simple at first sight. However, deconvolution is an ill-posed inverse problem and not trivial to solve. In addition, all recorded images contain noise which is a major problem in deconvolution.

In confocal fluorescence microscopy which is one application addressed in this thesis the recorded images are degraded by blur and usually a strong noise signal. Such an image of a human cell is shown in figure 1.1 on the left side. For a reliable understanding of cellular processes, a good quality of the images is necessary and many discoveries are based on the possibility to analyse fine details in the images. Since the quality of the recorded images is sometimes not sufficient, restoration methods to reverse the degradations are required. The blur in the image can be described by a convolution with an appropriate filter mask and thus a deconvolution is a suitable tool to remove the blurring in the image. Additionally, the recorded image contains noise and thus the reconstruction of the image becomes more difficult. The restoration of microscopy images is usually denoted as deblurring and a deblurring result of the cell is shown in figure 1.1 on the right side. The noise given in the measured microscopy image is removed and the resolution of the image is enhanced. Finer structures of the cell are visible and a more detailed analysis of the cell is possible. In order to emphasize the improvement of the image quality given by the deblurring method, the measured image and the reconstructed image are merged in figure 1.2.

Cells are three-dimensional entities and the ability of fluorescence microscopes to image a cell in 3D is limited. The resolution of the acquired volumes in direction along the optical axis is considerably smaller than in transversal direction. Image deblurring techniques are able to improve the resolution but the problem of a lower resolution in direction along the optical axis remains. It is however possible to overcome this problem using Axial Tomography providing tilted views of the object by rotating it under the microscope. The rotated images contain additional information about the objects which can be used to improve the resolution along the optical axis. An approach to reconstruct a high resolution image on basis of the rotated images is presented. This approach is based on deblurring methods and the components of the deconvolution framework

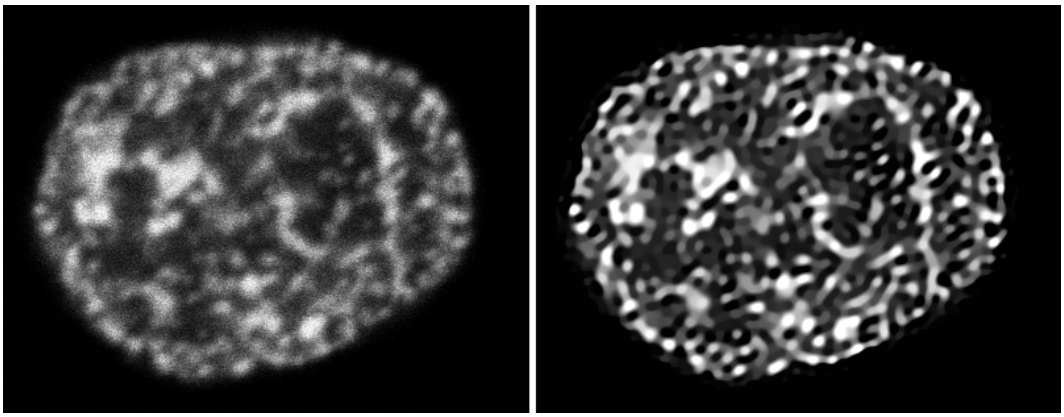

Fig. 1.1.: Measured fluorescence microscopy image (Left) and deblurring result of human cell (Right).

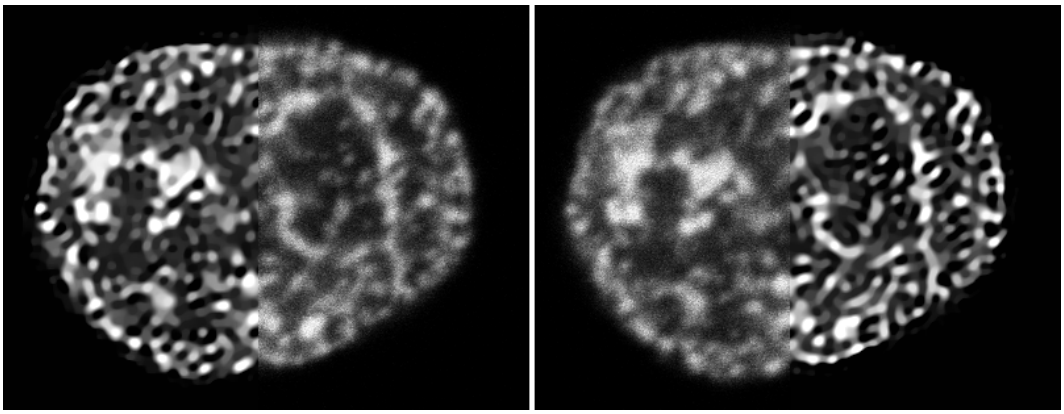

Fig. 1.2.: Overlapping of measured cell image and deblurring result.

are used to reconstruct the Axial Tomography image. Prior to the reconstruction, a bleaching correction is necessary and the additional images have to be aligned correcting translational and rotational shifts. A multi-resolution rigid registration method is used for that purpose.

Another application of the deconvolution framework is the dose reconstruction in proton radiotherapy based on PET images. The main purpose of the PET treatment verification is currently the verification of the proton beam range. The objective of the dose reconstruction approach is to improve the range verification by reconstructing the delivered dose and to eventually extend the method from range verification to overall treatment verification. Since a PET image is not directly proportional to the delivered radiation dose distribution, predicted PET images are compared to measured PET images and an agreement of both indicates a successful irradiation. Such predictions are given on basis of Monte Carlo calculations or a filtering approach which uses a convolution of the planned dose with specific filter functions to estimate the PET activity. A deconvolution is thus able to reverse the PET prediction based on the convolution approach and allows the dose reconstruction on basis of measured PET signals obtained after the irradiation. In addition, the PET images are degraded by a point spread function convolution and contain noise. Not considering these degradation leads to large artifacts in the dose reconstruction result and removing this convolution is thus mandatory by applying another suitable deconvolution method.

The outline of this thesis is as follows. First, a detailed definition of ill-posed inverse problems is given and the underlying imaging systems of the medical and biological applications of the deconvolution framework are described. A RNAi-based high-throughput microscopy screen to investigate intracellular trafficking and targeting of acylated Src kinases is presented in order to motivate the topic of image deblurring. An automated software tool was developed to interpret the images acquired in this screen and structural information in the fluorescence microscopy images have to be analysed. A good image quality is therefore required and a preprocessing deblurring step can improve the image quality and allow more reliable results. The architecture of the realized deconvolution framework and its basic components are presented in chapter 6. The improved deconvolution methods are described in chapter 7 and the methods to evaluate the reconstruction results can be found in chapter 8. Results using the standard components of the deconvolution framework and results of the improved deconvolution methods are presented in chapter 9. The reconstruction methods for the Axial Tomography and corresponding results are shown in chapter 10 while chapter 11 contains the dose reconstruction methods for the proton radiotherapy based on PET images. A conclusion chapter completes the main part of this thesis. Before an outlook is given in the last chapter, a feasibility test for a new denoising approach using higher order statistics is presented in chapter 13.

2. Deconvolution as ill-posed Inverse Problem

Inverse problems were introduced in medical image processing when the first CT images were reconstructed. A CT provides a series of projections of the investigated object which cannot be directly interpreted by a physician. First, an image about the original object has to be reconstructed using the projections. The reconstruction is hereby called the inverse problem in relation to the forward or direct problem of generating the projections. Another example for an inverse problem is microscopy deconvolution also called microscopy deblurring. Due to the diffraction limit of light and the optical aperture of a microscope, the images are blurred with a point spread function (PSF) which represents the forward problem in this case. In order to reconstruct the original image, the inverse problem of deconvolving the recorded image with the PSF has to be solved. PET images and microscopy images are in fact quite similar because a PET image is also degraded by a PSF as well. Furthermore, the dose reconstruction method presented in this thesis is realized by a deconvolution as well and thus also belongs to this class of problems.

Unfortunately, a typical property of inverse problems is ill-posedness which means by definition that these problems are not well-posed. The concept of well-posed problems was introduced by Hadamard [62] on boundary value problems for partial differential equations and their physical interpretation. A well-posed problem has an unique solution and exists for arbitrary data according to this first formulation. Later, Hadamard added the continuous dependence of the solution on the data claiming that a solution which varies considerably on small variations is not really a solution in the physical sense. In addition, this third property is of importance since physical data is never known exactly due to noise and other degradations which occur during measurements. In general, a direct or forward problem, i.e. a problem oriented along a cause-effect sequence, is well-posed while the corresponding inverse problem, which implies a reversal of the cause-effect sequence, is ill-posed. A forward problem, e.g. a convolution, can be described by $y = Ax$. Hereby, x represents the original object, A is a matrix describing the properties of the imaging system and y denotes the result of the measurement. x is an element of X, y an element of Y and thus A describes a transformation from $X \rightarrow Y$. The corresponding inverse problem which implies a reversal of the cause-effect sequence is well-posed if the following properties are fulfilled:

- The solution of the problem exists:

$\forall y \in Y, \exists x \in X : Ax = y$

- The solution of the problem is unique:
  $y_1 = y_2 \Leftrightarrow Ax_1 = Ax_2 \Rightarrow x_1 = x_2$
- The solution depends with continuity on the data:
  A^{-1} exisits and describes a continuous transformation.

If one of these properties is violated, the inverse problem is called an ill-posed problem. Ill-posed inverse problems are in particular sensitive to noise since the third property is usually violated. If not considered correctly, noise or other small variations in the data can be amplified and degrade the reconstruction result considerably.

3. Fluorescence Microscopy Imaging

3.1. Fluorescence Microscopy

Fluorescence microscopy is a widely spread imaging technique used in nearly all fields of cell and molecular biology. The principle of fluorescence is the excitation of a fluorescent molecule with light of a specific wavelength and the almost instantly responding emission of light with a longer characteristic wavelength (Figure 3.1). The excitation light is absorbed and the released energy moves an electron from an inner orbital of the fluorescent molecule to an orbital being farther away from the nucleus. After usually losing a bit of its energy by vibrational relaxation the electron moves back to its initial ground state while emitting the remaining energy as fluorescence light. The difference in the wavelengths between the absorbed and emitted light, known as Stokes shift, is the reason that fluorescence can be used as powerful imaging technique. The exciting light is completely filtered while the emitted fluorescence light can be detected (Figure 3.2). As result, the fluorescent object can be seen in high contrast because the background, assuming no other light sources of the given wavelength, remains dark. Over the last decades many thousands of fluorescent probes have been developed and these probes can be used to label virtually any imaginable aspect of biological systems. It is even possible to use more fluorophores to image different components simultaneously [92].

In principle, there are two different types of fluorescence microscopes: widefield microscopes and confocal microscopes. Both microscope types are low-photon imaging techniques suffering from Poisson noise typical for such techniques. In conventional widefield microscopy, a slice of the imaged specimen is excited and imaged at once (Figure 3.3). This procedure can be repeated at different depths within the whole specimen resulting in an image stack forming a complete 3D volume. Exciting a huge area of the specimen leads to a high degree of fluorescence emission and most of the fine detail is lost. Especially when imaging thicker specimen, emission light from outside the focal plane can be seen in the images. Confocal microscopy is able to exclude the surrounding fluorescence light and thus provides a higher resolution [154], [89].

In confocal microscopy, the specimen is scanned and imaged point-by-point in 3D [109] [38] [176] [37] (Figure 3.4). A focused laser beam is used to excite the actually scanned region. The rest of the specimen mostly remains dark and no fluorescence light

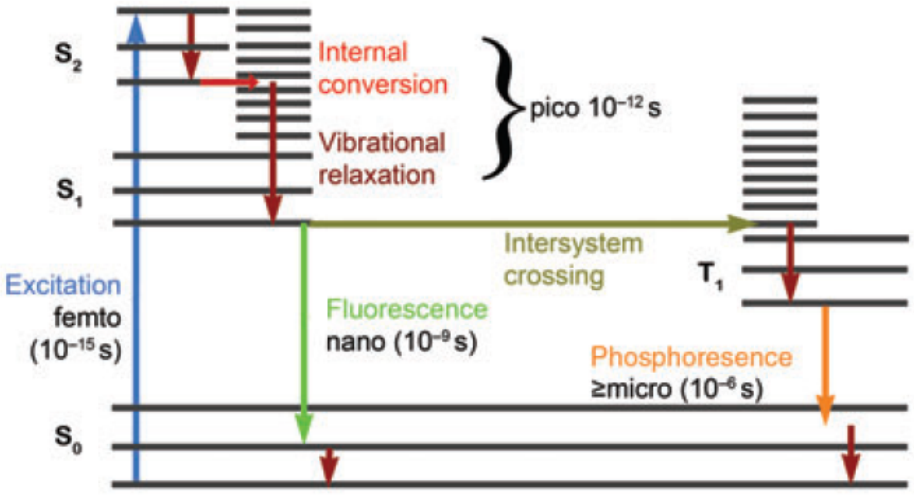

Fig. 3.1.: Fluorescence principle.

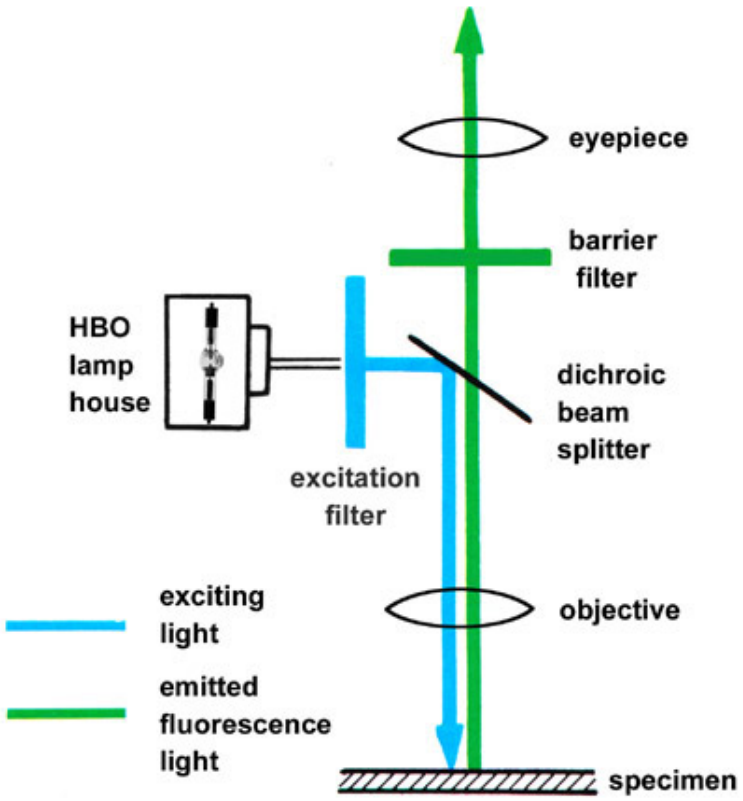

Fig. 3.2.: Basic schema of fluorescence microscope.

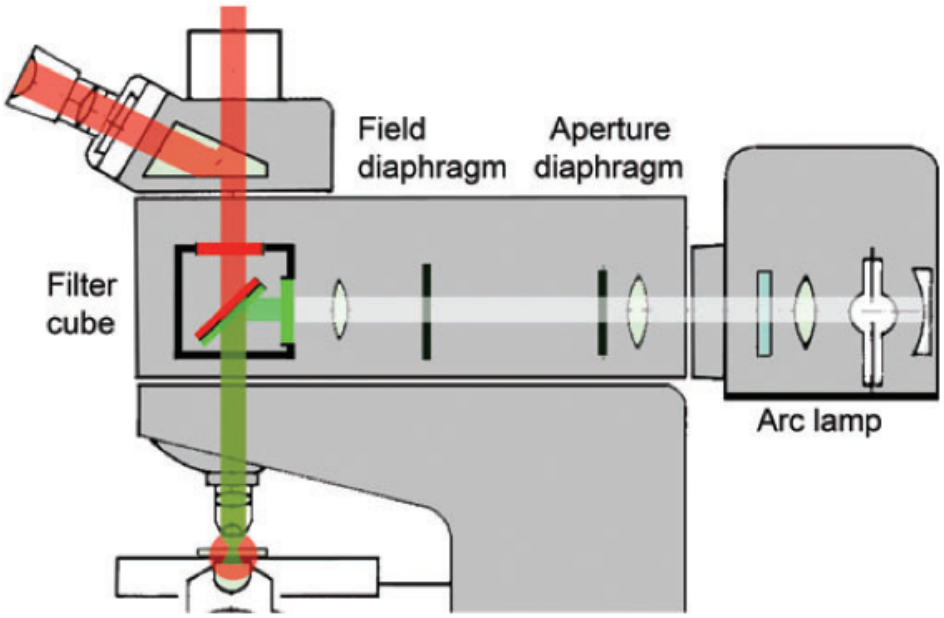

Fig. 3.3.: Imaging schema of a widefield microscope [92].

should arise from there. In addition, most out-of-focus light is excluded by a pinhole. Therefore, the acquired image has a higher resolution in x, y and z direction compared to widefield microscopy [154], [89] but there is still blur in these images. There are two properties that still influence the quality of the images. The pinhole is able to reject most out-of-focus light but the diffraction limited nature of the optics and light itself remains. Furthermore, the pinhole strongly reduces the amount of detectable light. It is not possible to increase the laser power in order to get a stronger signal because the risk of photo bleaching and photo toxicity increases at the same time. In general, the photo bleaching effect is stronger in confocal than in widefield microscopy imaging and it takes more time to acquire the image.

3.2. Image Formation Model

Widefield and confocal microscopy degrades the acquired images like any other optical system. The out-of-focus light blurs the image and can be described by a point spread function (PSF) convolution. Figure 3.5 shows the PSFs of a widefield and a confocal fluorescence microscope. Since fluorescence microscopy is a low-photon imaging technique, the noise statistics in the image is well described by a Poisson process which is represented by $\phi(.)$. A suitable image formation model with i being the observed image, o the original image and $*$ describing a convolution is given by:

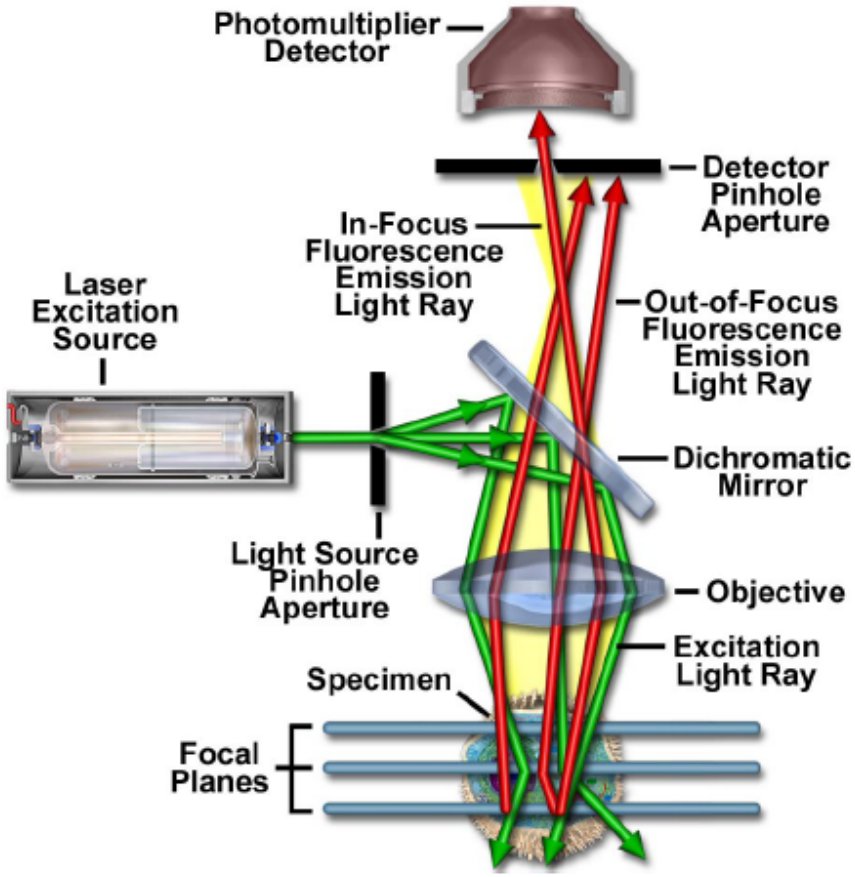

Fig. 3.4.: Imaging schema of a confocal microscope [35].

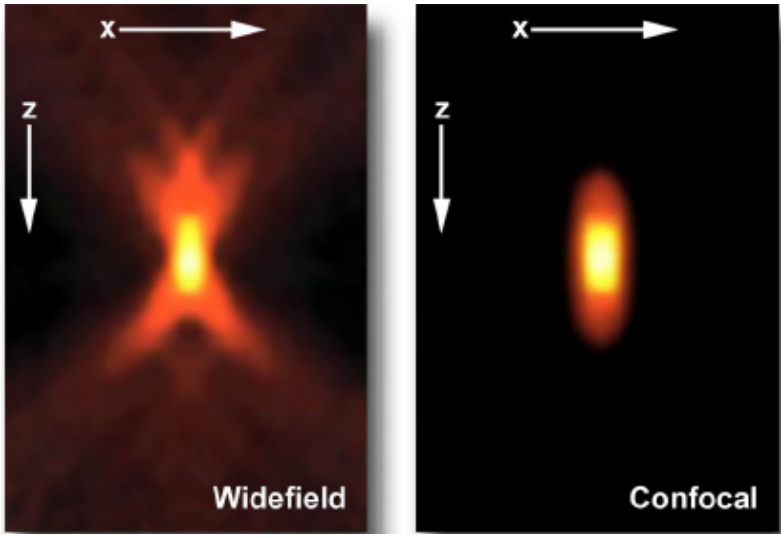

Fig. 3.5.: PSF of widefield and confocal Microscopy [35].

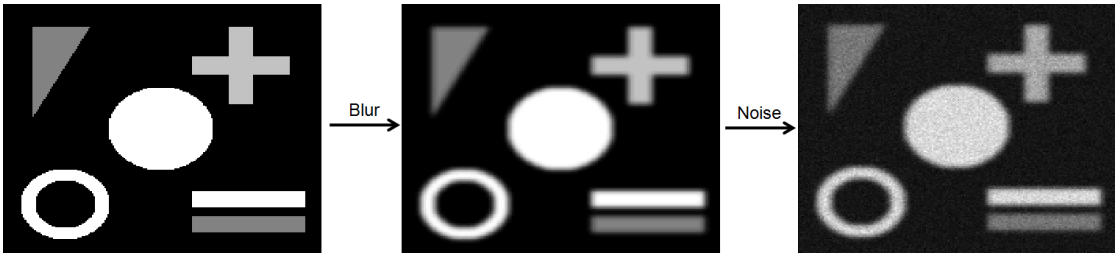

Fig. 3.6.: Illustration of image formation model.

$$i = \phi(o * PSF) \tag{3.2.1}$$

Hereby, the three-dimensional digital images i and o are given as functions of the form $f : \Omega \to R$ defined on a restricted image domain $\Omega \subset Z^3$. In fact, there are no negative values in the images and because of the discretisation to integer values, the range of these functions is actually N_0 with an upper boundary given by the data format. There is a background signal b in fluorescence microscopy images and an extended image formation model was thus suggested [163]:

$$i = \phi(o * PSF + b) \tag{3.2.2}$$

Figure 3.6 illustrates the image formation model step by step. The image is blurred in a first step and additional Poisson noise is added in a second step resulting in the degraded image.

3.2.1. PSF

For most deblurring methods, it is assumed that the PSF is already known. It is possible to use a second image with beads to estimate the PSF in a preceding step [178] or to calculate the PSF due to the physical properties of the used microscope. A centered and normalized Gaussian PSF with a certain variance is usually used. In general, the PSF is assumed to be constant all over the image plane but there are also approaches suggesting that the PSF varies in different depths. In [127] the authors assume that spherical aberrations worsen as the microscope is focused deeper and thus suggest a depth-varying image formation model. For the synthetic images used in this thesis, a centered normalized 3D Gaussian PSF with certain variances in all dimensions (σ_x, σ_y, σ_z) is used:

$$G(x,y,z) = \frac{1}{\sqrt{2\pi}^3 \sigma_x \sigma_y \sigma_z} e^{-\left(\frac{x^2}{2\sigma_x^2}+\frac{y^2}{2\sigma_y^2}+\frac{z^2}{2\sigma_z^2}\right)} \tag{3.2.3}$$

Fortunately, a Gaussian filter mask is separable. This means that it is possible to use three 1D convolutions with according 1D filter masks instead of one 3D convolution with a size given by the product of the sizes of the 1D filter masks. A one dimensional Gaussian filter function with a variance σ^2 is given by:

$$G(x) = \frac{1}{\sqrt{2\pi}\sigma} e^{-\frac{x^2}{2\sigma^2}} \tag{3.2.4}$$

The principle of separable filters is described in the following using two dimensional functions. Separable filters based on three dimensional functions can be created in the same way using an additional analogous extension for the third dimension. An arbitrary two dimensional filter mask H_{xy} is separable if the condition in equation 3.2.5 is fulfilled, i.e. the filter function of H_{xy} can be separated in a product with each factor containing the according components of the filter mask for one dimension. A two dimensional Gaussian filter function can thus be separated according to equation 3.2.6.

$$H_{xy} = H_x \cdot H_y \tag{3.2.5}$$

$$G(x,y) = \frac{1}{2\pi\sigma_x\sigma_y} e^{-\left(\frac{x^2}{2\sigma_x^2}+\frac{y^2}{2\sigma_y^2}\right)} = \frac{1}{\sqrt{2\pi}\sigma_x} e^{-\frac{x^2}{2\sigma_x^2}} \cdot \frac{1}{\sqrt{2\pi}\sigma_y} e^{-\frac{y^2}{2\sigma_y^2}} \tag{3.2.6}$$

3.2.2. Poisson Noise

A major problem for ill-posed inverse problems is noise. If not considered properly noise is amplified and creates artifacts. There is Poisson noise in the fluorescence microscopy images. A Poisson noise distribution at point $x \in \Omega$ is described by:

$$P(i(x)|(o * PSF)(x)) = \frac{[(o * PSF)(x)]^{i(x)}\, e^{-(o*PSF)(x)}}{i(x)!} \tag{3.2.7}$$

i is the observed image and $o * PSF$ is the original image blurred by the PSF. Ω again denotes the image domain. Since it can be assumed that the noise in the observed fluorescence microscopy images is statistically uncorrelated, the present statistics is the likelihood distribution given by:

$$P(i|(o * PSF)) = \prod_{x \in \Omega} \frac{[(o * PSF)(x)]^{i(x)}\, e^{-(o*PSF)(x)}}{i(x)!} \tag{3.2.8}$$

4. PET Imaging in Proton Radiotherapy

Positron emitters are produced as a by-product in tissue which is penetrated by a proton beam (Figure 4.1). Hereby, nuclear interactions cause separations of neutrons from nuclei in the tissue leading to β^+-decays in the residual nuclei. During a β^+-decay a proton turns into a neuron while emitting a positron e^+ and a neurino ν_e.

$$A(Z, N) \rightarrow A(Z-1, N+1) + e^+ + \nu_e \tag{4.0.1}$$

In the β^+-decay the positron and the neutrino share the available energy in an arbitrary proportion leading to a continuous energy spectrum. The positron loses energy while traveling through matter due to inelastic Coulomb collisions with atomic electrons. After losing most of its energy, the positron either annihilates with an electron from surrounding tissue into two photons or captures an electron forming an unstable bound state. There are different possible bound states which annihilates into two or three photons. However, the 3γ-emission can be neglected and the 2γ-annihilation is assumed to form the detectable radiation. In detail, both photons carry an energy of $511\ keV$ equal to the positron and electron rest mass and are emitted in opposite directions. A PET scanner is able to detect the photons using opposite detectors working synchronised. The spatial distribution of the positron emitters can then be determined using suitable reconstruction algorithms leading to a three dimensional image. The reconstruction is based on two assumptions [15]: (i) the nucleus from which the positron

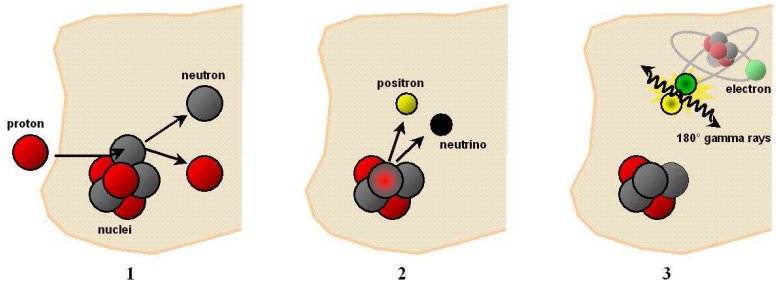

Fig. 4.1.: β^+ decay: 1. Neutron separation, 2. Positron emission and 3. Positron annihilation.

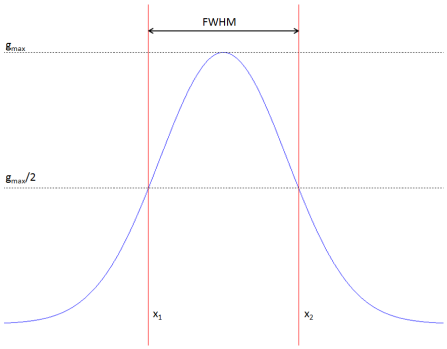

Fig. 4.2.: FWHM for a Gaussian function.

originated is exactly located along the line at which the two photons are emitted and (ii) the two annihilation photons are emitted at $180°$. These assumptions are inaccurate since a positron travels in the tissue due to its initial energy. Besides, biological washout effects can also influence the position of the positron annihilation. Due to these and other factors, the authors in [83] state that the accuracy of the proton beam range verification using PET imaging is of 1-2 mm in case of head and neck patients. However, depending on the position of the tumor, other factors like patient motion can have a far greater influence.

The PET images are degraded by noise like any other recorded image. Since positron emission tomography is a low-photon imaging technique, the acquired image signals s are degraded by Poisson noise. In addition, Gaussian noise can also be found in the images caused by the detectors acquiring the image data. Poisson noise is multiplicative while Gaussian noise is additive. The PET images are also degraded by a point spread function (PSF) convolution. A PET image is not recorded directly but reconstructed using suitable algorithms and the PSF reflects blur caused by smoothing in the image reconstruction but also many other sources like e.g. positron range and PET camera resolution. The PSF of the PET images is approximated by a three dimensional Gaussian convolution kernel which is usually described by a specific full width at half maximum (FWHM). A PSF with a FWHM of 7 mm is used to account for the response of the PET imaging system given by the systems specifications. Gaussian functions are often characterized by a variance σ^2 and the correlation between FWHM and variance is given by:

$$FWHM = 2\sigma\sqrt{2ln(2)} \quad \sigma^2 = \frac{FWHM^2}{8ln(2)} \tag{4.0.2}$$

The FWHM is basically the distance between the two points where the Gaussian function reaches half of its maximum value as illustrated in figure 4.2. In summary, the PET images are smoothed using a PSF convolution and suffer from both Gaussian and Poisson noise.

Positron emitter	Reaction channel	Threshold energy (MeV)	Half-life time (min)	Decay constant (min^{-1})	Positron max E. (MeV)
^{11}C	$^{12}C(p,pn)$	20.61	20.39	0.0340	0.96
^{11}C	$^{16}O(p,3p3n)$	59.64	20.39	0.0340	0.96
^{13}N	$^{16}O(p,2p2n)$	5.66	9.965	0.0696	1.19
^{15}O	$^{16}O(p,pn)$	16.79	2.037	0.3398	1.72

Table 4.1.: Relevant positron emitters for proton therapy

Protons cause the production of β^+-emitting target fragments along the penetration path as long as their energy is beyond a certain energy threshold of nuclear interactions. E.g., the energy thresholds for the production of ^{11}C and ^{15}O in the main reaction channels are 16.6 MeV and 20.3 MeV [168]. Besides the (p,pn) reaction channel on ^{12}C, the $(p,2p2n)$ and $(p,3p3n)$ reaction channels on ^{16}O are relevant for the PET imaging in proton therapy. In case of a longer delay time between irradiation and PET measurement, ^{11}C positron emitters from $^{12}C(p,pn)$ and $^{16}O(p,3p3n)$ reaction channels were considered primarily [115] [119]. Since in-room PET imaging allows decreased delay times, positron emitters with a smaller half-life time are of importance as well. Hereby, ^{15}O and ^{13}N were investigated lately [7]. The reduction of the PET activity I of different emitters in dependence of the delay time Δt with I_0 being the initial PET activity after the irradiation is given by:

$$I(\Delta t) = I_0 \cdot e^{-\lambda \Delta t} \tag{4.0.3}$$

Hereby, a positron emitter specific decay constant λ which depends on the half-life time $T_{1/2}$ is used. The connection between half-life time and decay constant is described by:

$$\lambda = \frac{-ln(0.5)}{T_{1/2}} \tag{4.0.4}$$

An overview of the relevant positron emitters and their properties is given in table 4.1 [14].

5. Automated Cell Analysis for Genome Wide RNAi Screens

5.1. Introduction

RNAi-based high-throughput microscopy screens have become an important tool in biological sciences in order to decrypt mostly unknown biological functions of human genes. Manual analysis is impossible for such screens since the amount of image data sets can often be in the hundred thousands. Reliable automated tools are thus required to analyse the fluorescence microscopy image data sets usually containing two or more reaction channels. Such an automated cell analysis tool which was developed in collaboration with Julia Ritzerfeld, Heidelberg University Biochemistry Centre is presented in this chapter. These tools have similar structures and functionalities but since each RNAi screen investigates a specific biological function, the visual representation of the cells is different leading to problem-specific techniques. The presented image analysis tool is designed to analyse a RNAi screen investigating the intracellular trafficking and targeting of acylated Src kinases. In this specific screen, a data set consists of three reaction channels and the investigated cells can appear in different phenotypes. The main issue of the image processing task is an automatic cell segmentation which has to be robust and accurate for all different phenotypes and a successive phenotype classification. The cell segmentation is done in two steps by segmenting the cell nuclei first and then using a classifier-enhanced region growing on basis of the cell nuclei to segment the cells. In a first version of the cell analysis tool, the cell classification was realized by a manually adapted classification function [135]. In the final version of the analysis tool, the classification of the cells is realized by a support vector machine which has to be trained using supervised learning [136]. Furthermore, the tool is brightness invariant allowing different staining qualities and it provides a quality control that copes with typical defects during preparation and acquisition. In order to evaluate the correctness of the tool the results are compared to a manual analysis done by an expect for a representative amount of images. Besides, there is a positive control in the RNAi screen giving the opportunity to evaluate the tool objectively. The first version of the tool has already been successfully applied for an RNAi-screen containing three hundred thousand image data sets and the SVM extended version is designed for additional screens.

This section is organized as follows: Section 5.2 describes the biological background

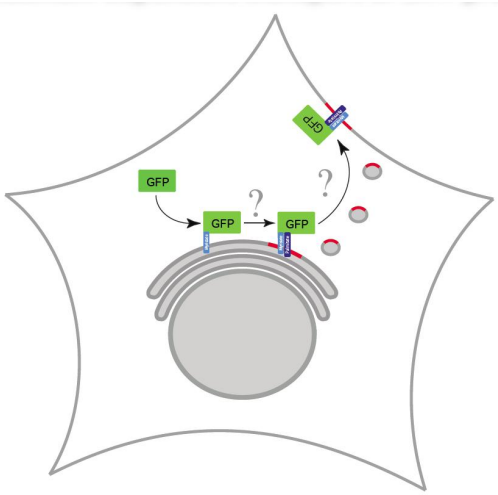

Fig. 5.1.: Intracellular transport of Src kinases labeled with GFP.

of the RNAi screen. In section 5.3, a short summary of the state of the art of cell segmentation and automated analysis tools is given. The analysis tool is described in detail in section 5.4 while section 5.5 contains an overview about the experiments used to evaluate the quality of the tool and the results of this evaluation. A summary and discussion concludes the chapter in section 5.6.

5.2. Biological Background

An important task in biomedical science is the decryption of the biological functions of human genes; which are mostly unknown. The identification of the genes and their corresponding functions are important for fundamental research as well as for the development of pharmaceutic agents. It is possible to reduce the expression of target genes by RNA interference (RNAi) which was discovered by Fire and Mello [54]. All known genes can be silenced separately with this screening method and existing functions of the genes can be observed. For a complete and systematic analysis for a specific biological function a genome-wide high-throughput RNAi screen has to be done. Such a screen requires a robust and automated methodology like that described in [74]. Besides, it provides a huge amount of data to be analysed. Since it is impossible to analyse this amount of data manually, suitable tools are required.

The analysis tool which is presented in this chapter was developed for a genome-wide RNAi screen investigating intracellular trafficking and targeting of acylated Src kinases. In this specific screen the investigated living cells can appear in three different phenotypes depending on the localization of the fluorescence marker: plasma membrane, cytoplasm and Golgi. In fact, two distinct kinases are investigated in this screen. These

two kinases were tagged with different fluorescent proteins (GFP/mCherry) and are expressed by a human model cell line. Both kinases localize to the plasma membrane, but the pathway and factors involved are unknown and the objective of the RNAi screen. As mentioned before, all genes are silenced separately during the RNAi screen. If a gene which is involved in the transport is silenced the fluorescent kinases are arrested before reaching the final position in the pathway and the cell appears in a different phenotype. In this case either the original location of the kinases can be seen or a different position revealing a part of the pathway of the kinases transport. Originally, the kinases are located in the cytoplasm of the cell. In the transport pathway of the Src kinases there is only one intermediate station that can be seen in the screen. The Src kinases are located at the golgi apparatus in case of this intermediate station. The golgi apparatus is a specialized subunit of the cell located next to cell nucleus. The final position in the investigated transport path is the plasma membrane. The whole pathway of the kinases transport is illustrated in figure 5.1 beginning with the localization of the kinases in the cytoplasm. In the next step the Src kinases are located at the golgi apperatus before finally being transported to the cell membrane. This means that there are two separated steps in the kinases transport: one step is the transport of the Src kinases from the cytoplasm to the Golgi while during the second step the kinases are transported to the plasma membrane. Silencing genes which are involved in the first step of the transport path of the kinases, from the cytoplasm to the golgi apperatus, results in the appearance of the cells in the original phenotype, meaning as cyroplasm cells. Other genes are involved in the second step from the golgi to the plasma membrane. Cells appearing as golgi phenotype imply an involvement of the gene in this part of the transport. Finally, if the cells appear as plasma membrane phenotype the investigated gene is not involved in the transport at all.

A confocal image of all three phenotypes can be seen in figure(5.2). The bright areas in the image are the locations where the fluorescence markers are located while all other parts of the cells are dark. In case of a plasma membrane cell, the fluorescence markers are located in the boundary of the cell while the markers in a cytoplasma cell can be found all over the cell. The Golgi apparatus, as mentioned before, is a small compartment of the cell located next to the cell nucleus and the fluorescence marker is situated there for the Golgi phenotype. Since there are different intensities within the Golgi phenotype, an additional class named Golgi strong was added for the purpose of a more accurate biological analysis. This additional class is not an additional phenotype but a subdivision of the Golgi phenotype in order to point out cells having a highly developed Golgi phenotype.

In total, the analysed screen includes 149 LabTeks in duplicates with 384 spots per LabTek resulting in 340000 single images and about one Terabyte of data. For each spot an image dataset containing three channels is acquired. The Hoechst channel contains the fluorophore-labeled cell nuclei while the actual cells in appearance of the three phe-

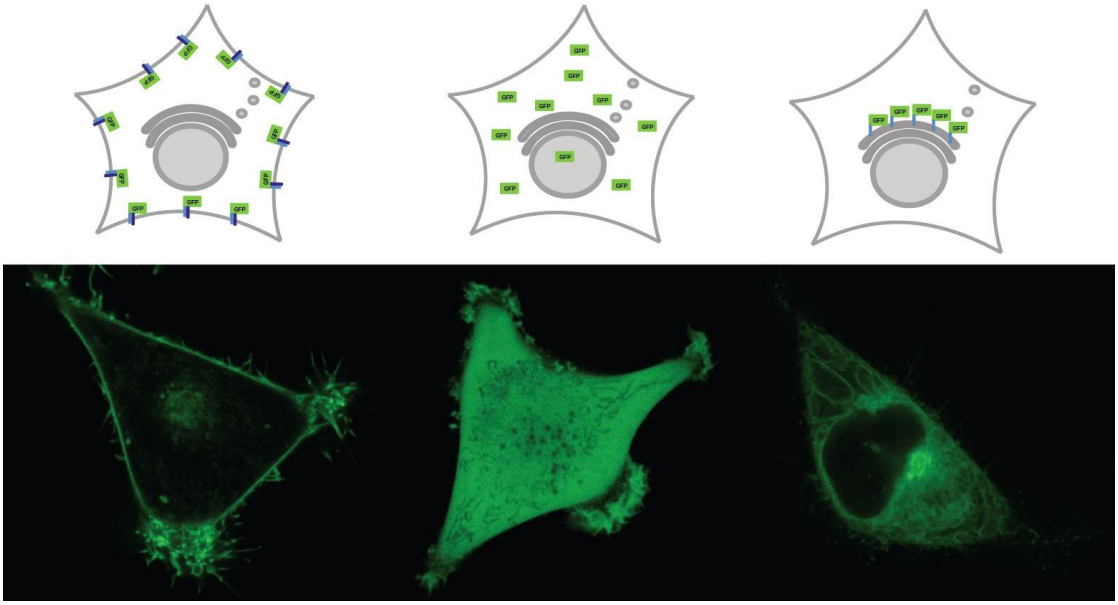

Fig. 5.2.: Confocal image of phenotypes (Left to right: plasma membrane, cytoplasm, Golgi).

notypes can be seen in both the GFP and the mCherry channel. These two channels are the result of the simultaneous expression of the two different Src kinases labeled with GFP and mCherry fluorophores and have to be analysed separately.

5.3. State of the Art

Various approaches for cell nuclei or whole cell segmentation have been published in recent years. Fernandez et al. [53] focused on cell nuclei segmentation and tried to detect directly neighbouring cell nuclei in order to separate them. In this approach, dominant or concave points on the binary contour of the region are detected and considered to be points where the nuclei can be split. In [107], Lezoray and Cardot described an active contour technique for the segmentation of cell nuclei. A whole cell segmentation using region growing and adaptive segmentation methods was presented in [4]. Wu et al. [82] used a two step method for coarse and fine segmentation which applied hierarchical thresholding for whole cell segmentation. In [121] the segmentation is done by a thresholding method and adaptive fuzzy c-means clustering. Alternatively, there are several approaches using a watershed algorithm for cell nuclei or whole cell segmentation (See [169] [91] and references therein). In addition, Wählby [169] is trying to separate cell aggregates by merging or deleting small regions in a second step following the watershed segmentation. The approach of Metzler et al. [108] is able

to separate touching cells and in this multi-scale approach, mathematical morphology operators are used. The cell segmentation in [110] is realized by a neural network approach but for this approach the cell contours have to be emphasized. Elter et al. [48] present a three-step segmentation called maximum-intensity-linking closely related to classic watershed methods. Here, the neighborhood of each pixel is evaluated and a smoothing preprocessing step is used in order to be robust against noise. In addition, a post-processing step merges oversegmented regions.

Harder et al. [63] presented an automated image analysis method focusing on cell nuclei. The method segments, tracks and classifies cell nuclei automatically and distinguishes the nuclei into different mitotic phases. In this approach, multi-cell 3D images are analysed while a 2D projection is used for segmentation and tracking. The segmentation of the cell nuclei is based on a local adaptive thresholding approach and the classification is using a Support Vector Machine. In [106], an analysis tool for high-throughput microscopy is described. The underlying RNAi screen investigates genes involved in Hepatitis C and Dengue virus replication. In a first step the cell nuclei are segmented by a gradient thresholding and in the following step the infection level is determined by investigating the neighbourhood of the cell nuclei. In order to determine the neighbourhood of the nuclei, different approaches from dilation to region growing were tested.

5.4. Methods

The analysis tool presented in this chapter was developed for a genome-wide RNAi screen investigating intracellular trafficking and targeting of acylated Src kinases [139]. In this specific screen, the investigated cells can appear in three different phenotypes: plasma membrane, cytoplasm and Golgi (Figure 5.2). Each image data set consists of three different reaction channels and a typical data set can be seen in figure 5.3. The Hoechst channel contains the fluorophore-labeled cell nuclei while the actual cells in appearance of the different phenotypes can be seen in both the GFP and the mCherry channel. These two channels are the result of the simultaneous expression of two different Src kinases labeled with GFP and mCherry fluorophores and have to be analysed separately but in the same way. A first version of the analysis tool was already presented [135] and contains the problem-specific segmentation and a manually adapted classification function. In addition, the image quality is analysed and the segmentation results for both nuclei and cell are reviewed in an additional step to guarantee a valid segmentation and to cope with local contamination. Several features are extracted on basis of the segmentation result and the classification is realized by a manually adjusted decision function. This approach is time consuming since it is not trivial to decide which features are relevant and the adjustment of the necessary coefficients in the decision function has to be done by hand. In addition, the decision function is valid for just one biological set

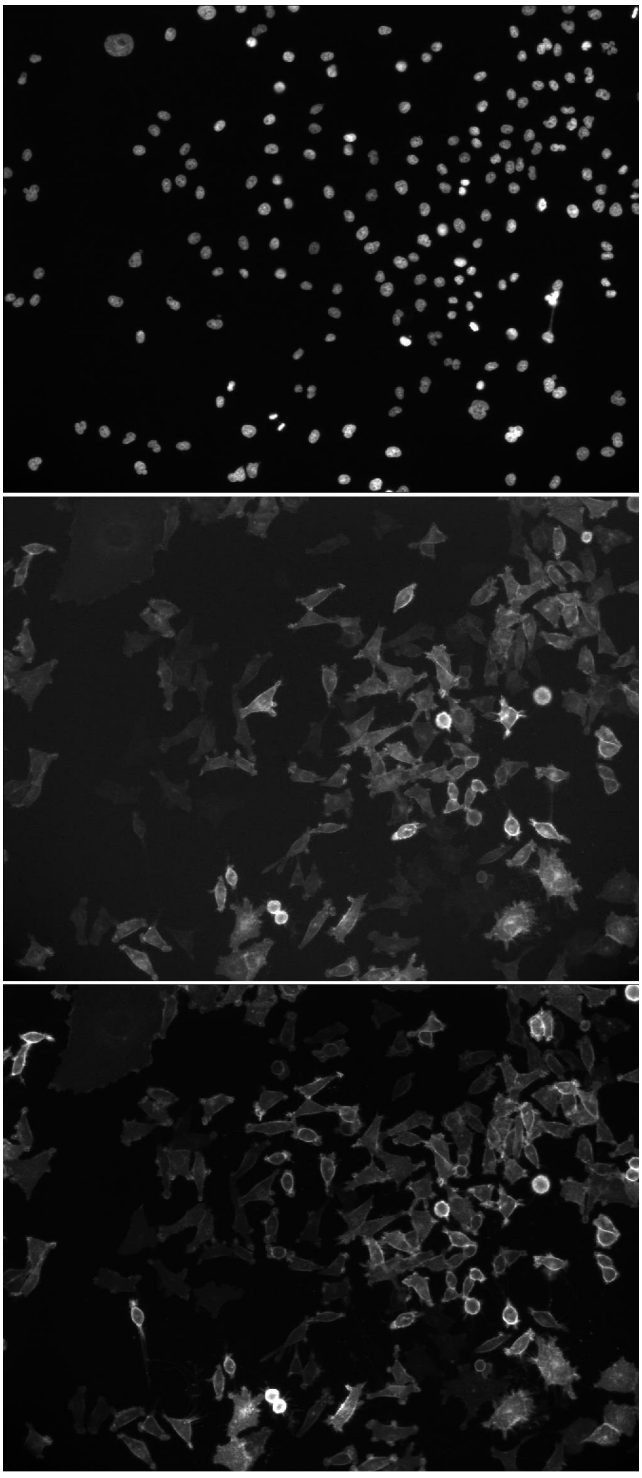

Fig. 5.3.: Cell image with Hoechst (Top), GFP (Middle) and mCherry (Bottom) channel.

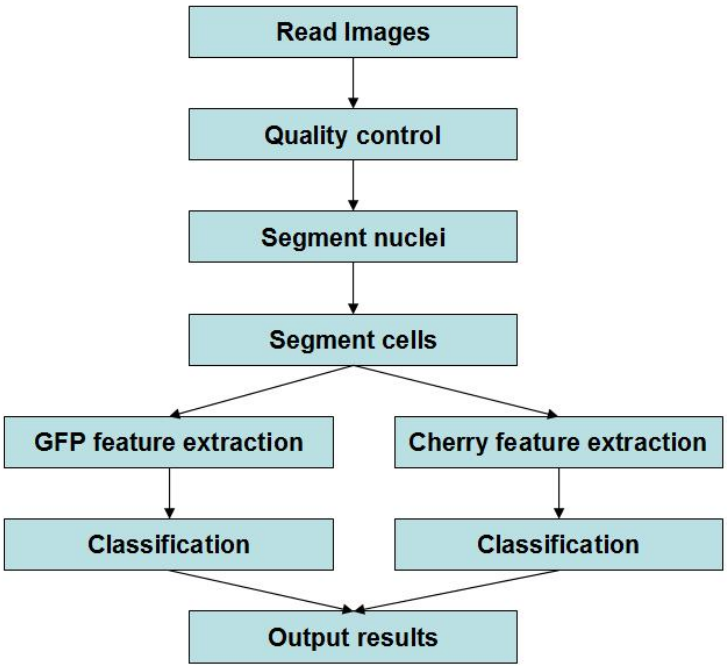

Fig. 5.4.: Image analysis strategy.

up and any changes like just using different microscope slides (E.g. well plates instead of LabTeks) require a new adjusted decision function. In order to provide a complete automated image analysis tool, a supervised learning approach realized by a Support Vector Machine is applied. Supervised learning can be used for various image analysis problems [151]. Using a Support Vector Machine, the analysis tool can be easily trained by manually classifying a certain amount of cells which is then used both to train and to adjust the parameter for the Support Vector Machine. In addition, this step provides an evaluation of the resulting classification set up. In order to perform an analysis for the genome-wide RNAi screen, it is necessary to detect the number of cells in each image and to differentiate the phenotypes shown in the GFP and the mCherry channel. The analysis tool processes many LabTeks at once by a batch process which is controlled by a Matlab GUI. The results of the analysis are stored in two text files, one for the GFP and one for the mCherry results. This way, the results can be easily imported into a spreadsheet application for further evaluation.

5.4.1. Analysis Algorithm

For the analysis of each three-channel image data set, the strategy which is sketched in figure 5.4 is used. The main parts in the strategy are:

- Quality control.
- Segmentation of cell nuclei and cell Segmentation.
- Classification of different phenotypes.

5.4.2. Quality Control

Three reasons for image degradation are considered: out-of-focus image acquisition, noise and local contamination. Additional noise in the image is handled by the robust segmentation technique. Furthermore, there are areas in the images which are corrupted by contaminations. These degradations are only local and do not influence the image quality in general. As an analysis shows, the best way to handle such degradations is to detect and exclude them after the segmentation. Finally, the focus of the microscope is determined by an auto focus functionality that is not always reliable. Hereby, the quality control of the three channels is performed by analyzing the quality of each channel separately. To measure this degradation, the image channels are transformed in the Fourier space and out-of-focus images are detected by their lacking in high frequency bands. In general, the quality of an image is described by one of four possible quality levels. The quality rating of each image channel is added to the analysis result and in this way a weighting of the results is possible.

5.4.3. Cell Nuclei Segmentation

First, the cell nuclei are segmented using the Hoechst channel. Since the intensity values of the cell nuclei in the Hoechst channel are within a certain range, threshold techniques are applied. An evaluation of several Hoechst images shows that the brightness in this image channel can vary and that a fixed threshold will not lead to a satisfactory segmentation for all Hoechst images. For this reason, an adaptive thresholding is applied: Starting with a high value, the threshold is decreased until an appropriate result is achieved. For each threshold parameter the segmentation generates connected regions of a certain size. An appropriate result is reached when the average size of these regions correspond to the assumed size of the cell nuclei. The threshold is decreased with a variable step-size becoming smaller according to the proximity of the current segmentation to the assumed result. In an additional step, holes in the nucleus regions are closed and local contaminations are excluded.

5.4.4. Cell Segmentation

The following cell segmentation process can either operate on the GFP or the mCherry channel. Both image channels contain the same cells and thus the segmentation can

be performed on both channels. The proposed region growing method requires a seed point and a stopping criterion fitting all phenotypes which is realized by a rule-based classifier. As seed points, the cell nuclei region segmented from the Hoechst channel are used and in addition this region serves as source for information used in the classifier. The classifier uses the minimal local cell brightness in the known nucleus region and the gradient of the cell image. The stopping criterion is fulfilled, if and only if the brightness of an inspected pixel is below the brightness in the nucleus region and the gradient magnitude at that point is above a certain threshold. Let the minimal local brightness in the nucleus region be t_1. The stopping criterion is fulfilled if both following rules are maintained. If one rule is violated the region growing is not stopped.

- Rule 1: The brightness of a new pixel must be below $t_1 - \epsilon$, where $\epsilon > 0$ is a suitable threshold.
- Rule 2: The gradient magnitude of a new pixel has to be above a threshold t_2.

This classifier-enhanced region growing approach is suitable for all three phenotypes and, in addition, it is fluorescence brightness invariant. The approach is successful for bright and dark cells since the local brightness is considered in the segmentation. A cytoplasm cell can be segmented correctly since there are only low gradient magnitudes inside the cell and therefore rule 2 is violated while rule 1 can be fulfilled inside the cell area. The Golgi phenotype can be segmented because the brightness of the pixels within the cell is beyond the threshold $t_1 - \epsilon$ of rule 1 and despite of the high gradient magnitudes inside the cells. Finally, the plasma membrane cells possess low gradient values inside the cells as well and the borders of the cells are recognized correctly even if the membrane is not displayed as a closed structure.

In an additional step, the segmented cells have to be inspected before they can be classified and thus a quality control for the segmentation results is required. Local contaminations or weak and noisy intensity signals can cause infeasible segmentation results. These results are detected by evaluating the size and the shape of the segmented cells and have to be excluded. In addition, a valid classification result cannot be guaranteed if a cell is too close to the edge of the image domain since essential areas of the cell can be missing. Besides, if two cell nuclei are too close to each other it is likely that the cells overlap and a valid segmentation is not possible in this case. Again, valid results which are free of artifacts and contaminations are obtained by excluding these cells from the segmentation output.

5.4.5. Classification

The segmentation result provides the basis for the classification and is used to divide the cell into complementary parts: nucleus, boundary and interior. The nucleus of the

cell is already characterized by the segmentation result of the Hoechst channel. In order to determine the cell boundary, a modified morphological gradient (Difference between original and eroded image) is applied. Finally, the interior is the difference between the complete cell region and the boundary unified with the nucleus. For each cell and its constituent parts, the mean value and standard deviation of the corresponding pixel values are feature candidates for the classification. The following features are considered as relevant due to several tests:

- Standard deviation and mean value of cell.
- Mean value of nucleus, boundary and interior.

It is important for the phenotype classification to be invariant to the fluorescence brightness of the different cells and therefore the features are defined using proportions between the different extracted mean values and standard deviation like e.g. mean interior vs mean nucleus or standard deviation vs mean value of the whole cell.

The classification for the GFP channel is independent from the mCherry channel and vice versa. These channels contain images of the same cells and the segmentation result is valid for both images while the feature extractions as well as the decision functionality are completely separated. Both channels are simultaneous expressions of two different protein kinases and contain the same phenotypes. Thus, the same features can be used for the classification.

Decision tree classifaction

In the first version of the tool, the rules for the decision functionality were the result of an intensive analysis of the extracted features for all phenotypes. The classification was performed by a decision tree containing the manually found rules. Cells which did not fit a phenotype criterion were classified as invalid. In addition, a subtype Golgi strong was added for the Golgi phenotype. This subtype contains cells with a highly developed Golgi phenotype and therefore the definition for this class is more restricted.

The classification of the phenotypes is performed by a decision functionality displayed as a decision tree in figure 5.5. In rare cases, there are cells changing their phenotype when the image is acquired. Such cells do not fit into one of the phenotype classes and they are thus marked as invalid. The rules for the decision functionality are the result of an intensive analysis of the extracted features for all phenotypes. This analysis contains the evaluation of more than three thousand cells of different phenotypes.

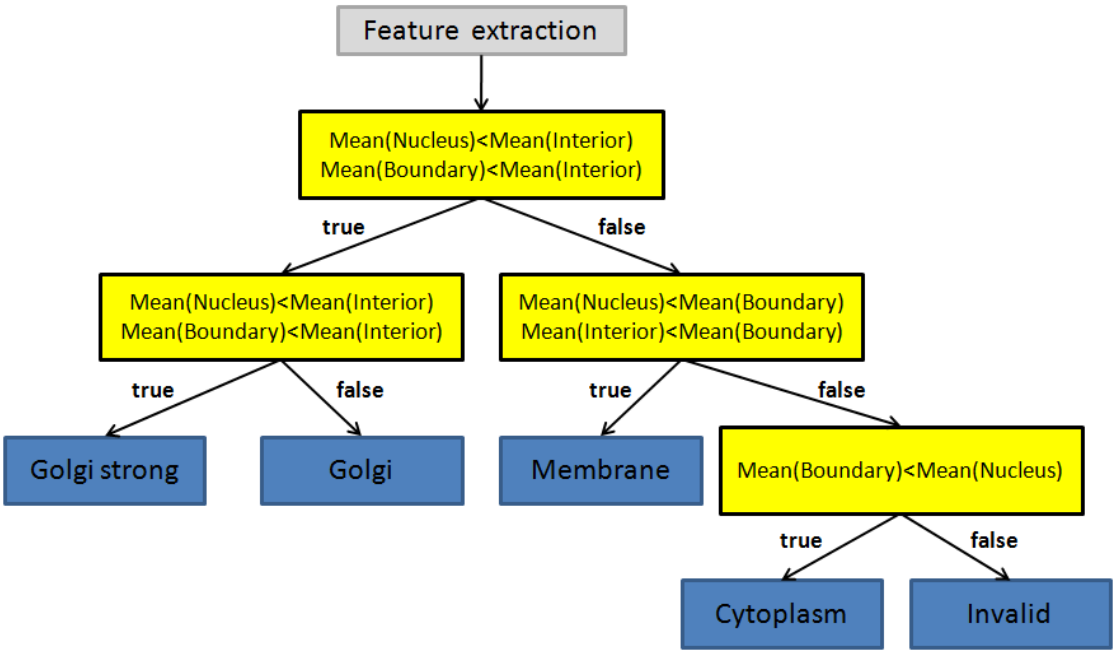

Fig. 5.5.: Decision tree for phenotype classification.

5.4.6. Support Vector Machine Classification and Supervised learning

In the final version, a supervised learning method based on a Support Vector Machine is applied. This method is flexible and a lot easier to handle than a manual adjusted decision function. In general, a Support Vector Machine requires a set of already classified examples which are used as training data.

$$D = \{(x_i, c_i)\,|x_i \in X^p, c_i \in \{-1, 1\}\} \quad for \quad i = 1, ..., n \tag{5.4.1}$$

Hereby, each x_i is a p dimensional feature vector representing the properties of one cell and c_i indicates the class to which the example cell i belongs. In total, the set D contains n classified examples and the aim is to find the maximum-margin hyperplane separating the points with $c_i = 1$ from those with $c_i = -1$. Any hyperplane can be written as a set of points x satisfying

$$\langle w, x\rangle - b = 0 \tag{5.4.2}$$

with w being the normal vector of the hyperplane. In addition, $\frac{b}{\|w\|}$ determines the offset of the hyperplane from the origin along the vector w. In order to determine the hyperplane for a given training data set D, w and b have to be chosen in a way that the margin is maximized, i.e. the distance between the hyperplanes described by

$$\langle w, x\rangle - b = 1 \quad \langle w, x\rangle - b = -1 \tag{5.4.3}$$

has to be maximized. In other words, w and b are chosen in a way that the smallest distance of the example points x_i with $i = 1, ..., n$ to the hyperplane $\langle w, x\rangle - b = 0$ is maximal. The hyperplane can be determined solving the optimization problem minimizing $\frac{1}{2}\|w\|^2$ with respect to the constraint

$$c_i\left(\langle w, x\rangle - b\right) \geq 1 \quad for \quad i = 1, ..., n \tag{5.4.4}$$

This constrained quadratic optimization problem can be efficiently solved using Lagrange multipliers. A hyperplane can be used to classify data which is linearly separable and the previously described method is thus named linear Support Vector Machine. There is a soft margin extension of the support vector machines which allows misclassified examples by using an additional penalty function in case the given data is not linear separable. In principle, several examples are not considered when the hyperplane is determined and the amount of those examples is controlled by a soft margin parameter.

In addition, a realization of proper non-linear classification is possible with Support Vector Machines by using the so called *kernel trick*. Instead of using scalar products of the form $\langle x_i, x_j\rangle$, kernel functions k which are mapping the input space to a higher dimensional space are used. Such a kernel function is defined by

$$k(x_i, x_j) = \langle \phi(x_i), \phi(x_j)\rangle \tag{5.4.5}$$

with ϕ being a non-linear mapping. The kernel functions allow non-linear classification with the Support Vector Machines because they transform the data to a higher dimension where a linear separation using a hyperplane is again possible. In order to use the full effectiveness of a support vector machine, it is important to both choose an appropriate kernel and to adjust a soft margin parameter. The choice of the kernel has to be appropriate to the location of the support vectors. In this case, a polynomial kernel function of order three is used to obtain a suitable result.

$$k(x_i, x_j) = (x_i \cdot x_j)^3 \tag{5.4.6}$$

In addition, the soft margin basically determines the amount of considered support vectors and thus allows mislabeled examples. This parameter has a huge influence on the overall classification result and is determined adaptively. Half of the manually classified data is used as training data and the other half is then used as test data to evaluate the training success. Varying the soft margin parameter and comparing the classification result of the test data with the manual classification allows both the determination of a suitable soft margin parameter and the evaluation of the classification. In general, the Support Vector Machine is able to distinguish between two categories and there are

various strategies to realize a multi-category classification which is required for the phenotype classification. In this approach, each phenotype is classified by comparing it to all other types by a separate Support Vector Machine.

5.5. Results

An expert evaluated the segmentation methods of the cell analysis tool manually. The images of the RNAi screen have a size of 1344×1024 pixels and contain 200 cells on average. Many of the images are difficult to segment because they are out-of-focus, contain local contamination or touching/overlapping cells. The evaluation contains many images with different quality levels and different fluorescence brightness. Before the segmentation is started, the quality of the image is determined and quantified into four classes named *excellent*, *good*, *acceptable* and *insufficient*. Prior to cell segmentation, the cell nuclei segmentation was evaluated. The nucleus segmentation has an error of less than 1% for *excellent* and *good* images independent of their fluorescence brightness. In addition, all local contaminations are detected due to their size and thus excluded. Cells can only be classified properly if they do not overlap. In case of cell clusters containing more layers of overlapping cells, the cell nuclei touch each other and form a large connected region in the segmentation result. The size of such a connected region is significant larger than the assumed size of a cell nucleus and these overlapping cells are excluded like contaminations. For images with an *acceptable* quality, fewer cell nuclei are segmented correctly (approximately 60% to 80% depending on the brightness of the Hoechst image). Other cell nuclei are excluded by the quality control because only parts of the nucleus area are segmented or the cell nuclei are not segmented at all. Albeit not all cell nuclei are included in the segmentation result, the considered nuclei are segmented correctly in general. For *insufficient* images the segmentation result contains less than 1% of the cell nuclei and is thus not usable at all.

In figure 5.6 the result of a segmentation including the cell nuclei and boundary is displayed. This is the segmentation result of the GFP channel shown in figure 5.3. Local contaminations and incorrectly segmented cells are already excluded. The segmentation result contains bright as well as dark cells. In both cases the cells are segmented accurately. A region with touching cells is extracted from this image. The original image and the segmentation result are displayed in figure 5.7. As it can be seen, the touching cells are segmented as expected. In case of touching cells with different brightness, the segmentation result is accurate. Neighboring cells with similar brightness are not segmented such accurately but nevertheless a reasonable classification is still possible.

In order to evaluate the cell segmentation, results of about three thousand cells were investigated by an expert cell-by-cell. Only less than 5% of all regarded cells are segmented incorrectly. Such a high quality is possible because of the strict quality criteria. About 15% to 30% of all segmented cells, depending on the image quality, are not

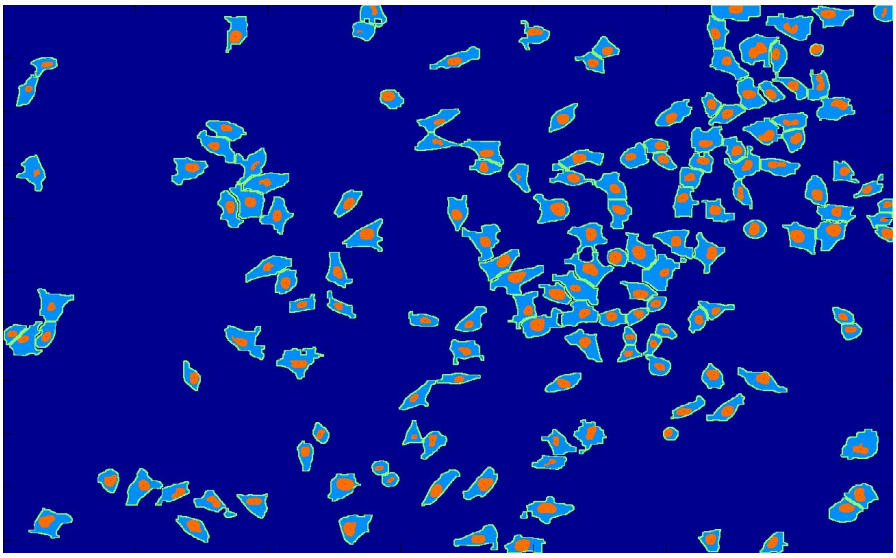

Fig. 5.6.: Segmentation result containing cell nuclei and boundary.

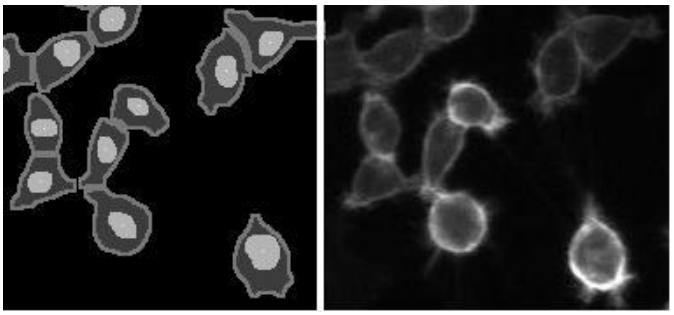

Fig. 5.7.: Segmentation for touching cells: segmentation result (Left) and original GFP channel (Right).

considered in the following classification. In addition, local contaminations and overlapping cells are identified and excluded. Some of the images in this evaluation were analyzed completely by an expert meaning cell count and classification by hand. These manually obtained results sometimes contain fewer cells than found by the segmentation. Dark cells in the images can hardly be seen in the GFP or mCherry channel and since the Hoechst channel is not considered in a manual analysis, these cells remain unnoticed.

The segmentation works properly for all three phenotypes: cytoplasm, plasma membrane and Golgi. Detailed segmentation results for all phenotypes based on the GFP channel are shown in the figures 5.8, 5.9 and 5.10. For each phenotype, the original data is displayed in the top row. On the right side the Hoechst channel can be seen which is used as basis for the cell nuclei segmentation while the GFP channel used for the cell segmentation is shown on the left side. In the bottom row the segmentation result is presented on the left side and the regions for nucleus, boundary and interior which are the basis for the classification are marked with different gray values. On the right side the stopping criterion for the region growing is illustrated. This image contains information about the regions where the gradient magnitude of the GFP image is above t_2 (Rule 2) as well as information about the region where the intensity values of the cells are too low according to the minimal local brightness t_1 of the cells (Rule 1). The region growing is stopped when both rules are fulfilled and these areas are marked as *red*. The *yellow* regions present the areas where the gradient magnitude is above t_2 and therefore rule 2 is fulfilled while rule 1 is still violated. The areas where the intensity values are low enough that rule 1 is fulfilled and rule 2 is violated are *cyan*. Finally, in the *blue* areas both rules are violated.

The segmentation result for all phenotypes is as expected. The segmentation for the cytoplasm cells in figure 5.8 is dominated by the *blue* areas in the centre of the cells where both rules necessary for the stopping criterion are violated. The actual edges of the cells are located where the intensity values of the GFP channel fall below the threshold determined by the local brightness of the cell (Rule 1) and the gradient magnitude is above t_2 (Rule 2). However, rule 2 is already fulfilled in the *yellow* regions next to the edges of the cell and thus rule 1 determines the exact location of the edge. In the Golgi cells displayed in figure 5.9, there are also some areas where both rules are violated (*Blue* regions) but in many areas within the cell one of both rules is fulfilled. Especially in the Golgi cell which is lower in the image, it can be seen that both rules are necessary for the segmentation of this phenotype. It would not be possible to segment such cells by using only one of the two criteria, the intensity values of the cells or the gradient magnitude. Due to the internal structures of the Golgi cells the gradient magnitude is above t_2 in many areas inside the cells and therefore rule 2 is fulfilled here (*Yellow* regions). In addition, in the upper right part of the cell, the intensity values are already too low according to the local brightness of the cell and rule 1 is fulfilled while

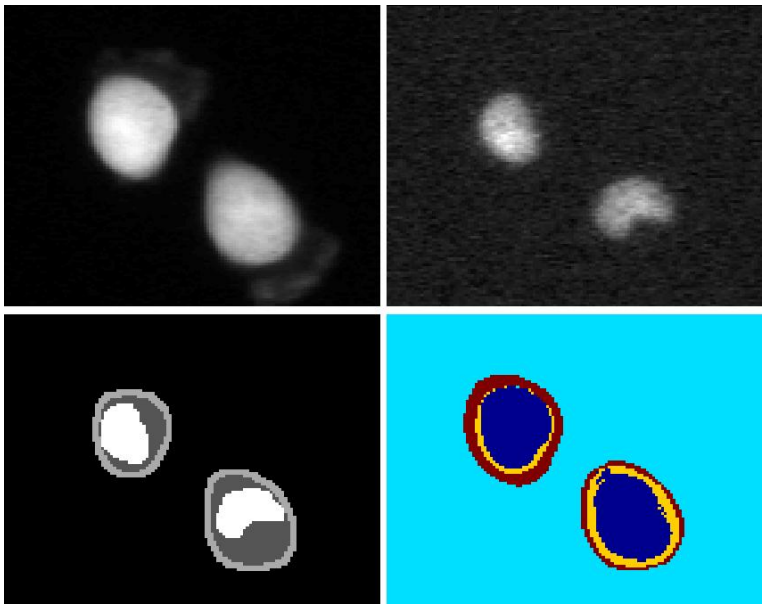

Fig. 5.8.: Cytoplasm cell segmentation with details.

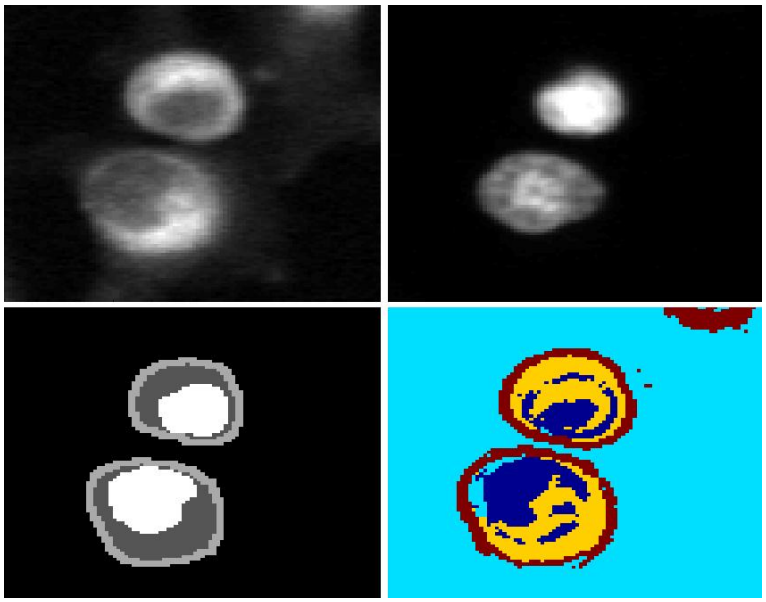

Fig. 5.9.: Golgi cell segmentation with details.

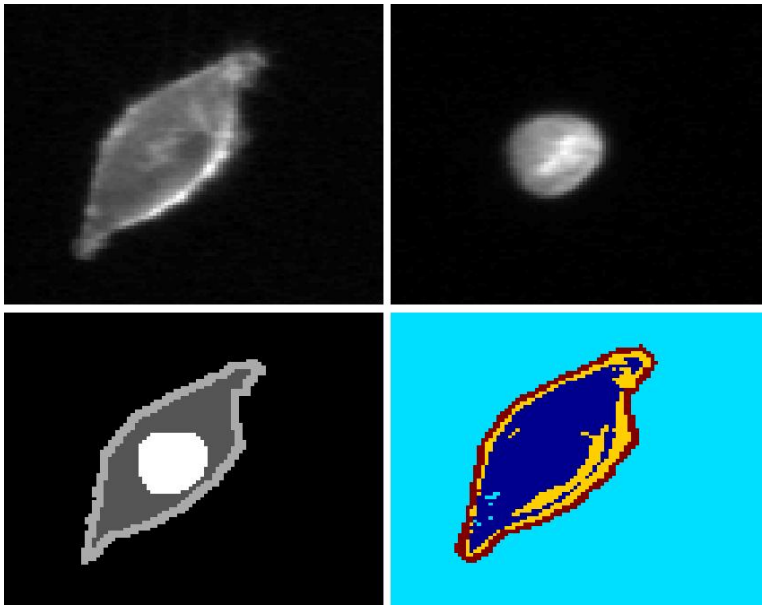

Fig. 5.10.: Plasma membrane cell segmentation with details.

	amount of found positive controls	proportion (in percentage)
manual recognition	78	97,5%
software tool	73	91,25%

Table 5.1.: Evaluation of positive control with 80 LabTek

the gradient magnitude is still too low and rule 2 is violated (*Cyan* regions). Both rules are also necessary to segment the plasma membrane cell properly (Figure 5.10). There are *cyan* and *yellow* regions inside of the cell where one of both rules is fulfilled although the *cyan* regions are not as large as in the example for the Golgi cell. In summary, the classifier-enhanced region growing approach is able to segment all phenotypes properly and, in addition, it is invariant to the fluorescence brightness of the segmented cells.

In order to define the rules for the decision functionality used in the manual classification, the extracted features of about three thousand cells used to evaluate the segmentation are considered. Afterwards, an expert verified the classification by evaluating the result for about a thousand cells manually and verified the correctness of the classification. In addition, there is a positive control in the RNAi screen on 80 LabTeks that is used to evaluate the cell analysis tool as well. Both the results of a manual evaluation of the positive control and the results of the cell analysis tool are listed in table 5.1.

The software tool recognizes 93,6% of the positive control being rated as valid by

a manual analysis of an expert. In this case the interpretation of the results from the software tool is done by evaluating the distribution of the different phenotypes in the images. In addition, the manual analysis of an expert is influenced by the location of the cells and therefore by the local distribution of the different phenotypes. In this way an image with a local conglomeration of a specific phenotype can be rated as valid in the manual analysis even if the total appearance of this phenotype is not dominating. This information is not considered in the software tool. Despite this limitation the result of the cell analysis tool is satisfying compared with a manual analysis.

In order to evaluate the supervised learning method, a small data set which is shown in figures 5.12 and 5.11 is used at first. The training data contains 13 Golgi, 16 Membrane and 15 Cytoplasm cells and is used to train the Support Vector Machine. The automated classification is then tested with the test data containing 20 Golgi, 16 Membrane and 20 Cytoplasm cells and the classification result was a 100% correct for all three different phenotypes. Hereby, the soft margin parameter was set manually and the result shows the potential of this method. In addition, the segmentation for all three phenotypes is robust and accurate despite of a different cell brightness.

In a second evaluation, a training data set and a test data set with each consisting of three complete image data sets is used and both data sets are manually classified by a biologist. The training data set contains 280 Golgi, 131 Membrane and 132 Cytoplasm cells and half of the cells are used to train the Support Vector Machine while the other half is used to adjust the soft margin parameter and to evaluate the classification. The classification result varies from 24.3% correctness up to 98.5% and leads to a choice of 0.013 as soft margin parameter. Afterwards, a test data set containing 127 Golgi, 129 Membrane and 221 Cytoplasm cells is classified. The classification correctness is 96.4% for the Golgi phenotype, 99.2% for Membrane and 96.7% for Cytoplasm.

5.6. Summary and Discussion

The presented analysis tool segments the images of the screen using a classifier-enhanced region growing. The seed points for this region growing are given by a preprocessing step segmenting the cell nuclei from the Hoechst channel of the image data sets using an adaptive threshold method. This approach yields a reliable segmentation of different phenotypes and is especially invariant to the fluorescence brightness of the segmented cells. In an additional step, the segmentation results are analysed and inadequate objects are removed to guarantee an artifact-free and valid segmentation result. A rule based classification is applied in a first version of the analysis tool using features from complementary parts of the cells. A Support Vector Machine is used for the classification in the final version allowing easy adaptations to new screening modalities. Supervised learning is used to train the Support Vector Machine and to adjust the soft margin parameter likewise. The evaluation results for the trained Support Vector Machine show a

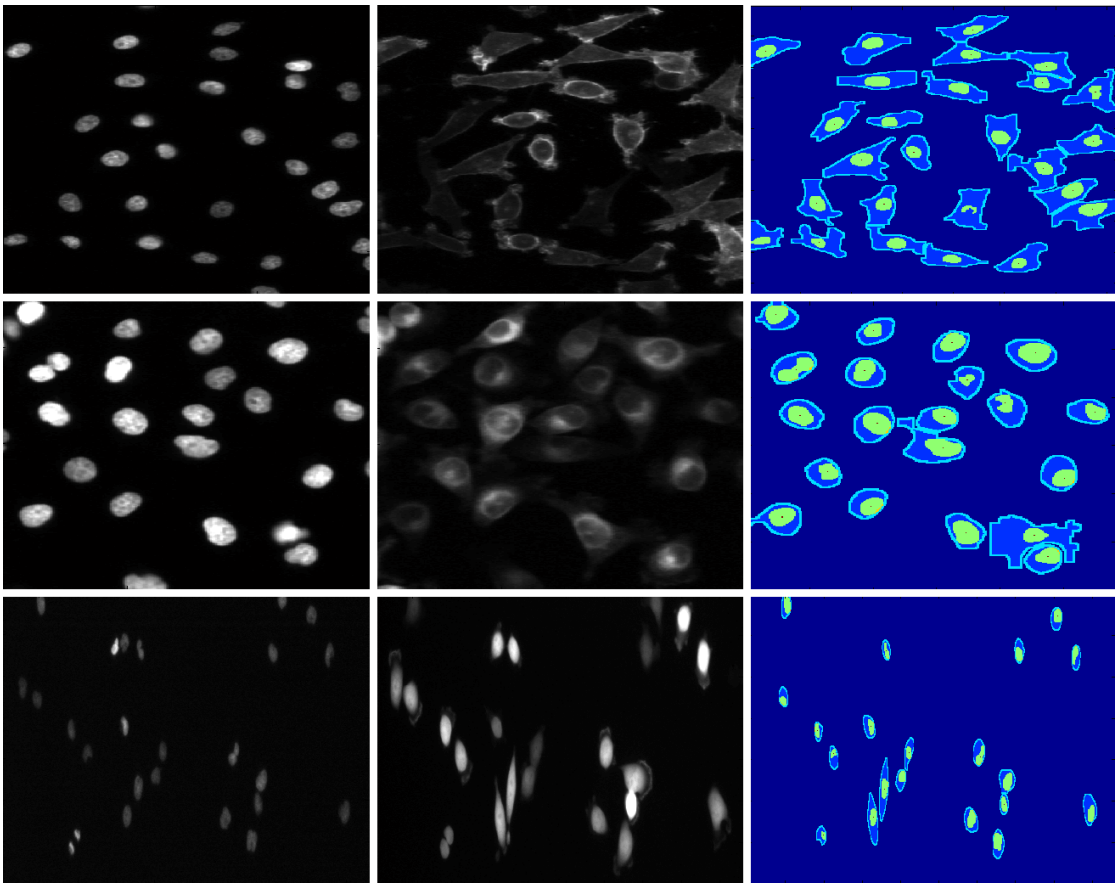

Fig. 5.11.: Training data sets (Hoechst, mCherry and segmentation) containing all different phenotypes: Plasma membrane, Golgi and cytoplasm (From top to bottom).

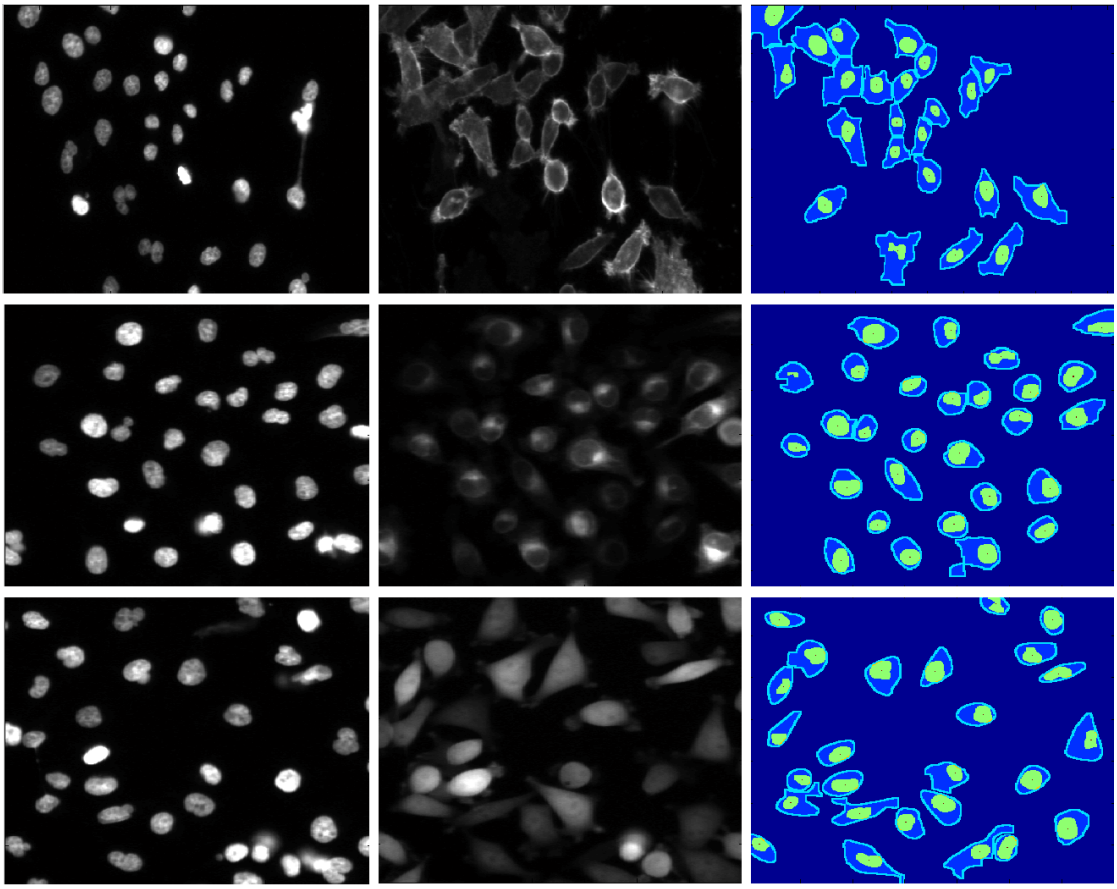

Fig. 5.12.: Test data sets (Hoechst, mCherry and segmentation) containing all different phenotypes: Plasma membrane, Golgi and cytoplasm (From top to bottom).

high accuracy for all phenotypes and a suitable adjustment of the soft margin parameter. Furthermore, the quality of the images is analyzed and added to the analysis result to allow an objective rating of the individual results. The software tool is well suited for the analysis of the genome-wide RNAi screen and the results allow a complete evaluation of the screen. In addition, the supervised learning allows an easy adjustment of the classification and therefore a simple application to different screening modalities.

Since the analysis tool is very robust, it is even possible to analyse images of moderate but still acceptable quality. In this case, however, the analysis is becoming more difficult and the results, nevertheless being correct, are not as obvious and clear as they are for images of good or excellent quality. The classification has to be brightness invariant and is thus using rules that compare the mean brightness values of different parts of the cell. For an image with good or excellent quality the differences between the values are quite high and the classification is easy and clear. With a decreasing quality these differences are becoming smaller and the classification is not that definite. The reasons for a worse image quality are noise on the one side and blurring on the other side. A little noise is neither influencing the segmentation nor the classification but blurring does have a considerable influence on both parts of the analysis algorithm. The main reason for blurring is that the images are not necessarily well focused. As mentioned before, the auto focus functionality of the microscopes is not always reliable and out-of-focus images are possible. A worse focusing of the image results in a more blurred image. In a blurred image the bright structures of the cells are not clear with sharp edges and influence their neighbourhood as well. In this case, the segmentation is becoming more difficult and the used region growing segmentation might stop a little too early or too late. Such a result leads to an inaccurate division of the cells into complementary parts which can contain other areas of the cell or the background that do not belong to that part. In addition, the bright structures in a blurred image are brightening their neighbourhood and thus creating signals in the bordering parts of the cell that do not belong to these parts. As example, the segmentation of a plasma membrane cell is not easy because the boundary of the cell is no longer well defined by a sharp edge but hard to detect because of the blurring. Additionally, part of the brightness of the plasma membrane is given to other parts of the cell or lost in the background. Another example is that part of the brightness of the interior part of a Golgi cell is given to the nucleus part of the cell in a blurred image.

In summary, the analysis of images with a moderate quality is more difficult and the results are not quite definite. A preprocessing deblurring step could improve the image quality and allow more reliable results. Furthermore, the analysis of images with a poor quality which was not possible before could be considered after deblurring the images.

Part II.

Deblurring Methods and the Deconvolution Framework

6. The Deconvolution Framework

In the following chapter, the architecture of the realized deconvolution framework and its basic components are presented in detail. The design and architecture of the framework is described and the framework is created as extension to the Volume Graphics Library (VGL - Volume Graphics GmbH [1]) as part of the ProInno Project. A suitable interface using the properties of a VGL standard filter template serves as basis to integrate the deconvolution framework into the VGL library.

6.1. State of the Art

Deblurring methods are necessary because it is impossible to build imaging instruments that produce arbitrarily sharp images uncorrupted by noise. In the recorded images there are, however, hidden information that can be used to reconstruct the underlying images with less blur and noise. It is not trivial to deblur the images and this problem belongs to the class of ill-posed inverse problems [80]. Noise can always be found in these images and is amplified and creates artifacts if not properly considered in the reconstruction. In this section, the state of the art in image deblurring, especially fluorescence microscopy images, is presented with a particular reflection of currently used methods. First the linear approaches are introduced and later the nonlinear approaches are described leading to the newest compound algorithms. Besides, since astronomy images show similar properties, deblurring methods developed for these images are presented as well. Deblurring methods are also applied to shaken camera images and the latest developments in this area are also discussed.

6.1.1. Linear Methods

A linear approach to deblur an image is to use an inverse filter. The PSF have to be known and both the PSF and the recorded image are transformed in the Fourier space. Then the blurring is removed by a division and the result is backtransformed from the frequency domain. Since noise is not considered in this approach there are artifacts in the reconstructed images. A more stable result can be obtained when using a Wiener filter. In principal, the Wiener filter works in the same way as the inverse filter but the noise is considered by a spectral density function and thus a better result can be achieved. An even more advanced linear approach is the Tikhonov-Miller filter method

[3]. Objective of this method is the find a reconstructed image that minimizes the error between reblurred result and recorded image and is regularized with a Tikhonov-Miller functional in order to get a stable solution. This minimization can be done analytically resulting in a linear algorithm. In this approach, adaptive Gaussian noise is assumed and thus this method is not suitable for microscopy images.

6.1.2. Nonlinear Methods

The possibilities of linear approaches are limited and thus nonlinear approaches are used to restore blurred images. The Jansson Van Cittert algorithm was introduced as one of the first nonlinear methods [88]. In this approach, the image is reconstructed iteratively by comparing the reblurred restored image with the recorded one and in each step the difference between these both images is minimized. If stopped before noise is amplified the Jansson Van Cittert approach is able to obtain acceptable results. The Jansson Van Cittert approach was later extended by non-negativity constraints and widely used for deconvolution in light microscopy [170]. An iterative version of the already introduced Tikhonov-Miller filter was presented in [167] and used for microscopy images. This approach shows better results than its linear version but in [164] the authors showed that using a Richardson Lucy (RL) algorithm further improves the results. The RL algorithm [101] [138] considers the Poisson noise in the image and is therefore perfectly suited for fluorescence microscopy images. Considering the noise statistics is critical and most standard image deconvolution methods rely on the Gaussian noise model. Different noise models require different deconvolution methods and there are e.g. deconvolution approaches suitable for salt and pepper, i.e. impulsive noise [11] [12]. The latter approach was originally designed for gray value images but was later extended to process color images [10]. The basic RL algorithm is not stable in its original form and noise is still amplified when using a large number of iterations. Therefore, it can be stopped before noise is amplified or the images can be denoised in a previous step [58]. A statistical information based analysis method is used to stop the iterative RL algorithm in [124]. The basic RL algorithm contains a non-negativity constraint and in [163], the authors showed that the performance of the RL algorithm can be further improved by adding a background signal to the image formation model in order to get near zero values. Later, an additional regularization term was added in order to get a stable result. A very popular choice for a regularization term is the Tikhonov-Miller (TM) regularization [126]. This regularization term suppresses noise amplification successfully and guarantees a stable solution [58]. Nevertheless, applying TM regularization leads to smoothed edges and thus Total variation (TV) regularization was introduced. TV regularization was first used to denoise images [142] and later applied to deblurring problems. While preserving edges, TV is able to smooth homogeneous areas and thus to suppress noise amplification. An algorithm containing the RL functional with

the TV regularization was proposed in [44]. In order to minimize the underlying combined functional a multiplicative gradient-based algorithm is used. The RL algorithm itself guarantees the non-negativity of the solution but in the RLTV algorithm negative values are possible. In order to avoid negative values the authors suggest using a small regularization parameter. Since the original RL algorithm has a slow convergence rate an adaptive accelerated RL method is presented in [148]. The acceleration is done by adding an exponent to the correction ratio which is computed adaptively by using the deblurred images from previous iterations. Since there is no regularization in this method, noise amplification is a problem. Therefore, the authors suggest to stop the algorithm at the optimum and to use a wavelet-domain denoising as post-processing step. In case of noise-free images, it is shown that the new accelerated method is able to obtain better results after less iterations. TV regularization is used in many image restoration methods and a main concern is how to minimize the objective functional and the convergence of the applied algorithms. First-order numerical schemes for TV image restoration are investigated in [8] and the convergence of the proposed schemes is proven. First-order numerical schemes are also evaluated in [100] [172]. The Bregman distance introduced in [24] was used in [64] to improve a blind deconvolution method assuming Gaussian noise. In [145], an advanced minimization technique based on a split Bregman technique is used to solve the RLTV optimization for a deblurring problem. This approach is less computational intensive than previously developed algorithms based on the split Bregman technique since no additional inner iteration loop is necessary. The original split Bregman method for TV regularization [59] was introduced to solve general TV-regularized problem. A Douglas-Rachford splitting method in combination with the I-divergence and the TV regularization is also used to denoise images suffering from multiplicative noise, e.g. Gamma noise [152]. There is a relation between the Douglas-Rachford splitting method and the split Bregman technique [144] and the known convergence properties of the Douglas-Rachford splitting are used to investigate the convergence of the split Bregman techniques [145]. The authors of [59] state that the split Bregman technique can also be applied to compressed sensing problems alongside to deconvolution problems. Compressed sensing allows the reconstruction of images from a small amount of data [30] [31] [46] and also belongs to the class of ill-posed inverse problems. There are many applications for methods based on compressed sensing like in medical imaging for sparse MR image reconstruction [102] [103]. Another possibility for regularization is to use the Mumford-Shah functional which gives preference to piecewise smooth images. Several variational deconvolution approaches with Mumford-Shah-like regularizing and nonlocal image information are investigated in [78] [79]. These algorithms are designed for Gaussian or Impulse noise and thus not suitable for images corrupted by Poisson noise. Regularization can also be given by favoring a wavelet expansions with a small number of nonzero coefficients [166] which is typical for piecewise smooth objects.

6.1.3. Deblurring in Astronomy

Astronomy images are quite similar to microscopy images since both are low-photon images and suffer from Poisson noise. Additionally, due to the diffraction limited nature of the optics and light the astronomy images are blurred as well. Similar as for microscopy images, it is usual to use deblurring to improve the image quality of the astronomy images before analysing them [23]. A good overview about the common and new deblurring techniques used in astronomy is given in [128]. In astronomy images, like in microscopy images, it is not possible to have negative values and in order to deblur an image a robust and fast optimization strategy is needed. A conjugate gradient method is presented that is modified to maintain the required non-negativity constraint by modifying the actual gradient and the restored image in each iteration step. This method guarantees a stable and fast convergence of the RL functional. It belongs to a class of iterative schemes called projections onto convex sets, which are guaranteed to converge.

In this review [128], regularization terms are discussed as well. The authors think that in future spatially adaptive regularization methods are used. These techniques are more flexible and can be adapted to different image conditions. The full Pixon method is one of these techniques and hereby the spatially adaptive image smoothness permitted by the data is maximized. In other words the objective of this method is to find the smoothest possible image under the restriction of non-negativity. A set of Pixon kernels which is rich enough to allow all images of interest but exclude unwanted images at the same time is used to reconstruct the image. The important point is that all shapes of the image features can be build. Besides, since the approach is more flexible it can be applied to images with different characteristics. Other approaches being specialized for a specific type of image may not be able to achieve good results for other image conditions.

6.1.4. Deblurring of Shaken Camera Images

A general problem with digital camera images is camera shake which can spoil the photos. This effect is especially distinctive when the shutter speed is relatively slow and the photo is taken in low-light conditions. The image degradation is usually modeled as the convolution of the image with a shift-invariant filter kernel representing the blurring [32]. Blind deconvolution approaches are usually used to deblur these images and an example of such an algorithm is the adapted blind deblurring method based on a variational inference approach [52]. This algorithm estimates the blur kernel and removes the camera shake blur by using the Richardson Lucy algorithm which deconvolves the blurry image with the estimated kernel. Blind deconvolution is difficult since the estimation of the blur kernel and the deblurring have to be done in one step. An approach which is modeling the physical properties of a 2-D rigid body movement was proposed [146] and is designed to deblur rotational motions from a single image. The authors state

that this method is superior to single image motion deblurring using pixel color/gradient information and that rotation and possible translations can be corrected. A different idea to improve the blind deblurring results correcting camera shake is to use a second noisy image which is hardly blurred. Such a second image can be obtained by a short exposure time resulting in a dark and noisy image. The proposed approach uses the help of the noisy image to estimate an accurate blur kernel which is difficult to obtain from a single blurred image. Afterwards, the deconvolution is performed using again both images to reduce ringing artifacts. The final result is then obtained by a further suppression of ringing artifacts in smooth image regions using a gain-controlled deconvolution process [180]. All previously described approaches assume a shift-invariant and thus uniform filter kernel. However, a real camera shake is in general not uniform and a non-uniform filter kernel is better suited to deblur the images [90]. In [174], a non-uniform filter kernel is used and applied to two deblurring algorithms: a blind deblurring based on a single image and an approach based on a blurry image and a sharp but noisy image of the same scene. The non-uniform filter kernel is realized by a parameterized geometric model of the non-uniform image blur. The authors state that this approach is able to remove a wider class of blurs than previous approaches and demonstrate its effectiveness using real images. Motion blurring when observing a distant scene is discussed in [157]. The blur is modeled as an integration of the clear scene under a sequence of planar projective transformations describing the path of the camera. The authors state that this method is more effective at modeling the spatially varying motion blur than conventional methods based on space-invariant blur kernels. A modified Richardson Lucy algorithm which incorporates state-of-the-art regularization is used to deblur the images. A recently presented approach is to use a hardware attachment consisting of a combination of sensors to support the blind deconvolution methods [77]. The data acquired by the sensors during an exposure is used to estimate a non-uniform blur function from the acceleration and angular velocity of the camera. This approach which the authors denote as "aided blind-deconvolution" is completely automatic and the authors claim that is outperforms the current leading image-based methods.

6.2. Architecture of the Deconvolution Framework

The deconvolution framework is designed to contain the maximum-likelihood and maximum-a-posteriori deconvolution algorithms. In addition, it is possible to extend the framework and to combine different components arbitrarily. The included deconvolution methods iteratively minimize a given functional containing the underlying noise model and additional regularization due to the ill-posed nature of the deconvolution problem. Considering the likelihood distribution $P(i|o)$ of the underlying noise distribution leads to a maximization likelihood (ML) algorithm [40]. Since noise is amplified after several iterations, an improved result can be obtained if regularization is

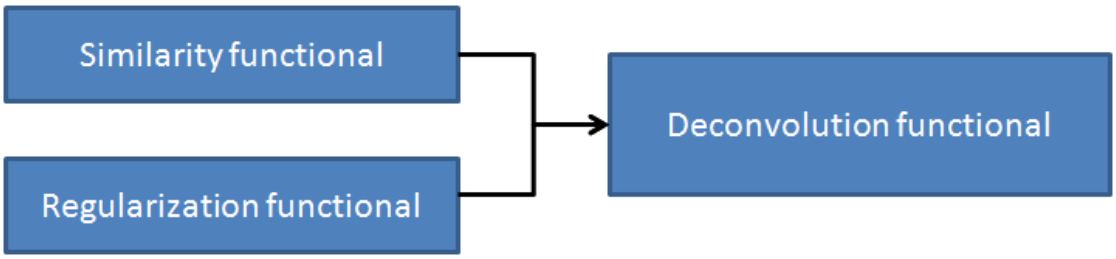

Fig. 6.1.: Deconvolution functional.

added. For this reason, a priori knowledge $P(o)$ is used in order to get a stable solution. Instead of maximizing the likelihood distribution $P(i|o)$, the a posteriori distribution $P(o|i) = P(i|o) \cdot P(o)$ is being maximized allowing a stable result of the ill-posed inverse problem by using additional information about the original image o. Instead of maximizing $P(o|i)$, it is also possible to minimize $-P(o|i)$ or even $-log(P(o|i))$ which is done e.g. for the Richardson Lucy functional.

In general, an iterative MAP approach to deconvolve an image consists of a similarity or fitting term S containing the convolution mask PSF and the given signal i and a regularization term R realizing the consideration of a priori knowledge. In addition, the similarity term contains the model for the underlying noise distribution. An initial estimation for o is required which is then iteratively modified to the reconstruction result. An illustration of a deconvolution functional is given in figure 6.1.

$$J(o) = S(i, PSF, o) + \lambda R(o) \tag{6.2.1}$$

The regularization term has to be weighted by a parameter λ in order to balance it against the similarity term. It is not trivial to determine a suitable value for λ since λ has a huge influence on the result of the deconvolution algorithm. In [58], the influence of the regularization parameter on a Tikhonov regularized RL algorithm was investigated. The a priori knowledge is meant to guarantee a stable result but it should not determine the result by overweighting the similarity term containing the recorded image. A stable solution can be obtained if the noise in the image is suppressed properly and thus a lower signal to noise radio (SNR) requires a higher value for λ. Later, simulations are used to evaluate the deconvolution methods, especially to investigate the possible quality of the results. In such a case, the original signals are known and can be compared to the deconvolution results. Therefore, a brute force search can be used to determine the best suitable value for λ.

In order to deconvolve a given image i with a filter mask PSF, the deconvolution functional J which contains S and R has to be minimized representing a formulation of the MAP distribution. The minimization is performed by a suitable optimizer. In addition, an initial signal o_0 is required and an empty signal is usually used for that purpose. Since the optimization methods used to minimize the functional J are gradient

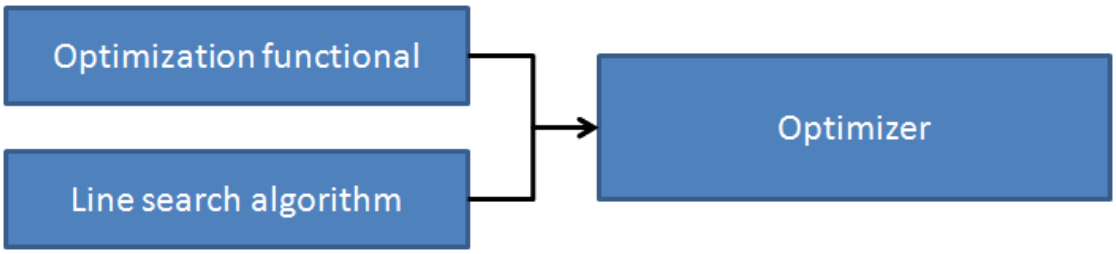

Fig. 6.2.: Optimizer.

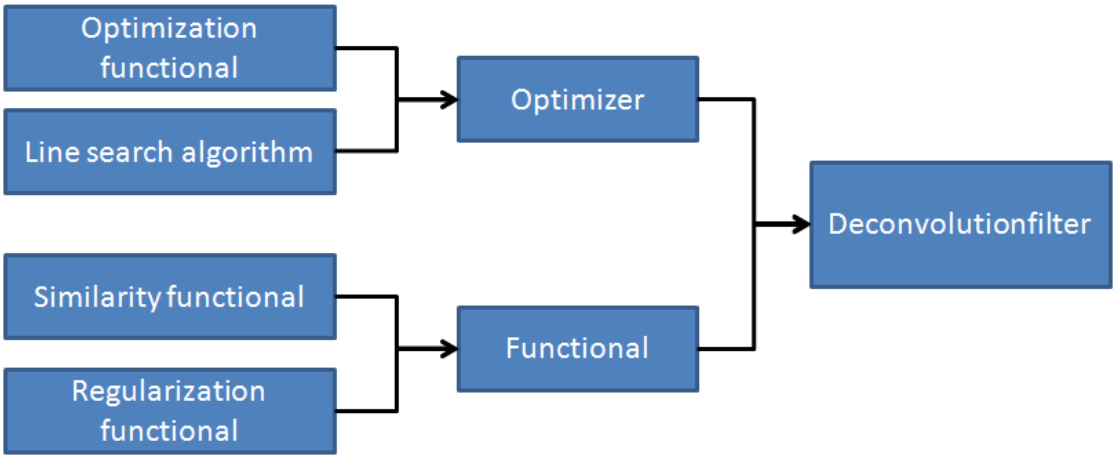

Fig. 6.3.: Architecture of deconvolution filter.

based, the gradient $\partial J/\partial o$ of J is required and has to be provided by the Functional object.

$$\frac{\partial J(o)}{\partial o} = \frac{\partial S(i, PSF, o)}{\partial o} + \lambda \frac{\partial R(o)}{\partial o} \tag{6.2.2}$$

Several optimization methods include a line search step which is realized as a separate component. In this way, different line search algorithms can be realized and arbitrarily selected in the different optimization techniques. The optimizer therefore consists of a optimization functional containing the actual optimization technique and an additional optional line search technique (Figure 6.2).

In summary, the deconvolution framework contains a deconvolution functional which is formed by the similarity and the regularization functional. In addition, an optimizer is required to minimize the deconvolution functional with an optional line search algorithm (Figure 6.3).

6.3. Implementation with VGL

According to the architecture of the filter framework, the implementation consists of the different already described components. Since the scope of the ProInno project is the implementation of microscopy deblurring methods, the interface class to the VGL library is called *VGLDeblurrFilter* instead of deconvolution filter. This class is derived from the class *VGLObject* and implemented in the current style for *VGLFilter* classes. *VGLObject* serves as basis for all high-level objects in the VGL library and is derived from *VGLClass*. The class *VGLClass* serves in general as basis for all VGL classes and the classes *Functional* and *Optimizer* are derived from this class as well. The *Functional* and the *Optimizer* class form the core of the deconvolution framework and are meant to be independent from every other component of the VGL library. The only direct connection between the framework and the VGL library is given by the required interface *VGLDeblurrFilter*. The *Functional* consists of a similarity functional and a regularization functional provided by the *SimilarityFunctional* and the *RegularizationFunctional* container. These container basically contain a collection of the required functionals enclosed by an own namespace *IPSolver*. The name of the namespace was chosen due to the fact that an inverse problem has to be solved to perform a deconvolution. The connection between the *Functional* class and the actual similarity and regularization functional implementations is given by using functional pointers which can be assigned easily. An extension of the framework thus requires a small additional component in the *Functional* class linking the according functional pointer. The actual implementation can be done in the *SimilarityFunctional* or the *RegularizationFunctional* container by providing an additional separate function. Each implementation of both the similarity and the regularization functional consists of a function to calculate the function value and the gradient of the functional for the current estimated deconvolution result. The design of the *Optimizer* class is similar to the *Functional* class. The actual implementation of the optimization algorithms and the line search techniques are located in a container and the connection is given by functional pointers within the *Optimizer* class. The *Optimizer* class can be updated with little effort while the actual implementation of additional methods is located in a separate container. Since functional pointers are used in both the *Optimizer* and the *Functional* class, the parameter and return variables of the different components are well defined and additional components can be used in collaboration of every other existing methods.

In addition, a separate class *Examiner* is used to supervise the iterative deconvolution process. The supervision of the iterative process requires several additional computations and has a considerable impact on the overall computational time of the deconvolution. The supervision is thus optional and offers different possibilities like the mere tracking of the functional value in each iteration step up to a calculation of the mean square error between the actual estimated deconvolution result and the original image if such a connection is provided. Another possibility is the determination of the

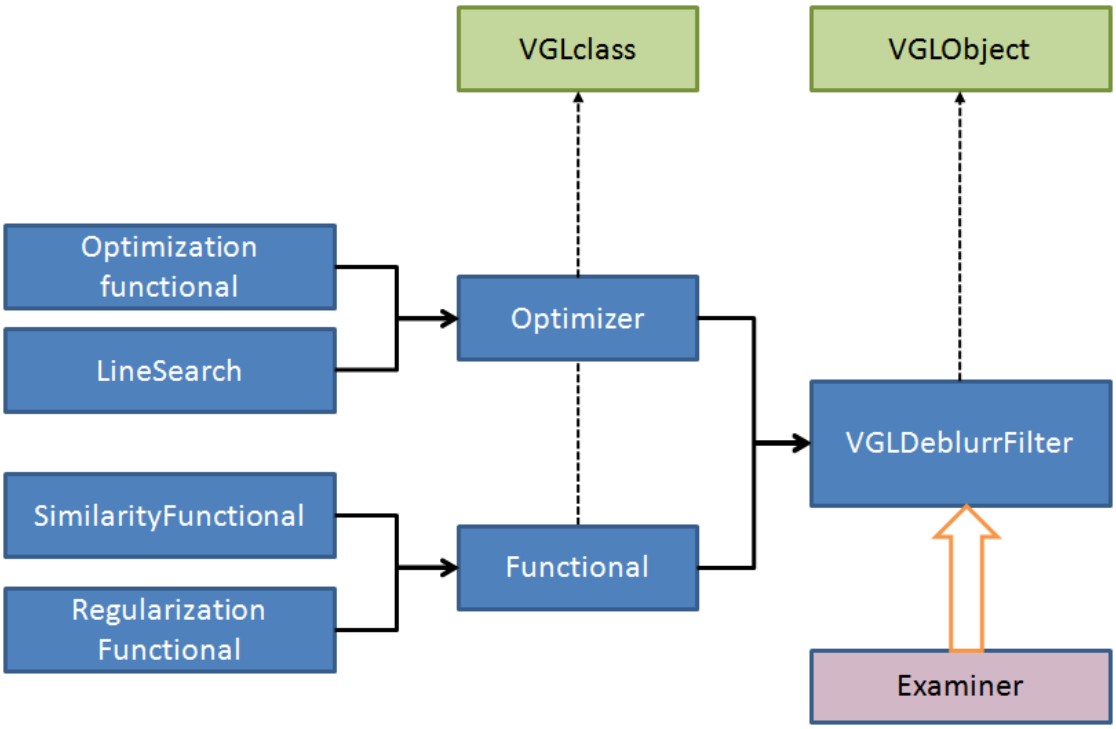

Fig. 6.4.: Overview of VGL deblurring framework.

I-divergence value of the measured image and the reblurred actual estimated deconvolution result in case the connections to the measured image and the PSF are given.

Figure 6.4 shows the schema of the VGL implementation of the deconvolution framework. The deconvolution framework consists of several different components and includes different similarity and regularization functionals and different optimization functionals which are sometimes supported by line search techniques.

The similarity functionals given by the included state-of-the-art deconvolution methods are:

- Least Square.
- Richardson Lucy.

The deconvolution functional is completed by an additional regularization functional and the following functionals are included in the deconvolution framework:

- Tikhonov-Miller.
- Total Variation.

The minimization of the deconvolution functional is performed by the following optimization functionals. Since it is possible that a deconvolution functional does not allow negative values in the estimated deconvolution result, constraint optimization functionals are provided as well.

- Descent Gradient.
- Gradient Line Search.
- Constraint Descent Gradient and Constraint Gradient Line Search.
- Conjugate Gradient.

Several line search techniques are included in the deconvolution framework and can be used in different optimization functionals.

- Interval.
- Descent.
- ThreePointParabolic.

6.3.1. Interface to VGL Library

The VGL classes derived from *VGLObject* contain properties, methods to access the properties like get/set and one action. There are standard properties which are available for all derived classes and additional properties can be defined. The functional pointer for the similarity functional, the regularization functional, the optimizer and the line search techniques do not have to be known but enumerated type (VGLenum) values with according names are used to identify them. The *VGLDeblurrFilter* contains all standard properties of *VGLFilter* classes like *FirstSource* and *FirstDestination*. In addition a PSF attribute and a start image attribute are added. In order to control the iterative process, it is the possible to determine the maximal amount of iteration steps and the λ parameter which weights the regularization functional. The action of this class performs the actual iterative process by using the *Functional* and *Optimizer* class. Which similarity functional, regularization functional and optimizer is used in the deconvolution is determined by three additional properties containing enum variables. There is no additional property for the line search since not every optimizer requires one. In case a line search is needed, it is determined by the optimizer.

An overview of the required properties is given by the following list:

Data containers:

- FirstSource.

- FirstDestination.
- PSF.
- StartImage.

Deconvolution method:

- SimularityFunctional.
- RegularizationFunctional.
- Optimizer.

Additional parameter:

- λ.
- NumberOfIterations.

6.4. Standard Components of the Deconvolution Framework

6.4.1. Similarity Term

The similarity term considers the noise distribution given in the recorded image. In most cases, the recorded images are degraded by Gaussian noise and a Least Square similarity term is used to cope with Gaussian noise. Since microscopy deblurring is also an objective of the deconvolution framework, images degraded by Poisson noise have to be considered as well and a Richardson Lucy similarity term is used in this case. In the following equations, i denotes the recorded image, o the reconstructed and PSF the point spread function. Furthermore, $*$ describes a convolution, x an arbitrary point and Ω the image domain.

Least Square

If the recorded image suffers from Gaussian noise, a least square (LS) fitting term is used since it considers the properties of Gaussian noise [141].

$$S_{LS}(o) = \int |o * PSF - i|^2 \, d\Omega \tag{6.4.1}$$

Instead of the continuous version of the LS term, the following discrete version is used in the implementation.

$$S_{LS}(o) = \sum_{x \in \Omega} |o(x) * PSF - i(x)|^2 \tag{6.4.2}$$

In addition, the gradient of the discrete LS term is required. The gradient is given by an image or a volume of the same dimension and size than the given image i. The gradient of the LS term in an arbitrary point x in the image domain Ω is given by:

$$\frac{\partial S_{LS}(o)}{\partial o}(x) = 2\,|o(x) * PSF - i(x)|\, abs(1, (o(x) * PSF - i(x))) * PSF^* \tag{6.4.3}$$

This equation contains a gradient of a norm and the following function is used to express the gradient.

$$\frac{\partial\,|y|}{\partial y} = abs(1, y) = \begin{cases} -1 & y > 0 \\ 1 & y < 0 \\ 0 & y = 0 \end{cases} \tag{6.4.4}$$

Richardson Lucy

The Richardson Lucy (RL) algorithm [101] [138] considers the Poisson noise in the image and is therefore perfectly suited for fluorescence microscopy images. In principle, the RL algorithm maximizes the Poisson likelihood distribution (Equation 3.2.8) with respect to o. Instead of maximizing $P(i|o)$ it is possible to minimize $-log(P(i|o))$ being equivalent to the minimization of the functional S_{RL1}. Besides, it is also possible to derive the RL algorithm by using the Expectation-Maximization algorithm [41].

$$S_{RL1} = \int (o * PSF) - i \cdot log\,(o * PSF) + log(i!) d\Omega \tag{6.4.5}$$

Since the functional S_{RL1} is minimized with respect to o, the all constant parts i.e. $log(i!)$ can be removed resulting in functional S_{RL2}.

$$S_{RL2} = \int (o * PSF) - i \cdot log\,(o * PSF)\, d\Omega \tag{6.4.6}$$

Instead of using the original version, a modified version of the RL functional has to be used. Regions of zero values in the images are possible and thus the original RL functional would contain a logarithm of zero which is not defined. A small $\epsilon > 0$ is introduced to overcome this problems and leads to the modified functional S_{RL}.

$$S_{RL}(o) = \int (o * PSF) - i \cdot log\,(o * PSF + \epsilon)\, d\Omega \tag{6.4.7}$$

A discrete version of the S_{RL} functional is necessary for the implementation.

$$S_{RL}(o) = \sum_{x \in \Omega} (o(x) * PSF) - i(x) \cdot log\left(o(x) * PSF + \epsilon\right) \tag{6.4.8}$$

Additionally, the gradient of the discrete S_{RL} term is required for the optimizer. The gradient of the modified RL term in an arbitrary point x in the image domain Ω is given by:

$$\frac{\partial S_{RL}(o)}{\partial o}(x) = \left(1 - \frac{i(x)}{o(x) * PSF + \epsilon}\right) * PSF^* \tag{6.4.9}$$

Hereby, PSF^* denotes the adjoint of the filter mask PSF. In case of a symmetric filter mask, the adjoint filter mask and the filter mask are the same.

6.4.2. Regularization Term

The already introduced Tikhonov-Miller (TM) regularization and the Total variation (TV) regularization are included in the deconvolution framework. Both the TM and the TV regularization assume a smooth result of the deconvolution problem and are thus able to suppress noise amplifications and artifacts caused by small variations. The Tikhonov-Miller (TM) regularization was used at first and guarantees a stable solution [58]. Nevertheless, applying this regularization term leads to smooth edges which is a drawback of this method. Due to its drawbacks, the TM regularization was later replaced by Total variation (TV) regularization which is able to overcome this problem. TV regularization was originally used to denoise images and later applied to deblurring problems. TV smoothes homogeneous areas while preserving edges because it smoothes the images in the tangential direction of the image levels and not in the orthogonal direction. However, the TV regularization also has some drawbacks. It does not smooth edges but there is a stair-casing effect when ramps are reconstructed. This effect is especially noticeable when 1D signals are deblurred but is also present in case of 2D and 3D images. Furthermore, TV rounds corners in the images which is not of importance for fluorescent microscopy since cells are structures without corners. Nevertheless, both techniques are very popular and commonly used. The choice for the regularization term should depend on the content of the given signals. Due to its property of preserving edges, the TV regularization should be used in case of sharp edges while the TM regularization is better suited in case of a continuous increase of signal values.

Tikhonov-Miller

A very popular choice for a regularization term is the Tikhonov-Miller (TM) regularization [126]. In its base form, the TM regularization is given by

$$R_{TM}(o) = \int |\Gamma o|^2 d\Omega \tag{6.4.10}$$

for a suitably chosen Tikhonov matrix Γ and with $|.|^2$ describing the L_2 norm. The identity matrix can be chosen a Tikhonov matrix, i.e. $\Gamma = I$, leading to the level 0 TM regularization which gives preference to solutions with smaller norms:

$$R_{TM0}(o) = \int |o|^2 d\Omega \tag{6.4.11}$$

Instead of the continuous version of the LS term, the following discrete version is used in the implementation:

$$R_{TM0}(o) = \sum_{x \in \Omega} |o(x)|^2 \tag{6.4.12}$$

Again, the gradient of the discrete level 0 TM term is required. The gradient of the level 0 TM term in an arbitrary point x in the image domain Ω is given by:

$$\frac{\partial R_{TM0}(o)}{\partial o}(x) = 2\,|o(x)|\,abs(1, (o(x))) \tag{6.4.13}$$

The level 0 TM regularization is able to suppress noise amplification but is not suitable for microscopy deblurring problems. Since this regularization favors solutions with smaller norms, parts of the signal content i are also suppressed leading to a deflated reconstruction result which is not desirable. The level 1 TM regularization which contains the gradient of the image o is better suited in this case since this regularization assumes a smooth solution.

$$R_{TM1}(o) = \int |\nabla o|^2 d\Omega \tag{6.4.14}$$

In this equation ∇o describes the gradient of the image o given by a Tikhonov matrix Γ containing a discrete derivative. The L_2 norm of the gradient of the image o is realized as square sum of the partial gradients of the image o in all dimensions of the image domain. Since microscopy images are acquired in a two or three dimensional image domain, the superior three dimensional case is investigated and the according parts containing the z dimension can be ignored in the two dimensional case.

$$R_{TM1}(o) = \int \left(\frac{\partial o}{\partial x}\right)^2 + \left(\frac{\partial o}{\partial y}\right)^2 + \left(\frac{\partial o}{\partial z}\right)^2 d\Omega \tag{6.4.15}$$

Instead of the continuous version of the level 1 TM term, the following discrete version is used in the implementation:

$$R_{TM1}(o) = \sum_{x \in \Omega} \left(\frac{\partial o}{\partial x}(x) \right)^2 + \left(\frac{\partial o}{\partial y}(x) \right)^2 + \left(\frac{\partial o}{\partial z}(x) \right)^2 \tag{6.4.16}$$

The necessary gradient of the level 1 TM term in an arbitrary point x in the image domain Ω is given by:

$$\frac{\partial R_{TM}(o)}{\partial o}(x) = 2\nabla(\nabla o(x)) = 2\Delta o(x) = 2\left(\frac{\partial o^2}{\partial^2 x}(x) + \frac{\partial o^2}{\partial^2 y}(x) + \frac{\partial o^2}{\partial^2 z}(x) \right) \tag{6.4.17}$$

Total-Variation

Total variation (TV) regularization was first used to denoise images and later applied to deblurring problems. Compared to the level 1 TM regularization, the TV regularization uses the L_1 norm instead of the L_2 norm.

$$R_{TV}(o) = \int |\nabla o| d\Omega \tag{6.4.18}$$

Again, ∇o describes the gradient of the image o and the L_1 norm of the gradient of the image o is used in the TV regularization term. The L_1 norm of ∇o is realized as square root of the square sum of the partial gradients of the image o in all dimensions of the image domain. The equation is given for a three dimensional case and the according parts containing the z dimension can be ignored in the two dimensional case.

$$R_{TV\beta}(o) = \int |\nabla o|_\beta = \int \sqrt{\left(\frac{\partial o}{\partial x} \right)^2 + \left(\frac{\partial o}{\partial y} \right)^2 + \left(\frac{\partial o}{\partial z} \right)^2} d\Omega \tag{6.4.19}$$

Unfortunately, the basic TV regularization term is not differentiable in case ∇o is equal to a zero vector because the L^1 norm is not differentiable at zero. Therefore, a modified version of the TV functional presented in [165] is used. Adding a small $\beta > 0$ prevents the norm from being zero and therefore the derivative of the TV term is well defined. In [33] the authors recommend to use $10^{-5}d$ as β with $[0, d]$ being the dynamic data range of the already reconstructed image o_k and β is set according to this recommendation. The 3D version of the modified TV functional is shown in equation 6.4.20 including the parameter β. In case of a 2D image, the partial derivative with respect to z can be neglected. In accordance with the 2D image case, the partial derivative with respect to y can also be ignored for 1D signals. Figure 6.5 shows the modified norm included in the stable TV regularization term for several β values in the 1D case.

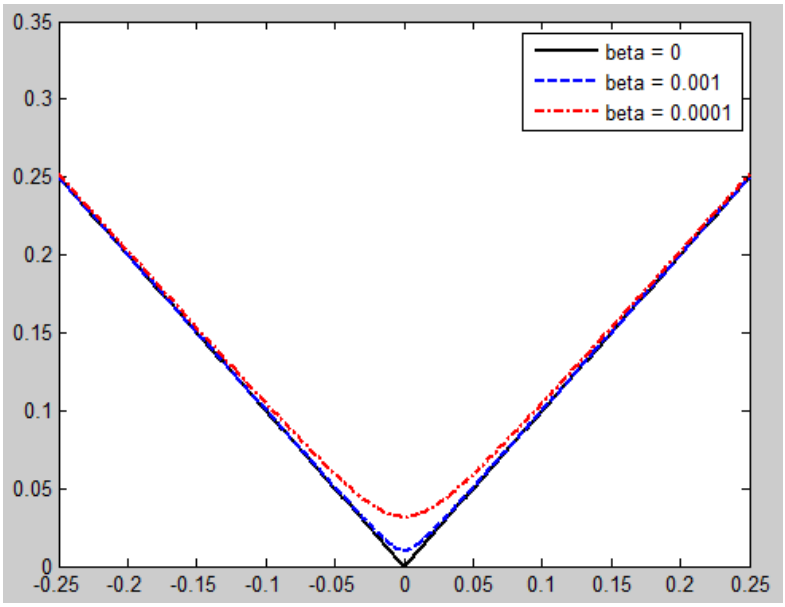

Fig. 6.5.: Illustration of stable TV regularization norm in 1D.

$$R_{TV\beta}(o) = \int |\nabla o|_\beta d\Omega = \int \sqrt{\left(\frac{\partial o}{\partial x}\right)^2 + \left(\frac{\partial o}{\partial y}\right)^2 + \left(\frac{\partial o}{\partial z}\right)^2 + \beta} d\Omega \tag{6.4.20}$$

In order to implement the TV regularization functional it has to be discretized:

$$R_{TV\beta}(o) = \sum_{x\in\Omega} \sqrt{\left(\frac{\partial o}{\partial x}(x)\right)^2 + \left(\frac{\partial o}{\partial y}(x)\right)^2 + \left(\frac{\partial o}{\partial z}(x)\right)^2 + \beta} \tag{6.4.21}$$

The gradient of the discrete TV regularization functional is necessary for the optimization:

$$\frac{\partial R_{TV\beta}(o)}{\partial o}(x) = \nabla \left(\frac{\nabla o}{|\nabla o(x)|_\beta}\right)(x) \tag{6.4.22}$$

This gradient contains the modified L^1 norm of ∇o at a investigated point x and is calculated using the same realization as in the original functional calculation:

$$|\nabla o(x)|_\beta = \sqrt{\left(\frac{\partial o}{\partial x}(x)\right)^2 + \left(\frac{\partial o}{\partial y}(x)\right)^2 + \left(\frac{\partial o}{\partial z}(x)\right)^2 + \beta} \tag{6.4.23}$$

The implementation of the actual gradient of $R_{TV\beta}$ using the just described norm $|\nabla o(x)|_\beta$ at each point x in the image domain is realized by:

$$\begin{aligned}\frac{\partial R_{TV\beta}(o)}{\partial o}(x) = & \left(\partial \frac{\frac{\partial o}{\partial x}}{|\nabla o(x)|_\beta}/\partial x\right)(x) + \left(\partial \frac{\frac{\partial o}{\partial y}}{|\nabla o(x)|_\beta}/\partial y\right)(x) \\ & + \left(\partial \frac{\frac{\partial o}{\partial z}}{|\nabla o(x)|_\beta}/\partial z\right)(x)\end{aligned} \tag{6.4.24}$$

6.4.3. Optimizer

In this section several optimization techniques are presented. The scope of the optimization is a minimization based on a given functional J. Details about the functional J are not important for the optimization but knowledge about the gradient of the functional $\frac{\partial J(x)}{\partial x}$ is required. In addition, several functionals are defined for a non-negative data range.

Descent Gradient

The descent gradient optimization technique is a quite simple optimization technique. The negative gradient of the functional is calculated and a certain fixed step size γ is used to alter the grid using the gradient (Figure 6.6).

$$f_{k+1} = f_k - \gamma \frac{\partial J(f_k)}{\partial x} \tag{6.4.25}$$

This technique is considered to be most accurate when the step size is small. On the other side it shows a slow convergence rate and is thus not a very practical choice. It is however very useful to verify the results of accelerated techniques and to investigate the true potential of different methods. A real drawback is that local minima cannot be overcome.

Gradient Line Search

In this method the gradient of the functional is calculated first. Then a linear search is used to determine the optimal step size γ_k meaning the minimal functional value possible on the line given by the actual position and the gradient (Figure 6.7).

$$f_{k+1} = f_k - \gamma_k \frac{\partial J(f_k)}{\partial x} \tag{6.4.26}$$

Constraint Descent Gradient and Constraint Gradient Line Search

These techniques contain the same optimization step than the normal version of the Descent Gradient and Gradient Line Search optimization. Since some functionals like the RL functional do not allow negative values, an additional step backprojects the grid

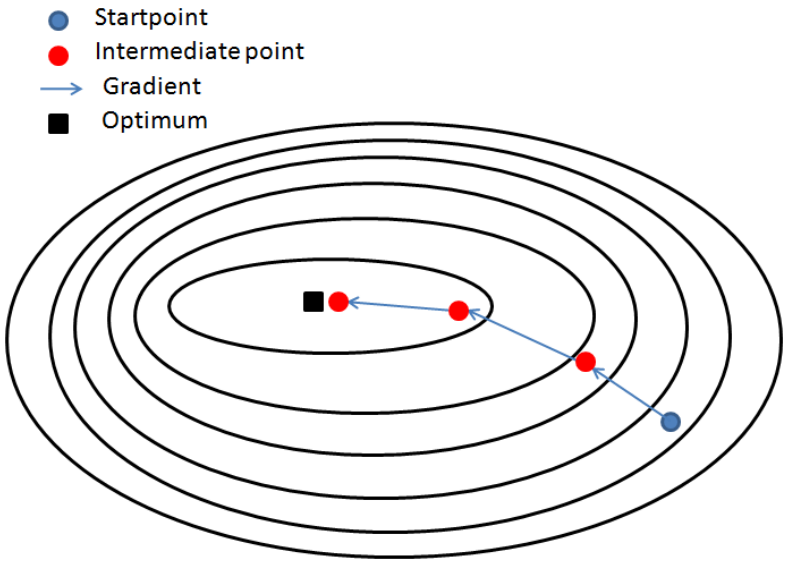

Fig. 6.6.: Illustration of *Descent Gradient* optimization.

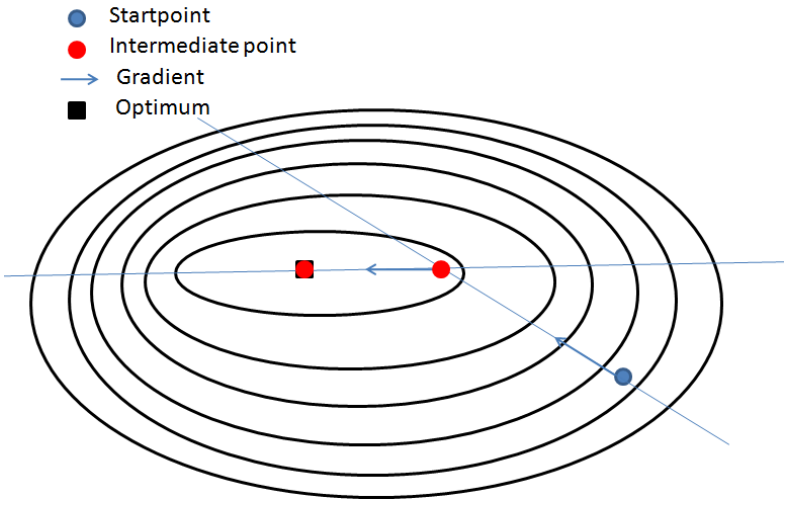

Fig. 6.7.: Illustration of *Gradient Line Search* optimization.

to the valid data range. All negative values which are not allowed in the constraint versions of the optimization techniques are set to zero providing a valid data range after each iteration step.

Conjugate Gradient

The conjugate gradient (CG) technique is a more sophisticated optimization technique. In order to minimize the deconvolution functionals, the nonlinear conjugate gradient method which generalizes the conjugate gradient method to nonlinear optimization is used. The gradient of the functional is required for the CG algorithm and is called *grad* in the following description. The CG algorithm uses a search direction to determine the next iteration step instead of simply using the current gradient. Each search direction is formed by the previous search direction and the current gradient weighted by a γ parameter. In order to calculate the current search direction for the CG algorithm, the Polack-Ribiere formula is used [126]. A discretized version of this formula with k being the actual iteration step is given by:

$$\gamma = \frac{\sum_\Omega grad_k \left(grad_k - grad_{k-1}\right)}{\sum_\Omega grad_{k-1} grad_{k-1}} \tag{6.4.27}$$

A description as pseudocode of the CG with a maximal allowed number of iterations M is as follows:

Require: initial image o_0
  k=0
  d = gradient(o_0)
  while $k < M$ **do**
    o_{k+1} = line search(o_k, d)
    g = gradient(o_{k+1})
    compute γ {using Polack Ribière}
    $d = g + \gamma d$
    $k = k + 1$
  end while

6.4.4. Line Search Methods

The purpose of a line search method is to find the optimal point on a given line defined by a start point and a direction vector. The optimal point is the point where the functional value is minimal in case of the deconvolution problem.

Interval

In the *Interval* line search method, a certain step size and amount of allowed steps are used in a first stage. The step size and amount of allowed steps lead to a set of sampling points on the direction vector and the minimal functional value for these sampling points can be determined resulting in an optimal point. Additional stages are used to improve the accuracy of the optimization result. The neighbourhood of the result point of the previous stage is investigated using a decreased step size and a more accurate solution can be determined. This stage can be repeated arbitrarily with further decreased step sizes until the designated accuracy is given.

Descent

The *Descent* line search method is similar to the *Interval* line search method except of the determination of the result point of the first stage. In the first stage, a certain step size is given but a variable amount of steps is possible. The line search method determines the functional value of the point given by a first step along the search direction. Additional points along the search line are then investigated until the functional value increases. The point with the minimal functional value, i.e. the next to last investigated point, serves as result for the first stage. A more accurate result is then obtained by using the same technique as in the additional stages of the *Interval* line search method. The neighbourhood of the result point of the previous stage is investigated using a decreased step size.

Parabolic Interpolation

The *Parabolic Interpolation* line search method is based on Brents method [126]. This method is illustrated in figure 6.8 and requires a suitable underlying function. The function should be nicely parabolic near to the minimum and a parabola is used to approximate the function near the optimum leading to an accurate estimation of the optimum which is independent from a step size. Three points are used to determine a parabola in each step and the vertex point of this parabola serves as new estimation for the optimum. The point with the highest functional value is then replaced by the vertex point and the interpolation is repeated until the procedure does not improve the result any further. Since the objective is to find an abscissa rather than an ordinate, the procedure is technically called inverse parabolic interpolation. In the figure, the original points 1,2,3 are first evaluated (dashed line) and then the minimum of the first parabola, 4, replaces point 3. A new parabola (dotted line) leads to point 5, which is close to the minimum of the function. This method is really fast because it requires just a small number of function evaluations.

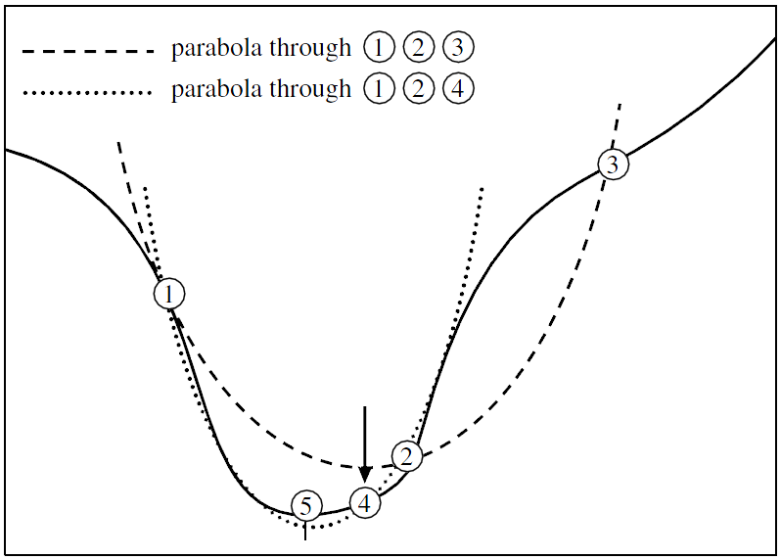

Fig. 6.8.: Illustration of line search using parabolic interpolation.

6.5. Additional Components of the Deconvolution Framework

6.5.1. Multiplicative RL Algorithm

An iterative multiplicative form of the RL algorithm is then given by

$$o_{k+1} = \left\{ \left[\frac{i}{o_k * PSF} \right] * PSF^* \right\} o_k \tag{6.5.1}$$

after removing the constant parts of the functional. Hereby, a start image o_0 which is non-zero is necessary. The RL algorithm does not converge for noisy images due to the ill-posed nature of the underlying problem. Instead, noise is amplified after several iterations and artifacts are generated. In order to allow a stable result, the RL algorithm can be stopped before noise is amplified [124] or the images can be denoised in a previous step [164].

6.5.2. Multiplicative RL Algorithm with Background Signal

The basic RL algorithm is maintaining a non-negativity constraint which is effective only when the restored intensities have near-zero values [163]. Therefore an advanced multiplicative RL algorithm was introduced including the extended image formation

model (Equation 3.2.2). The background estimation has an influence on the effectiveness of the non-negativity constraint of the algorithm and an accurate estimation is mandatory.

$$o_{k+1} = \left\{ \left[\frac{i}{o_k * PSF + b} \right] * PSF^* \right\} o_k \tag{6.5.2}$$

6.5.3. Multiplicative RLTV Algorithm

An algorithm containing the RL functional with the TV regularization was proposed in [44]. In order to minimize the underlying combined functional a multiplicative gradient-based algorithm is used. This algorithm is iterative, a start image o_0 is necessary and in each step the following calculation has to be done:

$$o_{k+1} = \left\{ \left[\frac{i}{o_k * PSF} \right] * PSF^* \right\} \frac{o_k}{1 - \lambda \nabla \left(\frac{\nabla o_k}{|\nabla o_k|} \right)} \tag{6.5.3}$$

As mentioned before, it is possible to have zero values in the images and in order to get a valid equation a slightly modified version is used:

$$o_{k+1} = \left\{ \left[\frac{i}{o_k * PSF + \epsilon} \right] * PSF^* \right\} \frac{o_k}{1 - \lambda \nabla \left(\frac{\nabla o_k}{|\nabla o_k|_\beta} \right)} \tag{6.5.4}$$

The modified version contains a small $\epsilon > 0$ avoiding a division by zero. In addition, since the derivative of the TV regularization is included in the RLTV the modified version for TV including a $\beta > 0$ value is used.

This algorithm is well-suited for microscopy image deblurring since it is adapted to Poisson noise and the TV regularization guarantees a stable solution with sharp edges. The algorithm was tested both with synthetic and real data and showed good results, both visually and quantitatively, compared with the unregularized RL version of the algorithm [44]. Nevertheless, this algorithm has an essential limitation. The values that can be used as λ are not allowed to be too high since the denominator in equation (6.5.3) can become zero or negative. This would cause very high intensities for small values or even a violation of the non-negativity constraint. In order to overcome this problem the authors suggested to use small values for λ and they used e.g. 0.002 as λ in their own experiments.

7. Improved and new Microscopy Deblurring Methods

7.1. Accelerated RLTV

The convergence speed of the multiplicative RLTV method is not satisfying and an acceleration method [17] is used to improve the convergence speed of the algorithm. This approach can be applied to various algorithms as long as the basic iterative algorithm contains a known independent functional ψ to calculate the next iteration step.

$$f_{k+1} = \psi\left(f_k\right) \tag{7.1.1}$$

The multiplicative RLTV algorithm fulfills this requirement. However, this requirement is not fulfilled for a conjugate gradient method because each iteration step depends on the direction of the previous iteration step. In the original RLTV algorithm, the functional ψ is calculated in each step using the result from the previous step as start point. A virtual point g_k is calculated in the accelerated version and this point is used in the functional ψ to determine the next point.

$$f_{k+1} = \psi\left(g_k\right) \tag{7.1.2}$$

In order to create this virtual point g_k, the direction d_k of the previous iteration step is used. These differences describe the actual changes made by the functional ψ.

$$d_k = f_k - f_{k-1} \tag{7.1.3}$$

The virtual point g_k is calculated by using the direction d_k and a weighting parameter α which has to be determined in each iteration step.

$$g_k = f_k + \alpha_k \cdot d_k \tag{7.1.4}$$

In order to estimate α_k, the differences l_k between the virtual point g_{k-1} and the respectively next iteration f_k are used.

$$l_k = f_k - g_{k-1} \tag{7.1.5}$$

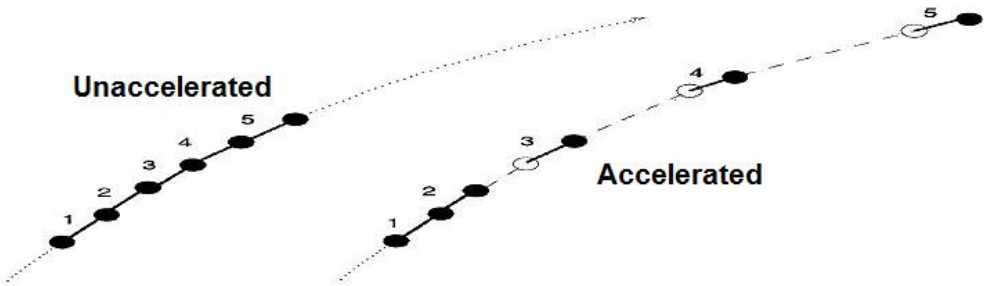

Fig. 7.1.: Illustration of acceleration.

The direction d_k has to be weighted by an acceleration parameter α_k which is estimated by using the previous two iteration steps. A more accurate solution could be obtained by a line search but this is no option because of the computational effort.

$$\alpha_k = \frac{\sum_\Omega (l_{k-1} \odot l_{k-2})}{\sum_\Omega (l_{k-1} \odot l_{k-1})} \tag{7.1.6}$$

Hereby, $\odot$ denotes an element-wise multiplication and $\sum$ sums all elements in the image domain Ω. In addition, each α has to fulfill the condition $0 \leq \alpha \leq 1$ and is modified after the estimation if necessary. Figure 7.1 shows graphically how the acceleration influences the calculation. It can be seen that instead of the original step size much larger changes can be achieved in each iteration step by using the virtual points. In the following, the accelerated RLTV algorithm is called $accRLTV$.

7.2. Bregman Distance

An alternative approach to reconstruct blurred and noisy images is using the Bregman distance introduced in [25]. This distance was first used for image denoising and several preliminary results for deblurring were shown [114]. The first step of this denoising approach is to denoise the image with the well-known ROF (Rudin, Osher and Fatemi) algorithm [142] which introduced the TV regularization. Instead of stopping after recovering this first result, it is used in the next step to compute the next result using the Bregman distance. This step is repeated resulting in a sequence of intermediate results which slowly and monotonically converges to the original noisy image. However, this sequence also monotonically gets closer to the noise free image before the noisy image is reconstructed. To stop the procedure at the right point leads to an improved denoising result. Later, the Bregman distance was added to a blind deconvolution algorithm [65] and also used to reconstruct a high resolution image on basis of a set of low resolution images [105]. In both approaches a L^2 norm based deblurring functional with TV regularization is used which is suitable for Gaussian noise. The blind deconvolution

algorithm [65] consists of two independent parts which alternately deblur the image and estimate the PSF. In the following approach, the PSF is supposed to be already known and the deblurring of the image is of interest. The new algorithm is using the Bregman distance D [25] which is defined as follows:

$$D_\vartheta(x, y) = \vartheta(x) - \vartheta(y) - \langle x - y, \partial\vartheta(y)\rangle \tag{7.2.1}$$

In this definition $< ., . >$ denotes the inner product and ∂ the gradient of ϑ. In order to reconstruct the blurred image, a minimization of a standard energy functional (Equation 6.2.1) containing a similarity and regularization functional is used in a first step. Since the objective is to deblur microscopy images, a RL term S_{RL} (Equation 6.4.7) is used to cope with the Poisson noise in the given images. A TV regularization term $R_{TV\beta}$ already known from equation (6.4.20) is added in order to guarantee a stable solution and this term is weighted by a regularization parameter λ. It is necessary to start this approach with an empty image and to do the first step without using the Bregman distance. In the following steps which are called Bregman iterations, the observed image i is modified using $i = i + v_m$ for the $(m + 1)$th Bregman iteration with $v_m = i + v_{m-1} - h * o_m$ being a result of the additional Bregman distance in the reconstruction algorithm. The general equation to calculate the result of the reconstruction in each Bregman iteration using the Bregman distance is:

$$o_m = argmin_o \left\{ S_{RL}(o, i) + \lambda \cdot D_{R_{TV\beta}}(o, o_{m-1}) \right\} \tag{7.2.2}$$

The RL deblurring term $S_{RL}(o, i)$ contains the known PSF and the regularization functional $R_{TV\beta}$ is used in the Bregman distance D. In order to reformulate and implement the algorithm, a new term named $Breg$ is introduced which represents an additional image with the same size as the observed image and is supposed to be empty at the beginning.

The further algorithm itself consists of two separate steps which have to be performed in every Bregman iteration. The first step is to reconstruct the image iteratively using the result of the previous step as start image. This reconstruction is done according to the following equation for $m = 1...n$ with n being the requested amount of Bregman iterations.

$$o_m = argmin_o \left\{ S_{RL}(o, i) + \lambda R_{TV}(o) - \lambda \langle o, Breg\rangle \right\} \tag{7.2.3}$$

This equation is based on equation (7.2.2) with the constant parts being removed and the additional $Breg$ term. The second step of the algorithm in each Bregman iteration step is the modification of the $Breg$ term according to the Bregman distance.

$$Breg = Breg - \frac{1}{\lambda}\partial S_{RL}(o_m, i) \tag{7.2.4}$$

$\partial S_{RL}(o_m, i)$ describes the gradient of the RL functional $S_{RL}(o, i)$ (Equation 6.4.9).

7.3. Constrained RLTV Method with Conjugate Gradient Optimization

The objective of this method is to deblur confocal fluorescence microscopy images and therefore the Richardson Lucy functional is used as basis. The new deblurring algorithm is based on a constraint conjugate gradient method using an additional TV regularization. Instead of using the original functionals, the stable versions already presented in equation 6.4.7 and 6.4.20 are used. In general, the more a priori knowledge can be applied, the better the deblurring result should be. Since fluorescence microscopy images are non-negative, a non-negativity constraint provides additional a prior information and thus allows an improvement of the deblurring result. However, the non-negativity constraint is effective for near zero values only. In order to provide near zero values, the alternative image formation model (Equation 3.2.2) suggested in [163] is used. A background signal b is added to the RL functional in accordance with the extended image formation model.

$$S_{RLb1} = \int (o * PSF + b) - i \cdot log\left(\frac{i}{o * PSF + b}\right) d\Omega \tag{7.3.1}$$

Since regions of zero values in the images are possible and the background value b can be zero as well, a modified version of the functional has to be used. A small $\epsilon > 0$ is introduced to guarantee that a logarithm can be zero which is not defined.

$$S_{RLb} = \int (o * PSF + b) - i \cdot log\left(\frac{i}{o * PSF + b + \epsilon}\right) d\Omega \tag{7.3.2}$$

A discrete version of the S_{RLb} functional is necessary for the implementation.

$$S_{RLb}(o) = \sum_{x \in \Omega} (o(x) * PSF + b) - i(x) \cdot log\left(o(x) * PSF + b + \epsilon\right) \tag{7.3.3}$$

Additionally, the gradient of the discrete S_{RLb} term is required for the optimizer. The gradient of the stable S_{RLb} term in an arbitrary point x in the image domain Ω is given by:

$$\frac{\partial S_{RLb}(o)}{\partial o}(x) = \left(1 - \frac{i(x)}{o(x) * PSF + b + \epsilon}\right) * PSF^* \tag{7.3.4}$$

Again, PSF^* denotes the adjoint of the filter mask PSF. A strong unregarded background signal causes the non-negativity clipping step to be needless and the algorithm is thus not working as expected. An additional background signal ensures near zero values and in this case the algorithm achieves improved results. A background enhanced image model is not necessary if only a TV regularization functional is used and the authors

[43] showed that it has no influence on the deblurring result for the multiplicative RLTV algorithm.

In order to reconstruct the image, the combined functional J_{CCG} has to be minimized.

$$J_{CCG}(o) = S_{RLb}(o) + \lambda R_{TV\beta}(o) \tag{7.3.5}$$

To minimize the functional J_{CCG}, a constrained conjugate gradient method (CCG) is used. Since this is a gradient based optimization technique, the gradient of J_{CCG} with respect to o has to be known including the gradient of the TV regularization term introduced in equation 6.4.22.

$$\frac{\partial J_{CCG}(o)}{\partial o} = \frac{\partial S_{RLb}(o)}{\partial o} + \lambda \frac{\partial R_{TV\beta}(o)}{\partial o} \tag{7.3.6}$$

$\frac{\partial J_{CCG}(o)}{\partial o}$ is called *grad* in the following. In order to calculate the current direction for the CCG, the Polack-Ribiere formula is used [126]. A discretized version of this formula with k being the actual iteration step is given by:

$$\gamma = \frac{\sum_\Omega grad_k \left(grad_k - grad_{k-1}\right)}{\sum_\Omega grad_{k-1} grad_{k-1}} \tag{7.3.7}$$

Additionally, a line search is necessary and Brents method already introduced as *Parabolic Interpolation* line search method is applied. Inspired by an algorithm discussed in [128], the non-negativity constraint is maintained by modifying the search direction and the reconstructed image itself after each iteration. Hereby, all negative values in the search direction with corresponding zero values in the reconstructed image are set to zero. This operation will be called *truncate(direction)*. At the end of each iteration step all negative values of the reconstructed image are set to zero. This step will be called *clip(image)*. In the basic algorithm [128] the negative gradient is processed before the current search direction is determined. In this case, it is possible to have negative value in the search direction leading to an inevitable violation of the non-negativity constraint being later corrected by the clipping operation. In order to avoid that behaviour, the search direction instead of the negative gradient is processed in this approach. A description as pseudocode of the CCG with a maximal allowed number of iterations M is as follows:

Require: initial image o_0
  k=0
  d = gradient(o_0)
  while $k < M \wedge$ solution not accurate **do**
    truncate(d)
    o_{k+1} = line search(o_k, d)
    clip(o_{k+1})
    g = gradient(o_{k+1})

compute γ {using Polack Ribière}
$d = g + \gamma d$
$k = k + 1$
end while

Besides, the algorithm is restarted every five iteration steps in order to maintain numerical stability. As accuracy criterion to stop the minimization, the norm of the gradient g can be evaluated and even compared with the norm of the gradient in the previous step. This approach is quite efficient since these values have already been calculated as part of the Polack-Ribière formula. The algorithm can be stopped when the norm of the gradient is becoming too small and further iterations would not improve the result any more.

In summary, this method is using a stable TV regularized RL functional that is minimized by a constrained conjugate gradient method including an efficient line search. A non-negativity constraint was added and considers additional a priori knowledge allowing further improved deblurring results. The advantage of this method compared with the multiplicative RLTV algorithm is that arbitrary values for λ can be used.

8. Evaluation of the Results

The results of the different reconstruction approaches can be evaluated quantitatively by using the mean square error (MSE), the root mean square error (RMSE) and the I-divergence (Idiv) criteria. All criteria can be applied to 2D and 3D images and the image domain is called Ω and a pixel or voxel is named x. In case the point spread function is needed, it is denoted as PSF and $*$ describes a convolution. The MSE criterion comparing the images or volumes A and B is given by:

$$MSE(A,B) = \sum_{x\in\Omega} (A(x) - B(x))^2 \tag{8.0.1}$$

and the RMSE criterion comparing the images or volumes A and B is described by:

$$RMSE(A,B) = \sqrt{\sum_{x\in\Omega} (A(x) - B(x))^2} \tag{8.0.2}$$

The MSE criterion measures the similarity of two images according to the L_2 norm and the RMSE is the square root of the MSE criteria. The MSE and the RMSE are commutative and good criteria to compare a reconstructed image with the original one.

The Idiv is commonly used to evaluate the result of microscopy deblurring methods since Poisson noise is considered. It is the only consistent measure in the presence of a non-negativity constraint [39]. The Idiv criterion comparing the images or volumes A and B is given by:

$$Idiv(A,B) = \sum_{x\in\Omega} \left(A(x) log\left(\frac{A(x)}{B(x)}\right) - A(x) + B(x) \right) \tag{8.0.3}$$

Since this functional is not defined in case the image or volume B contains zero values, it is necessary to add a small value $\epsilon > 0$ to A and B in equivalence to the RL functional.

$$Idiv^*(A,B) = \sum_{x\in\Omega} \left((A(x)+\epsilon)\, log\left(\frac{A(x)+\epsilon}{B(x)+\epsilon}\right) - A(x) + B(x) \right) \tag{8.0.4}$$

The I-divergence is not commutative and thus the same order of the images has to be used.

In case of synthetic data the original image o^* is known and can be used in the evaluation by comparing it directly with the reconstructed image o using the MSE or RMSE criteria. For real data the measured image i is compared to the reblurred reconstructed image $o * PSF$. Since there is noise in the recorded image which is not present in the reblurred reconstruction result, the results of this evaluation are not that significant and must be interpreted with caution. The Idiv is used for microscopy images suffering from Poisson noise since this criterion considers the Poisson noise distribution. In case of Gaussian noise or the presence of a mixed noise signal containing both noise distributions, an according MSE or RMSE criteria is used.

If the criteria are used in their current form an evaluation of the whole image domain Ω is given. The used synthetic test images consist of simple geometric objects with known gray value intensities. A threshold t is used to distinguish the objects (Ω_{obj}) from the background (Ω_{bg}) and the MSE or RMSE of the different image regions is analysed separately. Additionally, the border areas Ω_{bor} where the object regions and the background regions are touching are of interest. Each pixel or voxel with a neighbour belonging to the other region is included in this case. With $d(x, y) = 1$ describing neighbour pixels x and y (Naturally, $d(x, y) = 0$ means that x and y are no neighbours) and considering only pixels or voxels in the image domain Ω, the different image regions are described by:

$$\begin{aligned} \Omega_{obj} = &\ \{x | o^*(x) \geq t\} \\ \Omega_{bg} = &\ \{x | o^*(x) < t\} \\ \Omega_{bor} = &\ \{x |\ (x \in \Omega_{obj} \wedge \exists x_2 \in \Omega_{bg} : d(x, x_2) = 1)\} \cup \\ &\ \{x |\ (x \in \Omega_{bg} \wedge \exists x_2 \in \Omega_{obj} : d(x, x_2) = 1)\} \end{aligned} \tag{8.0.5}$$

Applying the quality criteria to the reconstruction results allows an evaluation of the final results of the algorithms but lacks an investigation of the intermediate results created during the underlying iterative processes. In order to evaluate the complete reconstruction process for the different algorithms, it is necessary to supervise the iterative process after each step. The applied criteria are thus calculated after each iteration step allowing an more extensive evaluation of the different methods. Since the functional value and the required calculation time are of interest as well those values are also investigated in each iteration step.

In case of synthetic image data sets, the strength of the noise signal is of interest and the signal-to-noise ratio (SNR) is used to quantify the noise strength compared to the signal strength. In general, the signal-to-noise ratio is defined as the power ratio between the signal and the noise. There are however different possibilities how to realize the calculation of the SNR and examples of different concrete definitions of the SNR are given by Young [179]. The blurred image $\tilde{o}$ is hereby compared with the degraded image i which simulates the measured image and contains additional noise. The following definition is used in order to calculate the SNR in dB:

$$SNR = 10 \cdot log \left(\frac{\sum_{x \in \Omega} \tilde{o}(x)}{\sum_{x \in \Omega} (\tilde{o}(x) - i(x))} \right) \tag{8.0.6}$$

The residuals of the reconstruction result allow an additional property to evaluate the reconstruction. The residuals are given as the difference between the reblurred reconstructed image and the recorded image.

$$Residuals = i - o * PSF \tag{8.0.7}$$

The residuals contain the information about the estimated noise in the recorded image and show how well the assumed noise model is considered in the reconstruction. Assuming the reconstruction is correct the residuals only contain the noise included in the recorded image. In case of an inaccurate reconstruction, structures of the image can be found in the residuals. It is hardly possible to evaluate the residuals automatically and thus they are commonly used to evaluate the reconstruction by a visual analysis. This criterion is well-suited for Gaussian noise since no structural information should be visible any more. In case of Poisson noise, it can be difficult to interpret the residuals since the local noise strength depends on the underlying image.

Using a Fourier transform of both the acquired and the reconstructed image allows a further evaluation of the reconstruction methods. The frequencies included in the according images are visible and this is especially useful for the Micro Axial Tomography since the aim is to reconstruct the combined support region of three different images. In case of synthetic images, the Fourier transform of the original image can also be taken into consideration.

Sometimes it is difficult to visualize 3D images in 2D. It is possible to show a slice of the volume or the surface using a threshold to extract the included objects. However, microscopy images contain sparse objects and most of the volume is background. Therefore maximum projections of the volume in x, y and z direction are used as well.

Part III.

Biological and Medical Applications

9. Microscopy Deblurring

9.1. Deblurring using Standard Components of the Deconvolution Framework

In this section, several deblurring results using the standard components of the deconvolution framework are presented. The original multiplicative RL algorithm is compared with the multiplicative RLTV algorithm which is the current state-of-the-art method in microscopy deblurring. In addition, a RL approach with TM regularization is used with a descent gradient optimization technique. Synthetic image data sets are used to evaluate the methods and deblurring results of a measured data set containing a cell are displayed.

9.1.1. Synthetic Data

Figure 9.1 shows the synthetic images used in this section. The first image is shown in the upper row and the second one in the lower row. Both images are blurred with a Gaussian PSF ($\sigma^2 = 2.0$) and degraded by Poisson noise resulting in a SNR of about $12dB$. The first image is referred to as *Image1* and the second dataset is denoted as *Image2*.

The results for the RL, RLTM and RLTV algorithm are displayed in figure 9.2. The RMSE values and Idiv values of the deblurring results compared with the original images are shown in table 9.4. The deblurring result of the RL algorithm contains strong artifacts since the noise signal in the degraded image is strong and no regularization is applied. The RLTM method improves the deblurring result due to the TM regularization. The value for the regularization parameter λ is determined by a brute force search leading to the best possible result. The quality of the result obtained by the RLTV algorithm is superior to the other two methods since the TV regularization is well suited for the underlying objects in the images. The TV regularization is able to reconstruct sharp edges and to suppress heavy noise amplification. The RMSE and Idiv values confirm this result.

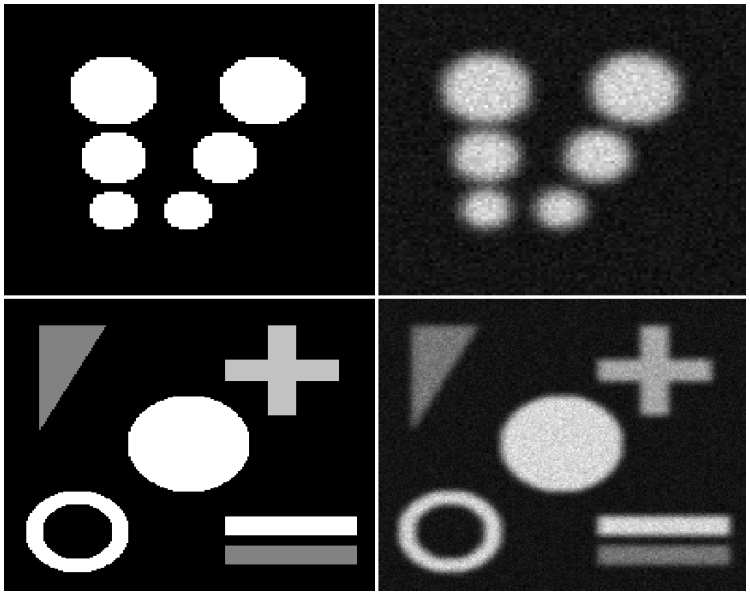

Fig. 9.1.: Original (Left) and degraded images (Right) for Image1 (Upper row) and Image2 (Lower row).

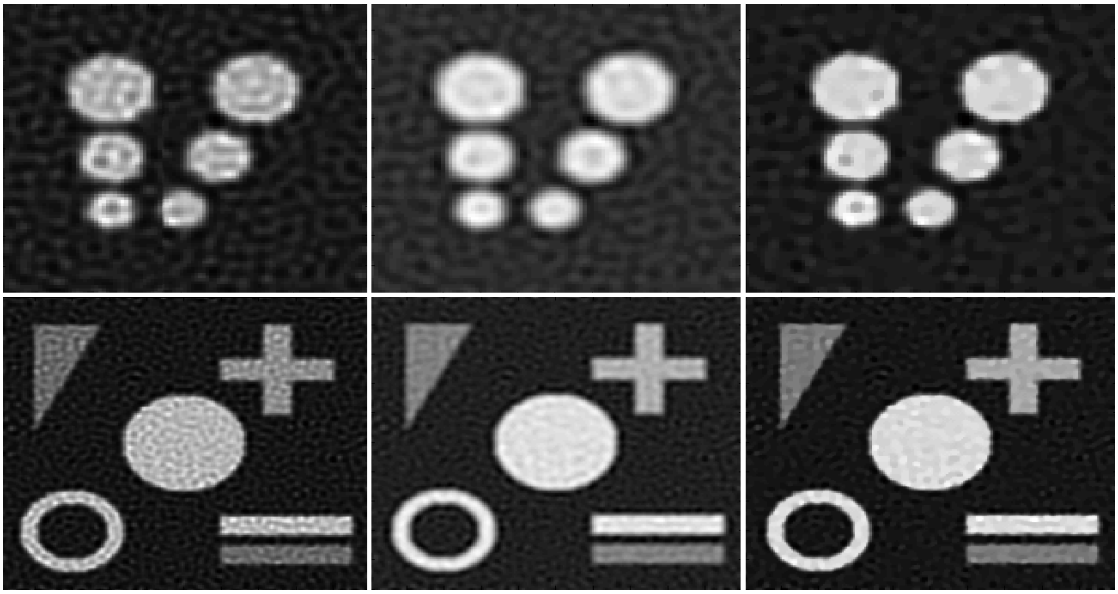

Fig. 9.2.: Deblurring results RL (Left), RLTM (Middle) and RLTV (Right) for Image1 (Upper row) and Image2 (Lower row).

Table 9.1.: RMSE and Idiv of synthetic data

RMSE	Degraded	RL	RLTM	RLTV
Image1	929	817	668	513
Image2	1719	1529	1430	1216
Idiv	Degraded	RL	RLTM	RLTV
Image1	9527	7824	7131	5123
Image2	32227	28007	25434	17587

9.1.2. Real Data

In order to demonstrate the possibilities of the standard components of the deconvolution framework, a cell image data set is deblurred using the RLTV algorithm. Several slices of the measured image data set are displayed in the upper part of figure 9.3. The measured images contain a strong noise signal comparable to the noise signal in the synthetic images. A Gaussian PSF with an estimated variance is used to deblur the image data set and the result is presented in the lower part of figure 9.3 by displaying the corresponding deblurred slices. The deblurring considerably improved the image quality and the result does not contain any noise. In addition, the resolution is enhanced and sharp edges can be seen. In fact, several cell structures are visible in the deblurring result which cannot be seen in the measured images.

9.2. Accelerated RLTV

For the evaluation of the accelerated RLTV algorithm, two synthetic test images (3D) with a size of $100 \times 100 \times 60$ voxels and $200 \times 200 \times 50$ voxels are used. The images are blurred with a Gaussian PSF of size $9 \times 9 \times 9$ voxels with a variance of 1.8 and corrupted by Poisson noise. One slice of each test image together with their degraded versions are shown in figure 9.4. Furthermore, the results of the deblurring for the RLTV and accRLTV are displayed.

In average, one iteration of the accRLTV algorithm takes 5% longer than the RLTV (Average time for one iteration image 1: RLTV 1.38 seconds and accRLTV 1.45 seconds with a 2.6 GHz Quad Core CPU). Each test image was degraded three times and restored with both the RLTV and the accRLTV. The deblurring is stopped when a certain MSE is reached and the amount of necessary iterations is shown in table 9.2. The progress of both the MSE and the IDiv are shown in figure 9.5 for one test image. In addition, figure 9.6 shows the deblurring results for a real Cell image.

In figure 9.4 it can be seen that the result images of both algorithms are nearly identical. Since the differences in the computational time for both algorithms are quite small the computational time can be neglected in the further evaluation. For the first test image

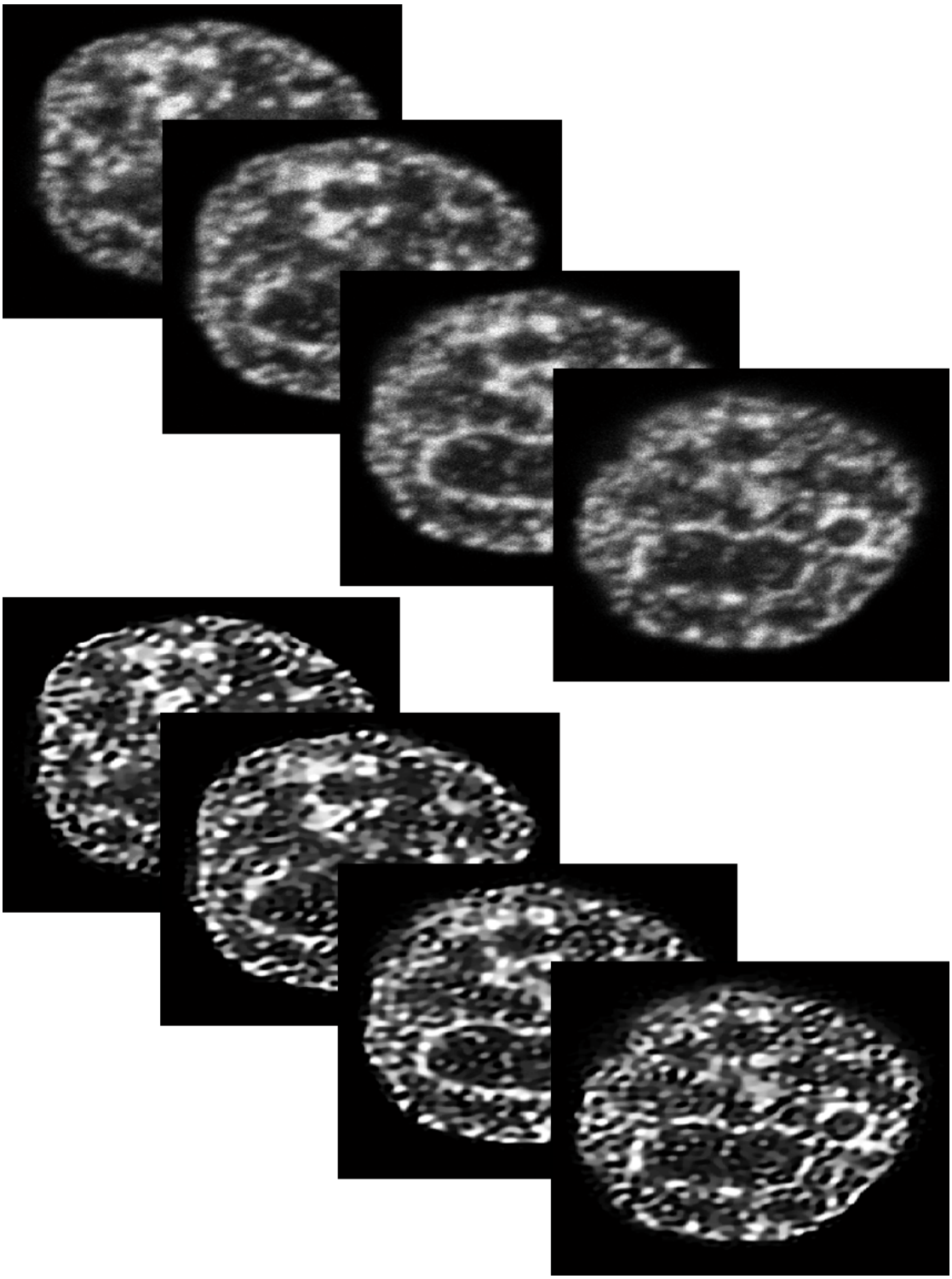

Fig. 9.3.: Slices of measured volume of cell and RLTV deblurred result.

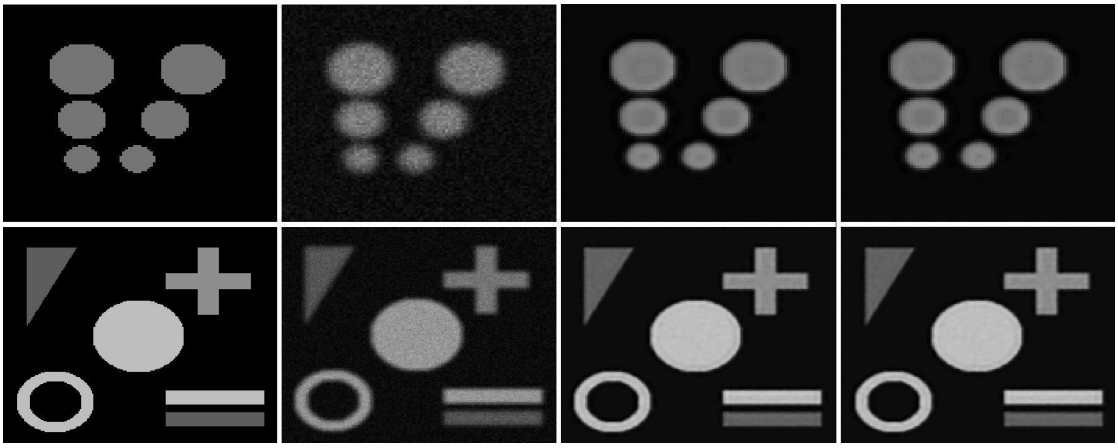

Fig. 9.4.: Left to right: original image, degraded image, RLTV and accRLTV.

	Test 1		Test 2		Test 3	
	RLTV	accRLTV	RLTV	accRLTV	RLTV	accRLTV
First image	29	18	31	21	30	19
Second image	25	15	25	14	26	16

Table 9.2.: Amount of iterations to deblur the images

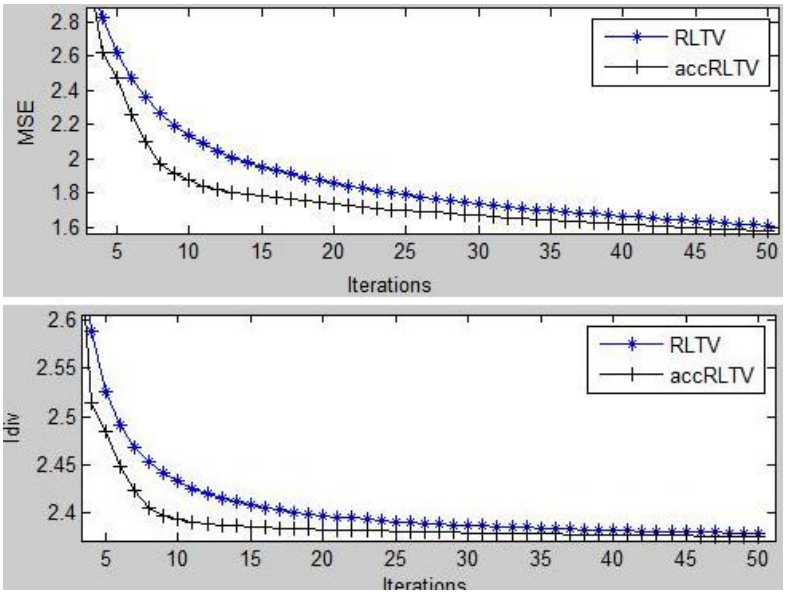

Fig. 9.5.: Progress of MSE and IDiv values of original and reconstructed results.

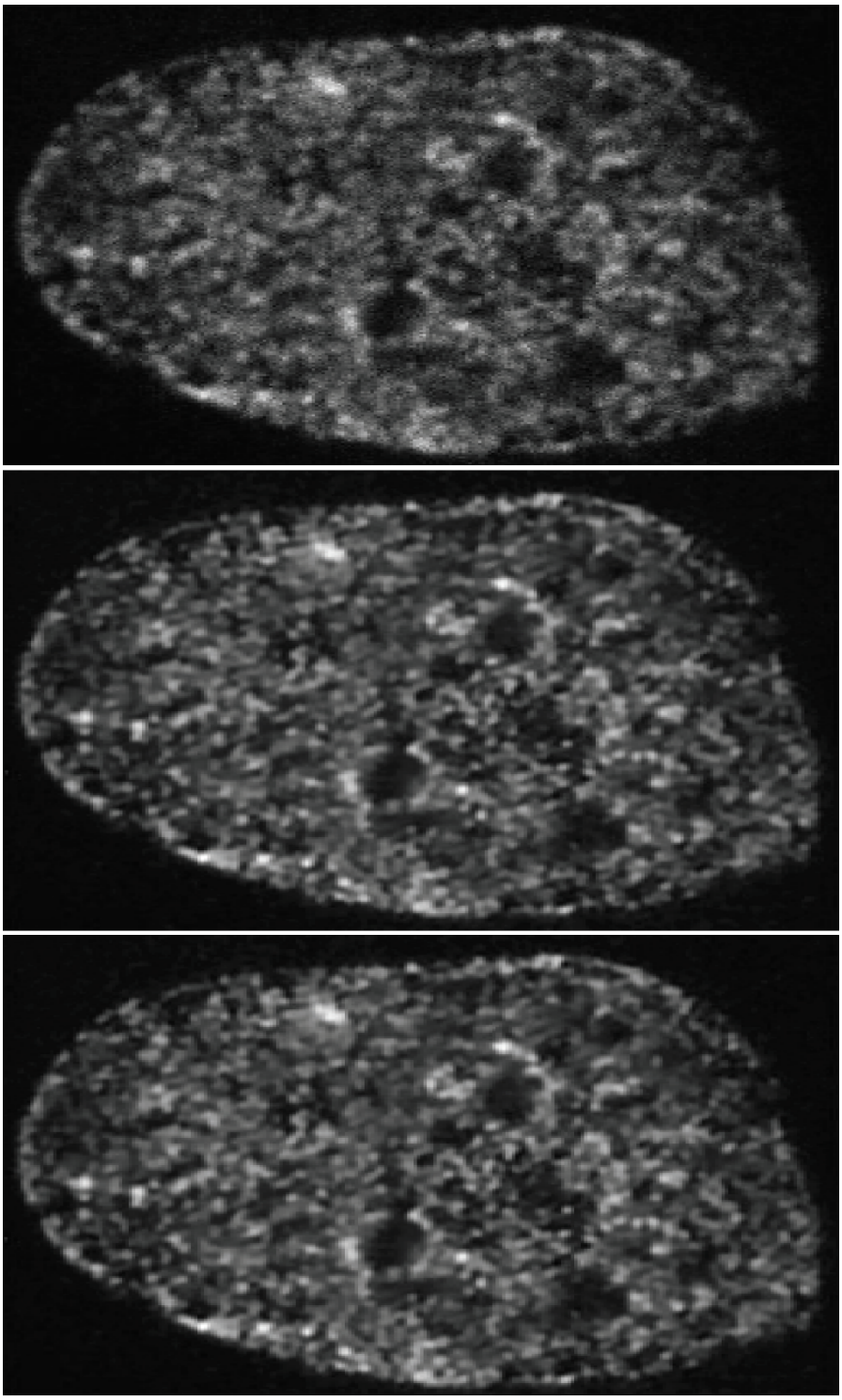

Fig. 9.6.: Cell image: measured image, RLTV and accRLTV (Top to bottom).

	Idiv	MSE
Original & Degraded	1.304.030	22.459.100
Original & Reconstructed (RLTV)	67.671	21.536.600
Original & Reconstructed (Bregman)	56.951	18.058.600

Table 9.3.: Idiv and MSE values of synthetic data

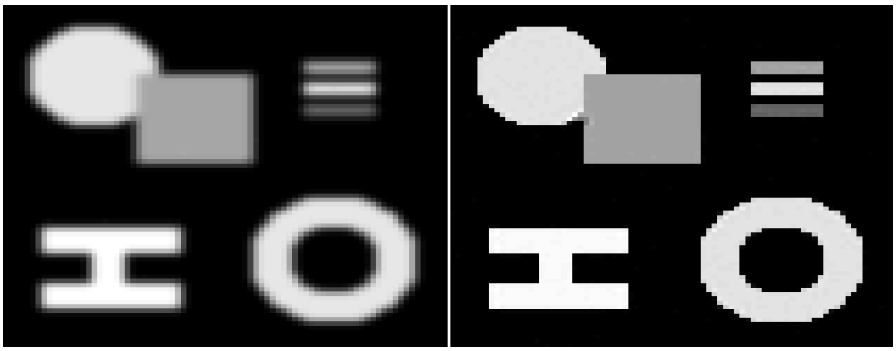

Fig. 9.7.: Degraded image (Left) and Bregman reconstructed image (Right).

the desired MSE is reached by the accRLTV within 30% less iterations compared with the RLTV. In case of the second test image the improvement is even higher: it takes 40% less iterations to reach the specified MSE for the accRLTV. The progress of the MSE and Idiv in figure 9.5 shows graphically that the accRLTV reconstructs the image faster than the original algorithm. In summary, the accRLTV produces similar results as the RLTV algorithm and requires considerably less computational time.

9.3. Bregman Distance

The quantitative results of a simulated test are shown in table 9.3. In the first row, the I-div and the MSE between the original and the degraded image are displayed. In the second row, the quality measurement of the multiplicative RLTV is listed and the results of the new algorithm can be seen in the last row. Figure 9.7 shows the result of a simulation. The degraded image and the reconstruction result using the Bregman approach can be seen.

This simulated test shows that the quality of the reconstructed images can be improved by using the new Bregman approach compared with the RLTV algorithm. Both the I-div and the MSE show an improvement of approximately 15%. The result of the new algorithm is highly dependent on the amount of Bregman iterations. With a very high number of iterations the algorithm would reconstruct the degraded image itself which is not the requested result. An empty image is used to start the algorithm and the

result is reconstructed iteratively. In every step finer structures are reconstructed which means that after some iterations the noise is reconstructed as well. There is an intermediate result during the iterative process which is very close to the original image and this result is a very good solution for the reconstruction. It is however difficult to stop the algorithm in case of real images since the original image is not known. One possibility would be to use the discrepancy principle [93] to stop the algorithm.

9.4. Constrained RLTV Method including Conjugate Gradient Optimization

The constrained RLTV method is compared with the original RL and the RLTV algorithms using synthetic and real images. Furthermore, the influence of the background signal is investigated. The constrained RLTV is referred to as CCG.

9.4.1. Synthetic Data

Figure 9.8 shows the synthetic images used in this section. The first dataset (Upper row) contains circles while the second one (Lower row) includes different objects. Both images are blurred with a Gaussian PSF ($\sigma^2 = 2.5$) and degraded by Poisson noise using two different photon counts (SNR $10.2dB$ and SNR $17.2dB$). The degraded first dataset is referred to as *Image1a* for the low photon count and *Image1b* for the high photon count. The second dataset is denoted *Image2a* and *Image2b* accordingly.

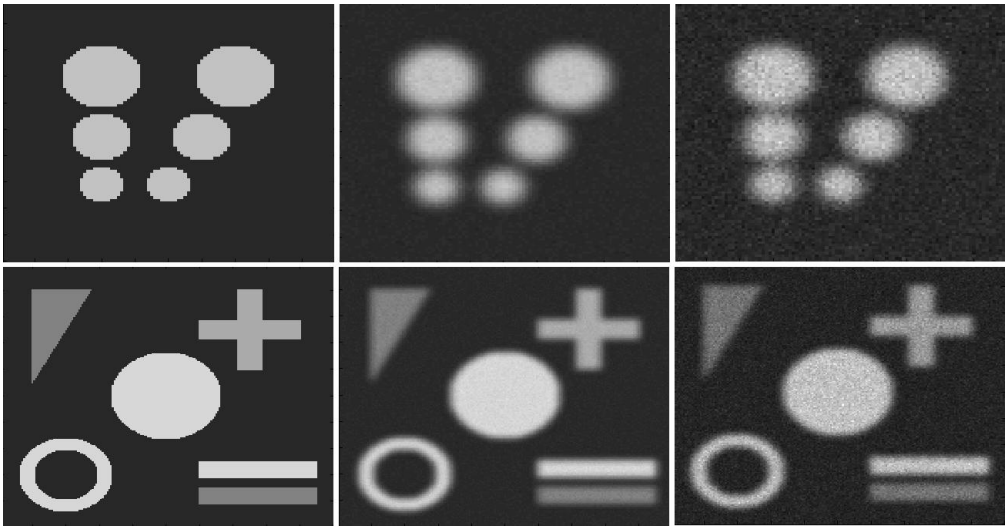

Fig. 9.8.: Synthetic images: original, degraded with high and low photon count (From left to right).

First, the influence of the background signal in the CCG algorithm is investigated. Figure 9.9 clearly shows that an improvement in the result can be achieved if the correct background signal is chosen. An underestimation of the background yields to a performance that is comparable with a model not including the background. An overestimation leads to poor results because too much information in the image is lost by clipping. A good estimation of the background signal is thus mandatory.

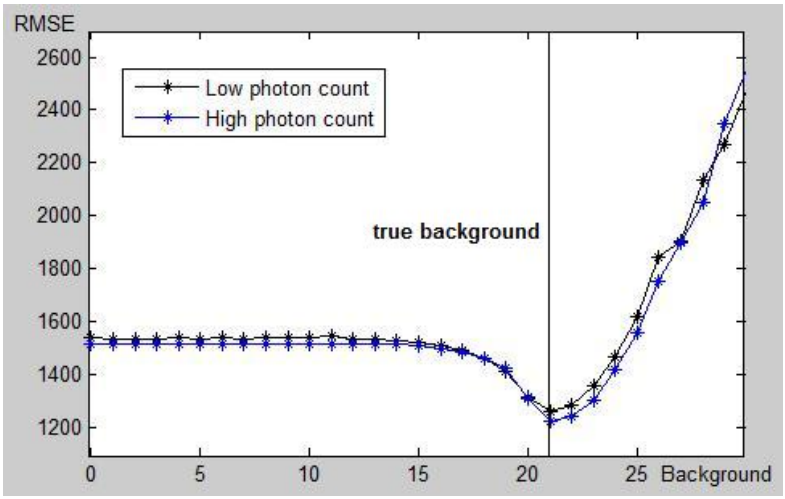

Fig. 9.9.: RMSE in dependence of background signal in CCG for Image1a and Image1b.

The results which are displayed in figures 9.10 and 9.11 show that the CCG algorithm further improves the quality of the deblurring results. Fewer artifacts are created for both low and high photon count and the object edges are significantly sharper than for the RL and the RLTV algorithm. The regularization in the RLTV is weighted by 0.002 as suggested. Since there are no limitations for the weighting in the CCG algorithm, 0.005 is used for Image1b and Image2b. In case of a high photon count 0.002 is used as well in the CCG algorithm. Because of the included background signal the results are improved in comparison to the RLTV algorithm. The RMSE values in table 9.4 confirm the improvement of the CCG algorithm. The quality of the deblurring is improved for the whole image region as well as for the object regions in the images.

9.4.2. Real Data

To evaluate the performance of the CCG method on real data, a cell image is used. The cell image together with the deblurring results are displayed in figure 9.12 while a region of interest (ROI) is shown in figure 9.13.

The resolution of the cell image is improved for all deblurring algorithms. However, the result of the RL algorithm does not contain sharp edges. The RLTV algorithm

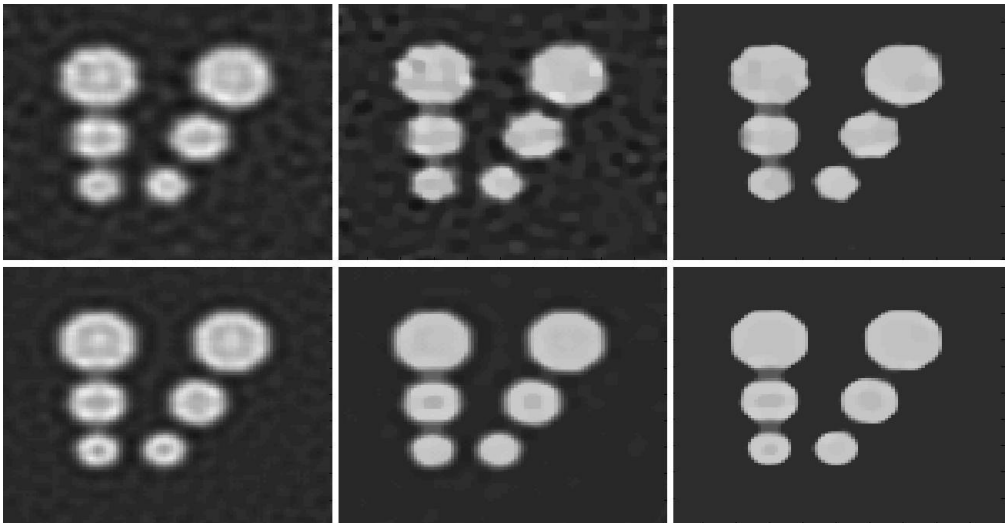

Fig. 9.10.: Deblurring results RL (Left), RLTV (Middle) and CCG (Right) for Image1a (Top) and Image1b (Bottom).

overcomes this problem but some areas are plain. This stair-casing effect is a well known drawback of the TV regularization. The CCG algorithm does not show this behaviour despite including TV. Figure 9.14 shows a profile of such an area and the advantage of the CCG can be seen.

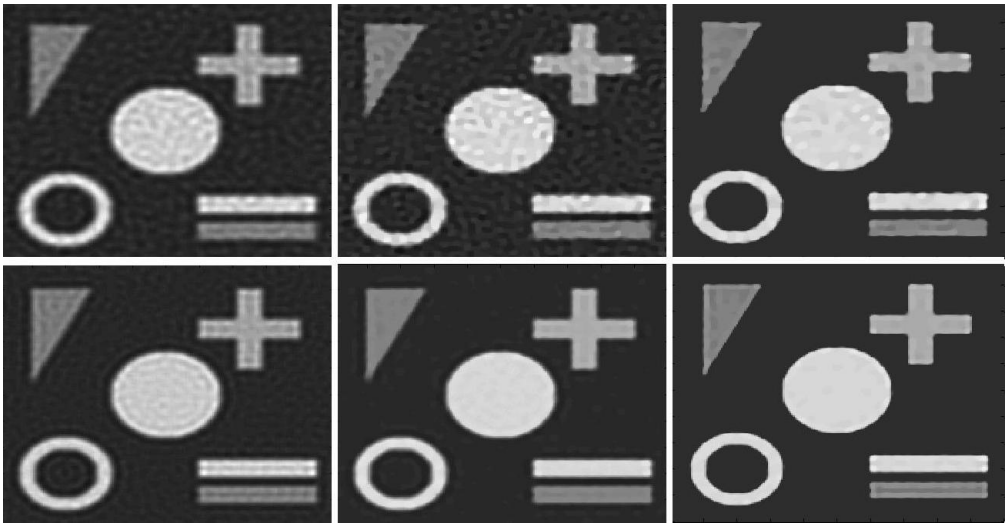

Fig. 9.11.: Deblurring results RL (Left), RLTV (Middle) and CCG (Right) for Image2a (Top) and Image2b (Bottom).

Table 9.4.: RMSE values for whole image region and object region

Whole image	RL	RLTV	CCG
Image1a	836	772	581
Image1b	765	678	477
Image2a	1562	1428	1025
Image2b	1381	1192	803
Object regions	RL	RLTV	CCG
Image1a	646	561	472
Image1b	621	539	417
Image2a	1248	1075	886
Image2b	1098	924	728

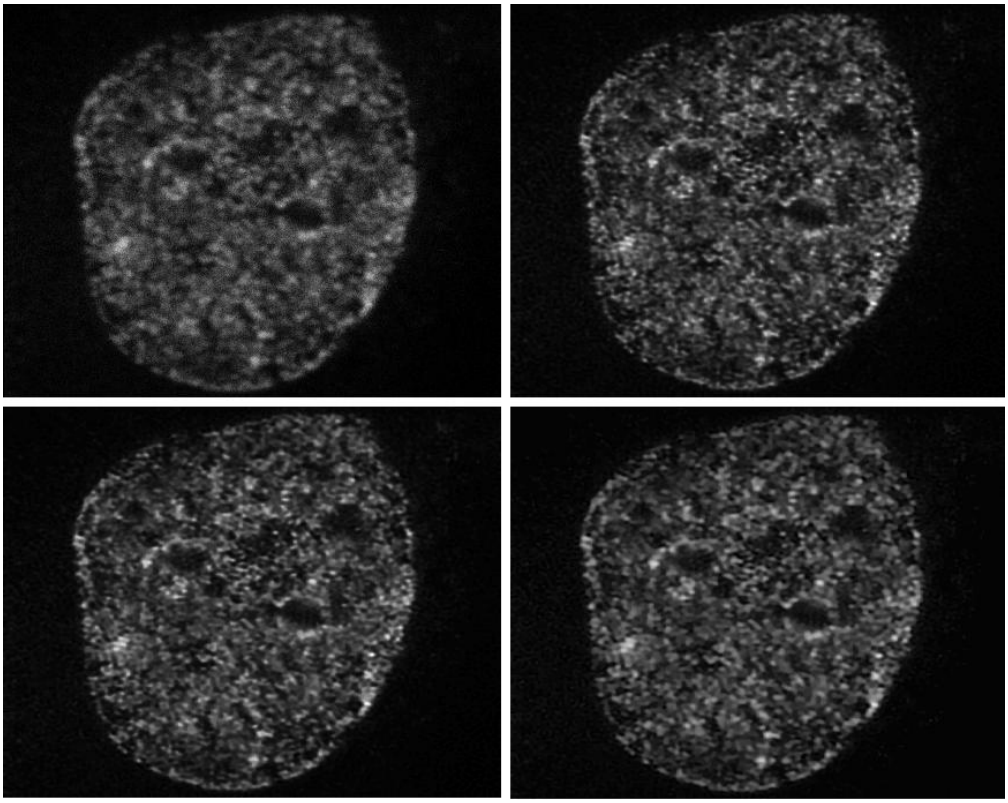

Fig. 9.12.: Cell image. Top row: Recorded image (Left) and RL result (Right). Bottom row: RLTV result (Left) and CCG result (Right).

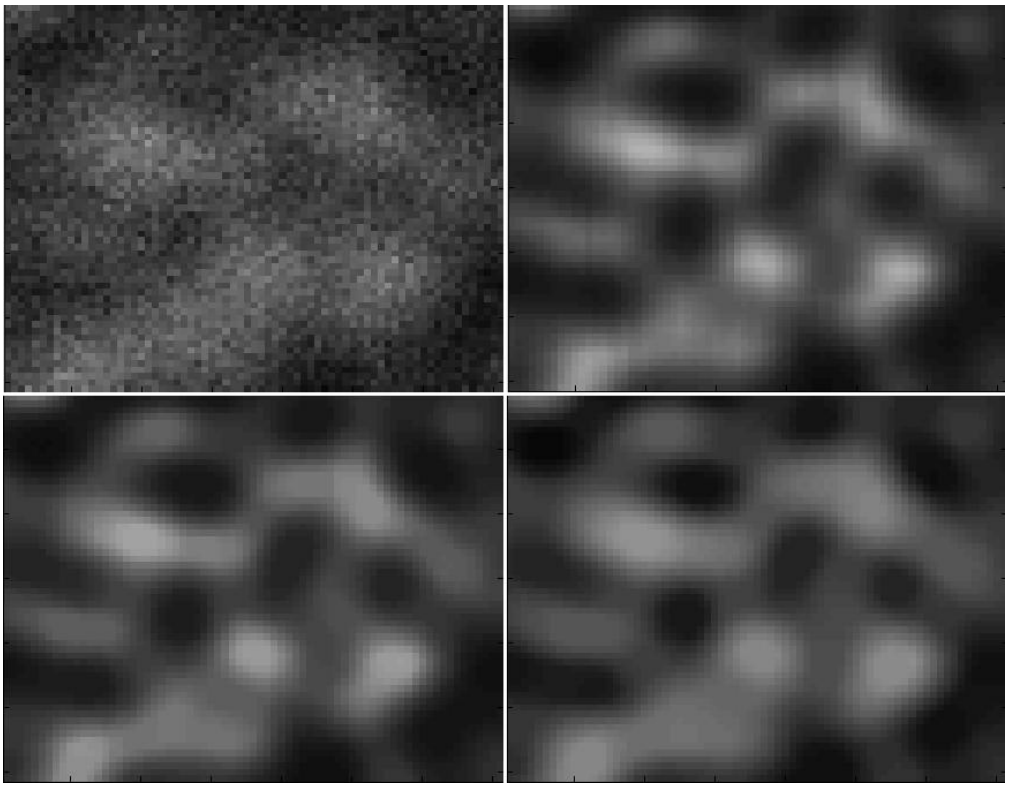

Fig. 9.13.: ROI of cell image. Top row: Recorded image (Left) and RL result (Right). Bottom row: RLTV result (Left) and CCG result (Right).

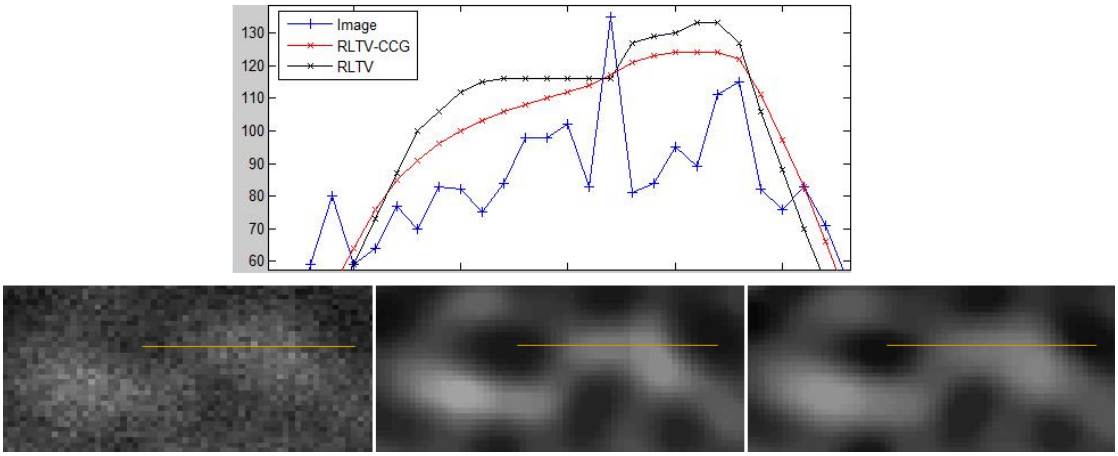

Fig. 9.14.: Profile of image, RLTV and CCG results.

10. Axial Tomography

10.1. Introduction

For a reliable understanding of cellular processes, it is necessary to develop light optical methods to acquire high resolution 3D images of the investigated cells. Cells are three-dimensional entities and a 2D image represents just a slice and thus only a small fragment of the whole object. Unfortunately, the ability of fluorescence microscopes (Widefield and confocal) to image a cell in 3D is limited. For both fluorescence microscopy types, the resolution of the acquired volumes in direction along the optical axis (Z-direction) is considerably smaller than in transversal (X- and Y-direction) direction [176]. In a conventional widefield microscope, the resolution in axial direction is about a factor of three lower than in lateral direction. The PSF and the optical-transfer-function (OTF) in X- and Z- direction of such a microscope are shown in figure 10.1. The OTF is the Fourier transform of the PSF and shows the spatial frequencies that can be imaged by the widefield microscope. As it can be seen, only relatively low frequencies can be imaged in Z-direction. The PSF was calculated due to the physical properties of the used microscope.

There have been various approaches to overcome the problem of a lower resolution in direction along the optical axis. It has been suggested to obtain tilted views in confocal theta microscopy using a double observation. The object is illuminated from one side and the emitted light is detected simultaneously in the direction parallel to the illumi-

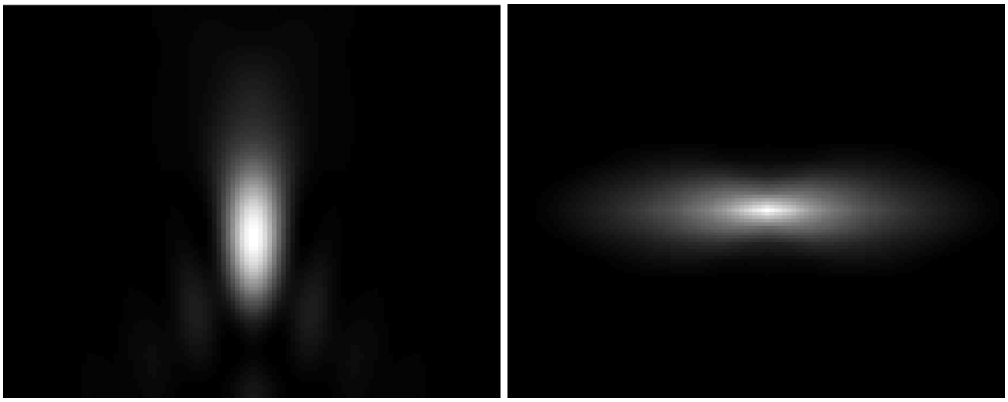

Fig. 10.1.: PSF (Left) and OTF (Right) of a Widefield Microscope.

nation direction and in a direction with an angle theta to the illumination direction [95]. In a 4Pi-confocal microscope, an illumination from two directions is applied. The specimen is illuminated and observed coherently from above and below improving the axial resolution [69] [71]. Both techniques have been combined in a 4Pi-confocal theta microscope [94]. Alternatively, two- and multi-photon excitation instead of single-photon excitation can be used to improve resolution [42] [70]. Hereby, light is emitted when at least two or more photons are absorbed which is less likely in the out-of-focus region and thus suppresses out-of-focus light. The two photon excitation approach and the 4Pi confocal fluorescence microscope were also combined improving the image quality [72].

It is also possible to get tilted views of the object by rotating the object under the microscope using a Micro-Axial-Tomograph [20] [47] [45]. The technique of axial tomography was introduced and applied to widefield microscopy by Shaw et al. [147]. Later it was again used for widefield microscopy [81] [36] and additionally, the technique is applicable to confocal microscopy [21] [36]. The Micro-Axial-Tomograph is an advanced device based on a microscope which allows the imaging of an object from different angles. Using at least three different viewing angles, it is possible to reconstruct a three-dimensional volume with a high resolution in all three dimensions. The cells or beads can be imaged from different angles since they are located on a round glass fibre as displayed in figure 10.2. The basic idea of the Micro-Axial-Tomograph is then to rotate the glass fibre as displayed in figure 10.3. Thus, it is possible to image the cells from different viewing angles. In principle, the images resulting from different viewing angles contain the same cells degraded with a rotated PSF when seen in an aligned position. Using three different viewing angles leads to three different PSFs and OTFs as displayed in figure 10.4. Each additional image based on a rotated imaging contains additional information that are missing in the other images. In this way, a larger area of the frequency domain can be covered and all of this information can be used to reconstruct a high resolution image. The combined OTF of three different PSFs can be seen in figure 10.5 and shows the available information. Images of the actual setup are displayed in figure 10.6. The glass fibre is fixed at two locations and connected to a motor that rotates the fibre. The fibre is fixed by using a spring force to press it in a bearing block. Like that, it is stable at three points while still being able to rotate. Figure 10.7 shows a real image of cells on a glass fibre. This image and the later displayed image data sets were acquired by Bianca Oehm (geb. Reinhard) during her diploma thesis [129].

10.2. State of the Art

As mentioned before, there are usually three different viewing angles in Micro Axial Tomography resulting from the rotation of the object under the microscope. The im-

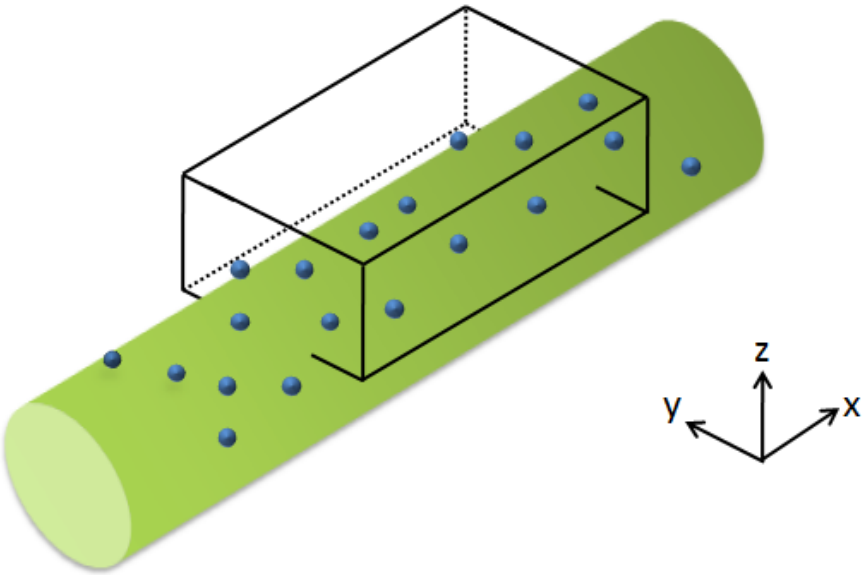

Fig. 10.2.: Schematic illustration of beads on fibre.

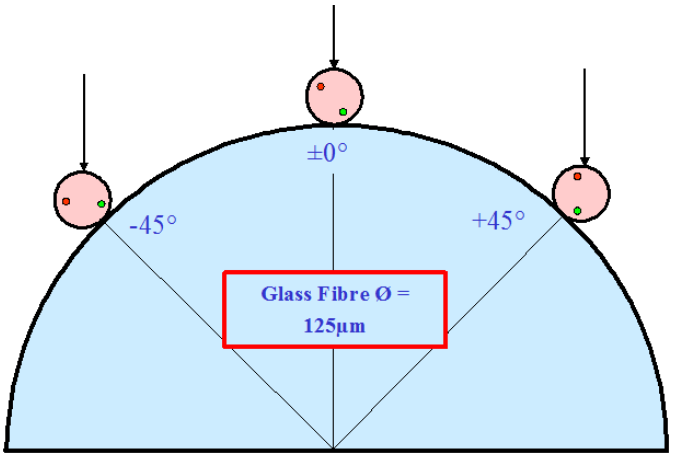

Fig. 10.3.: Basic Idea of Micro Axial Tomography.

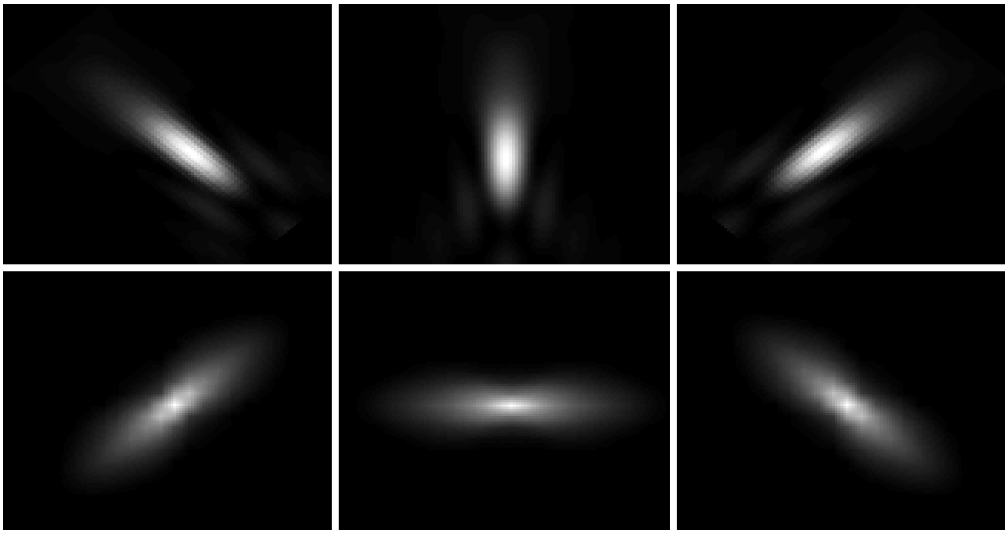

Fig. 10.4.: PSFs (Upper row) and OTFs (Lower row) of three different viewing angles.

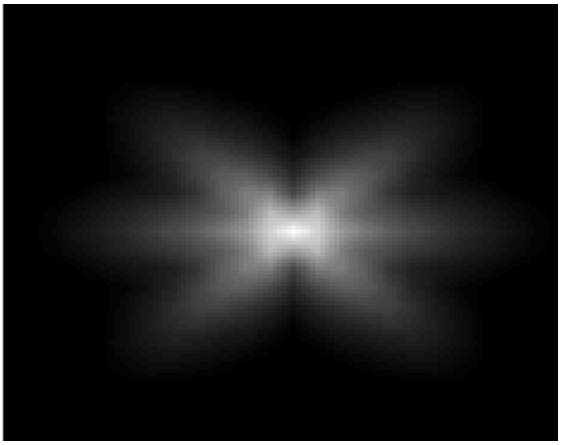

Fig. 10.5.: Combined OTF of all three different viewing angles.

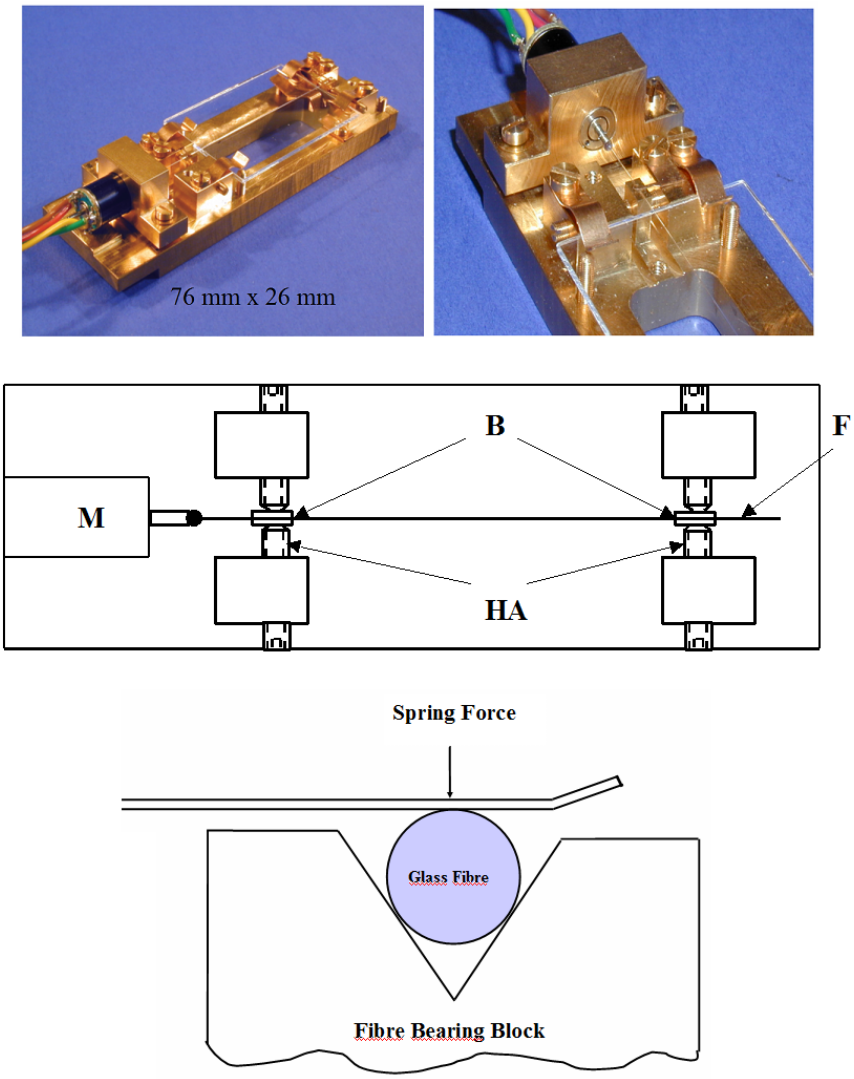

Fig. 10.6.: Method to fix the glass fibre.

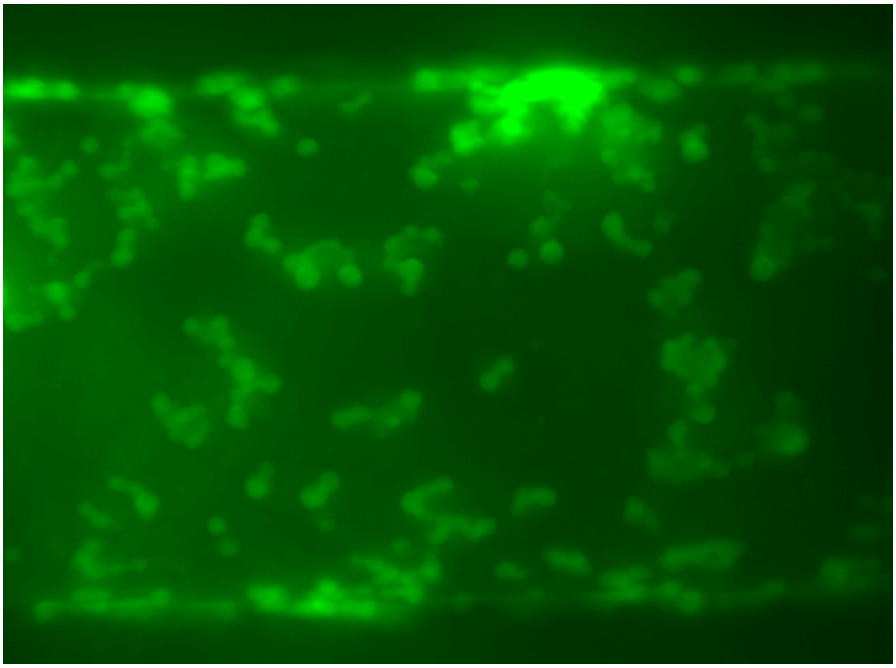

Fig. 10.7.: Image of cells on fibre.

age of each direction covers another area of the frequency domain and thus additional information is available to improve the resolution. However, the result image must be reconstructed from these three images using appropriate methods regarding the different PSFs. Note that in axial tomography, the different images have to be aligned before the actual reconstruction can be done. Hereby, possible translational and rotational shifts between the tilted views caused by instabilities of the tilt axis have to be corrected. The tilted view reconstruction problem was first addressed in [147]. The relative rotation and translation between a pair of tilted views are estimated from the images by a modified phase cross correlation function. Thereafter, the reoriented and deconvolved images are merged treating the amplitude and phase data separately. In [143], the image is reconstructed by maintaining the frequencies with the highest amplitudes from the different tilted views in each single object point. This method provides a gain in axial resolution without significant decrease in lateral resolution. However, simulations demonstrated that this method is sensitive to noise and to even small misalignments of the datasets. An Axial Tomography reconstruction method using a maximum likelihood approach has been published in [68]. This approach is based on the RL image deblurring method for confocal microscopy images described above. First, the image data sets have to be aligned which is done manually. In the next step, the three aligned data sets are simultaneously used to iteratively reconstruct a single high resolution data set using an unconstrained maximum likelihood deconvolution. This method combines

the quality improvements gained by RL deconvolution with the refinement allowed by the use of additional information acquired from different viewing angles. Additionally, over-relaxation factors are used to improve the convergence speed. In [67], this method was extended by an automatic alignment determining the relative angles of rotation between the different data sets. The alignment method uses the measured image data and is based on the computation of a modified (High frequency enhanced) cross-correlation function. This function includes Fourier and inverse Fourier transforms and is maximized over the angles of rotation. For each unknown rotation angle an iterative technique is used comparing one image with another at a time. Furthermore, the complete automated method was compared to standard confocal data reconstruction using a known sample. The automated alignment is superior to manual methods since hereby sub-voxel accuracy is possible. In [86], the whole process starting with cell preparation, image acquisition and finally the reconstruction is investigated and automated as far as possible. For that purpose, a special software module has been developed. The software module then drives all hardware components required for automated Micro Axial Tomography and performs the image acquisition. Finally, the already discussed reconstruction algorithm [143] using the point-wise maximum in Fourier space is used to obtain a high-resolution image. This automated method was then used to image fluorescence in situ hybridisation-stained (FISH) cell nuclei which were fixed on a glass fibre [87]. In addition, a method for the preparation of cell nuclei attached to glass fibres has been developed and the advantages of a glass fibre compared to a glass capillary are discussed. A image processing technique that fuses multi-view image data sets into a high quality three-dimensional image is presented in [155]. The method is non-blind and shift-invariant and furthermore able to cope with partially opaque samples when each view shows only a portion of the specimen. As multi-view deconvolution method either an iterated Wiener filter approach or a maximum a posteriori methods adapted for Gaussian noise is used. The method described here shows good results especially for a high number of image data sets.

10.3. Materials and Methods

Three images obtained from different viewing angles are the basis of the Micro Axial Tomography reconstruction. These three images are usually given in a *uint16* file format while just the first 12 Bits are used allowing a data range from 0 to 4096. The images have to be acquired properly using a main part of the data range without allowing overexposure. In order to perform a high quality reconstruction, the given data format is not suitable. Using an integral range of values causes a lot of errors and artifacts when performing necessary interpolations during the registration or in the reconstruction algorithm. Therefore, a *floating point* data range is used in all calculations.

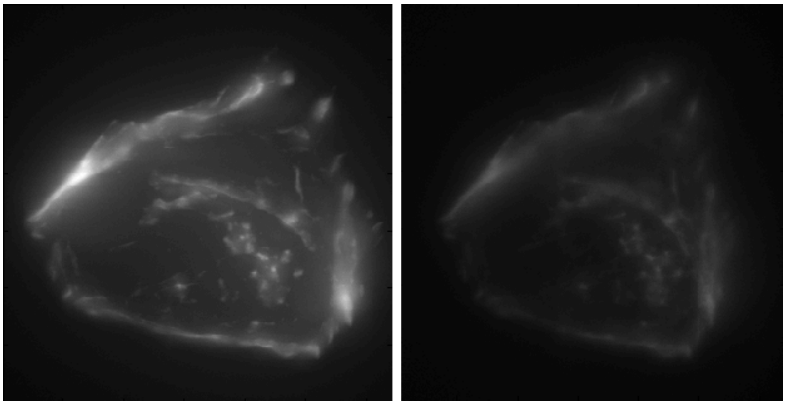

Fig. 10.8.: Illustration of bleaching in image data set: first image (Left) and third image (Right).

10.3.1. Background and Bleaching

It is well known that fluorescence proteins tend to bleach and thus the signal strength is decreasing after a certain excitation time [66]. Especially when the movement and mobility of proteins inside the cell is of interest, this problem has to be considered properly [9]. Fluorescence agents that are designed to show a reduced photo bleaching behaviour are investigated in [99]. In addition, there are techniques to correct this effect like the fluorescence recovery after photobleaching (FRAP) method presented in [97].

The Micro Axial Tomography images are acquired with the same microscope one after the other. Thus, the second image might already suffer from bleaching and this effect is even stronger for the third image. Furthermore, due to a different background activity and possible differences in the exposure times, the background signal can vary from image to image. Both, the background signal and bleaching have to be corrected before the images can be processed. Besides, some tools like Matlab scale the data range when showing the images and thus the bleaching effect cannot be seen. If the images are scaled correctly the photo bleaching is obvious as it is shown in figure 10.8. Hereby, the first and the third image of the cell data set are shown. In order to correct bleaching and the background signal, the model presented in equation 10.3.1 is used. This model includes an additional constant background signal b and a factor f to cope with the bleaching.

$$o_{bleach} = f_{bleach} \cdot o_{original} + b_{recording} \tag{10.3.1}$$

First, the background signal has to be estimated and has to be removed before the bleaching can be determined. However, an evaluation of the histogram does not provide a reliable estimate for the cell images. This method is quite common for background estimation but the cells illuminate their surrounding areas and thus alter the histogram.

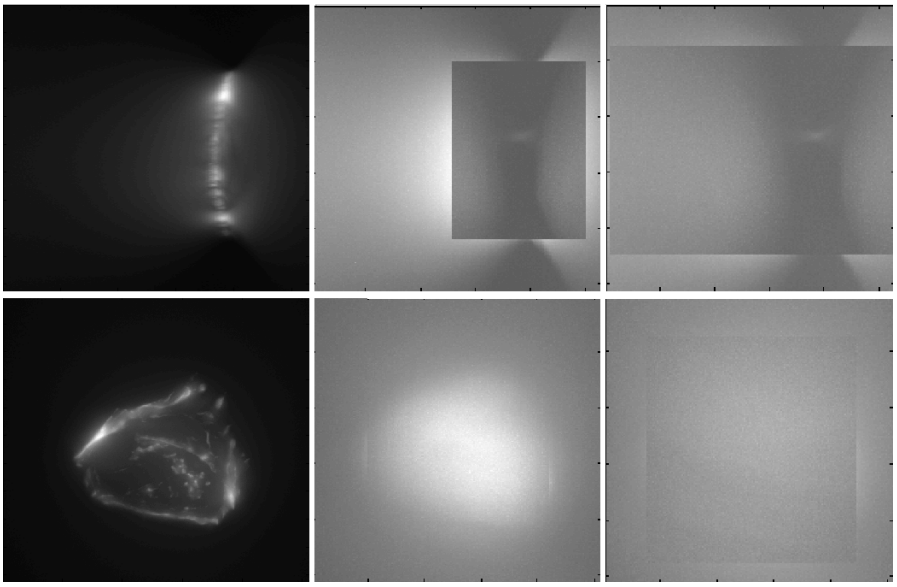

Fig. 10.9.: Cell images with removed areas to estimate the background signal.

This illumination can be found in all images and is thus influenced by the bleaching factor as well. It should be excluded from the background estimation and therefore, the areas around the cells are cut out and the remaining data values are analysed. In figure 10.9 x and z maximum projections of the cell images are shown. On the left, the original image can be seen while some areas are removed from the image in the middle and in the right image. The illumination of the surrounding area is obvious and the right image was then used to estimate the background signal b_{image}.

Next, the bleaching factor has to be estimated but the background signal has to be removed first.

$$o_{data} = o_{recorded} - b_{image} \tag{10.3.2}$$

The bleaching factor is determined by evaluating a certain amount of the brightest voxels after removing the background signal. An evaluation showed that this method is quite stable and the factors do not vary in case of considering 0.01% of the highest intensity values up to 5%. The brightest image is used as reference image and 0.5% of the brightest voxels are used to estimate the bleaching factors for the other images. These images are corrected using their own background signal b_i and their bleaching factor according to equation 10.3.3. b_{ref} is the background signal of the reference image and like that, all images are of the same appearance and can be further processed.

$$o_i^* = \frac{o_i - b_i}{f_i} + b_{ref} \tag{10.3.3}$$

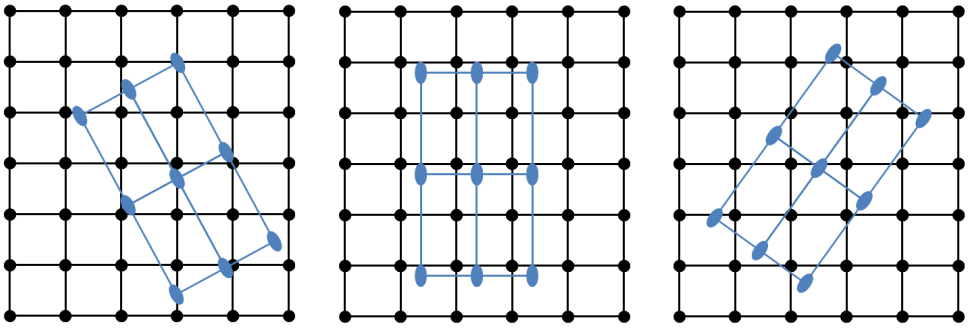

Fig. 10.10.: Rotated and shifted grid structures of the Axial Tomography image data set with an underlying isotropic grid structure.

10.3.2. Registration

Before the reconstruction of the high resolution image can be done, the three images have to be aligned. It has been shown that a accurate alignment is mandatory and otherwise an acceptable reconstruction result is not possible. In the past, a cross correlation coefficient has been used to correct the rotation and some tests showed that this method is reliable to correct rotational misalignment. However, the results in case of an additional translation have not been satisfying and thus a more advanced technique to align the three images is used. The objects appear differently in the three images due to noise and blurring under different rotation angles. Thus, misalignments in the registration process are possible and have to be avoided. In order to allow an optimal registration result, the three different images are deblurred separately and the deblurring results are used to estimate the rotation and translation. Additionally, the sampling distance in axial direction is of factor two larger than in lateral direction for normal imaging. This has to be considered in the alignment process as well since isotropic well-aligned images are required for the reconstruction. An illustration of the image grids regarding sampling, rotation and translation is given in figure 10.10.

In a first step before the actual alignment, isotropic images are created using a B-Spline interpolation correcting the higher sampling distance in axial direction. These images are deblurred separately and serve as basis of the multi-resolution, rigid, versor 3D registration process which is used for the estimation of the three dimensional rotation and three dimensional translation. In a last step, the aligned isotropic images used in the reconstruction are then created on basis of the original images. This step is important because only one B-Spline interpolation has to be applied in this way. If the already created isotropic grids were used the quality of the result would be worse since additional errors and artifacts are possible with every additional interpolation even when a B-Spline method is used. Besides, this effect would be even stronger when integral data values would be used.

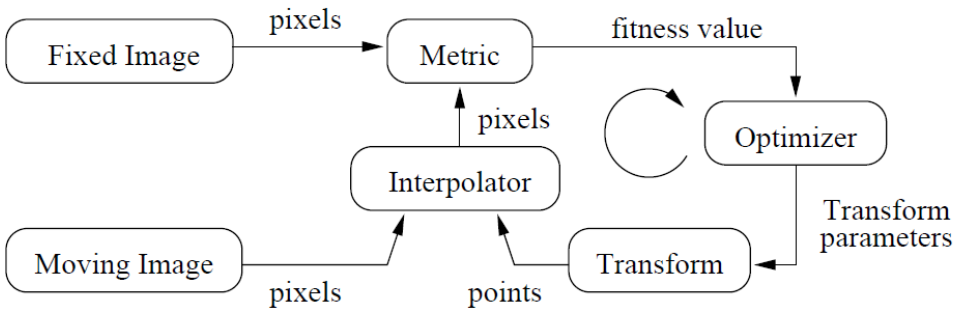

Fig. 10.11.: The basic components of the registration framework [76].

Rigid Versor 3D Registration

In general, each registration algorithm consists of four components necessary to align two images. These components are transform, optimizer, metric and interpolator. During the registration, one image is considered to be moving while the other one is fixed and the transform describes how the first image should be aligned. Hereby, it is possible to use a simple rotation in 2D represented by just one parameter up to an affine transforms including even anisotropic scaling or shearing with many parameters to be determined. The estimation of the according parameter is done by the optimizer which has to be well-suited for the used transform. Affine transforms with many parameters for example require advanced optimization techniques to obtain a good registration result. The interpolator is used to create the moved image which is then compared with the fixed image using a specified metric. The metric has to be minimal for a correct registration and should not have other local minima. If those conditions are not fulfilled the registration cannot work properly and the images cannot be aligned correctly. The metric has to be adapted to the image types especially when multi-modal images like CT and MR are registered and in such a case, a mutual information metric is recommendable. When choosing the interpolation method, a compromise between computational time and accuracy has to be made. An interpolation has to be performed in every registration step investigating modified parameters and generates almost the whole computational effort necessary for the registration. A more accurate interpolation slows down the registration considerably but allows an improved result. The whole registration process and the interaction between the different components is shown in figure 10.11.

There is a well-established, open source framework for registration in ITK [76] and this framework is used to perform the registration necessary for the Micro Axial Tomography reconstruction. First, an according transform has to be chosen and the objective is to have as less parameters as possible. In that way, the registration is more stable and reliable and the computational time is shorter which is important since relatively huge images have to be registered. Isotropic grids are used as basis of the registration and

thus neither anisotropic scaling nor shearing has to be considered. In addition, the cells are not deformed during the image acquisition and therefore a rigid transform can be used. However, a three dimensional rotation and a three dimensional translation must be corrected leading to a so called *VersorRigid3DTransform* including six parameters. The translation is represented by a vector while the rotation is specified by a versor. In principle, there are different methods to describe a three dimensional rotation. It can be described by a normalized vector and a rotation angle, three rotation angles (r_x, r_y and r_z) or by a versor consisting of three values (q_1-q_3). Since the description of the rotation in three angles is interesting regarding the Micro Axial Tomography, the according conversion from a versor is shown:

$$\begin{pmatrix} r_x \\ r_y \\ r_z \end{pmatrix} = 2\frac{arcsin\left(\sqrt{q_1^2+q_2^2+q_3^2}\right)}{\sqrt{q_1^2+q_2^2+q_3^2}} \begin{pmatrix} q_1 \\ q_2 \\ q_3 \end{pmatrix} \tag{10.3.4}$$

As mentioned before, the optimizer should be well suited for the underlying transform. There is an optimizer especially designed for the *VersorRigid3DTransform* in the ITK framework which is called *VersorRigid3DTransformOptimizer*. Since all images are acquired with the same microscope and both bleaching and background signal are corrected, a mean square metric called *MeanSquaresImageToImageMetric* is suitable. At last, a linear or a B-Spline interpolator can be used. The B-Spline interpolator is more accurate in general but the computational effort is considerably larger and thus the linear version is used mostly. This issue is again discussed in the next section.

Multi-Resolution Registration

When using the rigid versor transform, there are six parameters and thus a six dimensional optimization problem has to be solved. Since the Micro Axial Tomography images are relatively large, especially in their isotopic version, the registration is quite computational intensive. Depending on the distance from the optimum to the initial transform, the effort for the registration can be enormous. The parameters for the rotation are roughly known due to the set up of the Micro Axial Tomograph but the translation is totally unknown and difficult to estimate beforehand. It is not possible to provide an initial transform being near to the optimum and thus, a multi-resolution approach is used to perform the registration. Such an approach is widely used to improve speed, accuracy and robustness of the registration. The basic idea is that registration is first performed at a coarse scale where the images have a considerably smaller size and thus the computational effort is reduced. The result from this step is then used as initialization of the next finer scale. This process is repeated until it reaches the finest possible scale. Therefore, with growing computational effort, the initialization is nearer to the optimum and less iterations are necessary. Such a coarse-to-fine strategy improves the

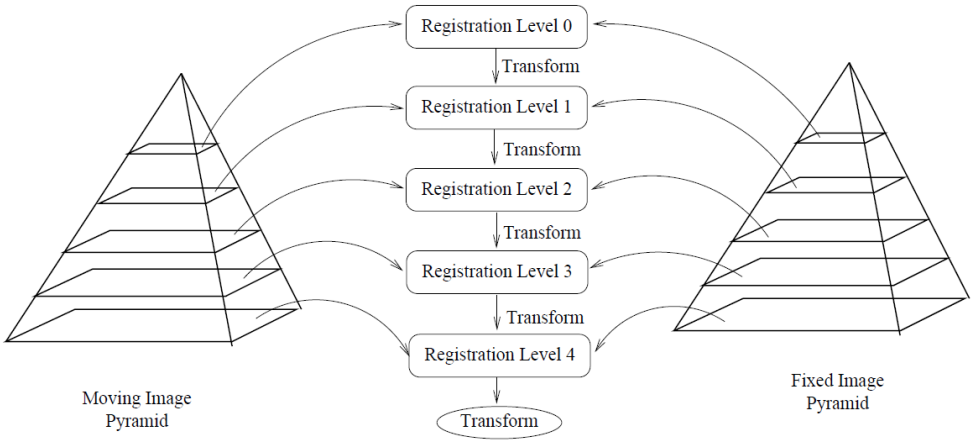

Fig. 10.12.: Illustration of the multi-resolution registration process [76].

registration and also increases robustness by eliminating local optima at coarser scales. The concept of the multi resolution registration is illustrated in 10.12.

In addition, it is possible to use a linear interpolator in the coarse scale steps. Hereby, the accuracy provided by a linear interpolation is quite adequate and the computational time can be reduced further. In the last step representing the finest scale when the original images are registered, a B-Spline interpolator is then used to guarantee a high accuracy.

After performing the registration, the transform result and the scaling information leading to an isotropic grid are used to create the registered images. Hereby, the original images are used and like that, only one interpolation is necessary avoiding additional errors and artifacts. The registered images are then used for the reconstruction.

10.3.3. PSF

The PSF of a fluorescence microscopy image can be approximated by a Gaussian function with a certain variance. This model is often used when applying blind deconvolution algorithms because it is simple and can be well described by few parameters. In the simulations done for the Micro Axial Tomography reconstruction, a Gaussian PSF is also used. As mentioned before, the axial resolution is of factor three worse than the axial resolution and thus the variance in z direction σ_z is three times the variance in x direction σ_x. The variance σ_y is equal to σ_x and the PSF is then given by:

$$f(x,y,z) = \frac{1}{\sqrt{2\pi}^3 \sigma_x \sigma_y \sigma_z} e^{-\left(\frac{(x)^2}{2\sigma_x^2}+\frac{(y)^2}{2\sigma_y^2}+\frac{(z)^2}{2\sigma_z^2}\right)} \tag{10.3.5}$$

This PSF is well suited for simulations but can always cause errors for real images since it is an approximation. For real images the PSF can be estimated using beads. The first processed Micro Axial Tomography images consist of beads and the images of single beads are used to create the PSFs used for the reconstruction. Three PSFs are needed and all three PSFs are created using the mean of two images of single beads. Therefore, the background has to be removed first and then the images of the beads have to be centered. This is not trivial since they are not symmetric. A simple center of mass calculation is not working but the inner kernel of each bead image is assumed to be symmetric and used for that purpose. After the mean of both images are calculated, the PSFs have to be normalized before being used in the reconstruction.

10.3.4. Micro Axial Tomography Reconstruction

In the reconstruction for the Micro Axial Tomography, one single, isotropic, high resolution image is reconstructed and therefore a similar functional as for the microscopy deblurring can be used. The major difference is that three recorded images (i_1, i_2 and i_3) with three PSFs (h_1, h_2 and h_3) have to be considered. These images are already registered and sampled on the same isotropic grid structure. The implementation of the regularization term remains exactly the same as before since those functionals only apply on the reconstructed image and are completely independent from the recorded images and PSFs. Now, three different methods are presented for the Micro Axial Tomography reconstruction. A multiplicative RL method containing no regularization is described at first [67]. Then a multiplicative RLTV approach will be presented and last but not least the CCG method is extended for the Micro Axial Tomography reconstruction.

The multiplicative RL method for the Axial Tomography is denoted as aRL in the following and this method contains no regularization and is based on the original RL algorithm. Stopping the aRL algorithm in order to get the best possible result is called aRL+.

$$o_{k+1} = \left\{ \left[\frac{i_1}{o_k \otimes h_1} \right] \otimes h_1^* + \left[\frac{i_2}{o_k \otimes h_2} \right] \otimes h_2^* + \left[\frac{i_3}{o_k \otimes h_3} \right] \otimes h_3^* \right\} \frac{o_k}{3} \tag{10.3.6}$$

In order to cope with the ill-posed nature of the reconstruction problem, the multiplicative aRL algorithm is extended by a TV regularization weighted by λ. This algorithm is called aRLTV in the following:

$$o_{k+1} = \left\{ \left[\frac{i_1}{o_k \otimes h_1} \right] \otimes h_1^* + \left[\frac{i_2}{o_k \otimes h_2} \right] \otimes h_2^* + \left[\frac{i_3}{o_k \otimes h_3} \right] \otimes h_3^* \right\} \frac{o_k}{3 \left(1 - \lambda \nabla \frac{\nabla o_k}{|\nabla o_k|} \right)} \tag{10.3.7}$$

In order to use the constrained conjugate gradient algorithm containing the non-negativity constraint, the similarity functional

$$S_{RLax}(o) = \begin{array}{l} \int o \otimes h_1 + o \otimes h_2 + o \otimes h_3 + 3b - i_1 \cdot log\,(o \otimes h_1 + b) \\ -i_2 \cdot log\,(o \otimes h_2 + b) - i_3 \cdot log\,(o \otimes h_3 + b)\, d\Omega \end{array} \tag{10.3.8}$$

which includes the background signal b and its gradient

$$\frac{\partial S_{RLax}(o)}{\partial o} = 3 - \frac{i_1}{o \otimes h_1 + b} \otimes h_1^* - \frac{i_2}{o \otimes h_2 + b} \otimes h_2^* - \frac{i_3}{o \otimes h_3 + b} \otimes h_3^* \tag{10.3.9}$$

are required. As before, the extended image formation model containing a background signal b is used and ϵ guarantees a well defined behaviour in case of regions with zero values. This algorithm is denoted as aCCG in the following.

10.4. Axial Reconstruction Results

The axial reconstruction algorithms can be used for 2D and 3D images likewise and for a first evaluation, 2D test images are used. The objective hereby is to focus on the investigation of the axial reconstruction algorithms without considering the other steps of the whole reconstruction process. In case of synthetic data sets, the results can be directly compared with the original image using a RMSE and the Fourier transform. The RL, the RLTV and the CCG algorithm are included in the evaluation and in addition a result obtained by stopping the RL algorithm at the minimal RMSE. This result is denoted as RL+. Besides the axial reconstruction methods, a deblurring with the respective algorithms on basis of one degraded image is performed and compared to the axial results. The axial results are labeled as aRL, aRL+, aRLTV and aCCG while the deblurring results based on a single degraded image are denoted by sRL, sRL+, sRLTV and sCCG. In addition, a synthetic 3D image is used to investigate the whole reconstruction process including the registration which is not considered in the 2D case. Last but not least, an image data set containing experimentally measured beads and a measured image data set illustrating a human cell are processed and the reconstruction results for the different methods are displayed. Before the results of the actual axial reconstruction are shown, the possible errors regarding the necessary interpolations and transformations are investigated.

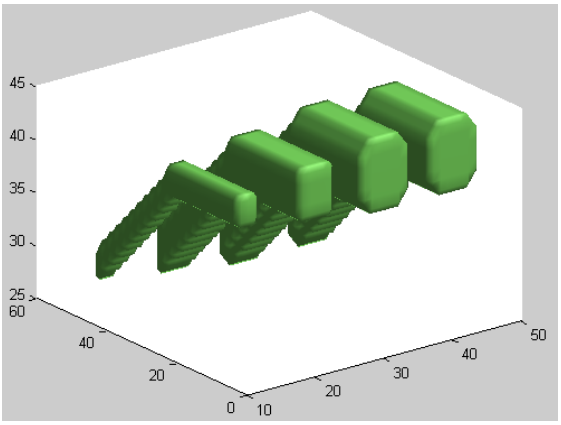

Fig. 10.13.: Surface of object in 3D test image.

10.4.1. Synthetic Image Data Sets

Transformation and Interpolation Errors

The quality of the processed data is essential and before the reconstruction can be started, a scaling, a three dimensional rotation and a three dimensional translation have to be done in order to create the necessary aligned data sets. All three steps are executed in a single combined operation including just one B-Spline interpolation. In addition, all calculations are performed using a *float* data type instead of the original *uint16* data type. In the following, a short demonstration on the importance of such things and what happens if they are not taken into consideration is given. Therefore, a simple three dimensional test image is used (Figure 10.13) and several operations like rotation and translation are performed. To evaluate the results, all operations are performed forth and back and the result is compared with the original image using the MSE criteria. It would be ideal if the MSE was zero but since this is hardly possible a minimal MSE value is best.

First, a rotation and a translation was done on the test image with a *uint16* data type. Hereby, the rotation is done with $1.3°$ in x, $-37.5°$ in y and $0.7°$ in z direction and the translation accordingly with -1.2, 5.4 and 8. The results can be seen in the upper row of figure 10.14 and the MSE values are 3588513 for the separate processing with two interpolations and 1750552 for the combined process. The separate process is almost of a factor two worse.

The results of the same experiment for a *float* data type are shown in the lower row of figure 10.14. Again, the combined processing is of factor two better with MSE values 2937779 and 1533508. Compared with the *uint16* result, the MSE values of the *float* processing are decreased by 14% showing the advantages of the *float* calculations.

It is possible to drastically improve this test by highsampling of the images before

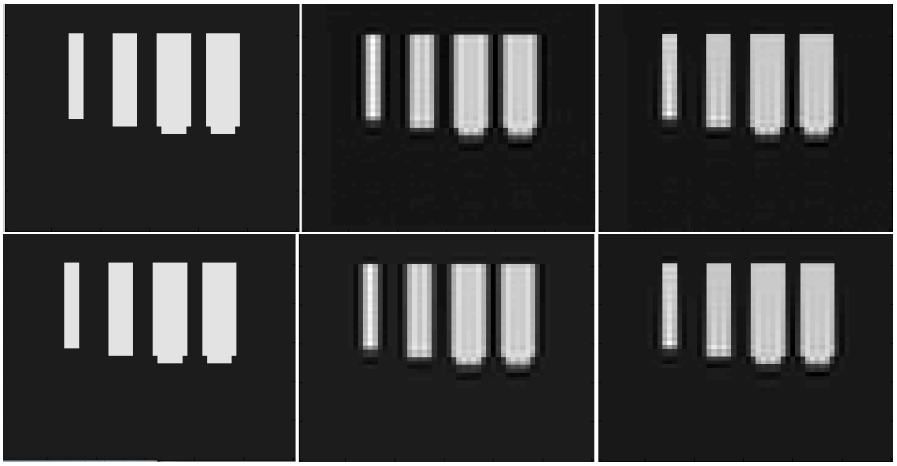

Fig. 10.14.: Original, separate and combined Transformation (From left to right). The $uint16$ data set is shown in the upper row while the $float$ data set is displayed in the lower row.

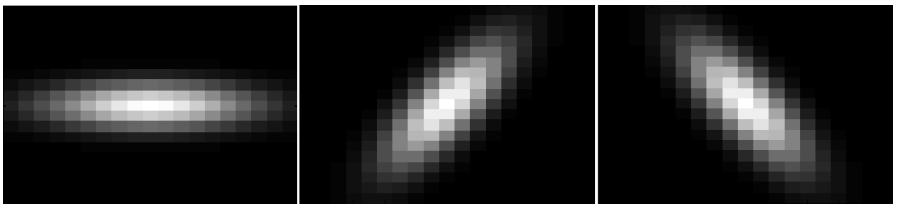

Fig. 10.15.: PSFs for 2D Simulation.

processing them and again downsampling the results. A highsampling of factor two in all dimensions leads to a result with a MSE value of 43629 being an improvement of factor 35. Unfortunately, the Micro Axial Tomography images have to be processed in the backward way and thus an advantage of this property cannot be realized. Using a higher sampling rate for the forth and back transformation separately with a downsampling between both operations does not improve the result.

Simulations with Synthetic 2D Data

In the 2D simulation, the objective is to evaluate the different reconstruction methods and not the other parts of the axial reconstruction process like e.g. registration. In this case, already rotated Gaussian PSFs are used for both the degradation of the original image and the axial reconstruction. The variances of the PSFs are $\sigma_x = 1.5$ and $\sigma_y = 4.5$ and the rotation angles are set to $-60°$ and $60°$. The Fourier domain is covered in the best possible way using these three viewing directions. The PSFs for the 2D simulation can be seen in Figure 10.15.

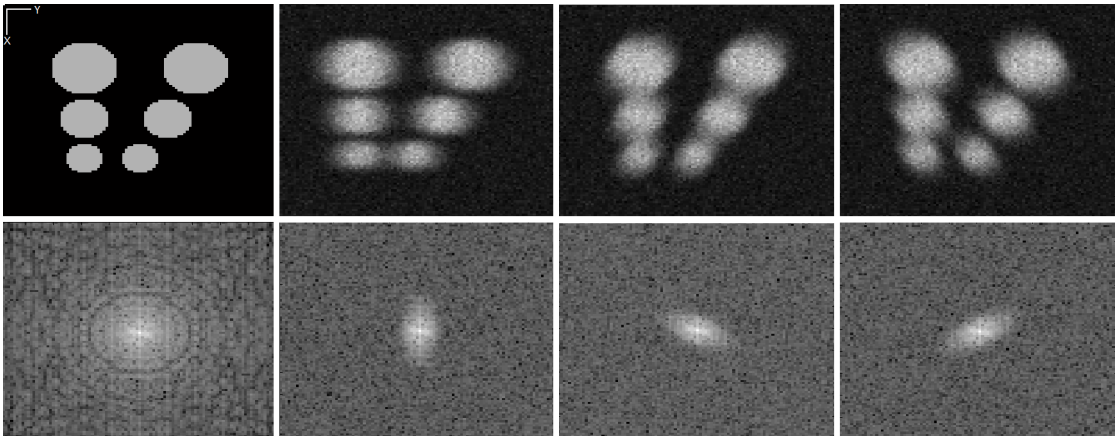

Fig. 10.16.: Simulated images of first test image (IDS1a) in upper row: original image (Left) and degraded images with different PSFs (Middle to right). The lower row shows the corresponding Fourier transforms.

These PSFs are used to create several test data sets on basis of the two previously used test images. Two different photon counts provide different test conditions by influencing the additional Poisson noise and lead to a SNR of about $10dB$ in a first case and a SNR of about $17dB$ in a second case. Figure 10.16 shows the first image data set (IDS) with a low photon count which is represented by IDS1a in the following. The Fourier transforms also displayed in this figure clearly illustrate which frequencies are imaged by the different viewing angles and which are suppressed. In addition, figure 10.17 shows the remaining image data sets. IDS1b denotes the first test image with a high photon count and the notation for the second test image is consistent as IDS2a and IDS2b.

In order to emphasize the possible benefit from the Axial Tomography, a deblurring on basis of a single viewing angle is done as well using all described algorithms. For both the deblurring and the axial reconstruction there are two results for the RL algorithm. The first result is obtained by a limited large number of allowed iterations which is usually not reached by the other algorithms since they converge earlier. The RL algorithm does not converge due to noise amplification and has to be stopped in this way. Since this result is not optimal for the RL algorithm, the reconstruction is repeated and stopped when the minimal MSE value is reached (RL+) showing the best possible solution using this method. The RLTV algorithm has to be weighted with a regularization parameter and $\lambda = 0.002$ is used following the recommendation in [44] for a strong noise signal and $\lambda = 0.001$ for a weak noise signal producing improved results. Last but not least, the new axial CCG method is used and in order to determine a suitable value of λ, a brute force search is applied. This search covers a suitable range of possible values and it is not necessary to use too many iterations within the reconstruction

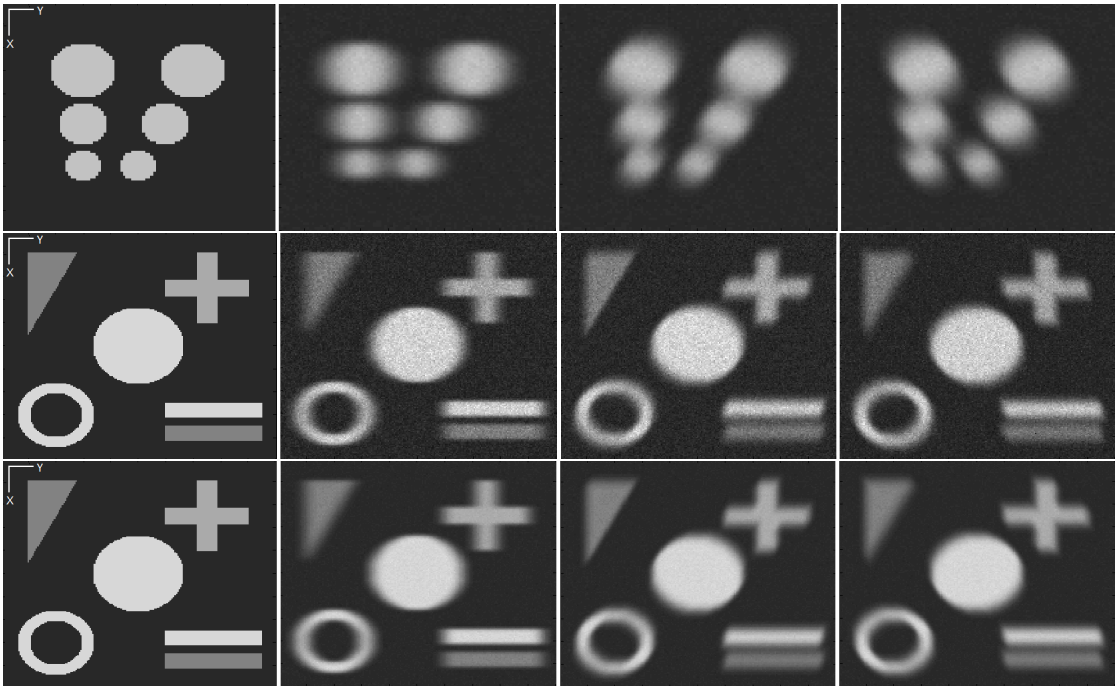

Fig. 10.17.: Simulated images of remaining image data sets (Top to bottom: IDS1b, IDS2a and IDS2b). Each original image is displayed on the left and the degraded images from the middle to the right.

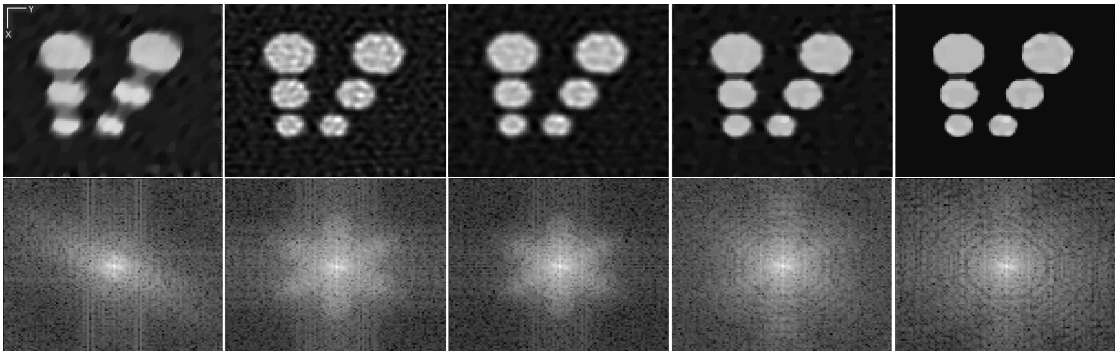

Fig. 10.18.: The upper row contains the results for IDS1a: sRLTV, aRL, aRL+, aRLTV, aCCG. The corresponding Fourier transforms are shown in the lower row.

since the effects of the different λ values can be seen quite early. The results of IDS1a for the axial reconstruction methods and the RLTV deblurring method on basis of a single degraded image together with the corresponding Fourier transforms are shown in figure 10.18. The results for the remaining image data sets are displayed in figure 10.19. The results of the aRL algorithms contain artifacts due to the amplified noise which are depleted for the aRL+ method but still visible. The results of the aRLTV algorithm are free of artifacts because of the additional regularization and thus superior to the aRL results. The quality of the results of the aCCG algorithm is however further improved compared to the aRLTV algorithms due to the additional regularization effect of the non-negativity constraint supported by the incorporated background signal. The Fourier transform of the sRLTV result shows the enhancement of the support region in the frequency domain that can be obtained by deblurring methods. However, the limitations in the axial directions cannot be overcome by deblurring a single image but by using the axial reconstruction methods. The Fourier transform of the results for the aRL and aRL+ algorithm show that all support regions of the three images can be combined but the possibilities to enhance them is limited. The additional regularization in the aRLTV and aCCG algorithm allows a further improvement of the resolution and a large coverage of the frequency domain.

Table 10.1 shows the RMSE values of the deblurred and reconstructed images compared to the original image for the whole image region. In addition, table 10.2 shows the RMSE values for the image regions containing objects which have been identified using threshold segmentation. The RMSE values confirm the improvements of both the axial reconstruction compared to a single deblurring and of the CCG algorithm to the RLTV and RL algorithms. As expected, it is possible to obtain an improved result if less noise is given in the degraded images. The RMSE values of the object regions prove that the CCG algorithm also improves the image quality within these areas. The background region is naturally improved due to the additional constraint influencing these areas.

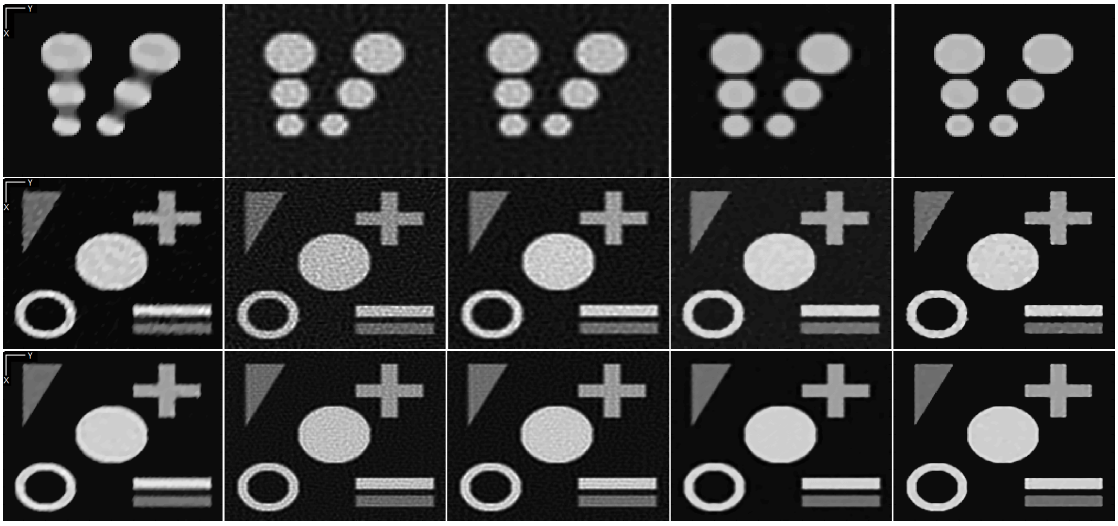

Fig. 10.19.: Results of remaining image data sets. From top to bottom: IDS1b, IDS2a and IDS2b. From left to right: sRLTV, aRL,aRL+, aRLTV, aCCG.

	Single deblur				Axial reconstruction			
	sRL	sRL+	sRLTV	sCCG	aRL	aRL+	aRLTV	aCCG
IDS1a	1018	932	799	648	801	749	627	485
IDS1b	859	837	749	543	652	648	581	405
IDS2a	1887	1632	1342	1061	1522	1393	1085	838
IDS2b	1506	1460	1249	911	1215	1192	1054	700

Table 10.1.: RMSE of 2D simulations for whole image region

Simulations with Synthetic 3D Data

The whole Axial Tomography reconstruction process including registration with rotation and translation is simulated in 3D. Again, a simple test image (Figure 10.20) is used and the reconstruction results are compared with the original data using the RMSE value.

In order to test the registration and the axial reconstruction, two image data sets are created with different rotation and translation values as displayed in table 10.3. The relocation values for the first 3D image data set (3D-IDS1) are inspired by the Axial Tomography set-up of the real image data sets which are processed later (Figure 10.21). The rotation for the second 3D image data set (3D-IDS2) allows an optimal coverage of the frequency domain and thus an investigation of the influence of the rotation angle. Each image data set contains three different separate images. The image created by a negative main rotation angle is denoted as 'Minus' and the second created image as 'Plus' accordingly. The original image which is also part of the image data set is referred

	Single deblur				Axial reconstruction			
	sRL	sRL+	sRLTV	sCCG	aRL	aRL+	aRLTV	aCCG
IDS1a	788	746	622	569	618	594	477	426
IDS1b	674	667	591	508	512	511	452	368
IDS2a	1489	1285	1020	924	1191	1102	811	744
IDS2b	1211	1177	979	838	979	959	814	640

Table 10.2.: RMSE of 2D simulations for object region

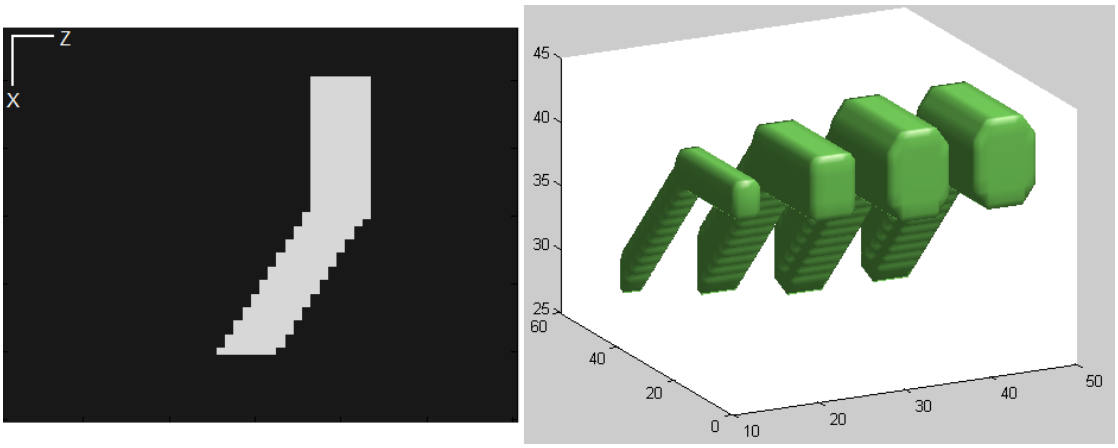

Fig. 10.20.: 3D test image: Slice (Left) and surface of the object (Right).

to as 'Base'.

	Rotation			Translation		
	θ_x	θ_y	θ_z	t_x	t_y	t_z
3D-IDS1 Minus	-1.3	37.5	-0.7	1.2	-5.4	-8.0
3D-IDS1 Plus	-0.4	-35.5	-0.1	-2.1	3.8	-6.0
3D-IDS2 Minus	-0.8	65.3	0.5	1.1	-2.4	4.0
3D-IDS2 Plus	0.6	-67.7	-0.4	-3.1	5.8	7.0

Table 10.3.: Initial rotation and translation for 3D Simulation

The rotation and translation are performed in the same order during the creation of the data and the registration. The rotation is done first in both cases and the registration would have to reverse this order to allow the usage of the original translation vector. The initial translation vector has to be rotated in order to compare it to the registration results. The rotation matrix R containing all three rotation angles (θ_x, θ_y and θ_z) is used for that purpose (s_i denotes $sin(\theta_i)$ and c_i denotes $cos(\theta_i)$). The rotated translation vectors for both image data sets are shown in table 10.4.

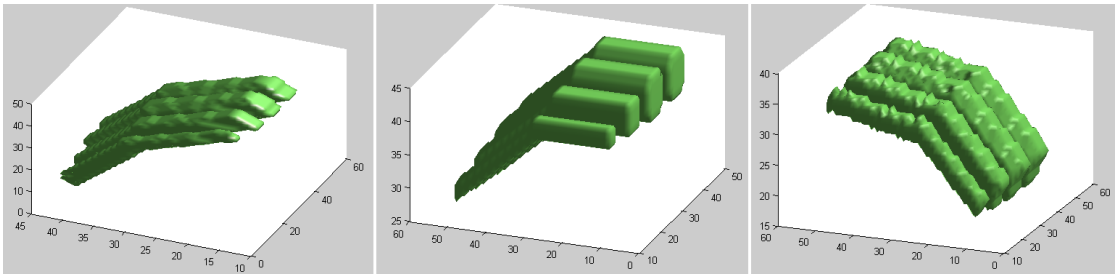

Fig. 10.21.: Surface of the rotated objects for 3D simulation (3D-IDS1).

$$R = \begin{pmatrix} 1 & 0 & 0 \\ 0 & c_x & -s_x \\ 0 & s_x & c_x \end{pmatrix} \begin{pmatrix} c_y & 0 & s_y \\ 0 & 1 & 0 \\ -s_y & 0 & c_y \end{pmatrix} \begin{pmatrix} c_z & -s_z & 0 \\ s_z & c_z & 0 \\ 0 & 0 & 1 \end{pmatrix} \tag{10.4.1}$$

	Rotated Translation		
	t_x	t_y	t_z
3D-IDS1 Minus	-3.97	-5.57	-6.91
3D-IDS1 Plus	1.78	3.76	-6.14
3D-IDS2 Minus	4.10	-2.38	0.69
3D-IDS2 Plus	-7.64	5.82	-0.11

Table 10.4.: Rotated translation vectors for 3D Simulation

The image data sets created by rotation and translation are degraded by a PSF and additional Poisson noise. A 3D Gaussian PSF is used for that purpose and the variances are set to $\sigma_x = 1.5$, $\sigma_y = 1.5$ and $\sigma_z = 4.5$. For each image data set, two different noise strengths are used resulting in a SNR of $15.8dB$ and $9.3dB$. Each image data set corrupted by weak noise is marked by an additional 'a' whereas the strong noise is indicated by an additional 'b'. Selected slices of the image data set 3D-IDS1a and 3D-IDS1b are shown in figure 10.22

The multi-resolution registration is performed using the image data set 3D-IDS1 on basis of different conditions in order to evaluate its accuracy. First, the basic relocated image data set 3D-IDS1 which does not contain any degradation is used for the registration. Both relocated images 'Minus' and 'Plus' are registered in reference to the 'Base' image. The same registration process is repeated with the degraded images for both noise levels. This case corresponds to the measured image data sets obtained by the microscope. In order to allow a more accurate registration, the degraded image data sets are separately deblurred with the sRLTV and the sCCG algorithm and the deblurring results are used as basis of the registration. In each case, the registration results have

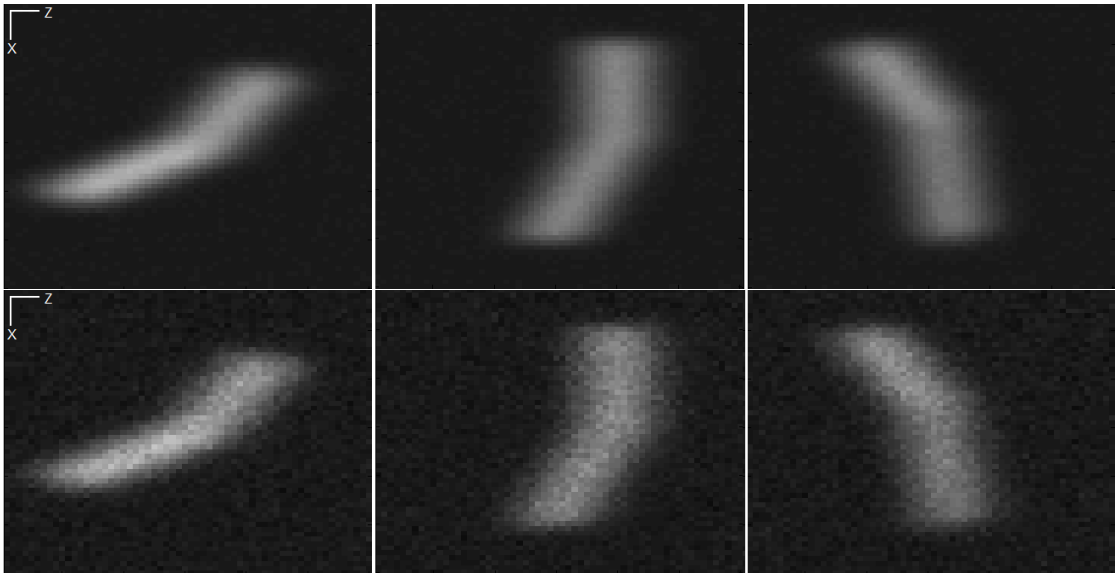

Fig. 10.22.: Selected slices of degraded image data sets 3D-IDS1a (Top row) and 3D-IDS1b (Bottom row).

to be used to align the underlying degraded images which are later used in the axial reconstruction. The registration results for all test cases are shown in table 10.5.

To analyse the registration result, the rotation and translation correction are evaluated separately. The estimated rotation given by the registration is compared to the initial rotation using the norm $n_\theta = \sqrt{\Delta\theta_x^2 + \Delta\theta_y^2 + \Delta\theta_z^2}$ with Δ representing the difference between each initial and estimated rotation angle. In addition, the norm $n_t = \sqrt{\Delta t_x^2 + \Delta t_y^2 + \Delta t_z^2}$ is used to evaluate the translation correction. The results of this evaluation are displayed in table 10.6 for all investigated conditions. There is a constant small error in the estimation of the translation which is present for all conditions. If the images are degraded the error of the rotation estimation is decreased considerably. A deblurring with the sRLTV or the sCCG algorithm allows an improvement of the accuracy of the registration which almost reaches the best possible quality given by images without any degradation. Since the degradations including noise and blurring are given in measured data, it is recommendable to use deblurred images for the registration. The registration results are then used to align the degraded images used in the axial reconstruction.

Selected slices of the aligned image data sets 3D-IDS1a and 3D-IDS1b are displayed in figure 10.23. The alignment of the degraded images is performed on basis of the registration result using the deblurring results with the sCCG algorithm. A single PSF is used to create all three images included in each image data set in accordance with the real imaging process. It is however necessary to use three aligned PSFs to perform the axial reconstruction. The original PSF has to be rotated according to the registration

	Rotation			Translation		
	θ_x	θ_y	θ_z	t_x	t_y	t_z
	Minus to Base image					
Relocated 3D-IDS1	-1.242	37.497	-0.6174	-3.554	-5.540	-6.686
Degraded 3D-IDS1a	-1.196	37.714	-0.787	-3.564	-5.537	-6.704
3D-IDS1a sRLTV	-1.297	37.370	-0.678	-3.576	-5.542	-6.654
3D-IDS1a sCCG	-1.268	37.434	-0.656	-3.559	-5.542	-6.683
Degraded 3D-IDS1b	-1.165	37.620	-0.853	-3.588	-5.526	-6.687
3D-IDS1b sRLTV	-1.264	37.340	-0.724	-3.586	-5.535	-6.661
3D-IDS1b sCCG	-1.267	37.390	-0.728	-3.578	-5.535	-6.670
	Plus to Base image					
Relocated 3D-IDS1	-0.403	-35.498	-0.113	1.639	3.729	-6.540
Degraded 3D-IDS1a	-0.364	-37.366	-0.134	1.544	3.752	-6.498
3D-IDS1a sRLTV	-0.420	-35.725	-0.130	1.608	3.739	-6.540
3D-IDS1a sCCG	-0.405	-35.565	-0.132	1.619	3.736	-6.545
Degraded 3D-IDS1b	-0.328	-37.450	-0.130	1.514	3.771	-6.519
3D-IDS1b sRLTV	-0.429	-35.912	-0.138	1.566	3.743	-6.569
3D-IDS1b sCCG	-0.391	-35.787	-0.136	1.556	3.748	-6.568

Table 10.5.: Registration results for image data set 3D-IDS1.

result to create the PSFs needed for the aligned 'Minus' and 'Plus' images. Note that the translation does not influence the PSFs and only the rotation has to be considered. A central slice of the three resulting PSFs is displayed in figure 10.24.

In order to evaluate the axial reconstruction and to compare its performance with the deblurring on basis of a single image, manually aligned image data sets are used. The initial rotation angles and translation vectors are used to create these image data sets and the according PSFs. These results represent an optimal axial reconstruction which is later compared to the results on basis of the registered image data sets. Selected slices of the axial reconstruction results for the image data sets 3D-IDS1a and 3D-IDS1b are shown in figure 10.25. The results of the aRL and aRL+ algorithm contain artifacts which are suppressed for the aRLTV result. A further improvement of the resolution is given in the result of the aCCG algorithm. In general, the results for the weaker noise signal are superior to those with a stronger noise signal. However, the aRLTV and aCCG algorithms are less sensitive to noise due to the additional regularization.

The RMSE values for the different results compared to the original images are given in table 10.7. In addition to the results for the axial reconstruction, the RMSE value of a degraded image and the results of the sRLTV and sCCG deblurring algorithms are shown. The RMSE values illustrate the improvements of the axial reconstruction compared to a single deblurring with one degraded image. In addition, the CCG algorithm

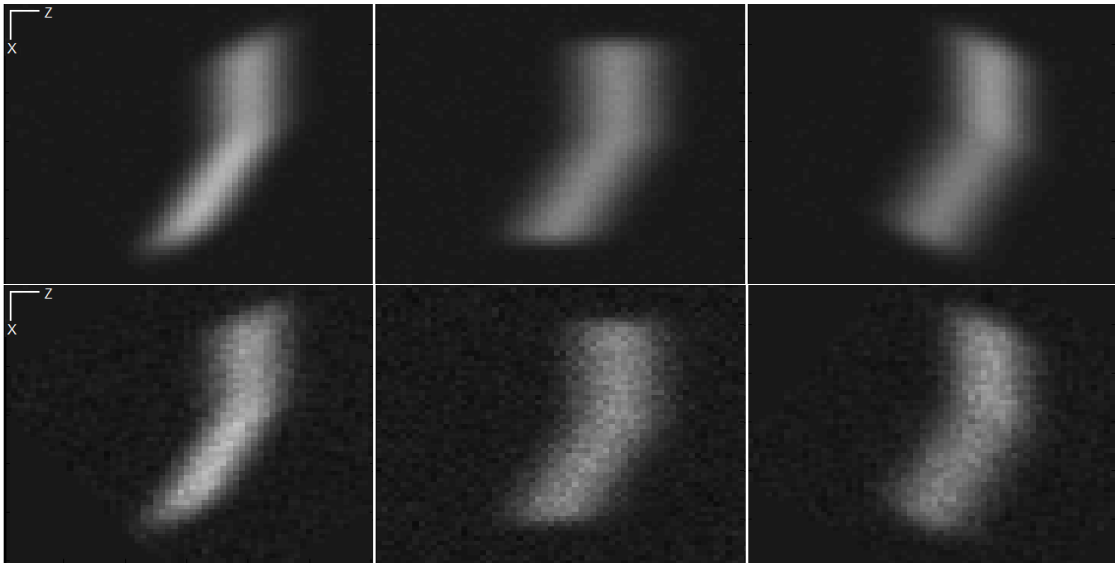

Fig. 10.23.: Slice of aligned image data sets 3D-IDS1a (Top) and 3D-IDS1b (Bottom).

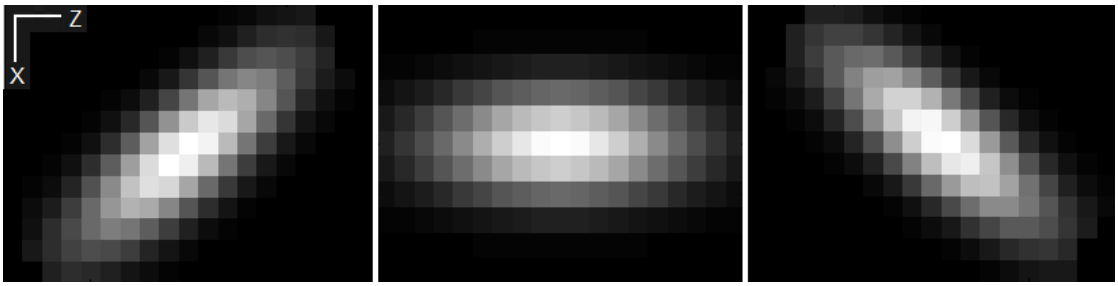

Fig. 10.24.: Registered PSFs for 3D simulation.

	relocated	Weak noise signal: 3D-IDS1a degraded	sRLTV	sCCG
Minus Rotation n_θ	0.142	0.404	0.154	0.140
Minus Translation n_t	0.673	0.648	0.683	0.670
Plus Rotation n_θ	0.018	1.936	0.276	0.103
Plus Translation n_t	0.585	0.616	0.607	0.604
	relocated	Strong noise signal: 3D-IDS1b degraded	sRLTV	sCCG
Minus Rotation n_θ	0.142	0.408	0.219	0.170
Minus Translation n_t	0.673	0.652	0.672	0.671
Plus Rotation n_θ	0.018	2.052	0.481	0.332
Plus Translation n_t	0.585	0.668	0.674	0.678

Table 10.6.: Rotation error n_θ and translation error n_t for simulated 3D registration.

for both the axial reconstruction and the deblurring is superior to the RLTV and RL algorithms. As expected, it is possible to obtain an improved result if the rotation angles is set to near $+/-60°$ since a better coverage of the frequency domains is given by the support regions of the single images. In addition, an improved result can be obtained if the noise signal is decreased.

		Deblur		Axial			
	degraded	sRLTV	sCCG	aRL	aRL+	aRLTV	aCCG
3D-IDS1a	7133	4434	3648	4047	4037	3793	3000
3D-IDS1b	7307	4627	4287	4538	4415	3948	3110
3D-IDS2a	7132	4233	3647	4096	3768	3492	2687
3D-IDS2b	7299	4451	4125	4331	4107	3745	2904

Table 10.7.: RMSE of reconstruction results based on manually aligned image data sets

At last, the axial reconstruction is performed on the aligned image data sets based on the registration results using both the degraded and the deblurred images. Selected slices of the reconstructed images are displayed in figure 10.26 and the RMSE values are shown in table 10.8. All according RMSE values are higher compared to the RMSE values of the manually aligned image data sets indicating a worse quality of the overall result despite the usage of the same axial reconstruction methods. However, the result obtained by using the aligned images on basis of the sCCG deblurred images is almost as good as the best possible result given by the manually aligned images. The quality of the results on basis of the registration with the degraded images is decreased and thus the effort of the additional deblurring step is justified and recommendable.

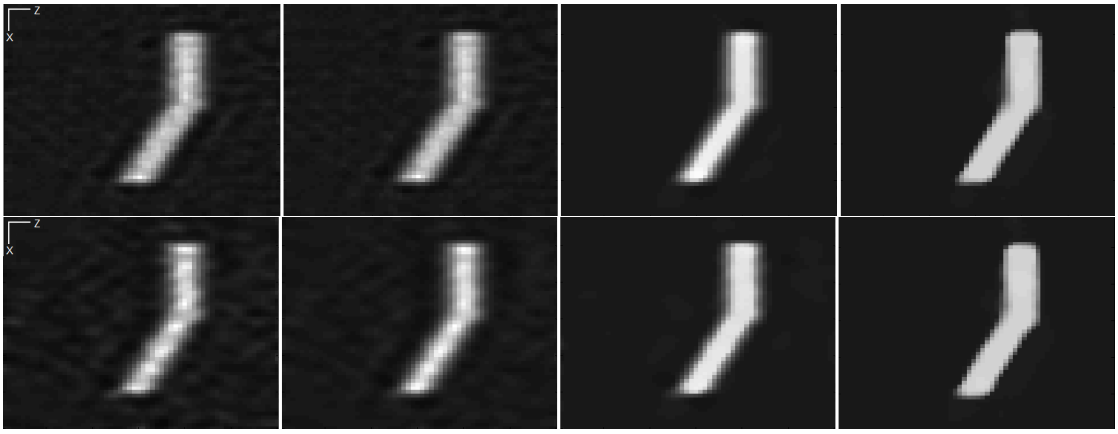

Fig. 10.25.: Reconstruction results on basis of manually aligned image data sets for 3D-IDS1a (Top) and 3D-IDS1b (Bottom): aRL, aRL+, aRLTV and aCCG (From left to right).

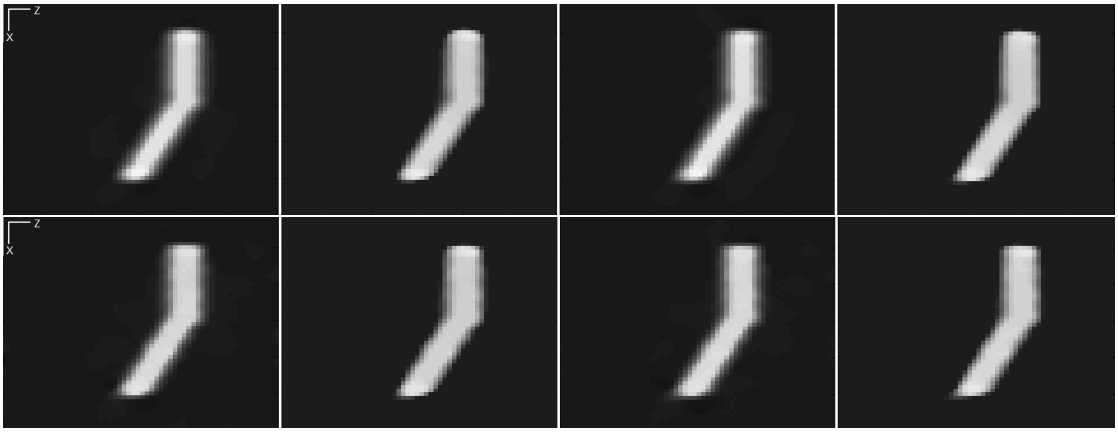

Fig. 10.26.: Axial reconstruction results on basis of registered image data sets. From left to right: aRLTV and aCCG result on basis of registration on degraded images and corresponding results on basis of registration on sCCG deblurred images. Results for image data sets 3D-IDS1a are shown in the upper row and for 3D-IDS1b in the lower row.

	Degraded registered		sCCG registered	
	aRLTV	aCCG	aRLTV	aCCG
3D-IDS1a	3995	3140	3857	3017
3D-IDS1b	4224	3276	4070	3196

Table 10.8.: Axial reconstruction results based on registration results.

	Rotation			Translation		
	θ_x	θ_y	θ_z	t_x	t_y	t_z
'Minus'	-32.562	-0.305	-0.103	3.385	28.318	-34.352
'Plus'	38.740	0.239	0.047	-2.017	-45.596	22.330

Table 10.9.: Bead registration results

10.4.2. Real Image Data Sets

Image Data Set Containing Beads

Maximum projections of the Axial Tomography image data set containing beads with a diameter of $100nm$ are shown in figure 10.27. The projections are done in x direction pointing along the glass fibre and in y direction. The image data set contains three images and these images are denoted as 'Minus', 'Base' and 'Plus' in accordance to their main rotation angle ($-36°$, $0°$ and $+36°$). The images of the bead image data set already have an isotropic grid structure. The spacing of the images is $200nm$ in z direction and usually $100nm$ in x and y direction. Unfortunately, binning was activated for the bead images which means that a 2×2 neighbourhood is used in x and y direction to create one voxel value using the mean of the four values. This method reduces noise at the expense of resolution and results in an isotropic grid structure with a spacing distance of $200nm$. The beads are located on the surface of the glass fibre and the intensity values of the beads are similar in all three images. There is practically no bleaching in the bead images since the fluorescence agent is synthetic and very robust. It is therefore not necessary to perform a bleaching correction and an adjustment of the background values is sufficient to prepare the images for further processing. The background is estimated using the mean of 60% of lowest intensity values and results in 340 for the Minus image, 348 for the 'Base' image and 371 for the 'Plus' image.

After the background signal is adapted, the registration is performed. A rotation angle of $+/-36°$ in x direction is used to initialize the registration and the rotation angles and the translation vector of the registration result are shown in table 10.9. A resampling of the images is not necessary in this case since the images already have a isotropic grid structure. Maximum projections of the aligned images are shown in figure 10.28 and a region of interest (ROI) is displayed in figure 10.29.

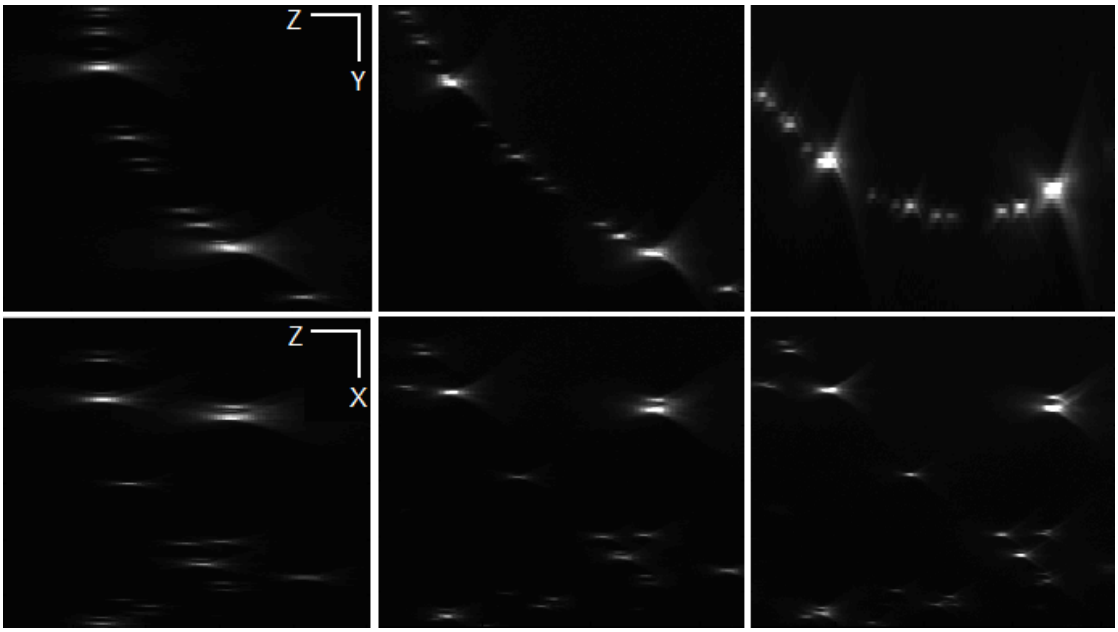

Fig. 10.27.: Maximum projections of the original bead image data set in x (Upper row) and y (Lower row) direction.

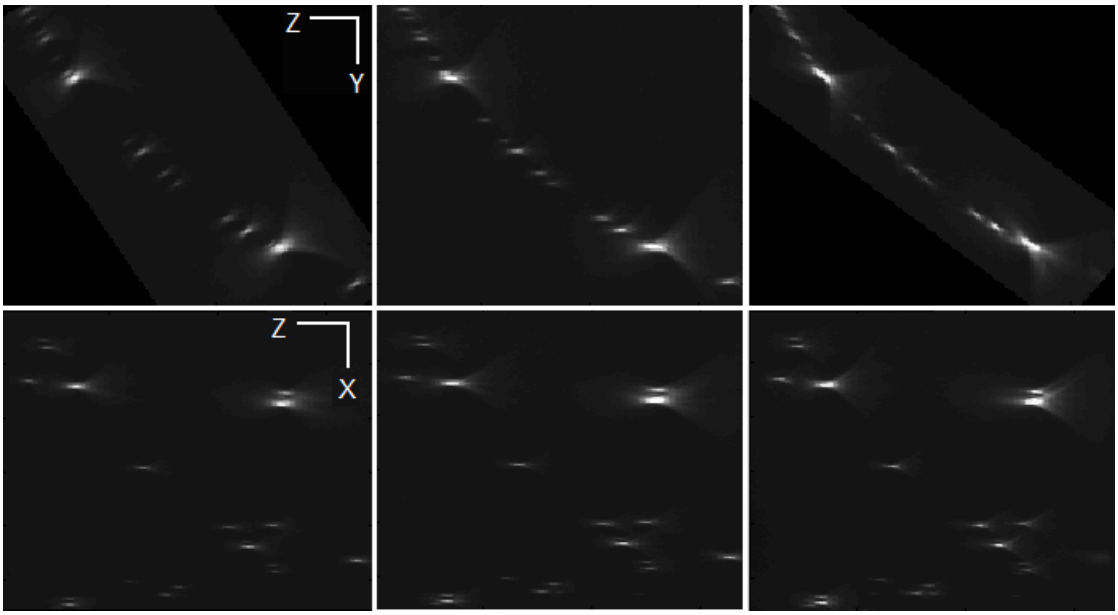

Fig. 10.28.: Maximum projections of the registered Bead image data set in x (Upper row) and y (Lower row) direction.

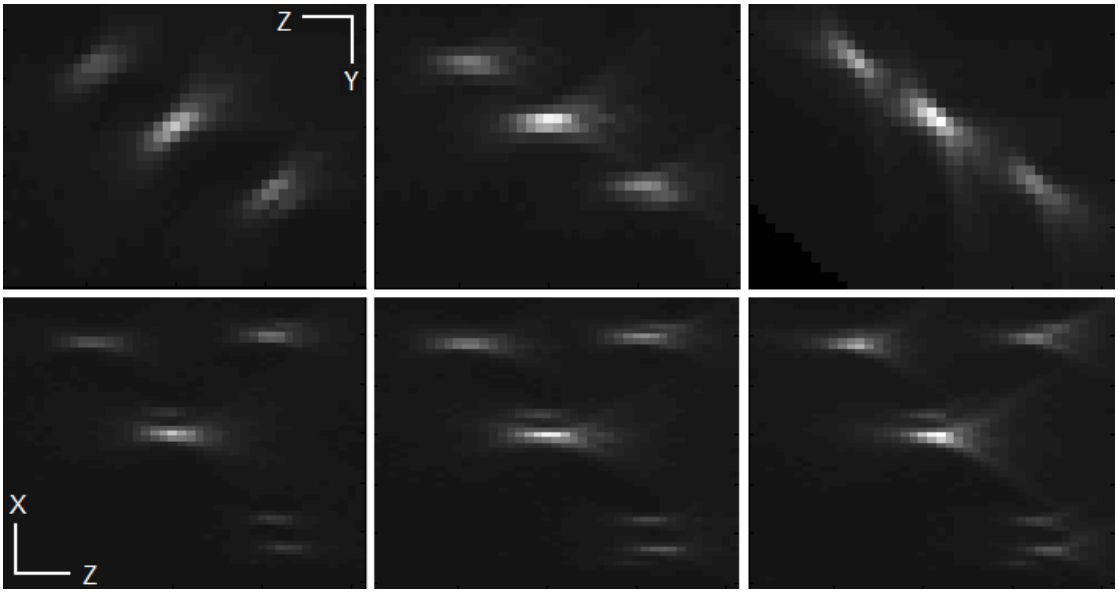

Fig. 10.29.: Maximum projections of ROI containing parts of the registered Bead image data set in x (Upper row) and y (Lower row) direction.

After the registration is completed, the registered images are used to extract the PSFs that are necessary for the axial reconstruction. The images of two beads are used to create each PSF. First, the background is removed and the bead images are centered. Then, the mean of both bead images is taken and the result is normalized. The extracted PSFs which are used in the axial reconstruction are shown in figure 10.30.

A reconstruction result using the RLTV method with $\lambda = 0.002$ is shown in figure 10.31 on the left side. The reconstruction results using the other methods look quite similar and it is not possible to see any differences when analysing the whole image region. In order to compare the different results, a ROI of all results is also shown. All results improve the resolution of the image considerably compared to the measured images. Since binning was activated while the images were measured there is little noise in the images and the need for regularization is essentially not present. As consequence, the results of the aRL and aRLTV algorithm look almost alike. The aCCG algorithm is able to further improve the quality of the reconstruction result within the given limitations caused by binning.

The aim of the Axial Tomography is to obtain an isotropic image with a high resolution in all dimensions. Analysing the Fourier transform of the registered images and the reconstruction result in figure 10.31 clearly shows that this aim is fulfilled for the bead reconstruction. The Fourier transforms of the aligned images shows their support region having the typical shape of the underlying OFTs. The reconstruction result however combines all support regions and even increases them due to the included deblurring

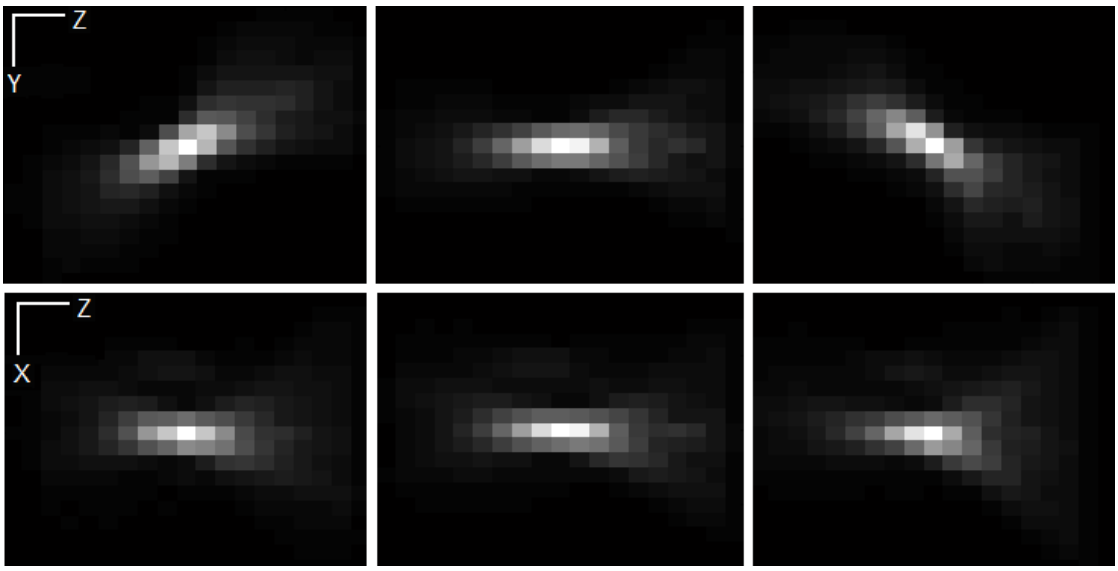

Fig. 10.30.: Maximum projections of extracted PSFs in x (Upper row) and y (Lower row) direction.

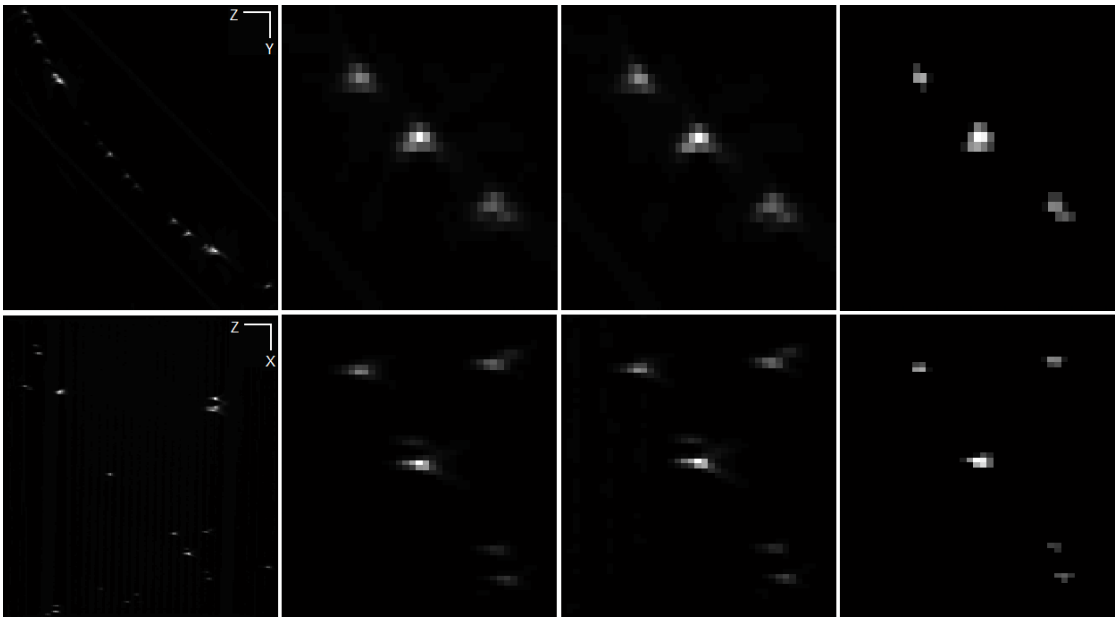

Fig. 10.31.: Maximum projections of axial reconstruction results in x (Upper row) and y (Lower row) direction. From left to right: aRLTV result of whole image region, aRL, aRLTV and aCCG results in ROI.

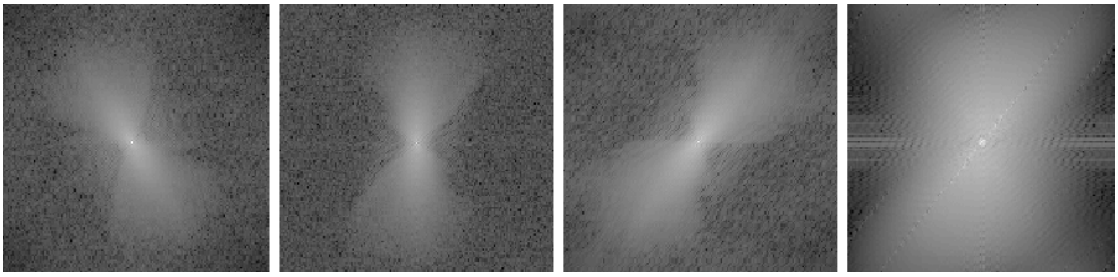

Fig. 10.32.: Fourier transform slices of registered bead image data set and of axial reconstruction result in x,z direction (From left to right).

methods.

Image Data Set Containing a Human Cell

The results of an image data set containing a human cell [129] are shown in this section. The used cell is called *CAL-51* and belongs to a human breast cancer cell line taken after irradiation and chemotherapy. These cells are a rare example for tumor cells with a normal karyotype. The *CAL-51* cells grow adhesive, i.e. its shape is long and thin in contrast to suspension cells and the actin fibres in the cell are stained with the Alexa Fluor 488 Phalloidin fluorescence agent. The cell has been imaged separately from three different angles ($-36°$, $0°$ and $+36°$) and these angles serve as initial guess for the registration. The spacing of the images is $100nm$ in x and y direction and $200nm$ in z direction. The aim is to create a single image containing all available information with an isotropic grid structure with a spacing distance of $100nm$. The cell is located on a glass fibre with a refractive index $n = 1,5168$ and Immersol^{TM} with a refractive index $n = 1,518$ is used as immersions medium in the image acquisition. Maximum projections of the cell image data set is shown in figure 10.33. As before, these images are denoted as 'Minus', 'Base' and 'Plus' in accordance to their main rotation angle.

The imaged cell suffers from bleaching especially for the 'Minus' image since it has been taken latest. Both bleaching and background signal have to be corrected in order to allow a processing of the data. First, the background is estimated and the results are 174, 207 and 184 for the 'Minus', 'Base' and 'Plus' image. Then the bleaching factors are estimated and the factors are 2.5267 for the 'Minus' image and 1.6204 for the 'Plus' image compared to the 'Base' image. These factors quantitatively show that the bleaching for the 'Minus' image is worse than for the 'Plus' image. Bleaching and background signal are correct using equation 10.3.3 and the result is shown in figure 10.34.

After adapting the different cell images, the images have to be registered before the actual axial reconstruction can be done. In order to allow an accurate registration, the cell images are deblurred and the deblurring result is used in the registration. The 3D

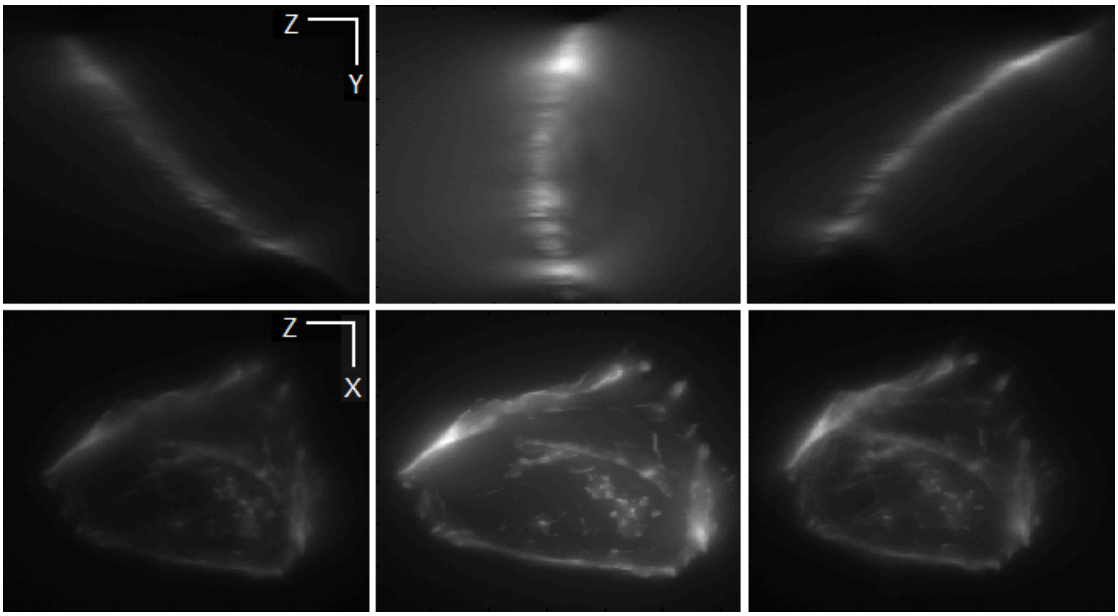

Fig. 10.33.: Maximum projections of original cell image date set ('Minus', 'Base' and 'Plus') in x (Upper row) and y (Lower row) direction.

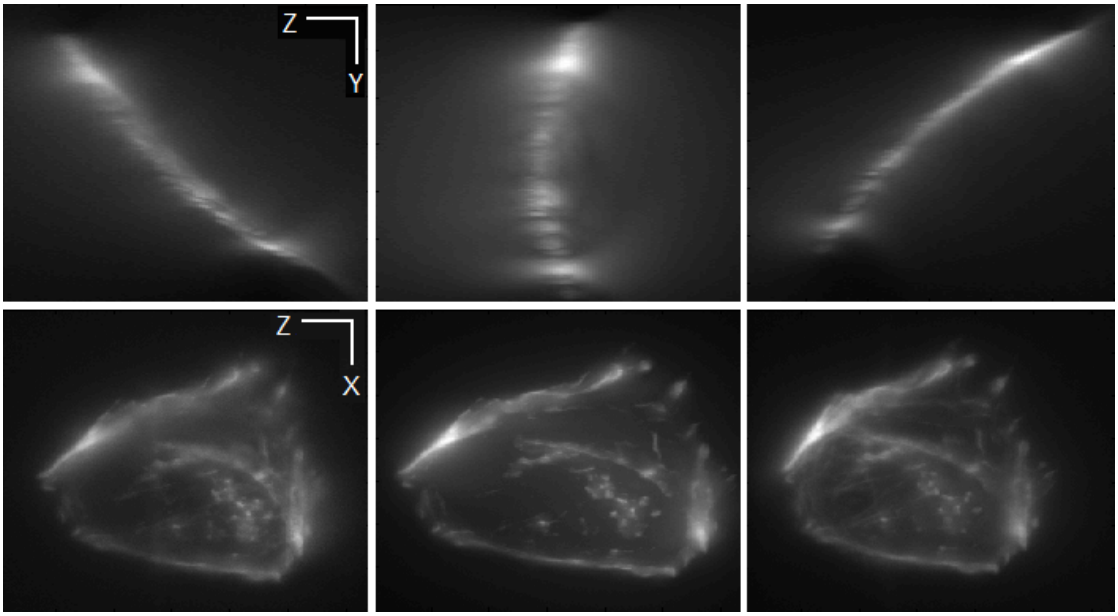

Fig. 10.34.: Maximum projections of adapted cell image date set ('Minus', 'Base' and 'Plus') in x (Upper row) and y (Lower row) direction.

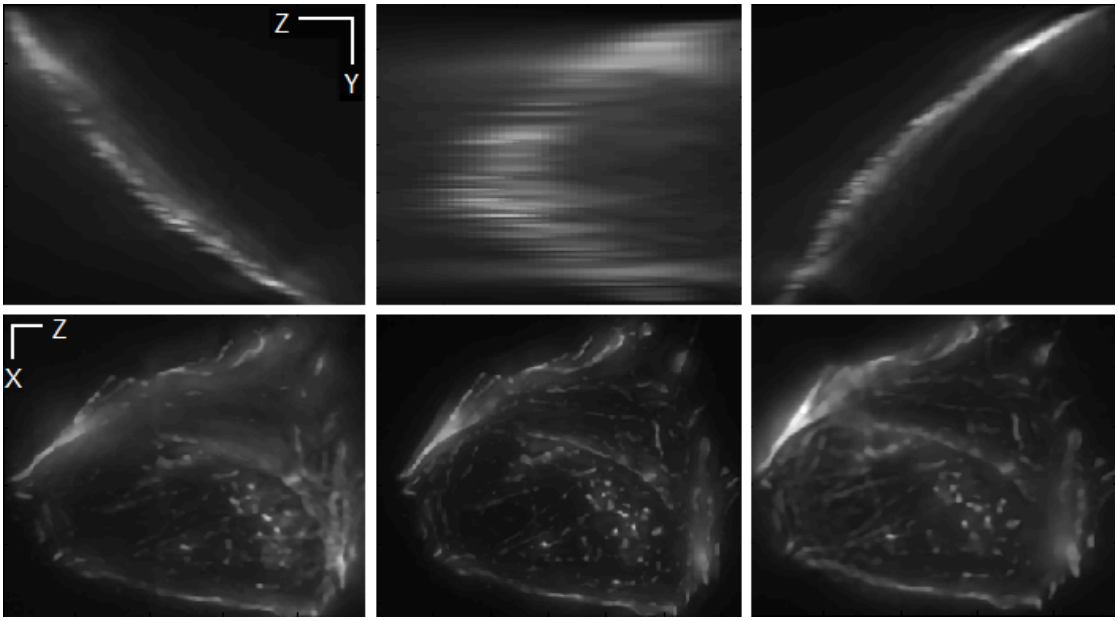

Fig. 10.35.: Maximum projections of deblurred cell image date set ('Minus', 'Base' and 'Plus') in x (Upper row) and y (Lower row) direction.

	Rotation			Translation		
	θ_x	θ_y	θ_z	t_x	t_y	t_z
'Minus' degraded	33.620	0.485	0.029	3.028	-30.254	46.919
'Plus' degraded	-35.068	-1.095	0.612	-5.104	-55.485	63.314
'Minus' sCCG	34.180	0.508	0.035	2.880	-30.835	45.930
'Plus' sCCG	-34.523	-0.292	0.377	-5.141	-54.939	61.476

Table 10.10.: Cell registration results

simulation has shown that a more accurate result was obtained by using deblurred images rather than the measured degraded images. The results of the deblurring of the different images are shown in figure 10.35.

The sampling distance of the cell image data set is not isotropic and the spacing of the underlying grid structure has to be changed in the registration process. As result, an isotropic grid structure with a spacing distance of $100nm$ is created. Both the measured and the deblurred images are used to perform the registration and the results are displayed in table 10.10. The differences between both cases are similar to the results of the 3D simulation and it can therefore be assumed that the result obtained by using the deblurred images is more accurate. The aligned isotropic images on basis of this registration result are shown in figure 10.36.

The PSFs already used for the bead images are used here as well since the cell images

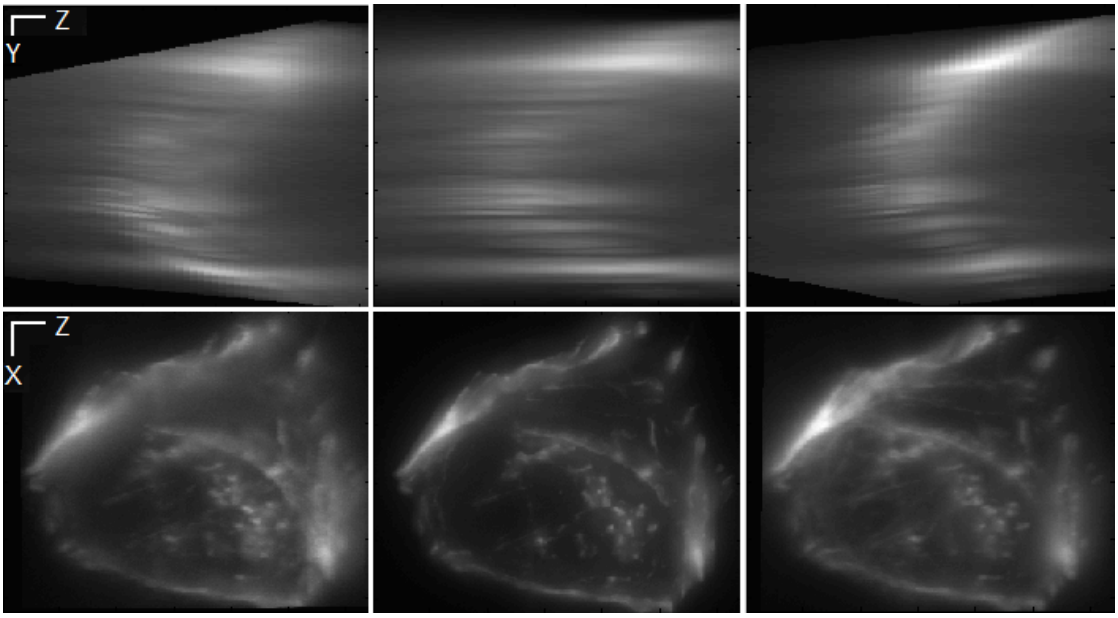

Fig. 10.36.: Maximum projections of registered cell image date set ('Minus', 'Base' and 'Plus') in x (Upper row) and y (Lower row) direction.

are acquired with the same microscope as the bead images. The differences in the rotation angles and sampling are corrected and the resulting PSFs that are shown in figure 10.37 are used in the axial reconstruction.

The results of the axial reconstruction and the original 'Base' image are shown in figure 10.38 and figure 10.39. In these figures, slices which are extracted from the volume are displayed instead of maximum projections. The resolution of the cell image is improved for all axial reconstruction algorithms especially in direction along the optical axis where additional information is provided by the different viewing angles. Despite improving the image quality and the resolution, the potential of the aRL algorithm is limited. The actin fibres which are stained with the fluorescence agent appear in a higher resolution but are still blurred. It is not possible to further improve the result of the aRL algorithm since noise amplification would degrade the result using more iterations. The quality of the aRLTV algorithm overcomes this problem using the additional TV regularization. The TV regularization is necessary to obtain a stable solution but assumes homogeneous areas with sharp edges. This assumption does not completely apply to the stained actin fibres which are in fact shaped like thin tubes. The axial reconstruction result therefore contains plain homogeneous areas instead of thin structures. This staircasing effect is a well known drawback of the TV regularization. The aCCG algorithm does not show this behaviour despite including TV. The actin fibres are reconstructed as thin tube-like structures as expected. The TV regularization is necessary to suppress noise amplifications but the additional non-negativity constraint provides a second reg-

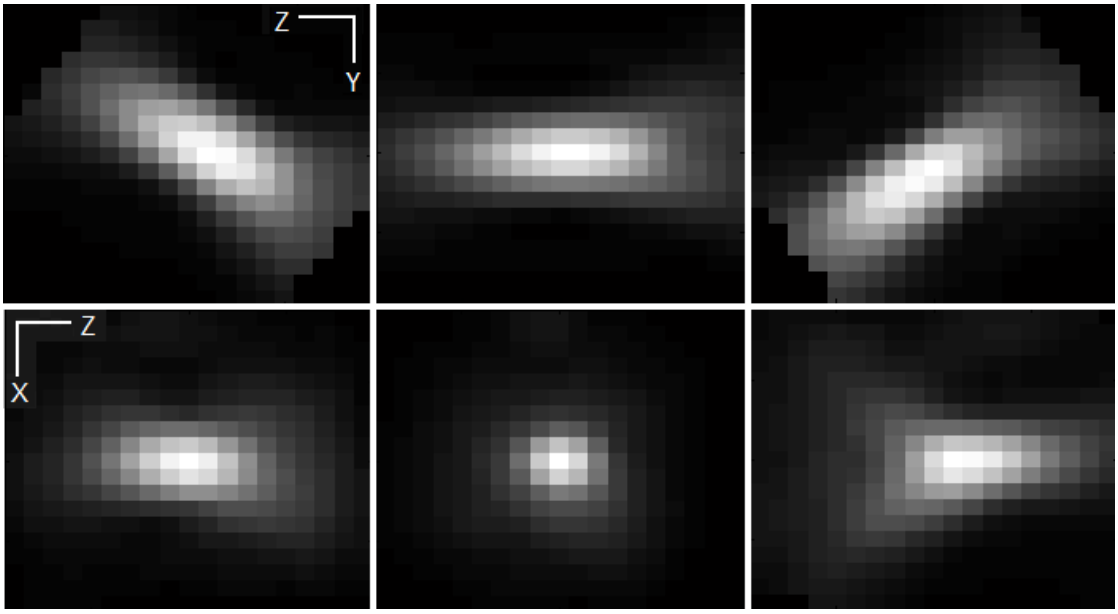

Fig. 10.37.: Maximum projections of resampled and aligned PSFs for cell image data set in x (Upper row) and y (Lower row) direction.

ularization mechanism and the cooperation of both leads to a stable solution without suffering from the drawbacks of a single TV regularization.

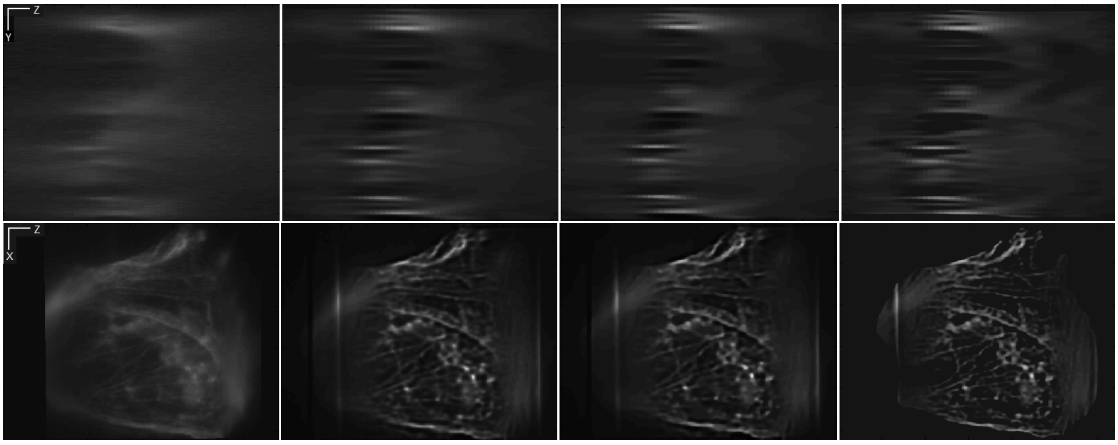

Fig. 10.38.: Slices of original 'Base' image and axial reconstruction results aRL, aRLTV and aCCG. zy slices are shown in the upper row and xz slices in the lower row.

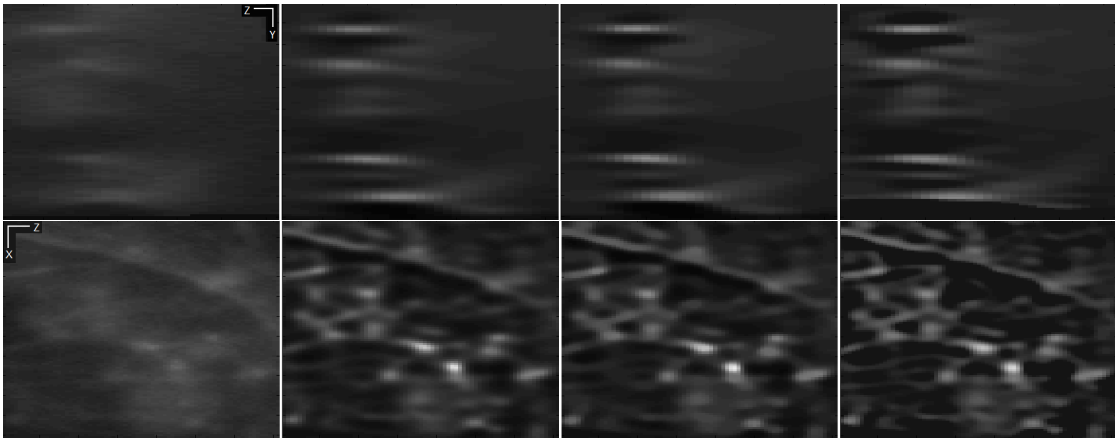

Fig. 10.39.: ROI of original 'Base' image and axial reconstruction results aRL, aRLTV and aCCG shown in figure 10.38.

11. Proton Dose Reconstruction

11.1. Introduction

Cancer is a class of diseases which caused about 13% of all human deaths in 2007 (7.6 million people) [150] [173]. Hereby, a cell or a group of cells display uncontrolled growth, invasion and sometimes metastasis. There are various different types of cancer and the search for diagnostic tools and options for cure has been a major research topic for more than a hundred years. The possibilities and strategies of cancer therapy are as multifaceted as cancer itself. Most cancers form a tumor but there are some, like leukemia, which do not form a tumor. Cancer can be treated by surgery, chemotherapy, radiation therapy, immunotherapy, monoclonal antibody therapy or other methods depending on the tumor, the state of the disease and the patient. The complete removal of the tumor without damaging the rest of the body is the ultimate goal of cancer therapy. In order to treat a tumor, the three main options are surgery, chemotherapy and last but not least radiation therapy (or radiotherapy). In radiation therapy, ionized radiation is used to control malignant cells with the chance to cure the disease or at least local disease control or symptomatic relief where a cure is not possible. The discovery of X-rays in 1895 formed the basis of radiation therapy and the concept of therapeutic radiation was invented by the German physicist Wilhelm Conrad Röntgen. The groundbreaking work of Marie Curie-Sklodowska lead to a new area in medical treatment and research [111]. Medical linear accelerators have been developed since the late 1940s and the invention of the computed tomography (CT) by Godfrey Hounsfield allowed a three dimensional (3D) planning and thus a 3D conformal radiation. In the last few decades, new techniques for radiation delivery and visualization have moved radiation therapy to intensity modulated radiotherapy (IMRT) and eventually to image guided radiotherapy (IGRT). In our days, 70% of cancer patients receive radiotherapy, at least as part of their treatment.

The majority of radiotherapy involves high energy photons with an increasing interest in treatment with proton beams as the number of clinical proton therapy facilities increases worldwide. Robert R. Wilson had the idea to use energetic proton beams to treat tumor patients [175] while being involved in the design of the Harvard Cyclotron Laboratory (HCL). The first treatments using particle accelerators took place in 1954 at the Berkley Radiation Laboratory and at Uppsala in Sweden in 1957. In 1961, the HCL and the Massachusetts General Hospital (MGH) started a collaboration for proton

therapy and treated 9116 patients in the next 41 years. The first hospital based proton therapy center in the United States was built in 1990 at the Loma Linda University Medical Center in Loma Linda, California (now named James M. Slater Proton Therapy Center). During 2001 to 2002, The HCL treatment program was transferred to the new established Northeast Proton Therapy Center at the MGH (recently named Francis H. Burr Therapy Center).

Proton radiotherapy allows the delivery of a high dose to the tumor while the dose to healthy tissue can be minimized. The most important interaction of the proton beam is the electromagnetic coulomb interaction between the projectile and electrons causing a continuous energy loss of the proton. Hereby, the energy loss increases with decreasing speed and therefore increasing depth of penetration. This phenomena leads to the characteristic Bragg curve describing the delivered dose in dependence of the penetration depth [22]. In the entrance region, a relatively low dose is delivered and a high-dose peak in the target area with no further dose delivery afterwards. This finite beam range is the main advantage of protons in radio therapy compared to photon beams delivering dose at any penetration depth. Several Bragg peaks with different penetration depths can be combined to a spread-out Bragg peak (SOBP) forming a stable plateau with a constant dose delivery (Figure 11.1). In order to generate such Bragg peaks, passive energy degraders can be used or the acceleration energy has to be varied. Such a SOBP is perfectly suited to irradiate a tumor while sparing surrounding tissue. Such a well-positioned dose delivery is not possible with photons (Figure 11.2).

A sketch of the beam modeling devices used at the MGH can be seen in figure 11.3. A longitudinal widening of the dose distribution is created through a modulation wheel and results in a SOBP. A successive scatterer is then able to spread the dose distribution in lateral direction. Another possibility to achieve a lateral spread of a proton dose distribution is to use magnetic deflection. Finally, custom milled apertures and compensators are used to provide a suitable lateral and distal shape of the dose distribution to a Patient specific treatment [85].

The differences of protons and photons for patient treatments are illustrated in figures 11.4 and 11.5. The dose delivery for the tumor is similar in both cases since the treatment would not be effective otherwise. It can be seen that the surrounding tissue has a higher dose delivery in case of photons which is called a "dose bath". Such a dose bath can be avoided using protons by taking advantage of the finite beam range. Surrounding healthy tissue is thus preserved from damage.

However, uncertainties in the treatment planning and delivery can have a considerable impact on the applied dose resulting in under dosage of the tumor or over dosage of surrounding healthy tissue. The reason for such uncertainties can be due to patient specific uncertainties, errors in the treatment planning algorithm, motion and anatomical changes [49]. In addition, artifacts in the planning CT and ambiguity in the Hounsfield Unit (HU) conversion can result in errors in the dose delivery [61]. Precise treatment

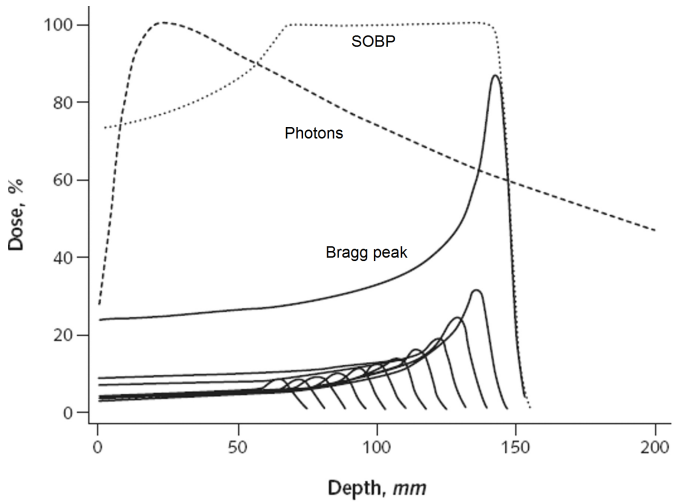

Fig. 11.1.: Bragg peak, SOBP and photon dose distribution.

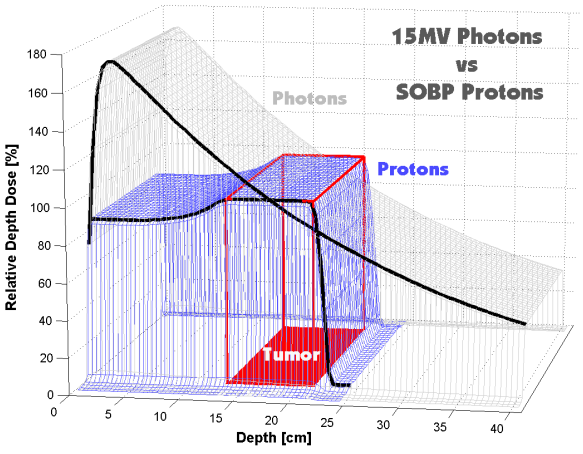

Fig. 11.2.: Photon and SOBP dose delivery.

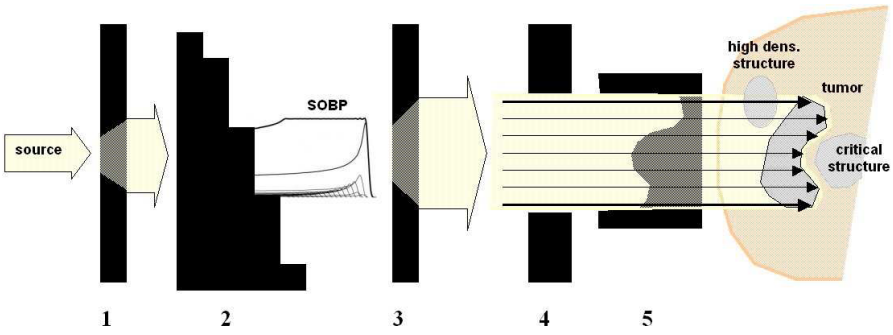

Fig. 11.3.: Beam line in gantry-treatment rooms at MGH: 1. First scatterer 2. Modulation wheel, 3. Second scatterer, 4. Aperture and 5. Range compensator.

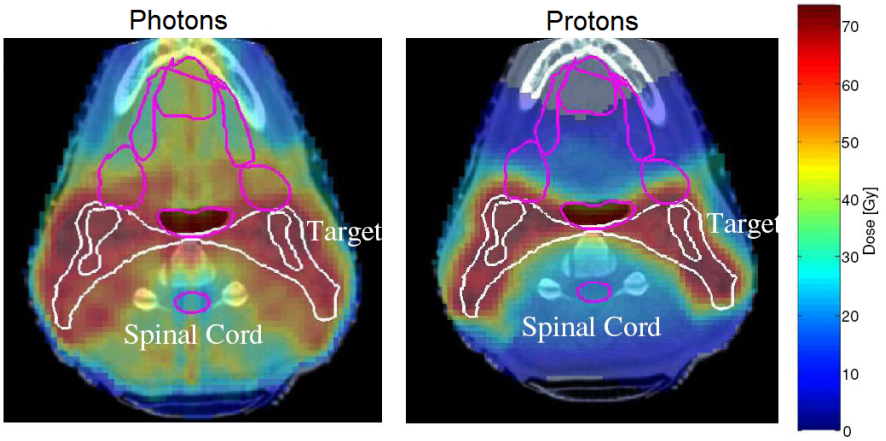

Fig. 11.4.: Photon and proton treatment for head and neck patient.

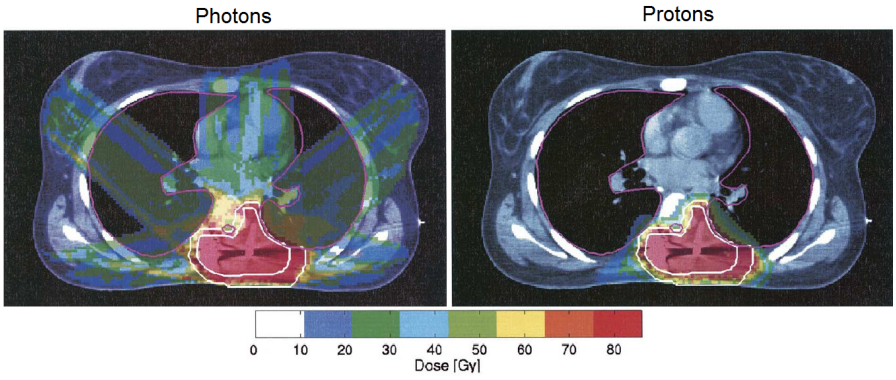

Fig. 11.5.: Photon and proton treatment.

delivery is important and additional verification methods are required due to the steep dose fall-off of a proton beam. In conventional radiotherapy, electronic portal imaging methods can be used detecting traversing photons. Such strategies cannot be applied to proton radiation because the proton beam is stopped completely. However, since proton beams activate positron emitters, Positron Emission Tomography (PET) can be used for in-vivo verification of radiotherapy [16] [56] [160] [98]. Unfortunately, the PET image and the delivered dose distribution are not proportional and thus cannot be compared directly. There is no proton induced nuclear reaction under an energy threshold of 15-20MeV [160] resulting in a lack of activity just before the proton beam is stopped and where most of the dose is delivered. In order to use the PET image for dose verification, it is compared with a predicted β^+-activity distribution following the approach of treatment monitoring for carbon ion therapy [50] [123]. Hereby, detailed Monte Carlo (MC) simulated activity distributions are compared with measured PET signals in order to verify the dose delivery [116] [117]. First investigations of the potential of PET based non-invasive proton radiotherapy monitoring methods showed a possible millimeter accuracy [118] [119]. The PET based approach to verify the proton beam range including a comparison with MC simulations was further investigated using phantom studies [84] and patients [83].

Alternatively, an analytical approach using Gaussian-powerlaw convolutions is able to predict the activity distribution [115]. Hereby, the planning dose is convolved with a positron emitter specific filter function resulting in the according PET activity prediction. At first, due to a relative long delay time between irradiation and PET measurement, only positron emitters with a long half-life time (i.e. ^{11}C with $T_{1/2} = 20.39min$) were considered. The therefore used PET/CT scanner was located within 10 min walking distance from the proton therapy unit. With an decreased delay time using in-room or even in-beam PET scanners [5], different short-lived emitters (e.g. ^{15}O, ^{13}N) have to be taken into account. A filter framework considering different isotopes was developed and tested using phantom measurements and corresponding MC calculation [7]. Later, the filter framework was also validated using simulations on real patient data and assuming an in-room PET data acquisition starting at the end of the irradiation [6].

Both the MC and the filtering approach are able to predict the PET activity distribution assuming a given dose delivery. Comparing these predictions and their distal fall-off regions with measured PET signals is used for treatment verification. An agreement of simulated and measured PET activity indicates a dose delivery to the right location but the actually delivered dose is not reconstructed from the measured PET image which is most desirable.

In [55], a method to reconstruct the dose delivery from measured PET signals using previously calculated positron emitters species matrices (PESM) is proposed. Once the PESM which are based on proton energy fluence distributions are known, the authors state that the absolute dose distribution in a patient can be found using a deconvolution

of the measured PET activity with the PESMs. In this framework, the PET and the dose distributions are described by:

$$PET(r,t) = \sum_{i,j} w_{i,j} \sum_{k} \Delta\tilde{N}_k(r, E_i) \cdot C(k,j,t) \tag{11.1.1}$$

$$DOSE(r,t) = \sum_{i,j} w_{i,j} \tilde{d}_k(r, E_i) \tag{11.1.2}$$

For the PET distribution, $\Delta\tilde{N}$ describes the PESM and C contains a weighting of the isotope specific activity due to irradiation and delay time. $\tilde{d}$ represents the dose kernels normalized per incident proton in the dose formula. The weights $w_{i,j}$ are included in the descriptions of both the PET and the dose distribution. Before a dose reconstruction can be done, the PESM have to be known and are calculated analytically. The actual reconstruction is done by determining the weights $w_{i,j}$ solving an inverse problem and using them to calculate the dose distribution based on the dose kernels. The authors used the random creep algorithm, which is a variation of the gradient search technique, to determine the weights. This approach showed good results for an initial reconstruction using a homogeneous tissue-phantom and is meant to perform in vivo dose reconstructions for patients. The authors predicated that the computational effort and the complexity of the inverse problem are extensive in this case. Inhomogeneities in the tissue have to be considered in the calculation of the PESMs using underlying CT scans. An additional large amount of beamlets in the dose delivery would lead to a large system of equations to be solved.

In general, an accurate knowledge of the dose delivery in radiation therapy is essential and even Gaussian blurring included in ion chamber measurements of dose deliveries is investigated [161]. In [162], the author proposes a linear combination of Gaussian convolution kernels to reconstruct the original dose distribution. A framework of Gaussian kernels with positive coefficients is used in case of transverse profiles of dose distributions (protons and photons). In addition, a so called Mexican hat containing Gaussian kernels with negative coefficients is applied in case of a proton Bragg curve.

In the following, an approach to reconstruct the dose distribution in proton radiotherapy using PET signals is described and its feasibility for measured PET signals is evaluated. Previous publications show that the main purpose of PET treatment verification is currently the verification of the proton beam range. Thus, the location of the fall-off is the most important aspect and this is one of the main concerns and uncertainties in proton beam therapy. The objective of the new method is to improve the range verification by reconstructing the delivered dose and to extend the method from range verification to overall treatment verification. The new method is based on the filtering approach using Gaussian-powerlaw convolutions [115]. Since an estimation of a PET signal is obtained by convolving a planned dose distribution with a corresponding filter mask in 1D, a 1D deconvolution is used to reconstruct the dose distribution from the PET signal.

Deconvolution is an ill-posed inverse problem and regularization techniques are thus used in order to obtain a stable solution. The application of the reconstruction method in case of homogeneous media is shown first and the generalization to inhomogeneous media is described afterwards. This advanced reconstruction approach is tested using 1D phantom signals and dose distributions for inhomogeneous 2D phantom data and a head and neck patient data set are also reconstructed. Last but not least, the dose reconstruction method is extended to process PET signals containing a combination of different positron emitters and simulated results for a patient data set are shown.

11.2. The Gaussian and Powerlaw Convolution Framework

As mentioned before, the new approach to reconstruct the dose delivery in proton radiation is based on the convolution framework introduced in [115]. Hereby, the PET activity distribution of an individual positron emitter introduced by a certain dose distribution can be estimated by a 1D convolution of the dose distribution with a corresponding filter function assuming homogeneous tissue. In principle, a given dose distribution D in homogeneous tissue can be described by a superposition of individual Bragg peaks b depending on a nominal range R. z describes the depth in direction of the proton beam.

$$D(z) = \int_0^\infty w(R)b(z,R)dR \tag{11.2.1}$$

The energy of a proton beam is equivalent to its nominal range in case of homogeneous tissue and the weights $w(R)$ describe the energy spectrum of the beam. The irradiation-induced PET signal P can be described in a similar way with p being the PET activity induced by a mono-energetic beam.

$$P(z) = \int_0^\infty w(R)p(z,R)dR \tag{11.2.2}$$

According to [115], it is possible to predict a specific PET activation p by convolving the corresponding Bragg peak b with a specific filter function f which is in fact indirectly defined by this equation.

$$p(z) = b(z) * f(z) \tag{11.2.3}$$

Hereby, $*$ describes a convolution. Since the dose distribution is given by a superposition of individual Bragg peaks, the total irradiation-induced PET signal is given by a convolution of the dose distribution with the filter function f.

$$P(z) = D(z) * f(z) \tag{11.2.4}$$

In order to determine a filter function using equation 11.2.3, an analytical representation of a Bragg peak and the corresponding PET signal is required. In [115], a set of $\tilde{Q}_\nu(x)$ functions already introduced to describe Bragg peaks in [19] is used for that purpose. The $\tilde{Q}_\nu(x)$ functions are generated by a convolution of a Gaussian

$$G(x) = \frac{1}{\sqrt{2\pi}} exp\left(-\frac{x^2}{2}\right) \tag{11.2.5}$$

and a powerlaw function

$$P_\nu(x) = \begin{cases} \frac{1}{\Gamma(\nu)} x^{\nu-1} & if x > 0 \\ 0 & otherwise \end{cases} \tag{11.2.6}$$

in which the gamma function $\Gamma(\nu)$ is used for normalization purposes. A closed form of the convolution in terms of parabolic cylinder functions D was introduced in [60] and is given by:

$$\tilde{Q}_\nu(x) = G(x) * P_\nu(x) = \frac{1}{\sqrt{2\pi}} exp\left(-\frac{x^2}{4}\right) D_{-\nu}(-x) \tag{11.2.7}$$

Depending on the parameter ν, the set of $\tilde{Q}_\nu$ functions contain several other interesting functions. For $\nu = 0$, the $\tilde{Q}_\nu$ function is equivalent to a Gaussian function and for $\nu = 1$, the $\tilde{Q}_\nu$ function can be expressed through an error function. The depth dose distribution of a therapeutic proton beam can be represented by a $\tilde{Q}_\nu$ function with $\nu \approx 0.6$. The graphs of different $\tilde{Q}_\nu$ functions can be seen in figure 11.6. Furthermore, another useful property is that the convolution of two arbitrary $\tilde{Q}_\nu$ functions is again a $\tilde{Q}_\nu$ function.

$$\tilde{Q}_{\nu_1}(x) * \tilde{Q}_{\nu_2}(x) = \sqrt{2}^{\nu_1+\nu_2-1} \tilde{Q}_{\nu_1+\nu_2}\left(\frac{x}{\sqrt{2}}\right) \tag{11.2.8}$$

In order to represent a Bragg peak or an irradiation-induced PET signal, a shifted and scaled versions of $\tilde{Q}_\nu$ functions is required.

$$\tilde{Q}_\nu\left(\frac{x-a}{b}\right) \tag{11.2.9}$$

The result of a convolution of two shifted and scaled $\tilde{Q}_\nu$ functions is then given by (see Appendix in [115]):

$$\tilde{Q}_{\nu 1}\left(\frac{x-a_1}{b_1}\right) * \tilde{Q}_{\nu 2}\left(\frac{x-a_2}{b_2}\right) = \frac{\sqrt{b_1^2+b_2^2}^{\nu 1+\nu 2-1}}{b_1^{\nu 1-1} b_2^{\nu 2-1}} \tilde{Q}_{\nu 1+\nu 2}\left(\frac{x-a_1-a_2}{\sqrt{b_1^2+b_2^2}}\right) \tag{11.2.10}$$

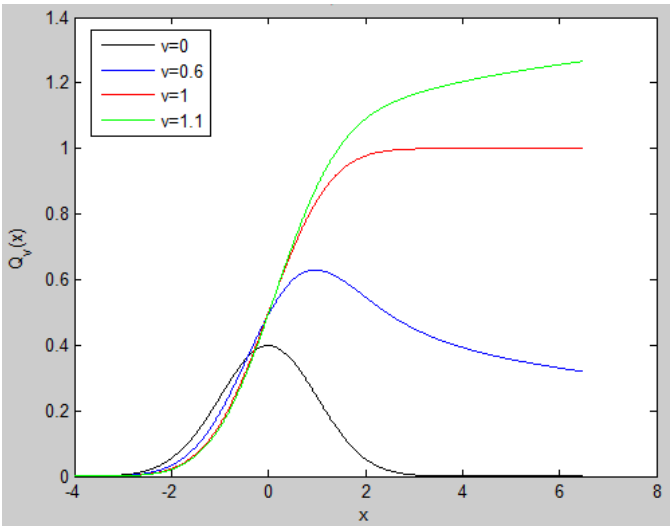

Fig. 11.6.: $\tilde{Q}_\nu$ functions with different ν.

Using the $\tilde{Q}_\nu$ functions, it is possible to determine a filter function for a specific positron emitter in homogeneous media. In this framework, an individual filter function is required for each positron emitter and each filter function is valid for the homogeneous tissue on which the underlying dose and PET signal are given. In order to determine the filter function, the Bragg curve and the corresponding PET signal have to be fitted with $\tilde{Q}_\nu$ functions. Hereby, the accuracy of the fit can be improved by using more than one $\tilde{Q}_\nu$ function. In [115], a filter function for a ^{11}C positron emitter was determined on basis of a homogeneous polymethyl methacrylate (PMMA) target. The required representation of a Bragg curve with a energy of $152.1MeV$ and the corresponding PET signal using $\tilde{Q}_\nu$ functions are given in the following equations.

$$b(x) = 6.46mGmm^2\tilde{Q}_{0.625}\left(\frac{-x+140.7mm}{1.53mm}\right) \tag{11.2.11}$$

$$\begin{aligned} p(x) = \quad & 4.6313mm^{-1}\tilde{Q}_{1.3353}\left(\tfrac{-x+136mm}{2.18mm}\right) \\ & +2.5769mm^{-1}\tilde{Q}_{1.4596}\left(\tfrac{-x+136mm}{2.18mm}\right) \end{aligned} \tag{11.2.12}$$

Both distributions were calculated using Monte Carlo (MC) simulations and fitted with $\tilde{Q}_\nu$ functions using suitable optimizers. The aim was to have an acceptable fit of the $\tilde{Q}_\nu$ functions for a relevant depth range containing the area around the distal fall-off region of both curves (Shown in figure 11.7). The corresponding filter function is then determined using equation 11.2.3. Assuming a filter function with two $\tilde{Q}_\nu$ functions, $b(z) * f(z)$ can be calculated using equation 11.2.10 and then be compared with $p(z)$ leading to a linear system of six equations containing six parameters determining the filter function f. The given Bragg peak (Equation 11.2.11) and the corresponding PET

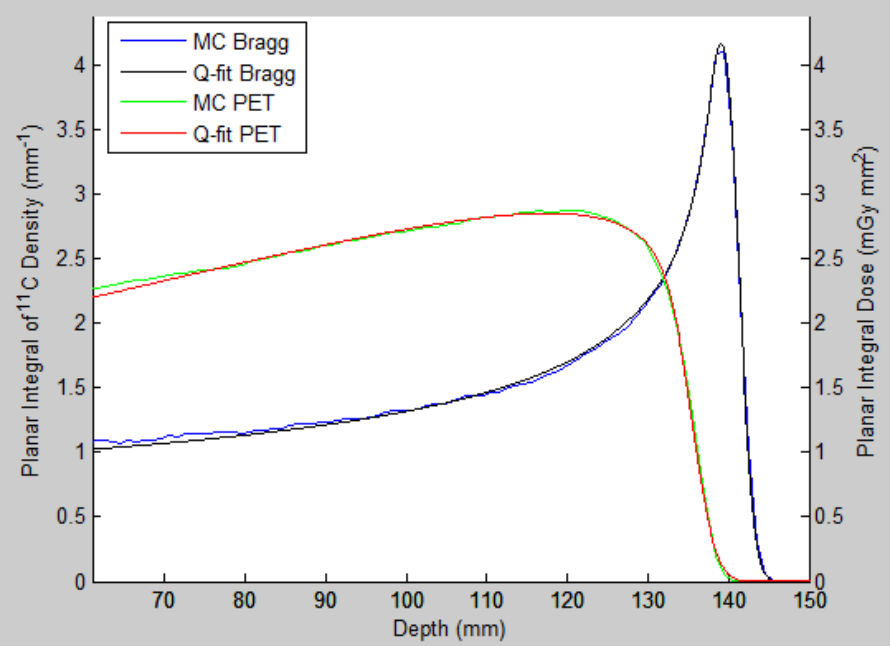

Fig. 11.7.: Fitting result of $\tilde{Q}_\nu$ functions to Bragg curve and PET signal.

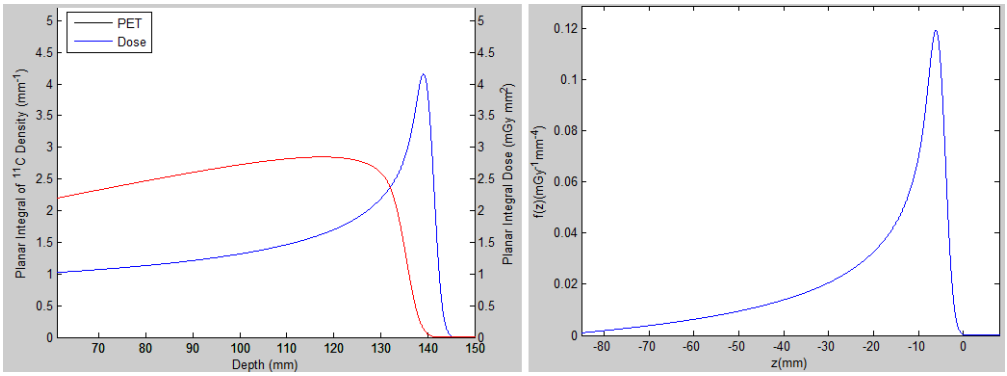

Fig. 11.8.: Left: Bragg curve and PET signal, right: filter function.

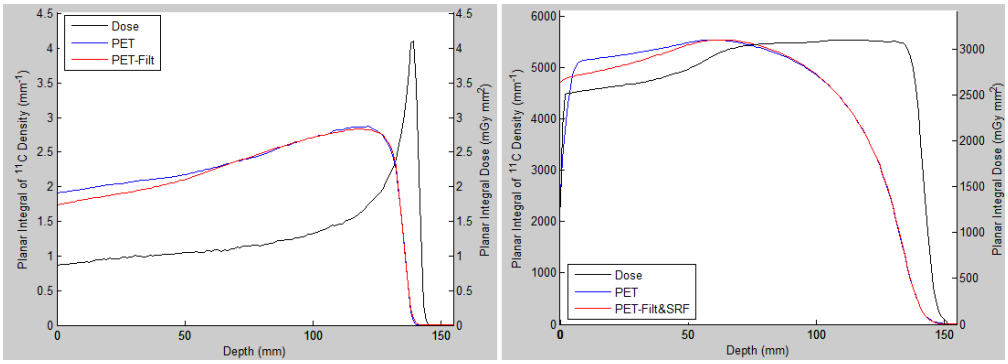

Fig. 11.9.: Forward filtering examples: Bragg curve (Left) and SOBP (Right).

signal (Equation 11.2.12) result in the filter function $f(x)$ and their graphs can be seen in figure 11.8.

$$\begin{aligned} f(x) = \quad & 0.4143 mGy - 1mm^{-4}\tilde{Q}_{0.7103}\left(\tfrac{-x-4.7mm}{1.553mm}\right) \\ & +0.2210 mGy - 1mm^{-4}\tilde{Q}_{0.8346}\left(\tfrac{-x-4.7mm}{1.553mm}\right) \end{aligned} \tag{11.2.13}$$

The filter function allows a prediction of the PET activity for the underlying positron emitter in homogeneous PMMA material or PMMA equivalent material. Hereby, the dose distribution is convolved with the filter function according to equation 11.2.4 which is called *forward filtering* in the following. Due to the superposition principle, the dose distribution is not limited to Bragg curves and e.g. SOBPs can be processed as well. A Bragg peak and a SOBP, the corresponding forward filtering results and PET signals predicted by MC simulations are shown in figure 11.9. It can be seen that the MC PET signals and the PET signals obtained by forward filtering are in good agreement in the relevant areas including the distal fall-off region.

The Bragg peak and the SOBP used for the forward filtering are results of MC simulations as well. Besides MC simulations of the dose distributions, treatments planning dose distributions can be used to predict the PET signal using the convolution framework as well. All of these signals are given in a discrete form with a specific sampling distance ($1mm$ in the previous case). The filter function is given by $\tilde{Q}_\nu$ functions and therefore in a continuous form. In order to apply the filter function to a given dose distribution, it has to be sampled using the same sampling distance as the dose signal. If the sampling distance is too large important information can be lost. According to the Nyquist-Shannon theorem, the sampling frequency $f_{sampling}$ should be at least two times the maximum frequency f_{max} of the sampled signal in case it is band-limited.

$$f_{sampling} > 2 f_{max} \tag{11.2.14}$$

In order to investigate what sampling distances can be allowed for the convolution framework, the Fourier transforms of the previously used filter function is investigated.

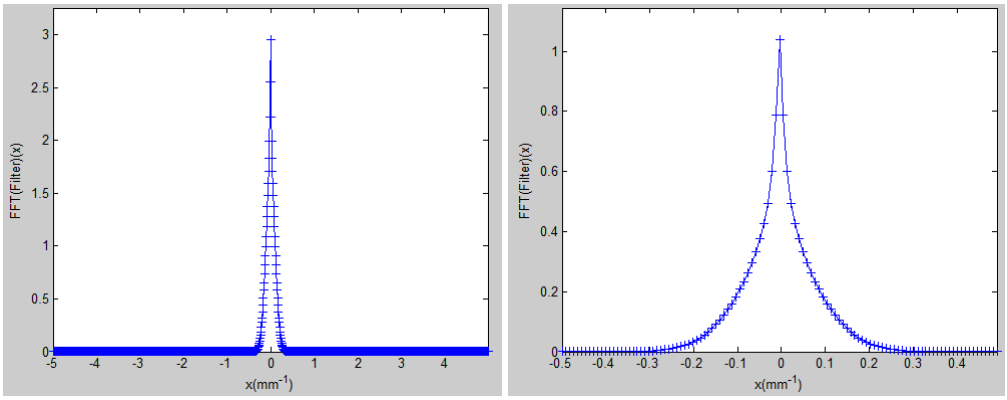

Fig. 11.10.: Fourier transform of filter (Sampling: left $0.1mm$, right $1mm$).

Hereby, the filter function is sampled with $0.1mm$ and $1mm$ using the continuous $\tilde{Q}_\nu$ function form. The according Fourier transforms can be seen in figure 11.10. The allowed maximum sampling distance is determined using the doubled frequency where the value of the Fourier transform falls below 1% of its maximum serving as cut off frequency to determine a band width. Thus, the allowed maximum sampling distance is $1.74mm$.

11.2.1. Detection of Distal Fall-off Region

In accordance with the shape of the delivered dose in proton therapy, a main focus of a dose verification is the detection of the distal fall-off region. Since measured data contains noise and deconvolution is a difficult problem, it is possible to have artifacts in the reconstructed dose distribution and thus a reliable determination of the distal fall-off region is required. In the proposed approach, the midpoint of the largest falling edge estimates the location of the distal fall-off region and is determined by using the gradient of the dose signal. A reconstructed dose signal can contain artifacts leading to larger gradient values compared to the fall-off region and thus a simple determination of the maximum value of the gradient is not sufficient. An artifact while containing large gradient values is quite small compared to the distal fall-off edge of a Bragg peak or a SOBP and this property is used by analysing a smoothed version of the gradient to determine the distal fall-off edge. The gradient is smoothed by a Gaussian convolution and a sharp peak of an artifact is thus deflated while the gradient of the distal fall-off region becomes dominant. The maximum value of the smoothed gradient indicates the location of the distal fall-off region. This method is quite robust against artifacts but limited in its accuracy since it depends on the sampling points of the underlying grid structure. In order to investigate the accuracy of the dose reconstruction, the reconstruction result is compared with the treatment planning dose and the distance between both distal fall-off

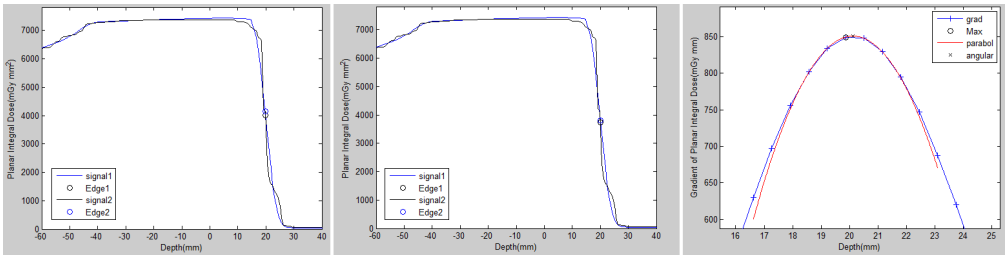

Fig. 11.11.: Gradient based edge detection: on grid (Left), parabolic estimation (Middle) and Gradient signals (Right).

regions is calculated. Such a distance can only be an integral multiple of the sampling distances which is quite inaccurate for a relative large sampling distance of e.g. $1mm$. The accuracy is improved by using a parabolic interpolation of the maximum area of the smoothed gradient and determining its angular point which represents the midpoint of the distal fall-off region. The results of an edge detection of a SOBP using a treatment planning dose and a reconstruction result is shown in figure 11.11. On the right side of the figure, details of the smoothed gradient and the parabolic interpolation are displayed.

The distance between the midpoints of the distal fall-off regions of a reconstructed dose and a treatment planning dose is used to evaluate the reconstruction result in case of 1D signals. For 2D or 3D signals the mean value μ and the variance σ^2 of the according distances $dist$ using a certain amount N of proton beams are used to evaluate the reconstruction result.

$$\mu = \frac{1}{N}\sum_{i=1}^{N} dist_i \tag{11.2.15}$$

$$\sigma^2 = \frac{1}{N-1}\sum_{i=1}^{N}(dist_i - \mu)^2 \tag{11.2.16}$$

11.3. Dose Reconstrution with Deconvolution Approach

Since the PET signal is predicted using the forward filtering on basis of the dose distribution, the dose distribution could be reconstructed using an inverse filter f^{-1}. It is not possible to represent such an inverse filter analytically and thus the dose $D(z)$ is reconstructed by deconvolving the PET signal $P(z)$ using the filter function f (Ψ describing a suitable deconvolution method in 1D):

$$D(z) = P(z) * f^{-1}(z) \approx \Psi(P(z), f(z)) \tag{11.3.1}$$

The deconvolution of the PET signal is called "dose deconvolution" in the following and the reconstruction of the distal fall-off region is the primary aim. In proton therapy, the tumor should be irradiated while the surrounding tissue should be spared as much as possible. Therefore, the distal fall-off region is crucial for treatment verification due to the shape of a Bragg peak and a SOBP. In general, deconvolution is an ill-posed inverse problem which is not trivial to solve. In the following, the methods which are used to deconvolve the PET signals are described in detail.

11.4. Dose Deconvolution in Homogeneous Tissue

In this section, the proposed dose reconstruction in case of homogeneous tissue is discussed and according results are shown. In order to keep things simple, just one filter function given by the ^{11}C activity is used here. At first, a MC simulated Bragg curve and its corresponding PET signal is used to test the dose deconvolution. Then, a SOBP is used with both a MC simulated PET signal and a real measured PET signal. The delay between irradiation and PET measurement is hereby considered long enough that only the ^{11}C positron emitter signal is of importance and other positron emitters can be neglected. The dose and PET signals for the Bragg curve and the SOBP are shown in figure 11.12 on basis of a sampling distance of $1mm$.

The PSF of the PET scanner is neglected for the Bragg curve, i.e. the MC PET signal does not contain an additional PSF. The forward filtering is quite simple in this case since it consists of one single step:

- Convolve dose distribution with filter function.

The dose deconvolution consists of one step as well but the deconvolution is a difficult problem as discussed before:

- Deconvolve PET signal with filter function.

The PSF included in real PET images is considered in the MC simulated PET signal for the SOBP since the according measured image is influenced by a PSF as well. Therefore, the forward filtering has to be modified and a convolution with the PSF has to be added in order to be comparable to the measured and the MC simulated PET signal. The forward filtering is thus given by:

- Convolve dose distribution with filter function.
- Convolve forward filtering result with PSF.

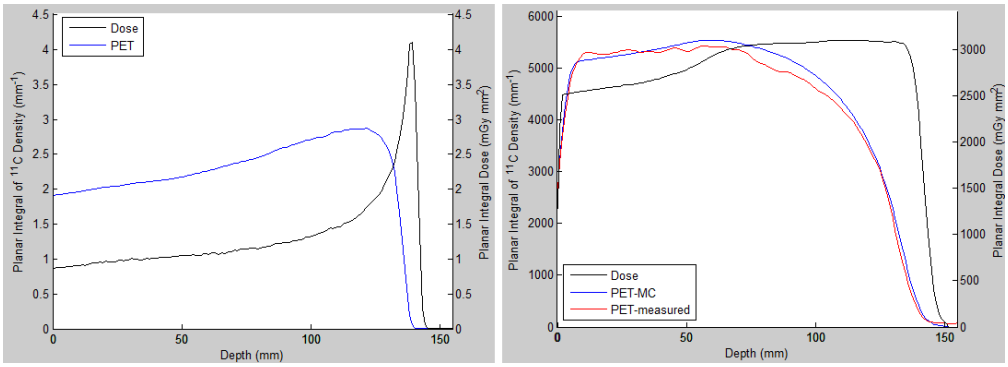

Fig. 11.12.: Left: Bragg peak and PET signal. Right: SOBP, MC PET signal and measured PET signal.

In case of homogeneous phantoms when a single proton beam line in the middle of the delivered dose is used, the PSF convolution can be modeled by a 1D convolution with a 1D Gaussian filter mask. This simplification cannot be used in case of real PET signals since the geometry of the irradiation dose and the composition of the irradiated material respectively tissue cannot be assumed to be the same in each beam direction. The PET estimation using the convolution approach has to be modified by adding a second convolution with the PSF [115] which has to be reversed in the dose deconvolution as well. It would be possible to deconvolve the PET signal with the PSF in a first step and then perform the actual dose deconvolution with the filter function using the result of the PSF deconvolution. Fortunately, convolutions are associative, i.e. $(D * f) * PSF = D * (f * PSF)$ and the dose reconstruction using the PET signal is performed in one step with a modified filter function $f_{PSF} = f * PSF$ in a single deconvolution. The modified filter function f_{PSF} is a smoothed version to the original PSF.

- Deconvolve PET signal with modified filter function f_{PSF}.

The forward filtering results using the filter function for the ^{11}C positron emitter have already be shown in figure 11.9 for both the Bragg peak and the SOBP. The PET signals obtained by the forward filtering are in good accordance with the MC PET signals. Several dose deconvolution results for the Bragg peak are shown in figure 11.13 and figure 11.14. A long delay between irradiation and imaging is assumed and thus just one filter function given by the ^{11}C activity is used. At first, the dose deconvolution method is tested with a MC simulated Bragg curve and its corresponding PET signal. The 1D deconvolution is performed using the MC simulated PET signal which contains several small variations. If no regularization is applied these small variations are amplified resulting in a degraded signal containing large oscillations (Figure 11.13). This result clearly shows the challenge when solving inverse problems and in this case, the used

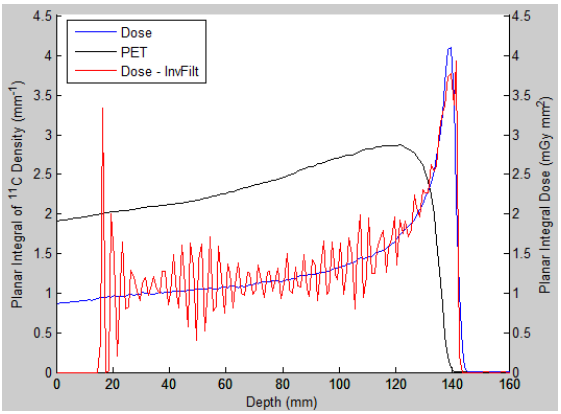

Fig. 11.13.: Bragg curve: Dose deconvolution without regularization.

signal was merely degraded by small variations. A noise signal in a real PET measurement can be considerably stronger. The other results are obtained by using TM (Left image in figure 11.14) and TV (Right image in figure 11.14) regularization and the regularization parameter λ was set to 0.19 for the TM and 0.7 for the TV regularization being the results of brute force searches. The TM regularization seems to be better suited for the given dose distribution since the distal fall-off region is reconstructed well and the peak of the Bragg curve is better shaped than in the reconstruction result with the TV regularization. The TV regularization forms a plateau instead of a peak and the distal fall-off region is reconstructed as a sharp edge instead of a continuous decrease of the signal values. As mentioned before, the TV regularization is meant to reconstruct sharp edges and shows a stair-casing effect in case of a continuously increased signal values. These properties obviously do not match the properties of the Bragg curve and the TM regularization seems to be better suited to reconstruct the peak and the distal fall-off region of the Bragg curve. The known behaviour of the TM regularization to smooth edges allows a better reconstruction of the dose distribution than the TV regularization.

The results of the SOBP dose reconstruction based on the MC simulated PET signal are shown in figure 11.15. The reconstructed dose distribution which is obtained without considering the PSF can be seen in the left image and the result using the modified filter function containing the PSF is displayed in the right image. It is obvious that considering the PSF leads to a better reconstruction of the distal fall-off region. The result without considering the PSF shows a smoothed distal fall-off edge still containing the smoothing of the PSF convolution. Since the MC simulated PET signals are hardly degraded by small variations in this case, a quite small value for the regularization parameter λ can be used and a brute force search leads to 0.01. The estimated distance between the distal fall-off region of the treatment planning dose and the reconstructed dose is $0.01mm$ using the proposed edge detection method.

Figure 11.16 shows the reconstruction result based on the measured PET signal in-

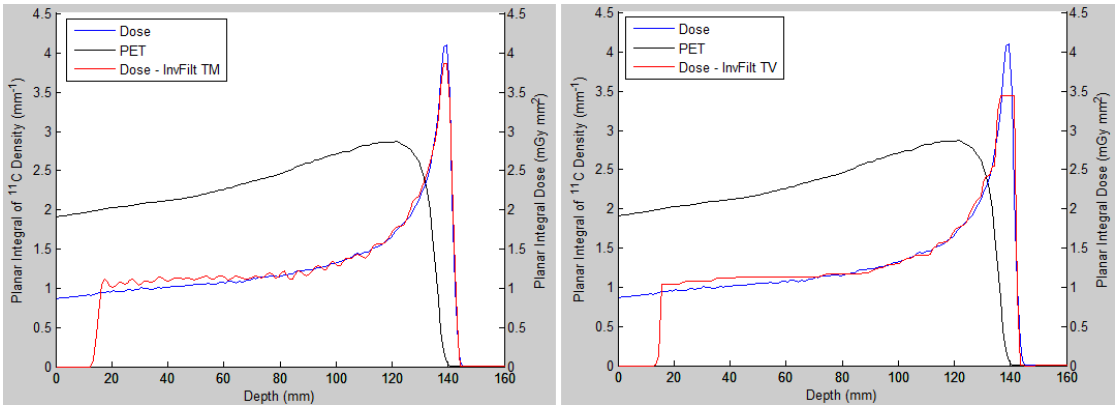

Fig. 11.14.: Bragg curve: Dose deconvolution using TM (Left) and TV (Right) regularization.

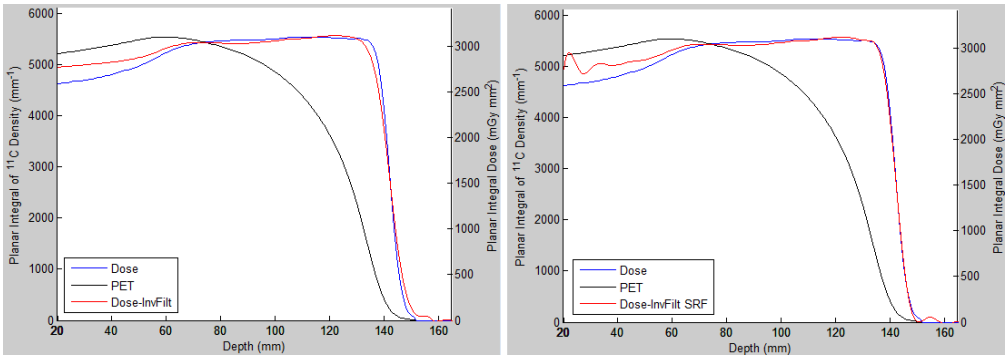

Fig. 11.15.: Dose deconvolution results SOBP based on MC PET signal: without PSF (Left) and with PSF (Right).

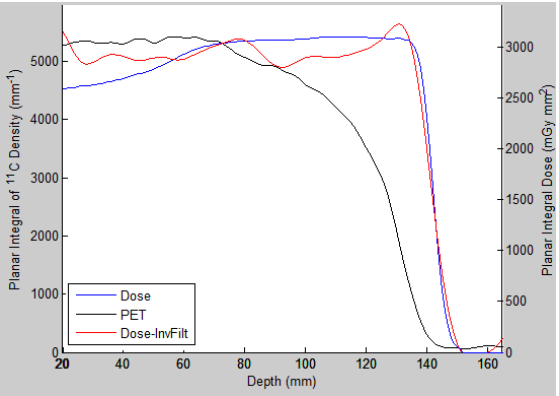

Fig. 11.16.: Dose deconvolution results for SOBP based on measured PET signal.

duced by an irradiation of a PMMA cylinder phantom with a dose of 8 Gy. Due to the noise and artifacts in the measured signal, a higher value for the regularization parameter λ has to be used and 1 is used in this case. The plateau of the SOBP is not completely reconstructed and the distance between the distal fall-off region of the reconstructed dose and the treatment planning dose is 0.6 mm.

If there are artifacts in a measured PET signal it is not possible to avoid artifacts in the dose reconstruction result. Suitable regularization techniques allow a stable reconstruction result and may be able to reduce artifacts to a minimum but a perfect result is not possible. Comparing the MC simulated PET signal with the measured PET signal in figure 11.12 shows that differences in both signals beyond noise can be found. The measured signal contains smaller values than the MC simulated signal in regions influencing the reconstruction of the plateau of the SOBP. However, the reconstruction of the distal fall-off region seems to be quite accurate and this reconstruction of the dose distribution based on a measured PET signal is thus considered as useful for range verification.

11.5. Dose Reconstruction in Inhomogeneous Tissue

In [115], the authors generalized the filter framework for the forward filtering to inhomogeneous media and this formalism is used for the dose deconvolution approach as well. There are several different aspects which have to be considered in order to generalize the filter framework. First of all, a CT image of the target material is required which is usually available because the treatment planning is based on a CT image as well. In order to use the already given filter function on inhomogeneous media, a range-conversion is necessary and then local factors have to be applied to determine the created amount of positron emitters depending on the irradiated material. In addition, the irradiation

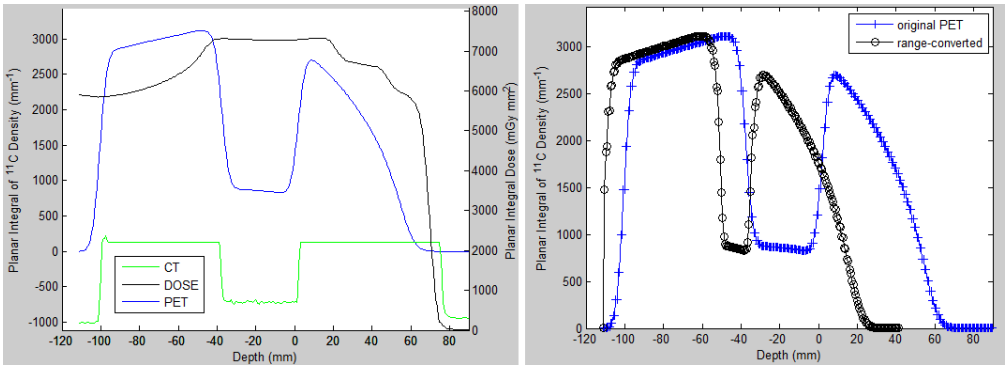

Fig. 11.17.: Example for phantom: base signals (Left) and range-conversion (Right).

time and the delay time between irradiation and PET imaging have to be considered. Last but not least, the PSF convolution included in the measured PET images has to be incorporated properly.

11.5.1. Range-conversion

The filter functions are only valid for a homogeneous reference media and it is really complicated to modify a filter function to be valid for inhomogeneous media. It would be necessary to have different locally adapted filter functions for each positron emitter dependent on the underlying media. Thus, a large amount of filter functions would be needed and the calculations for just the forward filtering would be extensive. In [115], another method is proposed which allows the use of the already given filter function on inhomogeneous media. Proton beams with the same energy result in different residual ranges in different media due to the fact that protons are slowed down differently in different materials. The unique filter function is defined for a specific homogeneous material and can be used for another material if the according spatial dose distribution is stretched to an equivalent path length in the reference material. A general range-conversion formalism which can transform a path containing different materials into an equivalent path length in the reference material is given in analogy to the water-equivalent range-conversion formalism well established in particle treatment planning [75]. In this formalism, the path length z is transformed to the water-equivalent path length l_w given by equation 11.5.1 using the electron density ρ_{el} of the traversed material at depth z' in relation to the electron density of water $\rho_{el,w}$. The electron density ρ_{el} of a material can be determined using a mapping table based on CT values which has to known.

$$l_w(z) = \int_0^z \frac{\rho_{el}(z')}{\rho_{el,w}} dz' \tag{11.5.1}$$

For the filtering approach, the range-conversion has to be based on the reference material which was used to calculate the filter function. This leads to a local path length operator F containing the electron density $\rho_{el,ref}$ of the reference material.

$$F : z \rightarrow z^* = \int_0^z \frac{\rho_{el}(z')}{\rho_{el,ref}} dz' \tag{11.5.2}$$

Since all signals are given in a discrete form with a specific sampling distance, a discrete version of F is used. Hereby, n denotes the index of the investigated sampling point:

$$F : z(n) \rightarrow z^*(n) = \sum_{i=1}^{n} \frac{\rho_{el}(z(i))}{\rho_{el,ref}} \tag{11.5.3}$$

A second path length operator F^{-1} is required to reverse the range-conversion. Both path length operators are realized by resampling the given signal on basis of irregular grids containing modified distances according to the range-conversion. The dose distribution D^* which can be filtered in the depth equivalent space z^* is calculated using F and denoted as $F(D)$ in the following. In addition, the filtered PET signal P^* is then back transformed to the original range system using F^{-1} and is described by $F^{-1}(P^*)$.

$$D^*(z^*) = D^*(F(z)) = D(z) \tag{11.5.4}$$

$$P(z) = P(F^{-1}(z^*)) = P^*(z^*) \tag{11.5.5}$$

A simple example of a range-conversion is shown in figure 11.17 using the PET signal of a phantom. The phantom consists of PMMA and lung equivalent material and the required CT signal is given. The electron density values needed for the range-conversion are given indirectly by the CT values. As it can be seen, the range inside the PMMA material is not converted since the filter function is defined on basis of that material. The electron density value of the lung equivalent material is lower than in the PMMA material resulting in a compression for the according area. The original range from $-111mm$ to $89mm$ is converted to a range from $-111mm$ to $41mm$ with the start point at $-111mm$ serving as fixed point in both range systems.

11.5.2. Tissue Dependent Factors

Besides the range-conversion, local factors have to be used to weight the PET signals in dependence of the underlying tissue composition. Therefore, several properties of the material which are all based on CT values are required. In addition to the electron density which was already used for the range modulation, the mass density of the irradiated material and a weighting based on the target nuclei involved in the according

HU	El. density	w_{12_C}	w_{16_O}		HU	el. density	w_{12_C}	w_{16_O}
< -950	0.0242	0	0.232		< 500	1.2395	0.361	0.38
< -120	0.476	0.105	0.749		< 600	1.2901	0.335	0.387
< -83	0.9286	0.681	0.198		< 700	1.3401	0.31	0.394
< -53	0.9577	0.567	0.308		< 800	1.3909	0.287	0.4
< -23	0.982	0.458	0.411		< 900	1.4403	0.265	0.405
< 7	1.0069	0.356	0.509		< 1000	1.4905	0.246	0.411
< 18	1.0229	0.284	0.578		< 1100	1.5418	0.227	0.416
< 80	1.0503	0.134	0.723		< 1200	1.5913	0.21	0.42
< 120	1.1004	0.207	0.622		< 1300	1.6424	0.194	0.425
< 200	1.0932	0.455	0.355		< 1400	1.6927	0.179	0.429
< 300	1.1391	0.423	0.363		< 1500	1.7427	0.165	0.432
< 400	1.1891	0.391	0.372		> 1500	1.7941	0.155	0.435

Table 11.1.: Electron densities and weights of involved target nuclei ^{12}C and ^{15}O

HU	Mass density
< -98	0.00121+(0.93-0.00121)/(-98+1000)*(hu+1000))
<= 14	1.018+0.893e-3*hu
< 23	1.03
<= 100	1.003+0.001.169*hu)
< 2000	1.017+0.000592*hu)
< 3060	2.2010 +(2.550-2.020)/(3060-2000)*(hu-2000)
>= 3060	4.5

Table 11.2.: Mass densities

reaction channels are needed. The mapping of the CT values to the electron density and to the weights based on the ^{12}C respectively ^{16}O reaction channels is shown in table 11.1 while the mapping to the mass density can be found in table 11.2.

All weighting coefficients and density values based on the CT values are illustrated in figure 11.18. The tissue dependent local factor g_{tissue} which is then used to weight the PET signals is given by:

$$g_{tissue} = \left[\frac{w_i(z)\rho(z)}{w_{i,ref}\rho_{ref}}\right]\left[\frac{\rho(z)}{\rho_{ref}}\frac{\rho_{el}(z)}{\rho_{el,ref}}\right] \tag{11.5.6}$$

In this equation, $w_i(z)/w_{i,ref}$ is the weight of the target nucleus (^{12}C and ^{16}O) involved in the given reaction channel at depth z in relation to the reference material. Additionally, $\rho(z)/\rho_{ref}$ and $\rho_{el}(z)/\rho_{el,ref}$ are the mass density and the electron density of the material at depth z relative to the reference material. In the forward filtering

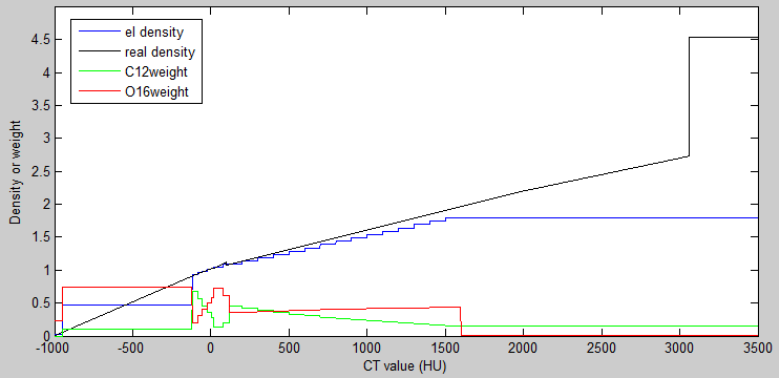

Fig. 11.18.: Weighting coefficients and densities based on CT.

formalism for inhomogeneous media, the predicted PET signal given by a convolution of the dose distribution with the filter function has to be weighted with factor g_{tissue} to consider the properties of the irradiated materials.

11.5.3. Time Dependent Factors

In addition to the tissue dependent weighting factor, a second weighting factor g_{time} considering the irradiation time t_{irr} and the delay time between irradiation and the image acquisition t_{del} is required. In order to calculate the factor g_{time}, the decay constant λ of the produced positron emitter is used. The predicted PET signal using the forward filtering has to be weighted with this time dependent factor as well.

$$g_{time} = \frac{1 - e^{-\lambda_i t_{irr}}}{t_{irr}} e^{-\lambda_i t_{del}} \tag{11.5.7}$$

11.5.4. Sampling Distances and Alignment of Images

The dose deconvolution approach will be tested on real measured phantom and patient data in the following section. In order to allow extensive investigations about the potential of the proposed methods, MC simulated PET signals are used as well leading to a large amount of different data sets including a CT image, a treatment planning dose and the measured PET signals as well. All of these different data sets have to be aligned and sampled using the same grid structure and sampling distance which should be as small as possible. Unfortunately, the data sets are usually given on shifted grid structures with different sampling distances. Before the data sets can be processed using the filtering framework, all data sets have to be aligned and resampled on the same grid structure. It is recommendable to use B-spline interpolators for this task in order to keep interpola-

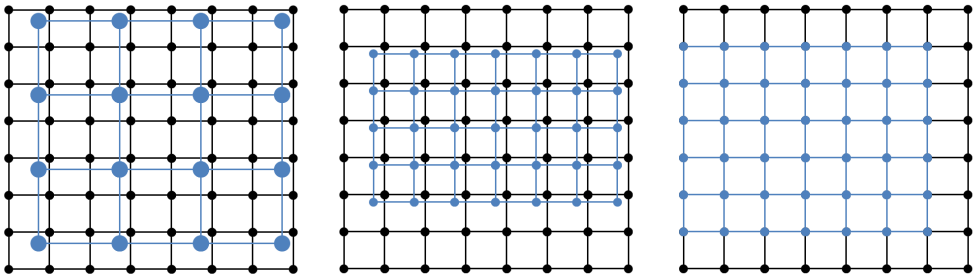

Fig. 11.19.: Different possible sampling grids in Reference to a basic isotropic grid.

tion errors as small as possible. An example of different possible grid structures with an underlying target grid structure is illustrated in figure 11.19.

Furthermore, it is possible that the direction of the proton beam is not conform to a direction of one of the dimensions of the grid structure. In such a case it is also necessary to rotate the data sets because the filter function can only be applied along the direction of the proton beam. Last but not least, it is sometimes helpful to focus on a region of interest and avoid processing the whole data set in order to limit the computational effort.

11.5.5. Dose Deconvolution Approach

In summary, the generalized approach for the forward filtering in inhomogeneous media is given by a course of tasks starting with the 1D convolution of each proton dose beam line with the filter mask enclosed by the range-conversion to cope with the inhomogeneous media. Afterwards, the local factors are applied and the 3D convolution with the PSF completes the result. The complete forward filtering approach is described by:

- Range conversion: $D_1^*(z^*) = F(D(z))$.
- 1D convolution with filter function: $P_2^*(z^*) = D_1^*(z^*) * f$.
- Inverse range conversion: $P_3(z) = F^{-1}(P_2^*(z^*))$.
- Apply local factors: $P_4(z) = P_3(z) \cdot g_{time} \cdot g_{tissue}$.
- 3D convolution with PSF: $P = P_4(z) * PSF$.

A closed form of the forward filtering approach is given by:

$$P = \left(g_{time} \cdot g_{tissue} \cdot F^{-1}\left(F(D) * f\right)\right) * PSF \tag{11.5.8}$$

A corresponding dose deconvolution approach has to reverse all necessary steps of the forward filtering in the correct order. Two deconvolutions are necessary since the filter function has to be applied on a range-converted signal while the original grid structure has to be used for the PSF. First, the PSF deconvolution has to be performed and since the PET signal suffers from Poisson noise, a RL similarity functional is used in this case. Furthermore, the PSF deconvolution result requires sharp edges since the local factors are removed afterwards and smooth edges would create large artifacts in areas where different tissues are next to each other. In order to provide sharp edges, TV regularization is used in the PSF deconvolution. Since the local factors can be zero at some points and thus the required reciprocal value is not defined, a minimum value minLF $>$ 0 is introduced and all values of the local factors below minLF are set to the minimum value. It is essential to consider the PSF in the dose deconvolution approach but it is not possible to obtain perfect results using a deconvolution with the PSF especially in case of a noisy signal. Not considering the PSF leads to large artifacts when removing the local factors g_{time} and g_{tissue} at locations with a large gradient in the CT image. Similar artifacts are found as well when the PSF is considered due to the limited possibilities of the deconvolution but the remaining artifacts are much smaller. In order to improve the signals after removing the local factors, a local smoothing which is dependent on the gradient of the underlying CT image is used. Thus, the signal is smoothed in locations where the described artifacts are possible and not altered elsewhere. The smoothing is performed using the median value of a certain amount of neighbour values whereat the CT gradient determines the amount of neighbour values. The median is known to be more robust than the mean value and is therefore used here. After smoothing the signal, the deconvolution with the filter function is performed using a LS similarity functional and a TM regularization which is better suited for the dose distribution as discussed before. In addition, the deconvolution with the filter functions is enclosed by the range-conversion. The complete dose deconvolution approach for inhomogeneous media is described by (With Ψ describing suitable deconvolutions):

- 3D deconvolution with PSF (RL and TV): $P_1(z) = \Psi(P(z), PSF)$.
- Reverse local factors: $P_2(z) = P_1(z)/(g_{time} \cdot g_{tissue})$.
- CT gradient dependent local smoothing: $P_3 = smooth(P_2)$.
- Range modulation: $P_4^*(z^*) = F(P_3(z))$.
- 1D deconvolution with filter function (LS with TM): $D_5^*(z^*) = \Psi(P_4^*(z^*), f)$.
- Inverse range modulation: $D(z) = F^{-1}(D_5^*(z^*))$.

A closed form of the dose deconvolution approach is given by:

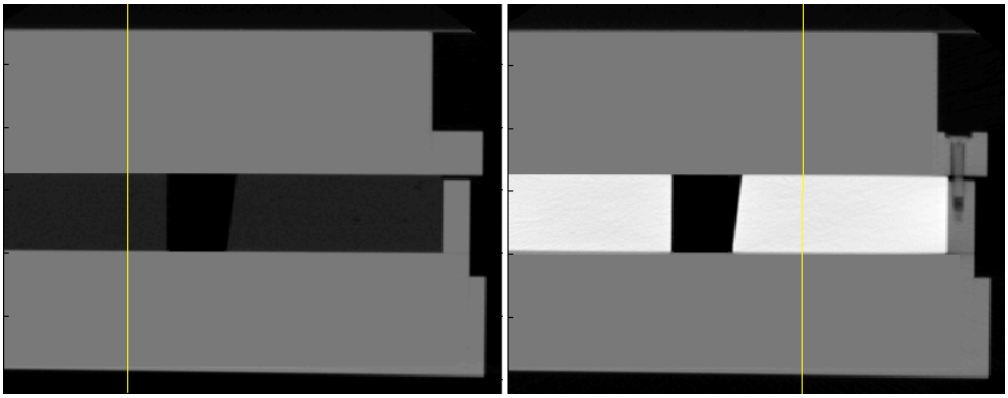

Fig. 11.20.: Phantom slices with lung (Left) and bone (Right) equivalent material.

$$D = F^{-1}\left(\Psi\left(F\left(smooth\left(\frac{\Psi(P, PSF)}{g_{time} \cdot g_{tissue}}\right)\right), f\right)\right) \tag{11.5.9}$$

11.6. Dose Deconvolution Results in Inhomogeneous Tissue

The dose deconvolution approach for inhomogeneous tissue is applied to phantom and patient data in this section. The phantom contains four different materials: PMMA, lung equivalent material, bone equivalent material and air. The phantom was irradiated with a total dose of 8 Gy and the delay between irradiation and PET imaging is approximately 14 min allowing the use of the ^{11}C filter function only. Two slices of a CT image of the phantom are shown in figure 11.20 with one containing lung equivalent material and the other bone equivalent material. At first, the dose deconvolution approach is applied to 1D profiles of the phantom shown as yellow lines in the figure. Hereby, several simulations using the forward filtering results as basis are performed before the measured PET signal is used to reconstruct the delivered dose. Subsequent, the measured phantom data is processed in 2D using the two shown slices. At last, a measured patient PET signal of a head and neck patient is used to reconstruct the delivered dose.

11.6.1. 1D Phantom Profiles

The available signals for the 1D phantom profiles can be seen in figure 11.21. The first profile consists of PMMA and lung equivalent material with surrounding air while the second profile contains bone equivalent instead of the lung equivalent material. The forward filtering results of both profiles using the treatment planning dose are shown in

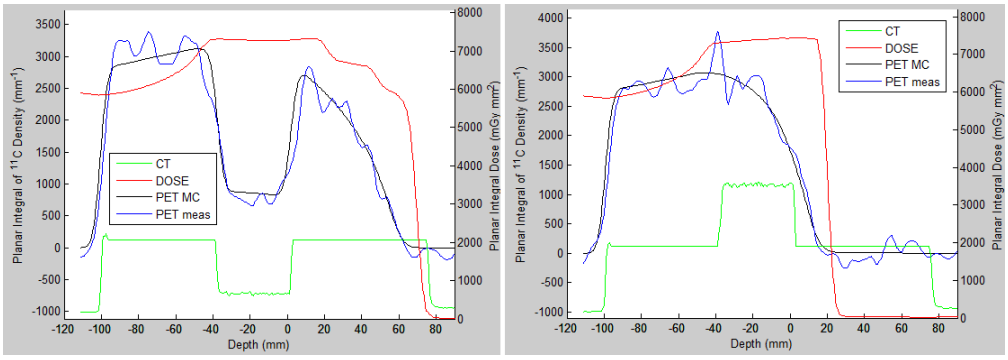

Fig. 11.21.: Phantom profiles with lung (Left) and bone (Right) equivalent material.

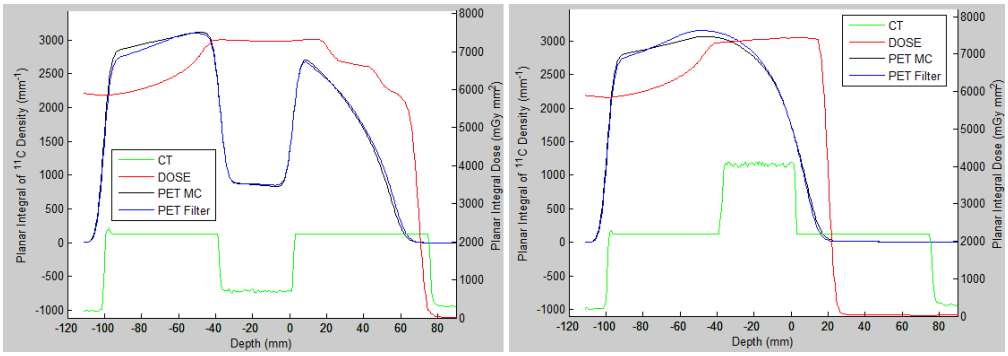

Fig. 11.22.: Forward filtering results for phantom profiles with lung (Left) and bone (Right) equivalent material.

figure 11.22. The filtering results are displayed with the MC simulated PET signals and it seems that both are in good agreement. A PSF with $FWHM = 7mm$ was used to account for the system response of the PET imaging system.

Figure 11.23 shows intermediate results of the dose deconvolution process for the first profile containing lung equivalent material. Removing the local factors (LF) without considering the PSF leads to large artifacts (Upper row, left image) and the additional PSF deconvolution is thus necessary to reverse the PET estimation. The deconvolution result after removing the PSF contains sharp edges necessary to reverse the LF (Upper row, right image). However, after removing the LF, similar but much smaller artifacts are found as well due to the limited possibilities of the deconvolution (Lower row, left image). The gradient dependent smoothing based on the CT image is able to remove those small artifacts without influencing the signal in general (Lower row, right image).

The locally smoothed signal is used for the actual dose reconstruction in the last step. Hereby, the range modulation is used to perform a range conversion to a reference material-equivalent range which is necessary for the filter function. The final results of the dose deconvolution for both profiles can be seen in figure 11.24. Since there is no

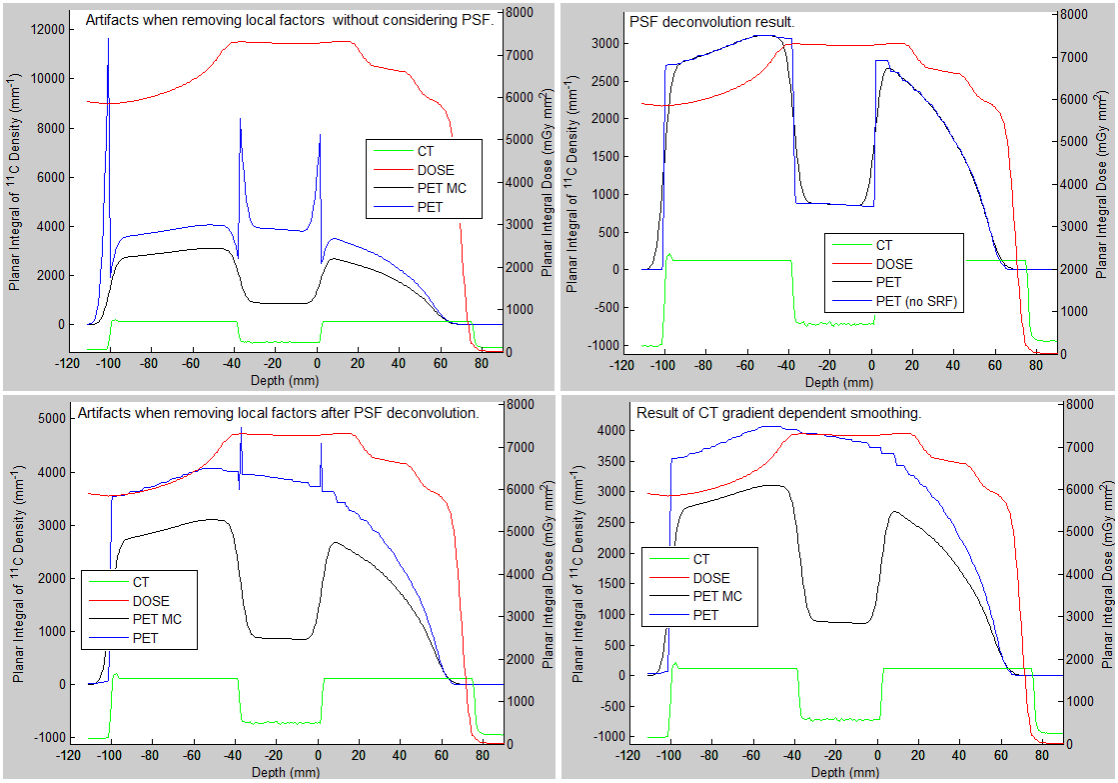

Fig. 11.23.: Intermediate dose deconvolution results: Remove LF without considering PSF, remove PSF, gradient dependent smoothing and remove LF afterwards.

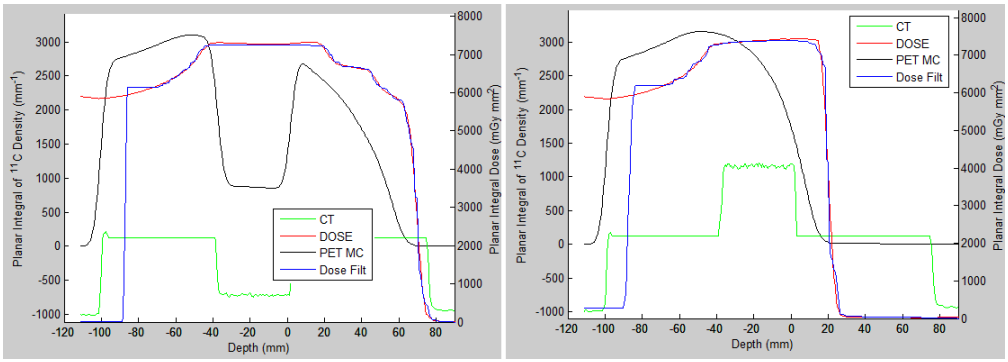

Fig. 11.24.: Dose deconvolution results for phantom profiles with lung (Left) and bone (Right) equivalent material.

noise in the PET signals and the signals are quite smooth, the necessity for regularization is quite weak and thus a small value for λ can be used. The reconstruction results are very satisfying in this case because they are almost identical to the treatment planning dose.

In order to simulate a more realistic PET signal and to test the robustness of the proposed method, Poisson noise is added to both PET signals and the dose deconvolution is repeated in the same way. The signal to noise ratio (SNR) for the first profile is $19.1dB$ in the first test case and $15.7dB$ in the second test case while the corresponding SNRs are $19.1dB$ and $15.2dB$ for the second profile. These test cases are called Noise1 and Noise2. The results of the dose deconvolution and the noise degraded PET signals are shown in figure 11.25 for the first profile and in figure 11.26 for the second profile. Due to the noise in the signals and in order to suppress noise amplification, suitable values for λ weighting the regularization term are required. Since the underlying PET signal was created using the given treatment planning dose, the latter can be used to evaluate the reconstruction result directly and thus allowing a brute force search to determine the weighting parameters. The deconvolution of the PSF is performed using a TV regularization with $\lambda \approx 20$ in the first case and $\lambda \approx 100$ in the second case handling the stronger noise signal. The second deconvolution which is based on the regularized and thus denoised result of the previous deconvolution does not require an equal strong TM regularization and therefore $\lambda \approx 10$ is sufficient in the first case and $\lambda \approx 30$ in the second case.

The simulated PET signals which are degraded by Poisson noise are not similar to the measured PET signals given for these profiles (See figure 11.21). The noise in the measured PET signals seems to be stronger and smoothed at the same time. As mentioned before, the PSF originates in the PET imaging process and the reconstruction algorithm which is necessary to convert the acquired data in a useable image. In addition, there is Gaussian noise in the images besides Poisson noise. The delay time between irradi-

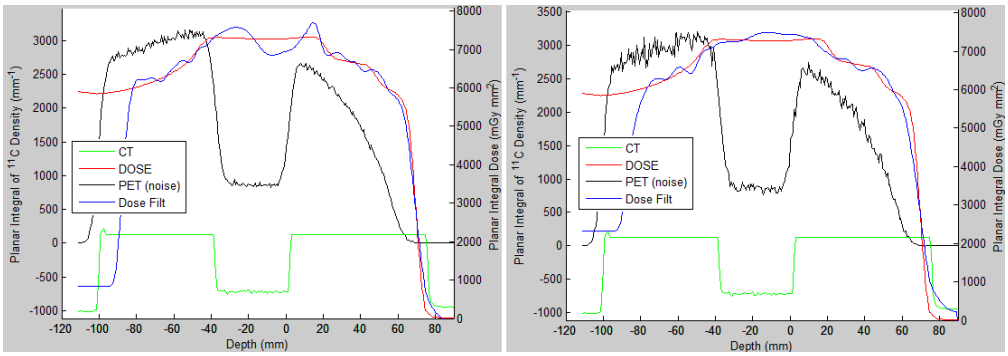

Fig. 11.25.: Dose deconvolution simulation for phantom profiles with lung equivalent material and Poisson noise.

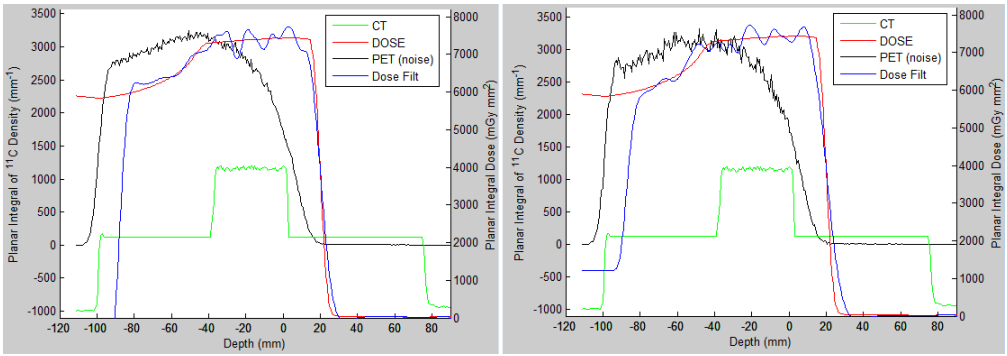

Fig. 11.26.: Dose deconvolution simulation for phantom profiles with bone equivalent material and Poisson noise.

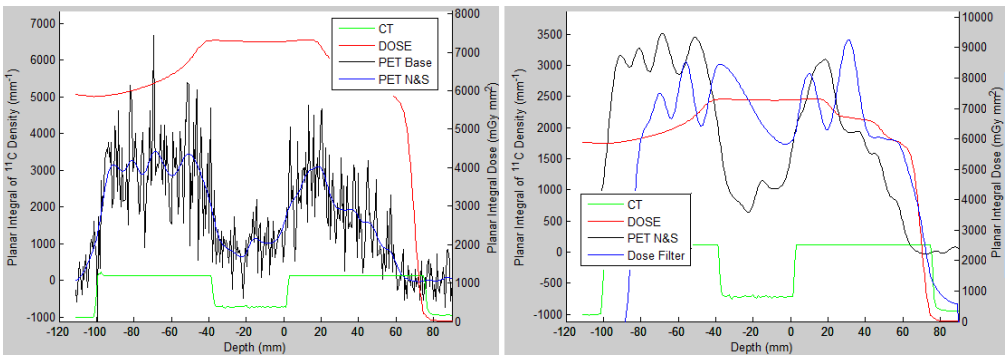

Fig. 11.27.: Dose deconvolution simulation for phantom profile 1 with advanced noise model.

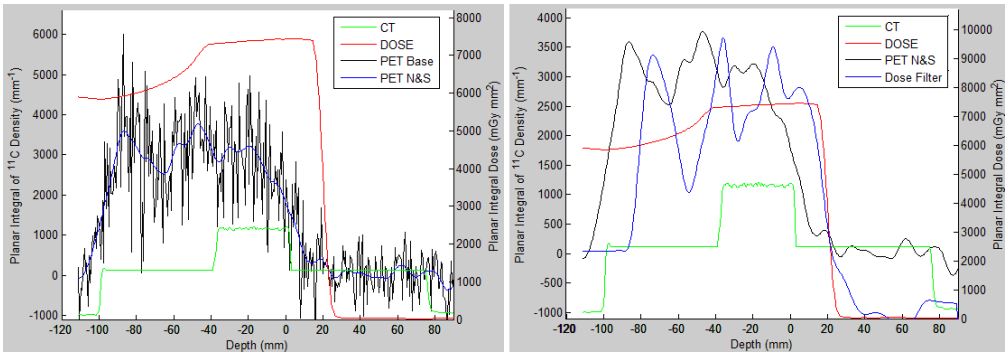

Fig. 11.28.: Dose deconvolution simulation for phantom profile 2 with advanced noise model.

ation and PET imaging was quite long resulting in a strongly degraded image. It can be assumed that a decreased delay time using in-room PET scanner leads to improved images comparable to the already simulated signals. In case of longer delay times another simulation approach including Gaussian noise and a Gaussian smoothing with the PSF after adding the noise signal is required. Such simulated PET signals can be seen for the first profile in figure 11.27 on the left side and for the second profile in figure 11.28. The base PET signal denotes the PET signal degraded by both the Gaussian and the Poisson noise signal while the final signal is obtained by smoothing the base signal using the PSF. This test case is called Noise&Smooth. The SNR for the Gaussian noise is $5.6dB$ and $5.0dB$ for the Poisson noise. Both figures also show the reconstruction results on the right side. A strong regularization is required in order to cope with the strong degradations in the simulated PET signals used for the deconvolutions. λ is therefore set to 500 for the TV regularization in the first deconvolution and to 50 for the TM regularization in the second deconvolution.

The simulated degradations based on the Gaussian and the Poisson noise in combination with the smoothing seems to be quite similar to the degradation which can be found in the measured PET signals. Therefore, the same λ values to weight the regularization are used to reconstruct the dose distribution using the measured PET signals. The reconstruction results of the measured PET signals are shown in figure 11.29 for both profiles.

In order to evaluate the dose reconstruction, the edge of the distal fall-off region for the treatment planning dose and the reconstructed dose is determined using the gradient based approach. The distance of both points can give an impression how accurate the dose reconstruction algorithm is working in case of the simulations using the forward filtering result. In addition, the robustness of the method is evaluated using additional degradations with noise or even smoothing. At last, the delivered dose is estimated using the measured PET signal and also compared with the treatment planning dose.

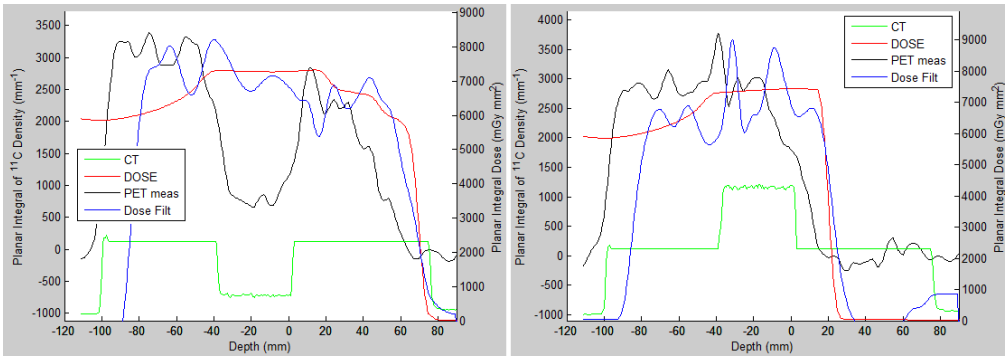

Fig. 11.29.: Dose deconvolution results for phantom profiles using measured PET signals.

	Profile1		Profile2	
		(parabolic)		(parabolic)
Simulated	0.0	0.05	0.0	0.14
Noise1	0.65	0.34	0.0	0.05
Noise2	0.65	0.50	0.65	0.27
Noise&Smooth	0.65	0.82	2.59	2.88
Measured	0.65	0.78	2.59	2.28

Table 11.3.: Distance of distal fall-off reconstructed dose to treatment planning dose (in mm)

Table 11.3 shows the distances for all cases and both profiles using the simple edge detection and the parabolic interpolation approach. The parabolic interpolation shows a more accurate evaluation since it is not connected to the sampling distance of 0.65 mm. The distance of the distal fall-off region between the treatment planning dose and the reconstruction result is very small for the simulation which confirms the good result. With a decreasing strength of degradations, the distance gets larger and the last simulation with the additional Gaussian noise and smoothing has a similar distance as the result for the measured PET signal. The distances for the first profile are all within 1 mm showing the robustness of our approach and the possible quality of the reconstruction results. However, the distance for the Noise&Smooth simulation and the measured PET signal are relatively large for the second profile with values up to almost 3 mm.

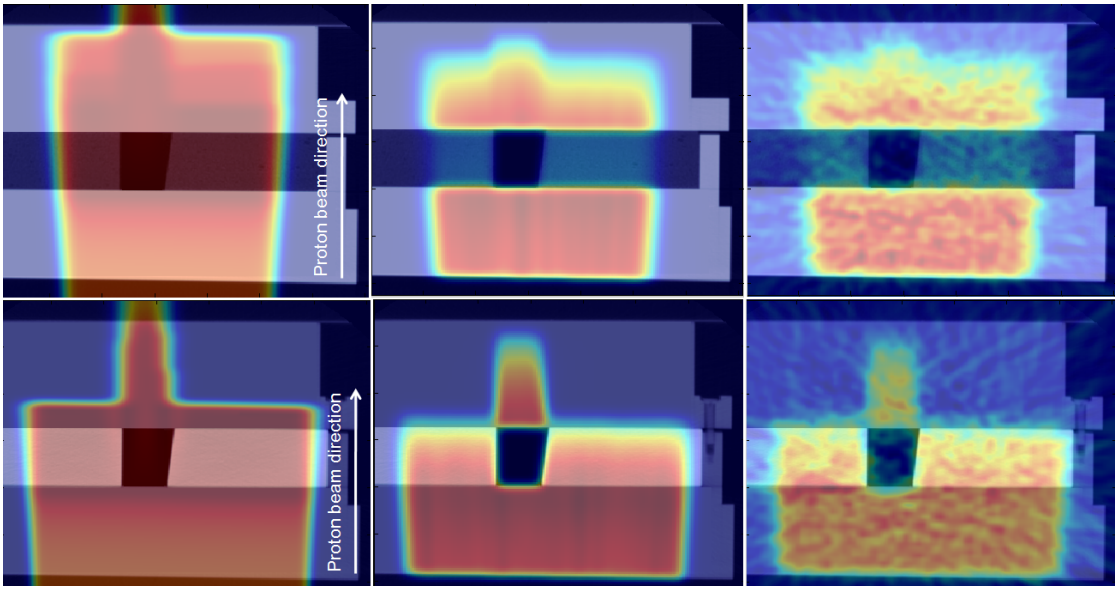

Fig. 11.30.: Given data of phantom slices showing treatment planning dose (Left), MC PET signal (Middle) and measured PET signal (Right). The top row displays the signals of first slice with a superimposed CT image and the bottom row corresponding signals of the second slice.

11.6.2. 2D Phantom Data

Two profiles from two different phantom slices were used to evaluate the dose reconstruction method in 1D in the previous section. Here, the two complete 2D slices of the phantom are used and the given image data including a MC simulation are shown in figure 11.30.

The PSF is removed by a 2D deconvolution in a first step and the actual dose reconstruction is performed along the beam line of the proton irradiation, i.e. line-by-line using a 1D deconvolution. In addition, the range modulation is performed line-by-line as well. However, before the processing of the data can be done, the grid structures of the different signals have to be considered. Since the CT signal and the measured PET signal are given on basis of different grid structures, it is first necessary to define a common grid structure which is denoted as $System$ in the following and resample the signals on this structure. In addition, the treatment planning dose is used to evaluate the reconstruction results and a MC simulated PET signal allows an evaluation of forward filtering results. In total, there are four different grid structures defined by the start and end point of the different regions and the sampling distances in both directions (Table 11.4). The grid structure of the measured PET signal is used as $System$ and all other signals are resampled on this basis using B-Spline interpolations to avoid unnecessary interpolation errors.

	Start X	End X	Sampling X	Start Y	End Y	Sampling Y
CT	-165.564	165.564	0.648	-214.064	117.064	0.648
TP dose	-154.800	139.200	2.000	-111.300	90.700	2.000
MC	-140.292	158.436	0.648	-188.792	109.936	0.648
Measured	-105.300	123.444	0.648	-141.488	117.064	0.648
System	-105.300	123.444	0.648	-111.032	90.496	0.648

Table 11.4.: Range and sampling distances (in mm)

The dose reconstruction results for both phantom slices are shown in figure 11.31 and 11.32. The first figure displays the simulated PET signals and the corresponding dose reconstruction results. The second figure shows the dose reconstruction results on basis of measured PET signals. The dose deconvolution results are shown on the right side. In addition, the underlying PET signals are displayed in the middle and the initial treatment planning dose on the left side. The measured PET signals are corrupted by strong artifacts resulting in artifacts in the reconstruction result which cannot be avoided.

The midpoints of the distal fall-off regions are estimated using the smoothed gradient of the reconstructed dose signal and compared to the treatment planning dose for several beam lines. The proton beam is not stopped within the image domain in case of the PMMA-air-PMMA beam line and the corresponding beam lines are excluded. In addition, the irradiated area in the first phantom slice is smaller resulting in less beam lines. 100 beam lines are used in the evaluation of the first phantom slice and 167 beam lines for the second phantom. The mean values and standard deviations of the calculated distances between the treatment planning dose and the reconstruction results are determined on bases of the given beam lines. Selected profiles of the phantom slices and the distances between the distal fall-off regions of the relevant beam lines are shown in figure 11.33. The distances between the distal fall-off regions can be up to are 8 mm and the estimation is unstable due to the strong artifacts in the reconstructed dose. Table 11.5 shows an overview of the mean values and variances of the calculated distances between the treatment planning dose and the reconstruction results for the measured PET signals and a simulation.

11.6.3. Measured Patient Data

The dose deconvolution method is now used for a real dose reconstruction of a head and neck patient who was irradiated with a dose of approximately 2 Gy. The dose deconvolution approach is simulated in a first step (Figure 11.34 top row) and the forward filtering result based on the treatment planning dose is used as basis for the dose reconstruction. The reconstruction result is satisfying since the conformity to the treatment

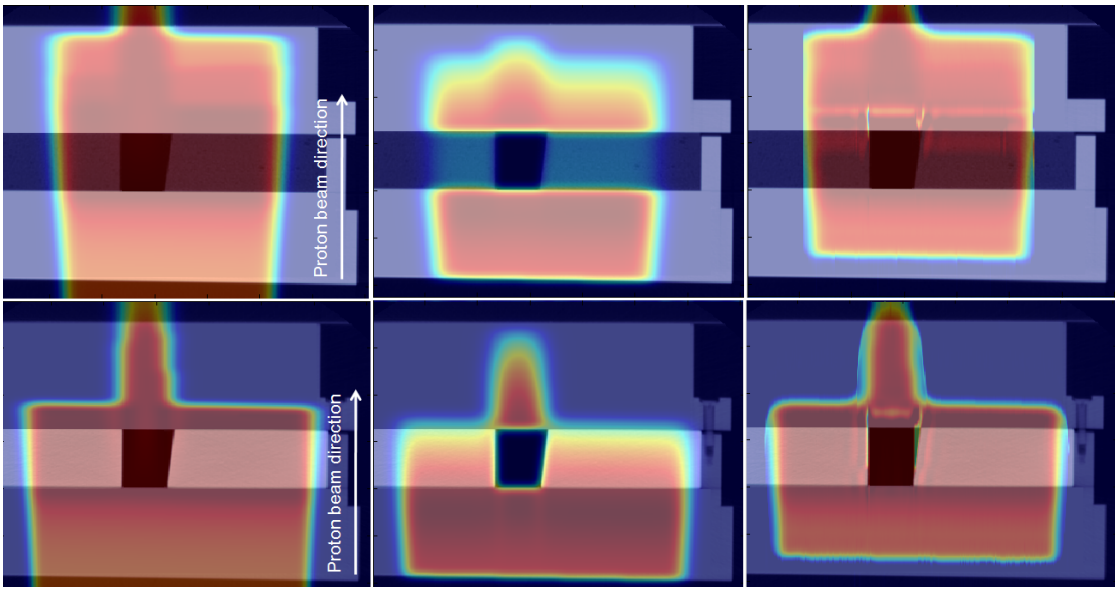

Fig. 11.31.: Processing of phantom slices showing treatment planning dose (Left), simulated PET signal (Middle) and reconstructed dose (Right). The top row displays the signals of first slice with a superimposed CT image and the bottom row corresponding signals of the second slice.

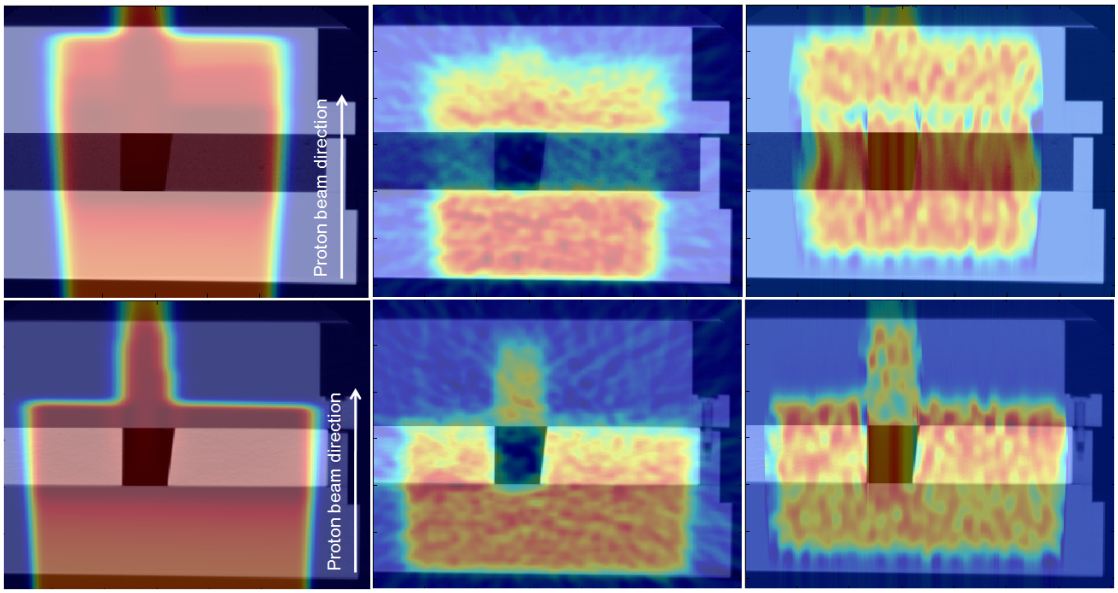

Fig. 11.32.: Processing of phantom slices showing treatment planning dose (Left), measured PET signal (Middle) and reconstructed dose (Right). The top row displays the signals of first slice with a superimposed CT image and the bottom row corresponding signals of the second slice.

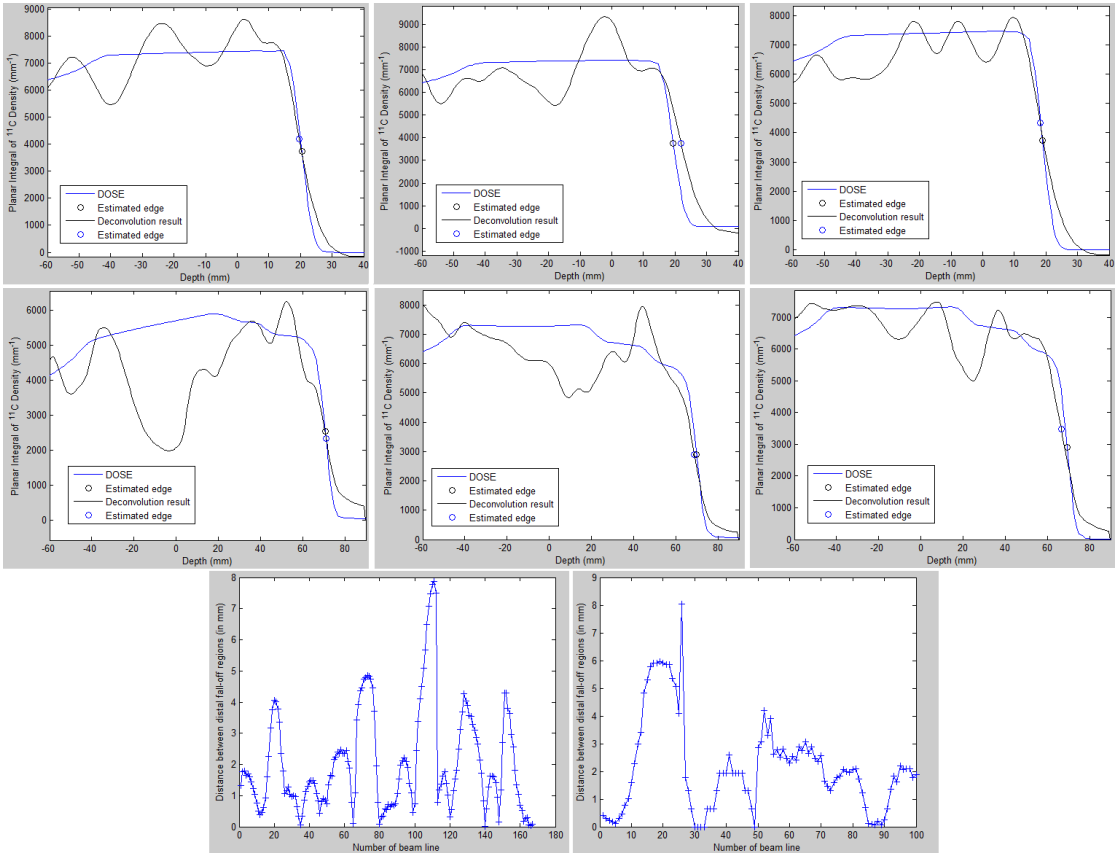

Fig. 11.33.: Details of edge detection method. Top row: Selected profiles of first phantom slice. Middle row: Selected profiles of second phantom slice. Bottom row: Distances between distal fall-off regions of treatment planning dose and reconstructed dose for relevant beam lines.

	Phantom1		Phantom1 (parabolic)		Phantom2		Phantom2 (parabolic)	
	μ	σ^2	μ	σ^2	μ	σ^2	μ	σ^2
Simulated	0.79	0.17	0.70	0.11	0.63	0.07	0.54	0.02
Measured	2.24	3.11	2.15	2.91	2.10	2.71	2.05	2.82
Amount of profiles	100		100		167		167	

Table 11.5.: Distance of distal fall-off reconstructed dose to treatment planning dose (in mm)

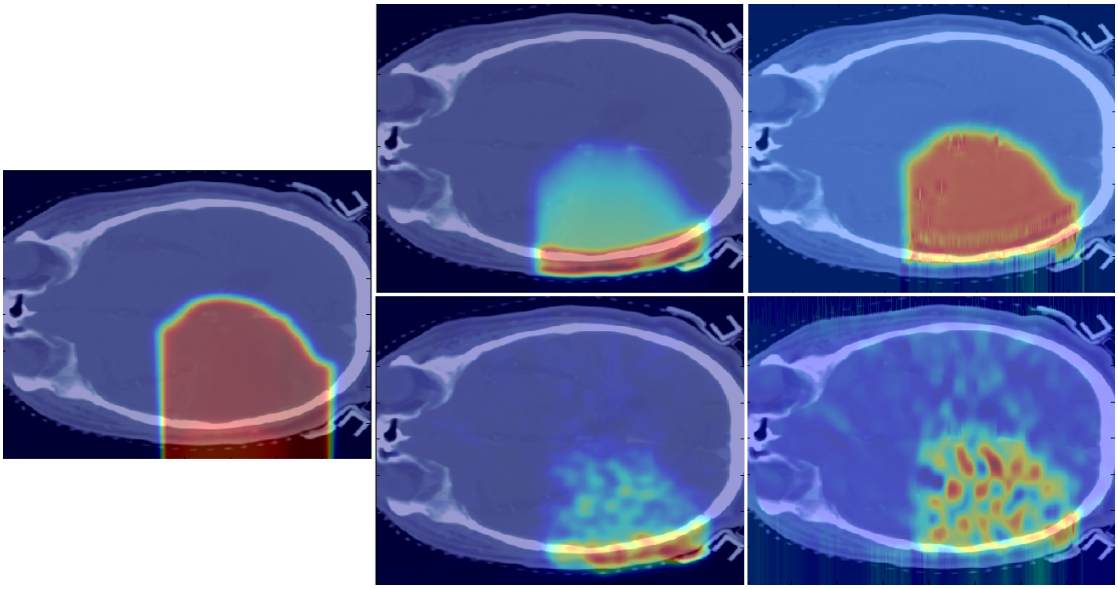

Fig. 11.34.: Dose reconstruction of head and neck patient: the treatment planning dose is displayed on the left side superimposed with the CT image. The top row shows simulation results of the forward and dose deconvolution. The reconstructed dose is hereby based on the forward filtering result. The bottom row shows the measured PET signal and the resulting dose distribution.

planning dose is good. The actually delivered dose is estimated using a measured PET signal (Figure 11.34 bottom row). The delay time between irradiation and PET imaging is relatively long in this case and it can thus be assumed that ^{11}C emitters dominate the measured PET image. Compared to the PET prediction using the forward filtering, the quality of the measured PET signal is poor and contains significant artifacts. The reconstruction result is thus degraded by many artifacts as well and it is not possible to use this result for an accurate dose verification. The original shape of the treatment planning dose is not clearly visible in the reconstruction result and the dose distribution is degraded by artifacts and inaccuracies.

11.7. Dose Reconstruction Combining Different Positron Emitters

In-room PET scanners allow shorter delay times between irradiation and PET imaging and the influence of additional positron emitters with smaller half-life times increases. In the following, a dose deconvolution method which is able to reconstruct a delivered dose distribution on basis of several positron emitters is presented. As mentioned be-

fore, each positron emitter requires a different filter function and different local factors. The local factors are influenced by the half-life time and the concentration of the basic isotopes (^{12}C and ^{16}O) in the activated tissue. The forward filtering approach is used to estimate a PET signal by simply combining the separate filtering results for the different positron emitters [7]:

$$P = \sum_{i=1}^{N} LF_i \cdot F^{-1}(F(D) * f_i) \tag{11.7.1}$$

N denotes the amount of different positron emitters, LF_i the corresponding local factor and f_i the corresponding filter function for the different positron emitters. The convolution of the dose distribution with the filter functions has to be done using the range modulation which is described by F and F^{-1}. The PSF is neglected in this case but has to be considered for measured PET signals as described in the previous section.

The corresponding dose reconstruction is based on the combined PET signal and has to consider all involved positron emitters. In addition, regularization is required to guarantee a stable solution and to cope with noise. The functional J has to be minimized in order to reconstruct the dose distribution:

$$J(D) = \int |P - simPET(D)|^2 + \lambda Reg(D) d\Omega \tag{11.7.2}$$

In this equation, P denotes the given PET signal and simPET represents a simulated PET signal on basis of the estimated dose D containing all positron emitters. In fact, simPET is calculated according to the forward filtering formalism already introduced in equation 11.7.1. Reg denotes a regularization term and the TM regularization is used for that purpose.

The proposed method including different positron emitters is applied to a head and neck patient. The CT image of the patient and a treatment planning dose distribution can be seen in figure 11.35. In addition, the electron density which is necessary for the range modulation and the local factors for the different reaction channels (^{12}C and ^{16}O) are displayed as well. The different filter functions (^{11}C, ^{13}N and ^{15}O) which are used in the filtering approach are displayed in figure 11.36.

MC simulations of the three PET signals are displayed in figure 11.37. The results of the forward filtering approach on basis of the treatment planning for the three positron emitters are shown in figure 11.38. The three different PET signals given by the forward filtering are used to create realistic PET signals containing all positron emitters (^{11}C, ^{13}N and ^{15}O) with proper weighting. An irradiation time of t_{irr}= 30 min is used and three different delay times are considered: t_{del1}= 2 min, t_{del2}= 6 min, t_{del3}= 12 min. The irradiation and delay times lead to time dependent factors g_{time} shown in table 11.6. The resulting combined PET signals for the different delay times are shown in figure 11.39. Last but not least, the reconstruction results of the combined PET signals are

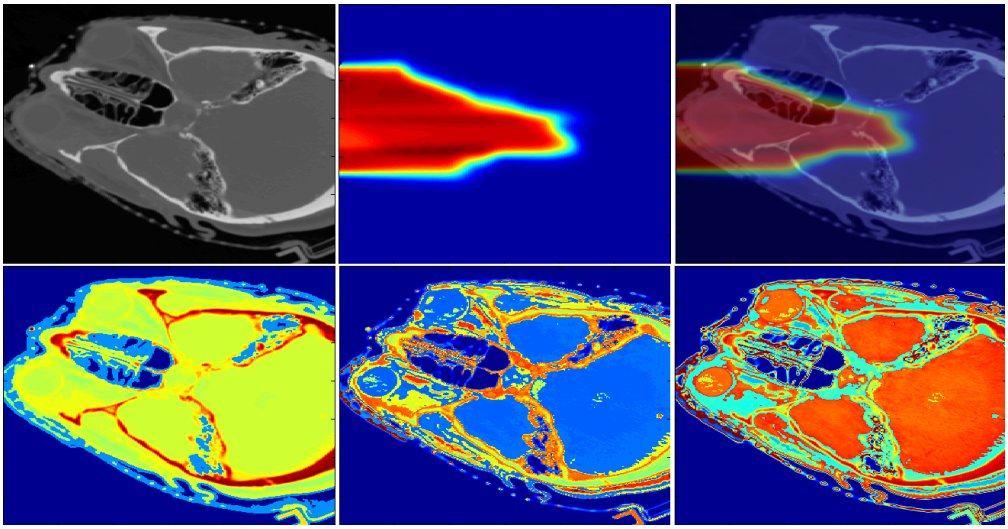

Fig. 11.35.: CT and treatment planning dose for patient (Upper row). Electron density and local factors for ^{12}C and ^{16}O (Lower row).

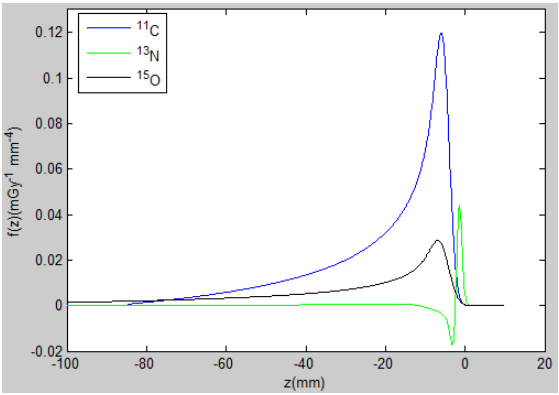

Fig. 11.36.: Filter functions (^{11}C, ^{13}N and ^{15}O).

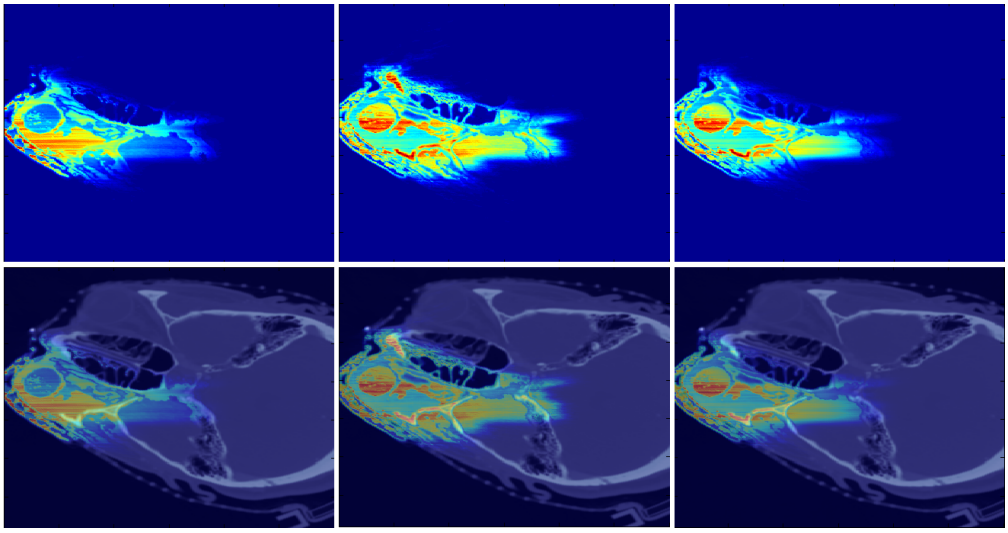

Fig. 11.37.: MC PET signals for different positron emitters (^{11}C, ^{13}N and ^{15}O).

	t_{del1}	t_{del2}	t_{del3}
delay time (min)	2	6	12
^{11}C factor	0.020	0.017	0.014
^{13}N factor	0.025	0.019	0.012
^{15}O factor	0.016	0.004	0.001

Table 11.6.: Time dependent factors g_{time} to create combined PET signals.

displayed in figure 11.40. Since the combined PET signals are generated using forward filtering results, there is no noise in the signals and the weighting for the regularization is set to $\lambda = 0.02$. The results show that the dose distribution is reconstructed properly in all cases, i.e. for all different delay times. This approach is thus suited for PET images obtained with shorter delay times and considers different positron emitters which influence the PET image.

11.8. Discussion

The objective of the presented method is to reconstruct the dose distribution in proton radiotherapy based on PET images. Previous work allowed PET range verification only with the use of Monte Carlo PET. In this case the treatment verification is done by comparing Monte Carlo PET with measured PET. The main goal of the new method is to improve the range verification and to eventually extend the method towards complete dose reconstruction. The basic concept of the presented method is to reverse the PET

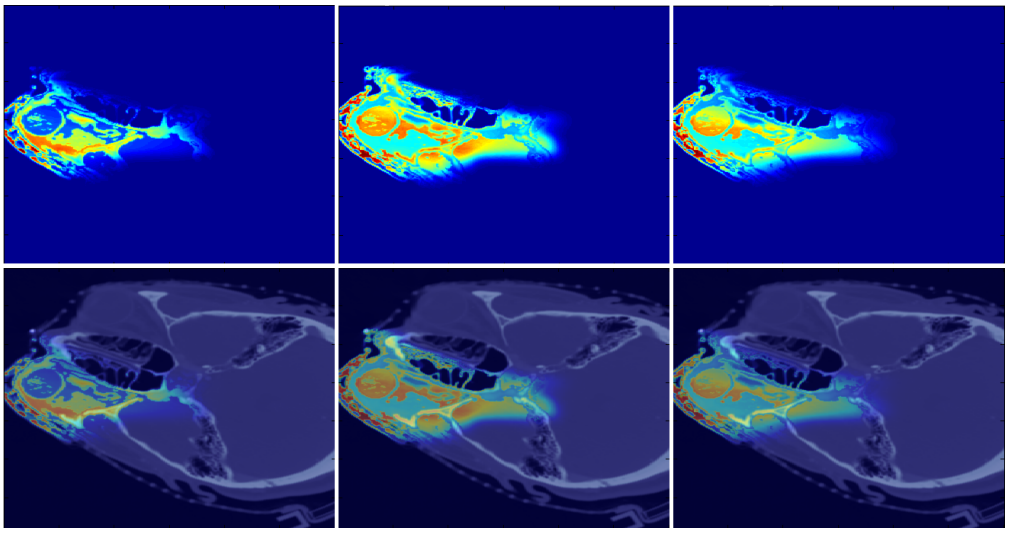

Fig. 11.38.: Forward filtering results (^{11}C, ^{13}N and ^{15}O).

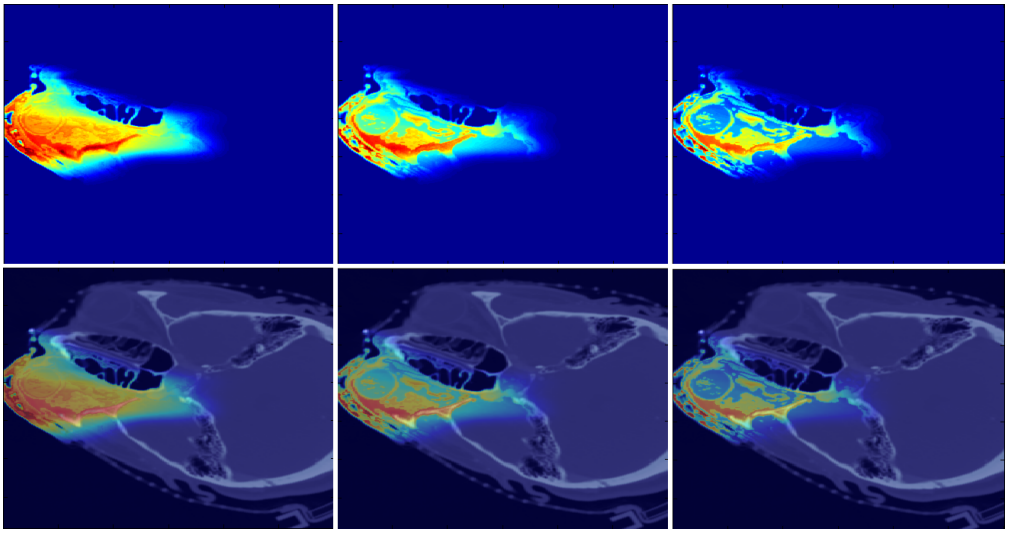

Fig. 11.39.: Combinations of PET signals (^{11}C, ^{13}N and ^{15}O) with different delay times.

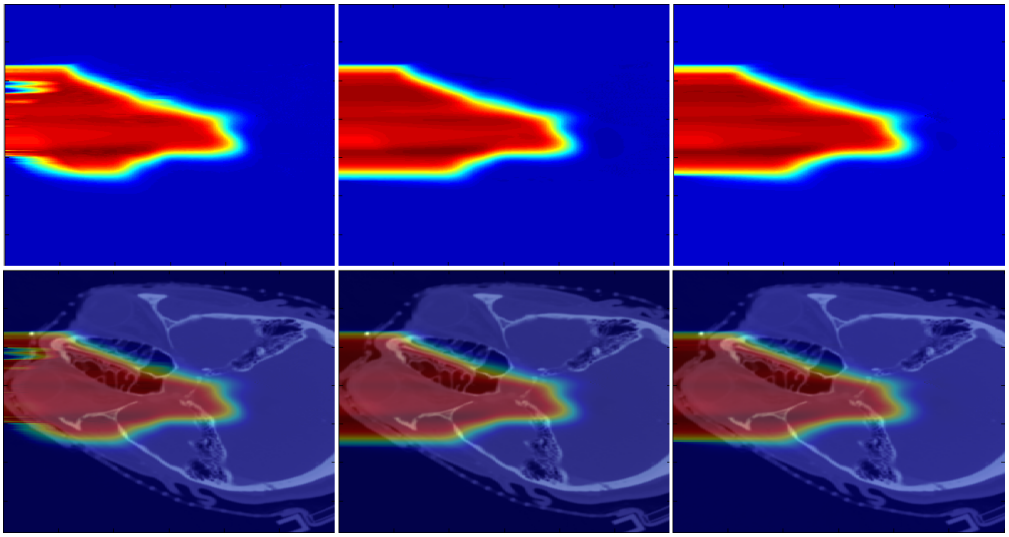

Fig. 11.40.: Dose deconvolution results for combined PET signals.

estimation given by a convolution approach [115] for one positron emitter. This convolution approach is valid for homogeneous media and additional procedures are necessary to generalize the PET estimation to inhomogeneous media. In addition, there is an advanced framework using additional short-lived positron emitters [6] and the proposed reconstruction method is extended to cope with additional positron emitters.

The basic reconstruction approach for homogeneous media requires a deconvolution to reverse the PET estimation process. Simulations show that it is possible to reconstruct a dose distribution on basis of PET signals generated by the underlying convolution approach and MC simulations. However, the reconstruction of measured PET signals is difficult and the quality of the results decreases. Measured PET signals usually contain artifacts and these artifacts influence the reconstruction result which cannot be avoided. Regularization allows a stable solution of the deconvolution problem but cannot compensate artifacts.

This problem intensifies in case of inhomogeneous media since additional components are necessary in the reconstruction method. An additional deconvolution is necessary to reverse the PSF of the PET imaging system. Removing the local weighting factors without considering the PSF would lead to large artifacts which would strongly degrade the reconstruction result. Simulations show that this extensive reconstruction method is able to completely reverse the PET estimation process in case of inhomogeneous media. The reconstructed dose is almost identical to the treatment planning dose used to estimate the PET signal which is identical to a MC simulation. In case of measured PET signals, the quality of the images for both the phantom data and the head and neck patient is poor and the images contain a lot of artifacts. It is not possible to reconstruct the accurate shape of the treatment planning dose and the dose distribution

is degraded by artifacts and inaccuracies caused by the poor quality of the PET images.

In case of measured PET signals, it is difficult to detect the distal fall-off region in the reconstructed dose distribution. A method which is based on the smoothed gradient of the dose distribution is therefore used to estimate the midpoint of the distal fall-off region. This method is able to cope with the artifacts in the reconstructed dose distribution and to overcome the typical resolution of a PET scanner since a dose gradient is analysed and not a point in the dose distribution. The average error between the distal fall-off region of the treatment planning dose and the reconstructed dose distribution is between 2 mm and 3 mm for the processed measured PET slices from the phantom data set. A maximal error of up to are 8 mm is possible for several beam lines because of large artifacts. However, the average error shows that the reconstruction result provides a basis for range verification despite the artifacts.

Considering additional positron emitters in the dose reconstruction leads to an extended method to reverse the PET estimation method. A simulation shows that the reconstruction method is able to reverse the PET estimation method. Unfortunately, a measured PET image was not available in such a case but it can be assumed that the PET image quality is improved. The delay time between irradiation and PET imaging can be decreased considerably resulting in an increased signal strength.

In addition, there is a physiological activity wash-out effect which also influences the measured PET images. This effect is not yet considered in the dose reconstruction method. The objective of this method is to reverse the PET estimation method and the wash-out effect is not included in this method. However, the wash-out effect has to be considered in order to provide a complete dose reconstruction method.

The proposed dose reconstruction method is limited to process PET signals generated by a single beam. A proton dose generated by several superimposed beams cannot be reconstructed properly since the actual dose deconvolution is working in 1D along the proton beam line. A second beam influences the PET signal and it is not possible to separate the different components of the PET signal generated by different proton beams.

Part IV.

Conclusion and Outlook

12. Conclusion

As motivation to image deblurring, a RNAi-based high-throughput microscopy screen to investigate intracellular trafficking and targeting of acylated Src kinases was presented and an automated software tool to analyse the images obtained during this screen was described. The analysis tool includes a stable and robust cell segmentation using a classifier-enhanced region growing method. This approach yields a reliable segmentation of different phenotypes and is especially invariant to fluorescence brightness of the segmented cells and cell nuclei. A Support Vector Machine is applied to classify the phenotype of the cells and supervised learning is used to train the Support Vector Machine and to adjust the soft margin parameter likewise. The software tool is well suited for the analysis of genome-wide RNAi screens and the supervised learning allows an easy adjustment of the classification. The underlying biological problem shows the need to analyse structural information of fluorescence images and a good image quality is thus required. The analysis of images with a moderate quality is more difficult and the results are not quite definite. A preprocessing deblurring step can improve the image quality and could allow more reliable results. Furthermore, the analysis of images with a poor quality which was not possible before could be considered after deblurring the images.

The deblurring results using the standard components of the deconvolution framework illustrate the potential of deblurring methods with synthetic and real images. The deblurring considerably improved the image quality and noise was removed almost completely. The resolution of a cell image is enhanced and sharp edges can be seen. In fact, several cell structures are visible in the deblurring result which cannot be seen in the measured images. Since the convergence speed of the iterative RLTV deblurring algorithm is slow, an accelerated version based on a vector extrapolation technique is presented. Several tests show that 30% to 40% less iterations are required with the accelerated algorithm to obtain the same quality improvement. A new algorithm using the Bregman distance is presented and improves the quality of the RLTV deblurring algorithm. It is difficult to use this new algorithm since it has the drawback that it is highly dependent on the amount of Bregman iterations. A high number of iterations would lead to the degraded image itself as reconstruction result and a low number would not improve the result compared to the standard algorithm. The Bregman deblurring method was tested once with a limited amount of data and not investigated further. Finally, a new deblurring approach is presented which incorporates an additional restriction by

enforcing non-negativity. The new deblurring method is based on a TV regularized RL functional considering an image formation model with a background signal. A constrained conjugate gradient method is used in the algorithm and enforces the non-negativity restriction. The TV regularization is necessary to allow a stable solution but has the drawback to enforce homogeneous areas and sharp edges which is well known as stair-casing effect. The non-negativity constraint which is supported by a background signal in order to ensure its full effectiveness provides an additional regularization allowing a stable solution without the drawback of the stair-casing effect. In fact, the non-negativity constraint incorporates a priori knowledge which is known to be true since there are no negative values in the reconstruction results. The TV regularization is an assumption which is not necessarily true for all processed images but required to guarantee a stable solution. The combination of both techniques allows an improved result which is not possible when using either technique alone. Synthetic tests show that the new deblurring method improves the quality of the results regarding both a visual analysis and the RMSE compared to the known original image. Additional tests with real microscopy images confirm the quality improvement of the new CCG method compared to the original RL algorithm and the regularized RLTV algorithm which is the current state of the art method in fluorescence microscopy deblurring.

Microscopy images suffer from a low resolution in direction of the optical axis and Axial Tomography is able to overcome this problem by providing images from different viewing angles. An axial reconstruction method is presented which uses the additional information in the rotated images to create a single image with an isotropic resolution containing all available information. This reconstruction method is based on the deblurring methods and the components of the deconvolution framework are used to reconstruct the Axial Tomography image. Before the actual axial reconstruction can be done, bleaching has to be corrected and the images have to be aligned. A bleaching factor is therefore estimated and a multi-resolution registration method is used. The deblurring results of the different images are used as basis for the registration and allow an improved registration accuracy. A high resolution image is then reconstructed on basis of the aligned Axial Tomography images using the information included in all images. The axial reconstruction algorithms are based on the deblurring methods allowing an additional enhancement of the resolution besides including the information in all images. Synthetic 2D tests show that the axial reconstruction methods both include all available information and improve the image quality in general. The results of the axial CCG algorithm are superior to the other reconstruction methods. The registration is tested in 3D showing that the accuracy of the registration is improved by using deblurred images instead of measured/degraded images. Again, the axial CCG algorithm generates the best 3D axial reconstruction results regarding the RMSE criterion. The proposed axial reconstruction process is used to reconstruct an image data set containing beads. The results show a considerable improvement of the resolution and the Fourier transforms

of the registered bead images and the corresponding reconstruction result illustrate the enhanced isotropic resolution. At last, an axial image data set is reconstructed including bleaching correction and a registration on basis of deblurring results of the single measured images. The axial reconstruction result of the axial CCG algorithm shows a high resolution image with well reconstructed actin fibres.

A novel approach for dose reconstruction in proton radiotherapy which is based on an existing filtering framework to predict the induced PET signals has been proposed. The PET signals are predicted by a convolution of the planned dose with specific filter functions and a deconvolution is thus able to reverse the PET prediction and allows the dose reconstruction on basis of PET signals. The new approach was first tested using Monte Carlo simulated PET signals given in homogeneous media for one positron emitter and then generalized to inhomogeneous media. Simulations on basis of estimated PET signals show that the proposed dose reconstruction method is able to reverse the underlying PET estimation method in case of homogeneous and inhomogeneous media. Measured PET signals of a phantom experiment are used to reconstruct the delivered dose and the delay between irradiation and imaging is relatively large in this case resulting in a poor quality of the PET signals. It is difficult to process measured PET images since there are artifacts in the images which leads to artifacts in the reconstructed dose distribution. A similar result was obtained by processing a head and neck patient data set: The reconstruction result on basis of the estimated PET signal is as expected but the quality of the reconstruction result on basis of measured PET signals is not satisfying. In-room PET scanners allow decreased delay times and additional short lived positron emitters have to be considered for such measurements. An extended version of the dose reconstruction approach allows the processing of PET images acquired with a considerably reduced delay time and an improved PET image quality should be possible in this case.

13. Higher Order Statistics Denosing

13.1. Introduction

All measured signals or images are corrupted by noise or even blur and therefore image denoising or reconstruction is necessary. Especially images with a low quality require reliable and robust methods. The proposed method is restricted image denoising with underlying Gaussian noise which is common for detectors and can thus be found in all digital images. Each pixel value is acquired by a light intensity measurement, usually made by a CCD matrix coupled with a light focusing system. The number of incoming photons for a fixed time period on a single CCD captor leads to the pixel value at the according position in the image. Even a constant light source results in varying pixel values and this effect is reduced in high quality cameras but cannot be eliminated. The image formation model for a measurement image corrupted by Gaussian noise is given by:

$$g = f + n \quad with \quad n \sim \mathcal{N}(\mu, \sigma) \tag{13.1.1}$$

Hereby, f is the unknown signal and g the measured signal. The signal is degraded by Gaussian noise n defined by a mean value μ and variance σ^2. The result of a denoising method is a decomposition of the measured image g in the estimated original image $\hat{f}$ and the additional noise. The difference between the measured and denoised image is called residuum and denoted as r.

$$r = g - \hat{f} \tag{13.1.2}$$

A perfect denoising would be able to reconstruct the original image f and thus the residuum r would contain the additional noise and no fraction of the original image f. A standard method for denoising is to use a Gaussian smoothing to reduce the noise in the image realized by a convolution with a Gaussian kernel [96]. The computational effort of this method is quite low since it contains a single convolution. However, a Gaussian filtering is a low pass filtering removing all high frequency parts of the image together with the noise. Since images usually contain high frequency parts, it is not possible to achieve a good denoising result with this method.

Another standard method is to use frequency domain filters like the Wiener Filter [177]. The denoising result of this method is usually corrupted by artifacts looking like periodic patterns [26] [27]. In theory, this effect can be avoided using additional information but therefore the Fourier transform of the original image has to be known. Additional denoising methods are the anisotropic filtering model [120] [2], neighborhood filters like the SUSAN filter [149] or the discrete universal denoiser DUDE [112]. According to [27] all of the previously mentioned methods are based on a local or global generic image smoothness resulting in an elimination of fine structures in the images which have a similar appearance as the underlying noise model. These methods are therefore not able to perfectly separate the image from the additional noise.

An improved result can be obtained using iterative methods but a priori knowledge $P(f)$ about the image is required and used in the denoising method leading to a maximum a posterior (MAP) algorithm instead of an expectation maximization (EM). The EM algorithm maximizes $P(g|f)$ while the MAP maximizes $P(f|g)$ considering the a priori knowledge $P(f)$ as described by the Bayes theorem.

$$P(f|g) = \frac{P(g|f)P(f)}{P(g)} \tag{13.1.3}$$

Hereby, $P(f|g)$ is the a posteriori probability distribution, $P(g|f)$ is the likelihood distribution or noise model, $P(f)$ is the a priori distribution of the signal and $P(g)$ is the distribution of the measured signal which is of course constant for a single measurement. A seminal result has been achieved by Tikhonov and Miller for introducing regularization (TM) which is limiting the noise amplification in the solution [159]. However, the TM regularization has the drawback to smooth edges and was therefore replaced by a non-linear approach named total variation regularization (TV) which is able to overcome that problem and produces sharp edges [153]. TV regularization was introduced in [142] and widely used and improved for image denoising [113] [156] [33]. Hereby, the denoising is based on the minimization of the combined functional:

$$\hat{f} = argmin_f \int_\Omega |\nabla f(x)| dx + \lambda \int_\Omega |f(x) - g(x)|^2 \, dx \tag{13.1.4}$$

The functional used in this maximum a posteriori (MAP) denoising consists of a fitting term given by a least square norm and the TV regularization. In addition, it requires a weighting parameter λ balancing between the fitting term and the regularization. The weighting parameter has a huge influence on the denoising result and requires an accurate estimation [165].

In [26], a non local means (NL) algorithm is presented which is designed to overcome this problem since no noise model or smoothness in the image is assumed. Hereby, pixels with a similar neighbourhood are averaged in order to provide a denoised image showing very promising results. The NL means method was improved [171] and used

for different applications like MR [122] or even movies [29]. For additional denoising methods, see [28].

In the following, a new denoising method based on higher moments of the underlying Gaussian noise distribution is presented. The new method is denoted as HOS method since it incorporates higher order statistics. The HOS method takes into account the limited number of data and the correlation of the values in the residuum r. The new method does not contain any a priori information and thus represents a maximum likelihood estimation. In principle, the fitting fidelity term $P(g|f)$ is extended by modeling the probability distribution of the residual by its moment representation whereby the HOS method is restricted to the first two moments. These two moments, for which an individual moment distribution is derived, are statistically independent in case of Gaussian noise and $P(g|\hat{f}) = P(g - \hat{f}) = P(r)$. Without loss of generalization, the independent identical distribution (i.i.d.) of the noise vector n can be assumed, i.e. the cross correlation matrix Σ is a scalar matrix with σ as diagonal value. Therefore, the data fidelity term of a MAP algorithm is minimal whenever all components $r_i = g_i - \hat{f}_i$ maximize $P(r_i)$. Consequently, without the regularization term or equivalently for $\lambda = 0$, the reconstructed noise vector r would be a constant vector and equal to the null vector in case of a least square norm. These estimates may seem reasonable for a signal length N close to one. Since the vector n is i.i.d. and there is usually a larger signal length N, the empirical distribution of the components of the estimated noise vector r should resemble the distribution of the noise vector n. In order to check how good a set of samples coincides with a given distribution, it is possible to apply the Kolmogorov-Smirnov [18] or the Anderson-Darling test [125]. The HOS method contains a representation of the distribution that depends both on moments and especially on the correlation of noise to individual signal elements (In contrast to [51][73]). The included noise correlation [34] allows achieving de-correlated residuals of the denoising results. Similar results are achieved ad hoc with non-local means denoising [26] according to empirical studies. In order to evaluate the HOS approach, several results are compared with the MAP denoising method already introduced in equation 13.1.4.

13.2. Material and Methods

The basic idea is to use higher order moments to demand that the residuum r is as consistent with the anticipated probability density function of the noise signal n as possible. The new algorithm is based on a 1D signal f of length N (i.e. $f \in \mathbb{R}^N$) and f_i denotes the ith component of the signal. The basis of the new algorithm is the expectation-maximization (EM) approach of a general Gaussian distribution. A discrete signal s of length N is Gaussian distributed $\mathcal{N}(\mu_G, \sigma_G)$ if the functional J_G in equation 13.2.1 is minimal (Except for $s_i = \mu_G \; \forall i = 1 \cdots N$).

$$J_G(s) = \sum_{i=1}^{N} \frac{(s_i - \mu_G)^2}{2\sigma_G^2} \tag{13.2.1}$$

13.2.1. HOS Functional

In case of a correct reconstruction, $\hat{f}$ is identical to the original signal and thus the residuum r contains the noise signal. If the statistical distribution of the noise signal is known (e.g. Gaussian $\mathcal{N}(\mu, \sigma)$), it is possible to force the reconstruction to produce such a residuum. However, using just the first moment of the Gaussian noise distribution is not sufficient to obtain that objective. In the new approach, the second moment of the Gaussian noise distribution is used to get an advanced and more powerful reconstruction algorithm. Note that hereby no a priori knowledge about the original signal is used and thus the new method is an EM algorithm. The new algorithm consists of the minimization of a HOS functional J containing the properties of the Gaussian noise signal.

$$J(r) = J^{(1)}_{mean}(r) + J^{(2)}_{var}(r) + J^{(2)}_{covar}(r) \tag{13.2.2}$$

Since this formulation has multiple minima, an empty initial guess of $\hat{f}$ is used to start the method resulting in a residuum r containing the noisy signal g. Later, a weighting of the different summand of J is added in order to cope with the details of the concrete implementation. The first moment of the underlying Gaussian noise signal is considered in $J^{(1)}_{mean}$ while the second moment containing variance and covariance values is differentiated in $J^{(2)}_{var}$ and $J^{(2)}_{covar}$. The distribution of each moment used in the new denoising method is described by the following lemma derived from the probabilistic theory theorems of Bienayme and Mood, Graybill and Boes.

Lemma 1. *Let X_i, $i = 1, \cdots, n$, be uncorrelated random variables which follow the same probability distribution. Set $Z := \frac{1}{n}\sum_{i=1}^{n} X_i$. Then, it holds that*

$$E(Z) = \tfrac{1}{n}\textstyle\sum_{i=1}^{n} E(X_i) = E(X_i) \quad and \quad V(Z) = \tfrac{1}{n^2}\textstyle\sum_{i=1}^{n} V(X_i) = \tfrac{1}{n}V(X_i)$$

Lemma 2. *Let X_i, $i = 1, \cdots, n$, be independent random variables which follow the same probability distribution. Set $Z := \frac{1}{n-1}\sum_{i=1}^{n}(X_i - E(X_i))^2$. Then*

$$E(Z) = \tfrac{n}{n-1}V(X_i) \quad and \quad V(Z) = \tfrac{n}{(n-1)^2}(E(X_i^4) - V(X_i)^2)$$

Lemma 3. *Let X_i, Y_i, $i = 1, \cdots, n$, be independent random variables which follow the same probability distribution. Set $Z := \frac{1}{n-1}\sum_{i=1}^{n}(X_i - E(X_i))(Y_i - E(Y_i))$. Then*

$$E(Z) = 0 \quad and \quad V(Z) = \tfrac{n}{(n-1)^2}V(X)V(Y)$$

In order to use these lemmas, the probability distributions of the underlying random variables have to be considered properly.

Definition 1. *A random variable X with density*

$$\chi_n^2(x) = \frac{1}{\Gamma(\frac{n}{2})2^{n/2}} x^{\frac{n}{2}-1} e^{-\frac{x}{2}} \quad 0 < x < \infty$$

is called chi-square distributed with n degrees of freedom. It holds that $E(X) = n$ *and* $V(X) = 2n$*. Note that this distribution is a special case of a Gamma distribution with parameters (n/2, 1/2).*

Theorem 1. *Let* X_i*,* $i = 1, \cdots, n$*, be independent random variables which follow the normal distribution* $\mathcal{N}(0, 1)$*. Then* $Z = \sum_{i=1}^{n} X^2$ *has a chi-square distribution with n degrees of freedom.*

Corollary 1. *Let* X_1*,* X_2 *be two independent, chi-square distributed random variables with* n_1 *and* n_2 *degrees of freedom, respectively. The sum* $X = X_1 + X_2$ *has a chi-square distribution with* $n_1 + n_2$ *degrees of freedom.*

Theorem 2. *Let* X_i*,* $i = 1, \cdots, n$*, be independent and identically distributed random variables with* $E(X_i) = \mu$ *and* $V(X) = \sigma^2 > 0$*. Then for all* $x \in \mathbb{R}$*, it holds that*

$$lim_{n\to\infty} P\left(\frac{X_1 + \cdots + X_n - n\mu}{\sqrt{n}\sigma} \leq x\right) = \Psi(x)$$

where Ψ *stands for the distribution function of the normal distribution* $\mathcal{N}(0, 1)$*.*

Corollary 2. *Let X be a chi-square distributed random variable with n degrees of freedom. For large n the random variable* $\frac{1}{\sqrt{2n}}(X - n)$ *approximates the normal distribution* $\mathcal{N}(0, 1)$*.*

The first moment is Gaussian distributed which is described by $\mathcal{N}(\mu_\mu, \sigma_\mu^2)$. The second moment is chi-square distributed and a chi-square distribution can be approximated by Gaussian distributions. The distribution of the variance values is given by $\mathcal{N}(\mu_\sigma, \sigma_\sigma^2)$ and the according distribution of the covariance values by $\mathcal{N}(\mu_0, \sigma_0^2)$. The mean values ($\mu_\mu$, μ_0 and μ_σ) and variances (σ_μ^2, σ_0^2 and σ_σ^2) of these Gaussian distributions can thus be calculated using the following equations 13.2.3. Note that these values are dependent on the window size M and the underlying Gaussian distribution $\mathcal{N}(0, \sigma)$ of the noise signal n.

$$\begin{array}{ll} \mu_\mu = 0.0 & \sigma_\mu^2 = \frac{1}{M}\sigma^2 \\ \mu_\sigma = \frac{M}{M-1}\sigma^2 & \sigma_\sigma^2 = \frac{2M}{(M-1)^2}\sigma^4 \\ \mu_0 = 0.0 & \sigma_0^2 = \frac{M}{(M-1)^2}\sigma^4 \end{array} \tag{13.2.3}$$

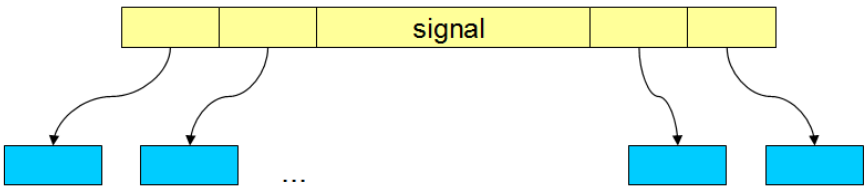

Fig. 13.1.: Decomposition of signal into separate boxes.

In order to calculate the values of the first and second moment, r is subdivided into separate boxes of size M leading to an amount of boxes K with $N = KM$. Naturally, M must be a divisor of N resulting in a integral amount of boxes K. The values of the residuum r in box Box_j with $j \in \{1, \cdots, K\}$ are given by equation 13.2.4 and the separation is displayed in figure 13.1.

$$Box_j = \{r((j-1) \cdot M + j), \cdots, r(j \cdot M)\} \tag{13.2.4}$$

The mean value of a certain box μ_{Box_j} can then be calculated using equation 13.2.5 and hereby $Box_j(i)$ denotes the ith value in box number j.

$$\mu_{Box_j} = \frac{1}{M} \sum_{i=1}^{M} Box_j(i) \quad j = 1..K \tag{13.2.5}$$

The distribution of μ_{Box} is considered in $J^{(1)}_{mean}$ which represents the first moment of the Gaussian noise distribution. This distribution is a Gaussian distribution with $\mathcal{N}(\mu_\mu, \sigma_\mu)$ and an EM approach leads to the functional in equation 13.2.6 according to the EM method for a general Gaussian distribution (Equation 13.2.1).

$$J^{(1)}_{mean}(r) = \sum_{i=1}^{K} \frac{(\mu_{Box_i} - \mu_\mu)^2}{2\sigma_\mu^2} \tag{13.2.6}$$

The second moment leads to a cross-correlation matrix Σ of size $K \times K$ where the diagonal entries are the variances within a block and the non-diagonal elements show the correlation in the residual (Covariance). Each component of the matrix Σ is calculated using equation 13.2.7 with μ being the mean value of the Gaussian noise signal n. An extract of such a matrix with an underlying discrete Gaussian distribution is shown in figure 13.2.

$$\Sigma_{i,j} = \frac{1}{M-1} \sum_{l=1}^{M} (Box_i(l) - \mu) \cdot (Box_j(l) - \mu) \quad i,j \in \{1...K\} \tag{13.2.7}$$

The variance and the covariance values are separated in two different sets and the variance values are examined in $J^{(2)}_{var}$ while the covariance values are considered in $J^{(2)}_{covar}$. The second moment is chi-square distributed and the separate variance and covariance distributions can be approximated by Gaussian distributions with $\mathcal{N}(\mu_\sigma, \sigma_\sigma)$

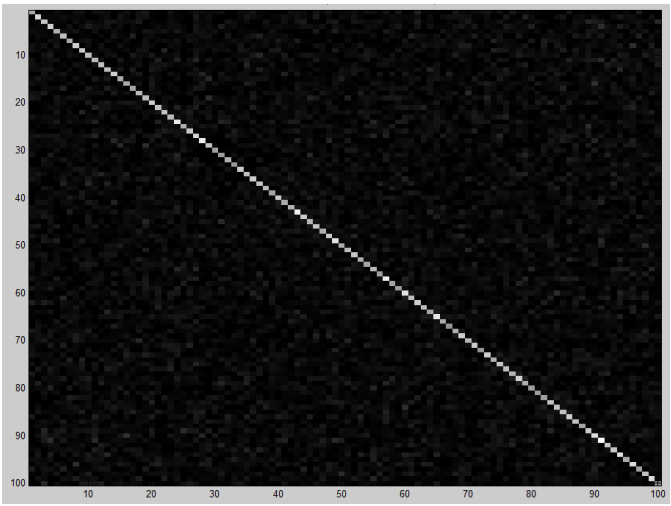

Fig. 13.2.: Extract of Second Moment matrix Σ (Variance and covariance).

and $\mathcal{N}(\mu_0, \sigma_0)$ leading to the functionals $J^{(2)}_{var}$ and $J^{(2)}_{covar}$. In equation 13.2.9, it is considered that the matrix Σ is symmetric.

$$J^{(2)}_{var}(r) = \sum_{i=1}^{K} \frac{(\Sigma_{i,i} - \mu_\sigma)^2}{2\sigma_\sigma^2} \tag{13.2.8}$$

$$J^{(2)}_{covar}(r) = 2 \sum_{i=2}^{K} \sum_{j=i+1}^{K} \frac{(\Sigma_{i,j} - \mu_0)^2}{2\sigma_0^2} \tag{13.2.9}$$

Equation 13.2.10 shows a weighted version of functional $J(r)$ and hereby, each single term has the same influence on the total functional meaning to be based on the relatively same amount of values. $J^{(1)}_{mean}$ and $J^{(2)}_{var}$ are based on K values since the separated boxes are considered here. $J^{(2)}_{covar}$ is based on $K(K-1)$ values and is thus multiplied with $\frac{1}{K-1}$ to even it up.

$$J(r) = J^{(1)}_{mean}(r) + J^{(2)}_{var}(r) + \frac{J^{(2)}_{covar}(r)}{K-1} \tag{13.2.10}$$

13.2.2. Gradient of HOS Functional

The minimization is performed to reconstruct a signal $\hat{f}$ using $J(r)$ with $r = \hat{f} - g$ and thus the gradient is calculated with respect to $\hat{f}$. Hereby, $\hat{f}_i$ denotes the ith component of $\hat{f}$ and the gradient has the same size N as the noisy signal g. In order to calculate the gradient, it is necessary to know the number of the box and the index inside the box for

the investigated value $\hat{f}_i$. The number of the box is given by $gB(i)$ and the index inside the box by $gI(i)$ using the Matlab indexing system starting at 1.

$$gB(i) = getBox(i) = \left\lfloor \frac{i-1}{M} \right\rfloor + 1 \tag{13.2.11}$$

$$gI(i) = getIndex(i) = mod(i-1, M) + 1; \tag{13.2.12}$$

The gradients are shown in equations 13.2.13-13.2.15 with $Box_l(k)$ denoting the kth value in the lth box.

$$\frac{\partial J^{(1)}_{mean}}{\partial f_i} = \frac{1}{\sigma^2_\mu M}\left(\frac{1}{M} - \sum_{k=1}^{M} Box_{gB(i)}(k)\mu_\mu\right) \tag{13.2.13}$$

$$\frac{\partial J^{(2)}_{var}}{\partial f_i} = \frac{2r(i)}{\sigma^2_\sigma(M-1)}\left(\frac{1}{(M-1)}\sum_{k=1}^{M}\left(Box_{gB(i)}(k) - \mu\right) - \mu_\sigma\right) \tag{13.2.14}$$

$$\begin{aligned}\frac{\partial J^{(2)}_{covar}}{\partial f_i} = \; & \frac{2(rI(i)-\mu)}{\sigma^2_0(M-1)}\sum_{k=1}^{K\neg gB(i)} \\ & \left(\frac{1}{(M-1)}\sum_{l=1}^{M}(Box_{gB(i)}(l)-\mu)(Box_k(l)-\mu) - \mu_0\right)\end{aligned} \tag{13.2.15}$$

13.2.3. Minimization of the HOS Functional

In order to minimize the HOS functional, the *fminunc* function provided by Matlab (Version: R2008b, www.mathworks.org) is used. This optimizer contains two different algorithms: a *Large-Scale* and a *Medium-Scale* algorithm. The Large-Scale algorithm approximates the underlying function by a quadratic approximation q based on the first two terms of a Taylor series.

$$q = \frac{1}{2}s^t H s + s^t g \tag{13.2.16}$$

Hereby, H is the Hessian matrix and g the gradient of the underlying function at the investigated point. This quadratic function is then minimized on a so called two dimensional *trust region* S. S is determined with the aid of a preconditioned conjugate gradient process defining it as the linear space spanned by s_1 and s_2. s_1 is the direction of the gradient g, and s_2 is either an approximate Newton direction $Hs_2 = -g$ or the direction of the negative curvature given by $s_2^t H s_2 < 0$. The idea is to force global convergence and achieve fast local convergence.

The *Medium-Scale* algorithm uses a Quasi-Newton Method including an iterative approximation of the Hessian matrix H based on an initial positive definite symmetric

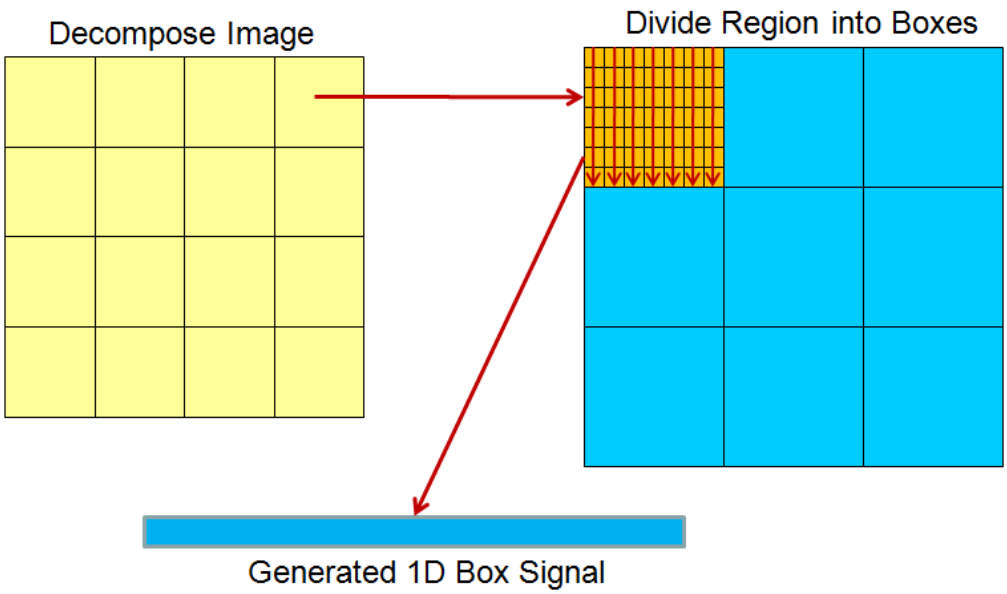

Fig. 13.3.: Divide image and create 1D box signals.

matrix H_0 (e.g. the identity matrix). In each iteration step k, the Hessian matrix H_{k-1} is then updated using the gradient g_k and the functional value at the investigated point. In addition, a line search based on a polynomial interpolation of the underlying functional is then performed using a search direction d_k given by $d_k = -H_k^{-1} g_k$.

The *Large-Scale* algorithm can only be used if a gradient g is provided manually. Additionally, the Hessian matrix H can be given manually or is approximated by *fminunc*. On the other side, providing a gradient g is optional for the *Medium-Scale* algorithm but recommendable since a considerable speed up can be achieved. A manual Hessian matrix H is ignored in that case. In addition, the manually provided gradient g can be tested by comparing it to the approximated gradient.

13.2.4. Decomposition of 2D Images

The used 2D test images are far too large to be processed at once and in fact, this is not necessary. It is important to divide a signal in a relatively large amount of different boxes but as long as the second order moments show the characteristic properties, a larger amount of boxes is not necessary. Additionally, the window size of the boxes should be relatively large as well but does not have to be increased further. In the following, 2D images are processed region by region with a constant region size. Each region is then divided into different boxes which values are converted to vectors and then form the boxes used in the HOS algorithm (See figure 13.3).

13.3. Results

Since synthetic signals are used to evaluate the new denoising method, the original signals are known and can be directly compared to the reconstruction results. To quantify the quality of the denoised signal, it is usual to use the mean square error (MSE) criteria. The HOS method is compared to the TV regularized denoising [142] (Equation 13.1.4) which is denoted as MAP-TV in the following. In order to get an optimal value for λ, a brute force (bf) search with a wide range of possible values is used. Hereby, the reconstruction results are compared to the original signals. In addition, a standard (std) value is used for λ.

13.3.1. 1D Signals

Four different synthetic 1D signals are denoised in this section. Each signal is degraded with another Gaussian noise signal ($\mu = 0$ and $\sigma^2 = 20$) but the same degraded signal is then used for both denoising algorithms. The first signal is denoted as $Signal1$ and contains mostly low frequency parts while the second signal $Signal2$ includes a zigzag signal all over the signal domain. The signals $Signal3$ and $Signal4$ are created by adding Sine signals with different frequencies h. Hereby, equation 13.3.1 is used and it is important that the frequencies h of the Sine functions do not violate the Nyquist Shannon sampling theorem, i.e. they have to be smaller than half the sampling frequency h_s. $Signal3$ consists of three Sine functions with $h_1 = 0.1h_s$, $h_2 = 0.001h_s$ and $h_3 = 0.0002h_s$. In the same way, $Signal4$ is composed of two Sine functions with $h_1 = 0.01h_s$ and $h_2 = 0.07h_s$. All signals and the reconstruction results of the HOS method and the MAP-TV method with the brute force determined λ are shown in figure 13.4. Table 13.1 shows the MSE values for the denoising results. The MSE results show that the HOS algorithm outperforms the MAP-TV method in case of signals with high frequency parts. The result for the MAP-TV methods is superior for the smooth signal since the included a priori knowledge assumes smoothness.

$$SineSignal(x) = w_1 sin\left(2\pi h_1 x\right) + w_2 sin\left(2\pi h_2 x\right) + w_3 sin\left(2\pi h_3 x\right) \tag{13.3.1}$$

Moreover, the HOS method produces a much better reconstruction of the original noise vector as illustrated in figure 13.5 for $Signal3$. The approximation of the histogram of the HOS residuum to the shape of the density function of the given noise signal is almost perfect while there are considerable differences in case of the MAP-TV denoising method. The sample mean $\tilde{\mu}$ and sample variance $\tilde{\sigma}^2$ defined by

$$\tilde{\mu} = \frac{1}{N}\sum_{i=1}^{N} r_i \quad \tilde{\sigma}^2 = \frac{1}{N-1}\sum_{i=1}^{N}(r_i - \mu)^2 \tag{13.3.2}$$

are very close to the original parameters $\mu = 0$ and $\sigma^2 = 20$ as shown in table 13.2.

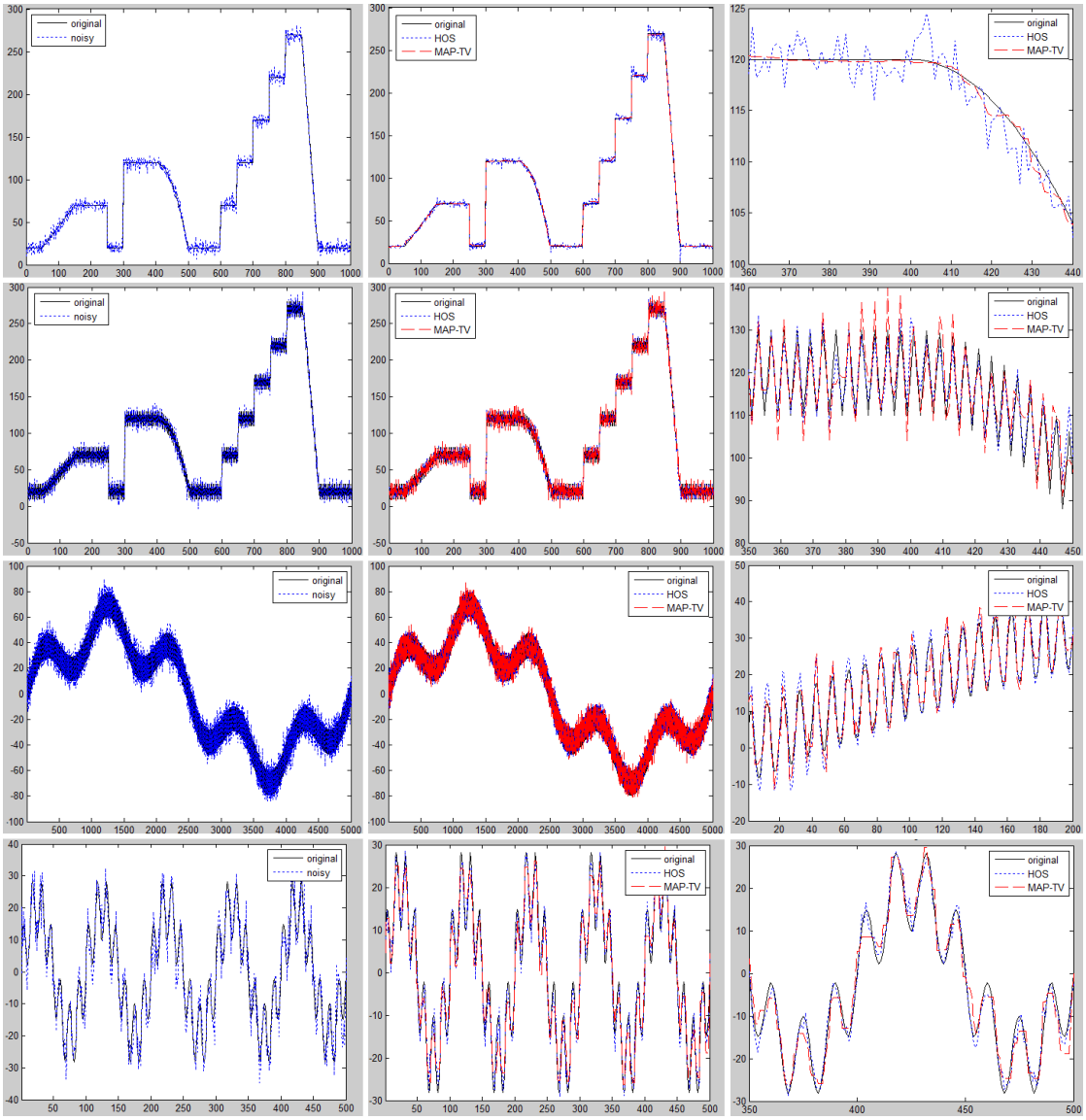

Fig. 13.4.: 1D signals degraded with Gaussian noise and reconstruction result (MAP-TV and HOS).

	Signal1	Signal2	Signal3	Signal4
Noisy signal	20294	20419	150626	20405
MAP-TV std	2358	48798	275731	22566
MAP-TV bf	2358	19163	96422	9364
HOS	8851	9727	29606	4720

Table 13.1.: MSE of denoising results for different 1D signals

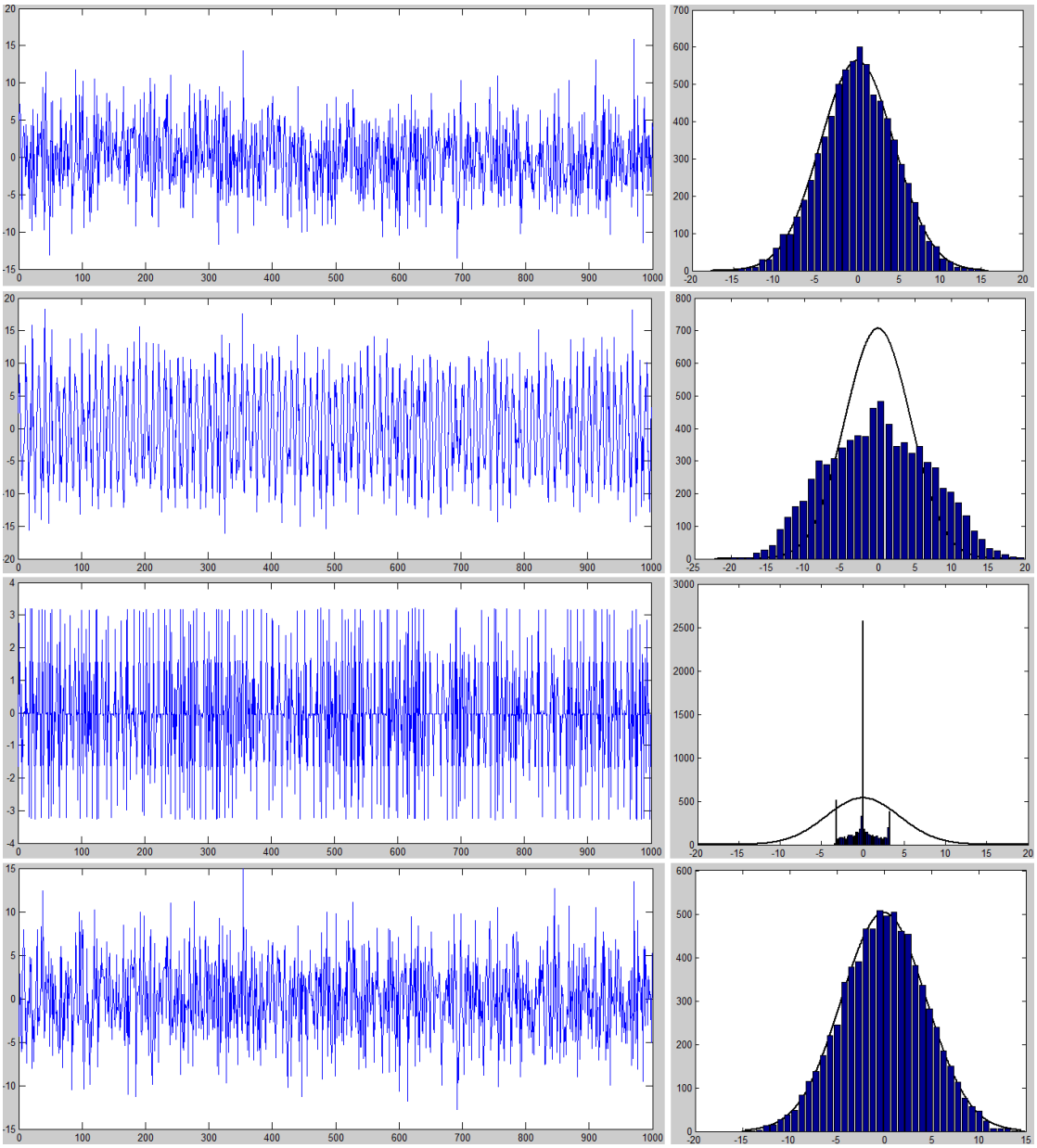

Fig. 13.5.: Left, top to bottom: True noise signal used for corrupting $Signal3$ and reconstructed noise signals by MAP-TV std, MAP-TV bf and HOS. Right: Histograms of the noise values and scaled Gaussian with $\mu = 0$ and $\sigma^2 = 20$ (Black curve) for comparison.

	Signal1		Signal2		Signal3		Signal4	
	$\tilde{\mu}$	$\tilde{\sigma}^2$	$\tilde{\mu}$	$\tilde{\sigma}^2$	$\tilde{\mu}$	$\tilde{\sigma}^2$	$\tilde{\mu}$	$\tilde{\sigma}^2$
MAP-TV std	0.1	17.2	-0.2	66.1	0.0	47.8	-0.1	33.4
MAP-TV bf	0.1	17.2	0.0	0.5	0.0	2.7	0.0	10.57
HOS	0.0	19.8	0.0	19.4	0.0	20.1	0.0	20.0

Table 13.2.: Estimated μ and σ^2 of original and reconstructed noise signals.

	Lena	Barbara	Barbara (ROI)
Noisy signal	125405234	125405234	13855805
MAP standard	56489875	64274267	8409265
MAP brute force	15241442	39799435	8281825
HOS	41659099	51750440	6773282

Table 13.3.: MSE of denoising results for 2D images

13.3.2. 2D Images

The 2D test images are corrupted by a Gaussian noise signal with $\mu = 0$ and $\sigma^2 = 500$. The images are given in a *uint8* format and thus include a maximal value range from 0 to 255. Since the Gaussian noise is additive and negative values are possible, all calculations are performed using a *float* representation of the images providing an unlimited and accurate data range. All images have a size of 500×500 and are processed as described before. The images are decomposed in regions of size 100×50 and the box size M is set to 100 being a 10×10 box. This partitioning results in 50 boxes per region (K) which is suitable for the HOS algorithm. A larger number is always desirable but causes a larger computational effort. As mentioned before, the regularization of the MAP algorithm is set to a standard value $\lambda = 10$ and then to an optimal result of a brute force search evaluating a broad range of different values. The results for the first image (Lena) can be seen in figure 13.6 with $\lambda = 43$ as result of the brute force search. The corresponding λ value for the second image (Barbara) is 30 and the denoising results are shown in figure 13.7. Since this image contains both high frequency and smooth parts, a region of interest (ROI) is extracted and analyzed in detail (Figure 13.8). In addition, table 13.3 shows the MSE values for all the denoising results and the ROI of the Barbara image. The HOS algorithm is able to improve the image quality for each image but due to large smooth areas, the results of MAP-TV method are superior especially with the brute force determined regularization parameter. However, in a ROI in the Barbara image containing mainly high frequency parts, the HOS algorithm outperforms the MAP-TV denoising.

Fig. 13.6.: Lena original and noisy image (Upper row) and denoising results (Lower row, from left to right: HOS, MAP-TV(std), MAP-TV(bf)).

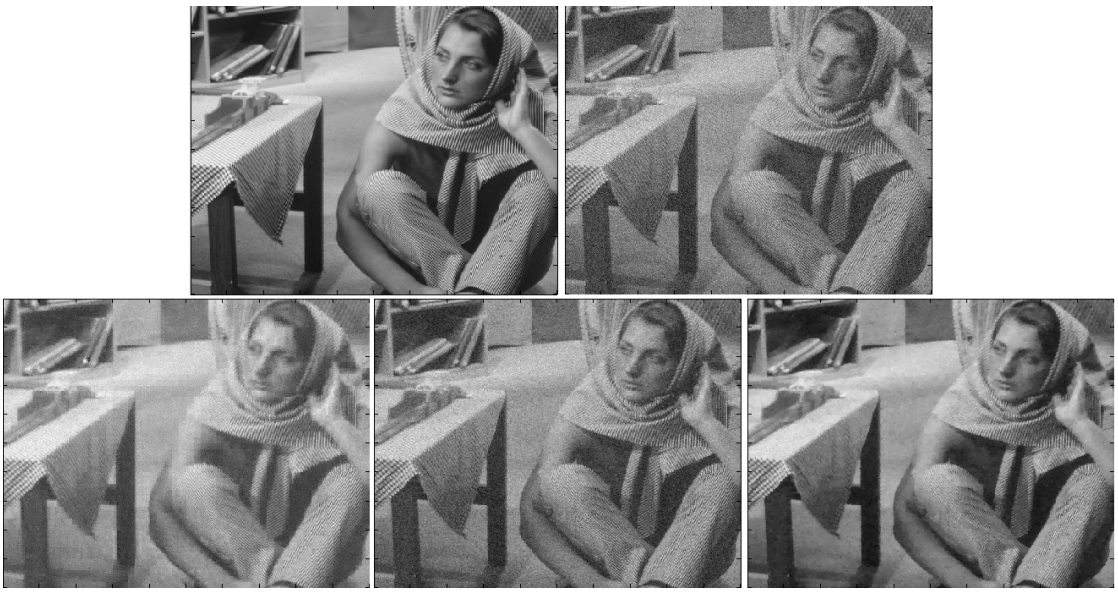

Fig. 13.7.: Barbara original and noisy image (Upper row) and denoising results (Lower row, from left to right: HOS, MAP-TV(std), MAP-TV(bf)).

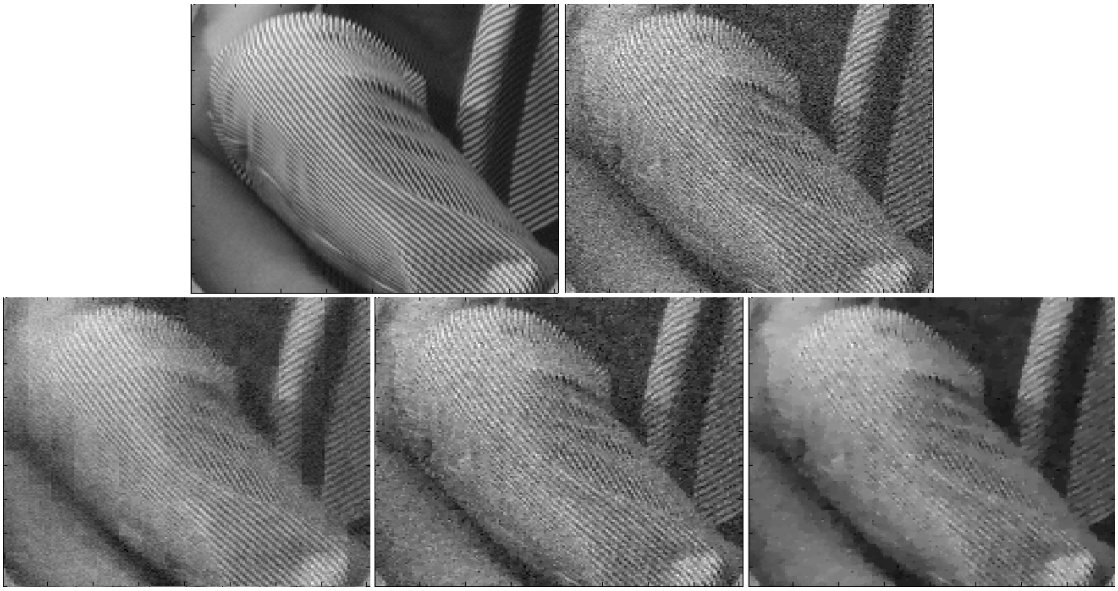

Fig. 13.8.: Barbara ROI original and noisy image (Upper row) and denoising results (Lower row, from left to right: HOS, MAP-TV(std), MAP-TV(bf)).

13.4. Discussion

In case of 1D signals, the HOS method allows a better reconstruction of signals containing high frequency parts than the MAP-TV method. Hereby, the MSE values of the HOS results are at least by a factor of 2 smaller than the according MSE values for the MAP-TV method. It is clear that the TV-term smoothes the solution and therefore cannot cope with high-frequency parts. On the contrary, the higher-order term leads to the next local optimum according to the first two moments and therefore without additional a priori information, smooth structures cannot be recovered since they are not attainable over local optimization. The same effect can be found in 2D signals. The denoising quality of the Barbara image is worse for the HOS method since there are many regions with smooth structures. However, the HOS method is superior to the MAP-TV method in a region of interest in the Barbara image containing mainly high frequency parts. As a problem that is connected with the block-based approach, there are block artifacts in the reconstruction which are considered in the MSE values.

14. Outlook

The first version of the cell analysis tool contains a rule based classification which worked as supposed for the first screen. However, this version of the tool failed to analyse a second small validation screen with different image modalities. The rule based classification had to be adjusted manually and therefore the tool was extended with a Support Vector Machine classification. Supervised learning is used to train the Support Vector Machine and first results are as expected. This final version of the cell analysis tool has not been used for a real RNAi screen so far but there are plans for a successive screen which would be a good opportunity to apply the final version of the cell analysis tool. The cell analysis tool was designed to provide a robust and stable analysis result. A conservative strategy was thus used and cell nuclei and cells were excluded in case the segmentation result was not satisfying. Furthermore, the general image quality was evaluated and added to the analysis result to allow an exclusion of image data sets with an insufficient image quality. It would be interesting to evaluate the potential of a preprocessing deblurring step and how an analysis result of an image with a poor quality could be improved.

There are some open questions regarding the deblurring methods. In order to apply the algorithms to fluorescence microscopy images, a PSF is required. It is possible to approximate the PSF of a confocal fluorescence microscope with a 3D Gaussian filter mask by estimating the required variances. Such an approximation is not suitable for widefield fluorescence microscopy images since the shape of the PSF is different in this case and does not match a Gaussian function. An accurate representation of a PSF of a widefield fluorescence microscope can be achieved by using Zernike moments [13]. Zernike moments offer a compact representation where e.g. low-order coefficients represent typical aberrations. In addition, the PSF might change significantly along the optical axis as the depth increases [57]. A recently published paper [104] proposes a depth variant PSF using Zernike moments. In this approach, the needed PSFs are interpolated from a limited number of measured PSFs instead of measuring all required PSFs. In this thesis, bead images have been used to estimate the PSFs for the widefield image data sets in the axial reconstruction chapter. However, the bead images were severely undersampled and the PSFs had to be interpolated in order to apply them to the cell image data set which is not optimal. In case of confocal fluorescence images, the PSFs were approximated by a Gaussian filter function and the variances were estimated. This procedure is reasonable but obtaining a PSF by measuring a sub-resolution

fluorescent bead allows a superior result. The collaboration on the axial reconstruction with the AG Cremer/Hausmann (Kirchhoff Institute for Physics, University of Heidelberg) continues and further experiments are currently being carried out which will be processed with the described axial reconstruction method.

Another open question is the modeling of the background signal. In this thesis, a constant background signal was used which is a considerable simplification. Widefield microscopy data is typically acquired using CCDs which have the following features: varying pixel sensitivity, camera offset (which can drift over time), dark noise build-up and hot pixels. In addition, the light source can fluctuate in intensity over time and the background signal may change with increasing depths. A constant background signal is therefore unlikely in real images and an advanced model may improve the deblurring and axial reconstruction results of real images.

A drawback of the deconvolution methods is the estimation of the λ parameter which is required. This parameter has a huge influence on the reconstruction result and depends on the quality of the underlying signal. In general, a stronger noise signal requires a larger value for λ. A brute force search can be used to determine the optimal value for λ in case of simulated signals. Using simulations help to get an idea of a suitable λ value for different conditions which is then used for measured data sets but does not necessarily have to be the optimal value. There are different strategies to estimate a regularization parameter which could be used for that purpose, e.g.: unbiased predictive risk estimator method, generalized cross validation or discrepancy principle [165].

The dose deconvolution approach does not include a physiological activity wash-out effect which also influences the measured PET images. The objective of the method is to reverse the PET estimation method and the wash-out effect is not included in this method. However, the wash-out effect has to be considered in order to provide a complete dose reconstruction method and this topic remains an open issue. In addition, an extended dose reconstruction method is presented considering additional positron emitters and has not been used to reconstruct a dose distribution on basis of measured PET images. The decreased delay time between irradiation and imaging given by in-room PET scanners might allow an improved image quality with fewer artifacts and thus an improved dose reconstruction result. Further research on this issue is necessary.

The proposed HOS denoising method is an extension of the standard maximum likelihood estimation and uses higher order moments. No a priori knowledge is used in the first version of the HOS method and the objective of this method is to proof the general feasibility of this approach. Several tests on 1D signals and 2D images show that the HOS method is superior to standard MAP-TV denoising methods in case of high

frequency signals and it allows recovering fine structures which are smoothed when applying standard TV regularization. This result gives hope that HOS allows for a more detailed and accurate reconstruction compared to standard techniques. However, the underlying minimization problem has multiple minima and a useful result can only be obtained by choosing a fitting start signal. A joint project with the AG Steidl (Mathematical Image Processing and Data Analysis Group, University of Kaiserslautern) was started and an extension of the original HOS method with a substantial theoretical introduction has been submitted to the Journal on Signal Processing [158].

List of Figures

List of Tables

Bibliography

[1] *www.volumegraphics.com*.

[2] L. Alvarez, P.-L. Lions, and J.-M. Morel. Image selective smoothing and edge detection by nonlinear diffusion. *SIAM J. Numer. Anal.*, 29:845–866, 1992.

[3] Harry C. Andrews and B. R. Hunt. *Digital Image Restoration*. Prentice Hall, 1977.

[4] Dwi Anoraganingrum. Cell image segmentation: Global vs. local adaptive segmentation. In *ISSM Kassel*, 1999.

[5] F. Attanasi, N. Belcari, A. Del Guerra, W. Enghardt, S. Moehrs, K. Parodi, V. Rosso, and S. Vecchio. Comparison of two dedicated in beam PET systems via simultaneous imaging of ^{12}C-induced β +-activity. *Phys. Med. Biol.*, 54(2):29–35, 2009.

[6] Francesca Attanasi, Antje Knopf, Katia Parodi, Thomas Bortfeld, Harald Paganetti, Valeria Rosso, and Alberto Del Guerra. Clinical validation of an analytical procedure for in vivo PET range verification in proton therapy. *IEEE Nuclear Science Symposium Conference Record*, pages 4167–4171, 2009.

[7] Francesca Attanasi, Antje Knopf, Katia Parodi, Thomas Bortfeld, Harald Paganetti, Valeria Rosso, and Alberto Del Guerra. Validation of An Analytical 1D Filtering of the Dose Distribution for the Calculation of the Expected PET Distributions in Proton Therapy. *Med. Phys.*, 36:2814, 2009.

[8] Jean-Francois Aujol. Some first-order algorithms for total variation based image restoration. *Journal of Mathematical Imaging and Vision*, 34(3):307–327, 2009.

[9] D. Axelrod, D. Koppel, J. Schlessinger, E. Elson, and W. Webb. Mobility measurement by analysis of fluorescence photobleaching recovery kinetics. *Biophysical J.*, 16:1055–1069, 1976.

[10] L. Bar, A. Brook, N. Sochen, and N. Kiryati. Deblurring of Color Images Corrupted by Impulsive Noise. In *IEEE Transactions on Image Processing*, volume 16, pages 1101–1111, 2007.

[11] L. Bar, N. Sochen, and N. Kiryati. Image Deblurring in the Presence of Salt and Pepper Noise. In *Scale Space*, pages 107–118, 2005.

[12] L. Bar, N. Sochen, and N. Kiryati. Image Deblurring in the Presence of Impulsive Noise. In *International Journal of Computer Vision*, volume 70, pages 279–298, 2006.

[13] N. Becherer, H. Jodicke, G. Schlosser, J. Hesser, F. Zeilfelder, and R. Manner. On soft clipping of Zernike moments for deblurring and enhancement of optical point spread functions. *Proc. SPIE 6065, 60650C-11*, 2006.

[14] J. Beebe-Wang, F. Dilmanian, S. Peggs, D. Schlyer, and P. Vaska. Feasibility of positron emission tomography of dose distribution in proton beam cancer therapy. *Proceedings of EPAC*, pages 2721–2723, 2002.

[15] B. Bendriem and D. Townsend. *The theory and practice of 3D PET*. Kluwer Academic Publishers, Dordrecht - Boston - London, 1998.

[16] G. Bennett, J. Archambeau, B. Archambeau, J. Meltzer, and C. Wingate. Visualization and transport of positron emission from proton activation in vivo. *ascience*, 200:1151–53, 1978.

[17] David Biggs and Mark Andrews. Acceleration of iterative image restoration algorithms. *Applied Optics*, 36:123–145, 1997.

[18] D. Boes, F. Graybill, and A. Mood. *Probability and statistical inference*. McGraw-Hill, New York, 3 edition, 1974.

[19] Thomas Bortfeld. An Analytical Approximation of the Bragg Curve for Therapeutic Proton Beams. *Med. Phys.*, 24:2024–2033, 1997.

[20] J. Bradl, M. Hausmann, V. Ehemann, D. Komitowski, and C. Cremer. A tilting device for three dimensional microscopy: application to in situ imaging of interphasecell nuclei. *J Microsc.*, 168:47–57, 1992.

[21] J. Bradl, B. Rinke, B. Schneider, P. Edelmann, H. Krieger, M. Hausmann, and C. Cremer. Resolution improvement in 3-D microscopy by object tilting. *Microsc. Anal.*, 44:9–11, 1996.

[22] W. Bragg and R. Kleeman. On the ionisation curves of radium. *Phil. Mag.*, 8:726, 1904.

[23] E. Bratsolis and M. Sigelle. A spatial regularization method preserving local photometry for Richardson-Lucy restoration. *Astronomy and Astrophysics*, 375(3):1120–1128, 2001.

[24] L. Bregman. The Relaxation Model of Finding the Common Points of Convex Sets and its Application to the Solution of Problems in Convex Programming. *U.S.S.R. Comput. Math. and Math. Phys.*, 7:200–217, 1967.

[25] L. Bregman. The Relaxation Model of Finding the Common Points of Convex Sets and its Application to the Solution of Problems in Convex Programming. In *Comput. Math. and Math. Phys.*, volume 7, pages 200–217, 1967.

[26] A. Buades, B. Coll, and J. Morel. A non-local algorithm for image denoising. In *Proceedings of the 2005 IEEE Computer Society Conference on Computer Vision and Pattern Recognition (CVPR'05)*, volume 2, pages 60–65, 2005.

[27] A. Buades, B. Coll, and J. Morel. A review of image denoising algorithms, with a new one. *Simul*, 4:490–530, 2005.

[28] Antoni Buades, Bartomeu Coll, and Jean Michel Morel. On image denoising methods. Technical report, Technical Note, CMLA, 2004.

[29] Antoni Buades, Bartomeu Coll, and Jean-Michel Morel. Nonlocal Image and Movie Denoising. *International Journal of Computer Vision*, pages 123–139, 2008.

[30] Emmanuel Candes and Justin Romberg. Partical Signal Recovery from Random Projections. *Proceedings of SPIE: Computational Imaging III*, 5674:76–86, 2005.

[31] Emmanuel Candes, Justin Romberg, and Terence Tao. Robust uncertainty principles: Exact signal reconstruction from highly incomplete frequency information. *IEEE Transactions on Information Theory*, 52:489–509, 2006.

[32] T. Chan and C. Wong. Total variation blind deconvolution. *IEEE Trans. Image Processing*, 7:370–375, 1998.

[33] Tony Chan, Antonio Marquina, and Pep Mulet. High-Order Total Variation-Based Image Restoration. *SIAM Journal on Scientific Computing*, 22:503–516, 2000.

[34] R. Clapp. Multiple realizations and data variance: Successes and failures. Technical report, Stanford Exploration Project, 2003. Tech. Rep. 113.

[35] Nathan Claxton, Thomas Fellers, and Michael Davidson. Laser Scanning Confocal Microscopy. Technical report, Department of Optical Microscopy and Digital Imaging, National High Magnetic Field Laboratory, Florida State University, 2006.

[36] Carol Cogswell, Kieran Larkin, and Hanno Klemm. Fluorescence microtomography: multi-angle image acquisition and 3D digital reconstruction. *SPIE*, 2655:109–115, 1996.

[37] José-Angel Conchello and Jeff W Lichtman. Optical sectioning microscopy. *Nature Methods*, 2(12):920–931, 2005.

[38] Cristoph Cremer and Thomas Cremer. Considerations on a laser-scanning microscope with high resolution and depth of field. *Microscopicy Acta*, 81(1):31–44, 1978.

[39] Imre Csiszar. Why Least Squares and Maximum Entropy? An Axiomatic Approach to Inference for Linear Inverse Problems. *Annals of Statistics*, 19(4):2031–3066, 1991.

[40] F. Dellard. The expectation maximization algorithm. In *Technical Report GIT-GVU-02-20*, 2002.

[41] A. P. Dempster, N. M. Laird, and D. B. Rubin. Maximum Likelihood from Incomplete Data via the EM Algorithm. *Journal of the Royal Statistical Society*, 39:1–38, 1977.

[42] W. Denk, J. Strickler, and W. Webb. Two photon fluorescence scanning microscopy. *Science*, 248(4951):73–76, 1990.

[43] Nicolas Dey, Laure Blanc-Féraud, Christophe Zimmer, Pascal Roux, Zvi Kam, Jean-Christophe Olivo-Marin, and Josiane Zerubia. 3D Microscopy Deconvolution using Richardson-Lucy Algorithm with Total Variation Regularization. Technical Report 5272, INRIA Technical report, 2004.

[44] Nicolas Dey, Laure Blanc-Féraud, Christophe Zimmer, Pascal Roux, Zvi Kam, Jean-Christophe Olivo-Marin, and Josiane Zerubia. Richardson-Lucy Algorithm with Total Variation Regularization for 3D Microscope Deconvolution. *Microscope Research Technique*, 69:260–266, 2006.

[45] S. Dietzel, E. Weilandt, R. Eils, C. Münkel, C. Cremer, and T. Cremer. Three-dimensional distribution of centromeric or paracentromeric heterochromatin of chromosomes 1, 7, 15, and 17 in human lymphocyte nuclei studied with light microscopic axial tomography. *Bioimaging*, 3:121–133, 1995.

[46] David Donoho. Compressed sensing. *IEEE Transactions on Information Theory*, 52:1289–1306, 2006.

[47] P. Edelmann, A. Esa, H. Bornfleth, R. Heintzmann, M. Hausmann, and C. Cremer. Correlation of chromatic shifts and focal depth in Spectral Precision Distance microscopy measured by micro axial tomography. *SPIE*, 3568:89–95, 1999.

[48] Matthias Elter, Volker Daum, and Thomas Wittenberg. Maximum-Intensity-Linking for Segmentation of Fluorescence-Stained Cells. In *Proc MIAAB*, pages 46–50, 2006.

[49] M. Engelsman and H. Kooy. Target volume dose considerations in proton beam treatment planning for lung tumors. *Med. Phys.*, 32(12):3549–57, 2005.

[50] W. Enghardt, J. Debus, T. Haberer, B. Hasch, R. Hinz, O. Jäkle, M. Krämer, K. Lauckner, J. Pawelke, and F. Pönsch. Positron emission tomography for quality assurance of cancer therapy with light ion beams. *Med. Phys.*, 654:1047c–50c, 1999.

[51] Heinz Engl, Andreas Hofinger, and Stefan Kindermann. Convergence rates in Prokhorov metric for assessing uncertainty in ill-posed problems. *Journal of Inverse Problems*, 21(1):399–412, 2005.

[52] R. Fergus, B. Singh, A. Hertzmann, S. Roweis, and W. Freeman. Removing camera shake from a single photograph. *SIGGRAPH*, 2006.

[53] G. Fernandez, Murat Kunt, and J.-P. Zryd. A New Plant Cell Image Segmentation Algorithm. In *ICIAP*, pages 229–234, 1995.

[54] A. Fire, S. Xu, M. Montgomery, S. Kostas, S. Driver, and C.C. Mello. Potent and specific genetic interference by double-stranded RNA in Caenorhabditis elegans. In *Nature*, volume 391, pages 806–811, 1998.

[55] E. Fourkal, J. Fan, and I. Veltchev. Absolute dose reconstruction in proton therapy using PET imaging modality: feasibility study. *Physics in Medicine and Biology*, 54(11):217–228, 2009.

[56] M. Gambaccini G. Del, G. Domenico and M. Marziani. A Monte Carlo simulation of the possible use of positron emission tomography in proton radiotherapy. *Nucl. Instr. Meth.*, 345:379–384, 1994.

[57] S. Gibson and F. Lanni. Experimental test of an analytical model of aberration in an oil-immersion objective lens used in three-dimensional light microscopy. *J. Opt. Soc. Am. A*, 9:154–166, 1992.

[58] Van Kempen G.M.P. and Van Vliet L.J. The influence of the regularization parameter and the first estimate on the performance of Tikhonov regularized nonlinear image restoration algorithms. In *Journal of Microscopy*, volume 198, pages 63–75, 2000.

[59] D. Goldstein and S. Osher. The Split Bregman method for L1 regularized problems. *SIAM Journal on Scientific Computing*, 2(2):323–343, 2009.

[60] I. Gradshteyn and I. Ryzhik. *Table of Integrals, Series and Products*. San Diego: Academic, 1980.

[61] J. Seco H. Jiang and H. Paganetti. Effects of Hounsfield number conversions on patient CT based Monte Carlo proton dose calculation. *Med. Phys.*, 34:1439–1449, 2007.

[62] Jacques Hadamard. Sur les problemes aux derivees partielles at le signification physique. *Princeton University Bulletin*, pages 49–52, 1902.

[63] N. Harder, F. Mora-Bermudez, William Godinez, Jan Ellenberg, Roland Eils, and Karl Rohr. Automated Analysis of the Mitotic Phases of Human Cells in 3D Fluorescence Microscopy Image Sequences. In *MICCAI*, pages 840–848, 2006.

[64] L. He, A. Marquina, and S. Osher. Blind deconvolution using TV regularization and Bregman iteration. *International Journal of Imaging Systems and Technology*, 15:74–83, 2005.

[65] Lin He, Antonio Marquina, and Stanley Osher. Blind deconvolution using TV regularization and Bregman iteration. In *IJIST*, volume 15, pages 74–83, 2005.

[66] C. Hegedüs, T. Bistey, E. Flóra-Nagy, G. Keszthelyi, and A. Jenei. An atomic force microscopy study on the effect of bleaching agents on enamel surface. *Journal of Dentistry*, 27:509–515, 1999.

[67] R. Heintzmann and C. Cremer. Axial tomographic confocal fluorescence microscopy. *Journal of Microscopy*, 206:7–23, 2002.

[68] R. Heintzmann, G. Kreth, and C. Cremer. Reconstruction of axial tomographic high resolution data from confocal fluorescence microscopy - a method for improving 3D FISH images. *Anal Cellular Pathol*, 20:7–15, 2000.

[69] S. Hell, S. Lindek, C. Cremer, and E. Stelzer. Confocal microscopy with an increased detection aperture: type B 4Pi-confocal microscopy. *Opt Lett*, 19(3):222–224, 1994.

[70] S. Hell, S. Lindek, C. Cremer, and E. Stelzer. Two- and multiphoton detection as an imaging mode and means of increasing the resolution in far-field light microscopy: a study based on photon-optics. *Opt Lett*, 19(3):222–224, 1994.

[71] S. Hell, S. Lindekand, C. Cremer, and E. Stelzer. Measurement of the 4Pi-confocal point spread function proves 75nm axial resolution. *Appl Phys Lett*, 64(11):1335–1337, 1994.

[72] S. Hell and E. Stelzer. Fundamental improvement of resolution with a 4Pi confocal fluorescence microscope using two photon excitation. *Opt Comm*, 93(5):277–282, 1992.

[73] A. Hofinger and H. Pikkarainen. Convergence rates in for linear inverse problems in presence of additive normal noise. *Journal of Stochastic Analysis and Applications*, 27(2):240–257, 2009.

[74] Erfle Holger, Simpson Jeremy, Bastiaens Philippe, and Pepperkok Rainer. siRNA cell arrays for high-content screening microscopy. In *Biotechnology*, volume 37, pages 454–462, 2004.

[75] Linda Hong, Michael Goitein, Marta Bucciolini, Robert Comiskey, Bernard Gottschalk, Skip Rosenthal, Chris Serago, , and Marcia Urie. A pencil beam algorithm for proton dose calculations. *Physics in Medicine and Biology*, 41(8):1305–1330, 1996.

[76] Luis Ibanez, Will Schroeder, Lydia Ng, and Josh Cates. *The ITK Software Guide*. www.itk.org.

[77] Neel Joshi, Sing Bing Kang, C. Lawrence Zitnick, and Richard Szeliski. Image Deblurring using Inertial Measurement Sensors. *SIGGRAPH*, 2010.

[78] M. Jung, X. Bresson, T. Chan, and L. Vese. Color image restoration using nonlocal Mumford-Shah regularizers. *Energy Minimization Methods in Computer Vision and Pattern Recognition*, 5681:373–387, 2009.

[79] M. Jung and L. Vese. Nonlocal variational image deblurring models in the presence of Gaussian or impulse noise. *Scale-Space and Variational Methods in Computer Vision*, 5567:402–413, 2009.

[80] Jari Kaipio and Erkki Somersalo. *Statistical and Computational Inverse Problems*. Springer, 2004.

[81] S. Kawata. The optical computed tomography microscope. *Advances in Optical and Electrical Microscopy*, 14:213–248, 1994.

[82] Wu Kenong, D. Gauthier, and M.D. Levine. Live cell image segmentation. In *IEEE Transactions on Biomedical Engineering*, volume 42, pages 1–12, 1995.

[83] A. Knopf, K. Parodi, T. Bortfeld, H. Shih, and H. Paganetti. Systematic analysis of biological and physical limitations of proton beam range verification with offline PET/CT scans. *Phys. Med. Biol.*, 54:4477–4495, 2009.

[84] A. Knopf, K. Parodi, H. Paganetti, E. Cascio, A. Bonab, and T. Bortfeld. Quantitative Assessment of the physical-potential of proton beam range verification with PET/CT. *Phys. Med. Biol.*, 53:4137–4151, 2008.

[85] Antje-Christin Knopf. *Physical and Clinical Potential of offine PET/CT Imaging after Proton Radiotherapy*. PhD thesis, University of Heidelberg, 2009.

[86] Michal Kozubek, Petr Matula, Heinz Eipel, and Michael Hausmann. Automated Multi-view 3D Image Acquisition in Human Genome Research. *International Symposium on 3D Data Processing Visualization and Transmission*, pages 91–98, 2002.

[87] Michal Kozubek, Magdalena Skalnikova, Petr Matula, Eva Bartova, Joachim Rauch, Friedrich Neuhaus, Heinz Eipel, and Michael Hausmann. Automated microaxial tomography of cell nuclei after specific labelling by fluorescence in situ hybridisation. *Micron*, 33(7):655–665, 2002.

[88] Reginald Lagendijk and Jan Biemond. *Iterative Identification and Restoration of Images*. Springer US, 1991.

[89] John J. Lemasters, Enrique Chacon, George Zahrebelski, Jeffrey M. Reece, and Anna-Lisa Nieminen. Laser Scanning Confocal Microscopy of Living Cells. In *Optical Microscopy*, pages 339–354. Academic Press, 1993.

[90] Anat Levin, Yair Weiss, Fredo Durand, and William Freeman. Understanding and evaluating blind deconvolution algorithms. *CVPR*, pages 1964–1971, 2009.

[91] Olivier Lezoray and Hubert Cardot. Cooperation of color pixel classification schemes and color watershed: A study for microscopical images. In *IEEE Transactions on Image Processing*, volume 11,, pages 783–789, 2002.

[92] Jeff W Lichtman and José-Angel Conchello. Fluorescence microscopy. *Nature Methods*, 2(12):910–919, 2005.

[93] J. Lie and J. Nordbotton. Inverse Scale Space for Nonlinear Regularization. In *Journal of Mathematical Imaging and Vision archive*, volume 27, pages 41–50, 2007.

[94] Steffen Lindeck and Ernst Stelzer. Confocal theta microscopy and 4Pi-confocal theta microscopy. *Proc. SPIE*, 2184:188–194, 1994.

[95] Steffen Lindeck and Ernst Stelzer. Optical transfer functions for confocal theta fluorescence microscopy. *Journal of the Optical Society of America A*, 13:479–482, 1996.

[96] M. Lindenbaum, M. Fischer, and A. Bruckstein. On Gabor Contribution To Image Enhancement. *Pattern Recognition*, 27:1–8, 1994.

[97] J. Lippincott-Schwarz, N. Altan-Bonnet, and G. Patterson. Photobleaching and photo-activation: following protein dynamics in living cells. *Nat. Cell Biol.*, pages 7–14, 2003.

[98] D. Litzenberg, D. Roberts, M. Lee, K. Pham, A. van der Molen, R. Ronningen, and D. Bechetti. On-line monitoring of radiotherapy beams: experimental results with proton beams. *Nucl. Phys. A*, 26:992–1007, 1999.

[99] A. Longin, C. Souchier, M. French, and P. Bryon. Comparison of Anti-fading Agents Used in Fluorescence Microscopy: Image Analysis and Laser Confocal Microscopy Study. *Journal of Histochemistry and Cytochemistry*, 41(12):1833–1840, 1993.

[100] I. Loris, M. Bertero, C. De Mol, R. Zanella, and L. Zanni. Accelerating gradient projection methods for l_1-constrained signal recovery by steplength selection rules. *Applied and Computational Harmonic Analysis*, 27(2):247–254, 2009.

[101] L.B. Lucy. An iterative technique for rectification of observed distributions. *The Astronomical Journal*, 79:745–765, 1974.

[102] Michael Lustig, David Donoho, and John Pauly. Sparse MRI: The application of compressed sensing for rapid MR imaging. *Magnetic Resonance in Medicine*, 58(6):1182–1195, 2007.

[103] Michael Lustig, Jin-Hyung Lee, David Donoho, and John Pauly. Faster imaging with randomly perturbed undersampled spirals and l1 reconstruction. *ISMRM*, page 685, 2005.

[104] Elie Maalouf, Bruno Colicchio, and Alain Dieterlen. Fluorescence microscopy three-dimensional depth variant point spread function interpolation using Zernike moments. *J. Opt. Soc. Am.*, 28(9):1864–1870, 2011.

[105] Antonio Marquina and Stanley Osher. Image super-resolution by TV-regularization. In *Journal of Scientific Computing*, volume 37, pages 367–382, 2008.

[106] P. Matula, A. Kumar, I. Worz, N. Harder, H. Erfle, R. Bartenschlager, R. Eils, and K. Rohr. Automated Analysis of RNAi Screens of Virus Infected Cells based on Immunofluorescence Microscopy. In *Proc BVM*, pages 453–457, 2008.

[107] V. Meas-Yedid, Florence Cloppet, A. Roumier, A. Alcover, J-C Olivo-Marin, and G. Stamon. Quantitative microscopic image analysis by active contours. In *IAPR-Vision Interface*, pages 277–284, 2001.

[108] Volker Metzler, Thomas Lehmann, Hans Bienert, Khosrow Mottaghy, and Klaus Spitzer. Scale-independent shape analysis for quantitative cytology using mathematical morphology. In *Computers in Medicine and Biology*, pages 135–151, 2000.

[109] Marvin Minsky. Microscopy apparatus. *US Patent*, 3.013.467, 1961.

[110] Tim Nattkemper, Heiko Wersing, Walter Schubert, and Helge Ritter. A neural network architecture for automatic segmentation of fluorescence micrographs. In *ESANN*, pages 177–182, 2000.

[111] University of Alabama at Birmingham Comprehensive Cancer Center. History of Radiation Oncology.

[112] E. Ordentlich, G. Seroussi, S. Verdu, M. Weinberger, and T. Weissman. A discrete universal denoiser and its application to binary images. *Proceedings of the IEEE International Conference on Image Processing*, 1:117–120, 2003.

[113] S. Osher, M. Burger, D. Goldfarb, J. Xu, and W. Yin. An iterative regularization method for total variation-based image restoration. *Multiscale Model. Simul.*, 4:460–489, 2005.

[114] S.J. Osher, M. Burger, D. Goldfarb, J. Xu, and W. Jin. An Iterative regularization method for total variation based image restoration. In *Multiscale Model and Simul*, volume 4, pages 460–489, 2005.

[115] K. Parodi and T. Bortfeld. A filtering approach based on Gaussian-powerlaw convolutions for local PET verification of proton therapy. *Phys. Med. Biol.*, 51(8):1991–2009, 2006.

[116] K. Parodi and W. Enghardt. Potential application of PET in quality assurance of proton therapy. *Phys. Med. Biol.*, 45(11):151–156, 2000.

[117] K. Parodi, A. Ferrari, F. Sommerer, and H. Paganetti. Clinical CT-based calculations of dose and positron emitter distributions in proton therapy using the FLUKA Monte Carlo code. *Phys. Med. Biol.*, 52(12):3369–3387, 2007.

[118] K. Parodi, H. Paganetti, E. Cascio, J. Flanz, A. Bonab, N. Alpert, K. Lohmann, and T. Bortfeld. PET/CT imaging for treatment verification after proton therapy: a study with plastic phantoms and metallic implants. *Med. Phys.*, 34:419–435, 2007.

[119] K. Parodi, H. Paganetti, H. Shih, S. Michaud, J. Loeffler, F. DeLaney, N. Liebsch, J. Munzenrider, A. Fishman, A. Knopf, and T. Bortfeld. Patient study on in-vivo verification of beam delivery and range using PET/CT imaging after proton therapy. *Int. Journal of Radiation Oncology, Biology, Physics*, 68(3):920–934, 2007.

[120] P. Perona and J. Malik. Scale space and edge detection using anisotropic diffusion. *IEEE Trans. Patt. Anal. Mach. Intell.*, 12:629–639, 1990.

[121] Tuan D. Pham, Denis I. Crane, Tuan H. Tran, and Tam H. Nguyen. Extraction of fluorescent cell puncta by adaptive fuzzy segmentation. In *Bioinformatics,*, volume 20, pages 2189–2196, 2004.

[122] Christian Barillot Pierrick Coupe, Pierre Yger. Fast Non Local Means Denoising for 3D MR Images. *Proceedings of MICCAI*, 9:33–40, 2006.

[123] F. Pönisch, K. Parodi, B. Hasch, and W. Enghardt. The modelling of positron emitter production and PET imaging during carbon ion therapy. *Phys. Med. Biol.*, 49:5217–32, 2004.

[124] Sudhakar Prasad. Statistical-information-based performance criteria for RL image deblurring. *Journal of the Optical Society of America*, 19(7):1286–1296, 2002.

[125] W. Press, B. Flannery, S. Teukolsky, and W. Vetterling. *Numerical Recipes in FORTRAN: The Art of Scientific Computing*. Cambridge University Press, Cambridge, England, 1992.

[126] William H. Press, William T. Vetterling, Saul A. Teukolsky, and Brian P. Flannery. *Numerical Recipes in C++: the art of scientific computing*. Cambridge University Press, 2002.

[127] Chrysanthe Preza and José-Angel Conchello. Depth-variant maximum-likelihood restoration for three-dimensional fluorescence microscopy. *Optical Society of America*, 21:1593–1601, 2004.

[128] R.C. Puetter, T.R. Gosnell, and Amos Yahil. Digital Image Reconstruction Deblurring and Denoising. *Rev. Astron Astrophys.*, 43:139–194, 2005.

[129] Bianca Reinhard. Mikro-Axial-Tomographie: Optimierung für die hochauflösende 3D-Rekonstruktion von zellulären Strukturen. Diplomarbeit, University of Heidelberg, 2007.

[130] Steffen Remmele and Jürgen Hesser. Constrained RLTV Deblurring for Confocal Microscopy. In *World Congress on Medical Physics and Biomedical Engineering - IFMBE Proceedings*, volume 25, pages 1940–1943, 2009. doi: 10.1007/978-3-642-03882-2515.

[131] Steffen Remmele and Jürgen Hesser. Vector Extrapolation Based Acceleration of Regularized Richardson Lucy Image Deblurring. In *BVM09*, pages 400–404, 2009.

[132] Steffen Remmele, Jürgen Hesser, Harald Paganetti, and Thomas Bortfeld. Deconvolution approach for PET based dose reconstruction in proton radiotherapy. *Accepted in Physics in Medicine and Biology*, 2011.

[133] Steffen Remmele, Jürgen Hesser, Harald Paganetti, and Thomas Bortfeld. In-vivo proton dose reconstruction from PET images. *Medical Physics*, 38(6), 2011. doi:10.1118/1.3612223.

[134] Steffen Remmele, Bianca Oehm, Florian Staier, Heinz Eipel, Christoph Cremer, and Jürgen Hesser. Reconstruction of high-resolution fluorescence microscopy images based on axial tomography. In *Proc. SPIE 7962, 79624O*, 2011. doi:10.1117/12.878260.

[135] Steffen Remmele, Julia Ritzerfeld, Walter Nickel, and Jürgen Hesser. Automated Cell Analysis Tool for a genome-wide RNAi screen. In *MIAAB workshop, New York*, 2008.

[136] Steffen Remmele, Julia Ritzerfeld, Walter Nickel, and Jürgen Hesser. Automated cell analysis tool for a genome-wide RNAi screen with support vector machine based supervised learning. In *Proc. SPIE 7962, 79624O*, 2011. doi:10.1117/12.878097.

[137] Steffen Remmele, Madeleine Seeland, and Jürgen Hesser. Fluorescence Microscopy Deconvolution based on Bregman Iteration and Richardson-Lucy Algorithm with TV Regularization. In *Proceedings of BVM*, pages 72–76, 2008.

[138] William H. Richardson. Bayesian-based iterative method of image restoration. *Journal of the Optical Society of America*, 62:55–59, 1972.

[139] Julia Ritzerfeld. *Identification of Components of the Intracellular Transport Machinery of Acylated Proteins by a Genome-wide RNAi Screen*. PhD thesis, University of Heidelberg, 2009.

[140] Julia Ritzerfeld, Steffen Remmele, Tao Wang, Koen Temmerman, Britta Brügger, Sabine Wegehingel, Stella Tournaviti, Jeroen R.P.M. Strating, Felix T. Wieland, Beate Neumann, Jan Ellenberg, Chris Lawerenz, Jürgen Hesser, Holger Erfle, Rainer Pepperkok, and Walter Nickel. Phenotypic Profiling of the Human Genome Reveals Gene Products Involved in Plasma Membrane Targeting of SRC Kinases. *Genome Research*, 2011.

[141] Leonid Rudin and Stanley Osher. Total Variation based image restoration with free local constraints. *Proc. IEEE ICIP*, 1:31–35, 1995.

[142] Leonid I. Rudin, Stanley Osher, and Emad Fatemi. Nonlinear total variation based noise removal algorithms. *Physica D*, 60:259–268, 1992.

[143] Kurt Sätzler and Roland Eils. Resolution improvement by 3-D reconstructions from tilted views in axial tomography and confocal theta microscopy. *Bioimaging*, 5:171–182, 1997.

[144] S. Setzer. Split Bregman algorithm, Douglas-Rachford splitting and frame shrinkage. *Scale Space and Variational Methods in Computer Vision*, 5567:464–476, 2009.

[145] S. Setzer, G. Steidl, and T. Teuber. Deblurring Poissonian images by split Bregman techniques. *Visual Communication and Image Representation*, 21(3):193–199, 2010.

[146] Q. Shan, W. Xiong, and J. Jia. Rotational motion deblurring of a rigid object from a single image. *ICCV*, 2007. doi:10.1109/ICCV.2007.4408922.

[147] P. Shaw, D. Agard, Y. Hiraoka, and J. Sedat. Tilted view reconstruction in optical microscopy. Three-dimensional reconstruction of Drosophila melanogaster embryo nuclei. *Biophysical Journal*, 55:101–110, 1989.

[148] Manoj Kumar Singh, Uma Shanker Tiwary, and Young-Hoon Kim. An adaptively accelerated Lucy-Richardson method for image deblurring. *EURASIP J. Adv. Signal Process*, 8:1–10, 2008.

[149] S. Smith and J. Brady. SUSAN - a new approach to low level image processing. *International Journal of Computer Vision*, 23:45–78, 1997.

[150] American Cancer Society. Report sees 7.6 million global 2007 cancer deaths. *Reuters*, 2007.

[151] Christoph Sommer. *Interactive Learning for the Analysis of Biomedical and Industrial Imagery*. PhD thesis, University of Heidelberg, 2010.

[152] G. Steidl and T. Teuber. Removing multiplicative noise by Douglas-Rachford splitting methods. *Journal of Mathematical Imaging and Vision*, 2:168–184, 2010.

[153] David Strong and Tony Chan. Edge-preserving and Scale-dependent Properties of Total Variation Regularization. In *Inverse Problems*, pages 165–187, 2000.

[154] Jason R. Swedlow, Ke Hu, Paul D. Andrews, David S. Roos, and John M. Murray. A comparison of laser-scanning confocal and wide-field fluorescence microscopy. *Proceedings of National Academy of Science*, 99:2014–2019, 2002.

[155] Jim Swoger, Peter Verveer, Klaus Greger, Jan Huisken, and Ernst Stelzer. Multiview image fusion improves resolution in three-dimensional microscopy. *Optics Express*, 15:8029–8042, 2007.

[156] E. Tadmor, S. Nezzar, and L. Vese. A multiscale image representation using hierarchical (BV,L2) decompositions. *Multiscale Model. Simul.*, 2:554–579, 2004.

[157] Yu-Wing Tai, Ping Tan, and Michael S. Brown. Richardson-Lucy Deblurring for Scenes under A Projective Motion Path. *IEEE Transactions on Pattern Analysis and Machine Intelligence*, 33:1603–1618, 2011.

[158] Tanja Teuber, Steffen Remmele, Jürgen Hesser, and Gabriele Steidl. Denoising by Higher Order Statistics. *submitted to Journal on Signal Processing*, 2011.

[159] A. Tikhonov. Regularization of incorrectly posed problems. *Soviet Mathematics Doklady*, 4:1624–1627, 1963.

[160] G. Lam U. Oelfke and M. Atkins. Proton dose monitoring with PET: quantitative studies in lucite. *Phys. Med. Biol.*, 41:177–196, 1996.

[161] W. Ulmer and W. Kaissl. The inverse problem of a Gaussian convolution and its application to the finite size of the measurement chambers/detectors in photon and proton dosimetry. *Physics in Medicine and Biology*, 48:707–727, 2003.

[162] Waldemar Ulmer. Inverse problem of linear combinations of Gaussian convolution kernels (deconvolution) and some applications to proton/photon dosimetry and image processing. *Inverse Problems*, 26(8), 2010.

[163] G.M. van Kempen and L. van Vliet. Background estimation in nonlinear image restoration. *Journal of the Optical Society of America*, 17:425–433, 2000.

[164] G.M. van Kempen, L. van Vliet, P.J. Verveer, and H.T.M. van der Voort. A quantitative comparison of image restoration methods for confocal microscopy. *Journal of Microscopy*, 185:354 – 365, 1997.

[165] Curtis R. Vogel. *Computational Methods for Inverse Problems*. SIAM, 2002.

[166] Cedric Vonesch and Michael Unser. A fast thresholded landweber algorithm for wavelet-regularized multidimensional deconvolution. *IEEE Trans. Image Process.*, 17:539–549, 2008.

[167] H.T.M. Van Der Voort and K.C. Strasters. Restoration of confocal images for quantitative image analysis. *Journal of Microscopy*, 178:165–181, 1995.

[168] S. Vynckier, S. Derreumaux, F. Richard, A. Bol, C. Michel, and A. Wambersie. Is it possible to verify directly a proton-treatment plan using positron emission tomogaphy? *Radiother. Oncol.*, 26:275–277, 1994.

[169] Carolina Waehlby, Joakim Lindblad, Mikael Vondrus, Ewert Bengtsson, and Lennart Björksten. Algorithm for cytoplasm segmentation of fluorescence labelled cells. In *Analytical Cellular Pathology*, volume 24, pages 101–111, 2002.

[170] W. Wallace, L.H. Schaefer, and J.R. Swedlow. A working persons guide to deconvolution in light microscopy. *BioTechniques*, 31(5):1076 – 1097, 2001.

[171] Jin Wang, Yanwen Guo, Yiting Ying, Yanli Liu, and Qunsheng Peng. Fast Non-Local Algorithm for Image Denoising. *Proceedings of the IEEE International Conference on Image Processing*, 1:1429–1432, 2006.

[172] P. Weiss, L. Blanc-Feraud, and G. Aubert. Efficient schemes for total variation minimization under constraints in image processing. *SIAM Journal on Scientific Computing*, 31(3):2047–2080, 2009.

[173] WHO. Cancer. *World Health Organization*, 2006.

[174] O. Whyte, J. Sivic, A. Zisserman, and J. Ponce. Non-uniform Deblurring for Shaken Images. In *Proceedings of the IEEE Conference on Computer Vision and Pattern Recognition*, pages 491–498, 2010.

[175] Robert Wilson. Radiological use of fast protons. *Radiology*, 47:487–491, 1946.

[176] Tony Wilson. *Confocal microscopy*. Academic Press, 1990.

[177] L. Yaroslavsky. *Digital Picture Processing - An Introduction*. Springer Verlag, 1985.

[178] H. Yoo, I. Song, and D.-G. Gweon. Measurement and restoration of the point spread function of fluorescence confocal microscopy. *Journal of Microscopy*, 221:172–176, 2005.

[179] I. Young, J. Gerbrands, and L. van Vliet. *Fundamentals of image processing. The Digital Signal Processing Handbook.* CRC Press, Boca Raton, Florida, 1998.

[180] L. Yuan, J. Sun, L. Quan, and H.-Y. Shum. Image deblurring with blurred/noisy image pairs. *SIGGRAPH*, 2007.